



**HAL**  
open science

# Towards a better understanding of the role of ITM2B in the retina

Juliette Wohlschlegel

► **To cite this version:**

Juliette Wohlschlegel. Towards a better understanding of the role of ITM2B in the retina. Sensory Organs. Sorbonne Université, 2020. English. NNT : 2020SORUS393 . tel-03795271

**HAL Id: tel-03795271**

**<https://theses.hal.science/tel-03795271>**

Submitted on 4 Oct 2022

**HAL** is a multi-disciplinary open access archive for the deposit and dissemination of scientific research documents, whether they are published or not. The documents may come from teaching and research institutions in France or abroad, or from public or private research centers.

L'archive ouverte pluridisciplinaire **HAL**, est destinée au dépôt et à la diffusion de documents scientifiques de niveau recherche, publiés ou non, émanant des établissements d'enseignement et de recherche français ou étrangers, des laboratoires publics ou privés.



Ecole doctorale physiologie, physiopathologie et thérapeutique (ED 394)

# **Towards a better understanding of the role of ITM2B in the retina**

Par **Juliette WOHLSCHEGEL**

Thèse de Doctorat de Neurosciences

Dirigée par **Isabelle AUDDO**

Présentée et soutenue publiquement le 2 Octobre 2020

Devant un jury composé de :

**Dr Luc Maroteaux**, Président du jury

**Pr Christelle Monville**, Rapporteur

**Dr David Gamm**, Rapporteur

**Dr Gordon Plant**, Examineur

**Pr Isabelle Audou**, Directrice de thèse



# Acknowledgments

First of all, I would like to thank the members of the jury for having accepted to be part of my thesis committee and for the time spent reviewing my work.

Je voudrais remercier Isabelle pour m'avoir permis de faire cette thèse. Merci d'avoir cru en moi et de m'avoir laissé la liberté de m'exprimer sur ce projet. Merci de m'avoir donné l'opportunité de participer à des congrès incroyables tout au long de ces années et de m'avoir transmis le goût de la rétine ! Je t'en suis extrêmement reconnaissante.

Je remercie aussi Christina pour m'avoir accepté dans l'équipe ainsi que toutes les personnes de mon équipe pour leurs encouragements durant cette thèse. Un grand merci à Camille pour son aide avec les iPSCs depuis le début de cette aventure !

Je tiens particulièrement à remercier Olivier ainsi que toute son équipe pour leur soutien tout au long de cette thèse. Merci d'avoir partagé votre savoir et de m'avoir initié au monde merveilleux des iPSCs. Merci d'avoir toujours pris le temps pour répondre à mes questions. Merci à Gaël pour tous ses bons conseils et sa patience.

Un énorme Merci à Manuela, Yvrick, Stéphane et Thibaut pour toute votre aide technique si précieuse mais pas uniquement. Merci de m'avoir aidée et encouragée pendant ces quatre années.

Merci à mes incroyables collègues et amies, Cécile et Juliette, pour votre amitié et votre soutien indéfectible. Merci pour tous ces bons moments, cette thèse n'aurait pas été la même sans vous. Vous avez su rendre les moments difficiles agréables. Merci de m'avoir supportée, j'ai tellement appris et grandi à vos côtés.

Nuría mil gracias por tu sonrisa y tu alegría de vivir contagiosa. Merci Marco pour tout ce que tu as fait pour moi, je ne l'oublierai pas.

Parmi mes superbes rencontres à l'institut, il y a aussi toute la « iPSCs family » passée et présente. Un énorme merci à Oriane pour nos discussions du vendredi soir.

Merci aussi à Johann, Sarah, Robin, Sergi, Alice, Oriol, Giuliana, Franck, Anna, Darine, Nassima, Amélie, Géraldine, Marie, Laurence et tous ceux que j'ai pu oublier, pour avoir partagé des moments au détour d'un café, d'une paillasse ou d'un verre au Gamin. Merci d'avoir égayé mon quotidien !

Merci à mes trois étudiantes en master 2 : Adia, Xiaochen et Tasnim pour leurs aides sur ce projet. Vous encadrer était une belle aventure !

Une mention spéciale pour toutes les personnes que j'ai pu rencontrer durant les cours de danse et d'aïkido. Ces cours ont été une source d'oxygène, et un défouloir qui m'ont appris à me dépasser.

Un énorme merci à tous mes amis ! Merci, Maxime, Pauline, Alexandre, Alexis, Valentin, Guillaume, Dana, Aziz, Olivier, et Elyad d'être à mes côtés depuis plus de dix ans (voir 15 !). Evoluer, grandir (et vieillir) à vos côtés est un privilège. Merci d'avoir été là dans les bons comme dans les moins bons moments. Merci pour notre amitié si spéciale, nos soirées, nos conversations et fous rires inoubliables. Tout cela est bien gravé dans ma mémoire. Merci à Garance et Anaïs pour toutes nos aventures et nos bonnes tranches de rigolade passées et à venir. Merci à Laure et Cécile pour tous ces si bons moments en votre compagnie. Merci à mes zouzies, Marion et Judith pour avoir partagé avec moi ces voyages magnifiques au bout du monde. Ces souvenirs ont une saveur particulière. J'espère qu'il en aura pleins d'autres à vos côtés. Merci à Marion pour m'avoir supportée et encouragée jusqu'au bout (du bout) et pendant les 3 ans et demi de coloc. Merci d'avoir relu cette thèse à 3 h du matin. C'était un plaisir de partager ce quotidien avec toi. Merci à Coralie pour avoir été là quand il le fallait. Cette rencontre n'était pas un hasard ! Merci à mon amie Liette, pour m'avoir fait découvrir tant de choses et pour ton aide inestimable sur ces derniers mois.

Je garde un sentiment particulier pour chacun d'entre vous, et des souvenirs pleins la tête. Merci encore d'être à mes côtés et d'avoir pris soin de moi, je sais à quel point j'ai de la chance d'être si bien entourée.

Je tiens à remercier ma famille, en particulier ma petite mamie. Merci pour tous tes messages de soutien et d'amour. Enfin, Merci à mes parents pour votre amour inconditionnel. Merci d'avoir toujours cru en moi, de m'avoir soutenue et encouragée depuis si longtemps. Merci d'avoir fait ce que je suis devenue. Vous êtes mon pilier, et ces derniers mots seront pour vous. Je vous serai à jamais reconnaissante de tout ce que vous avez fait pour moi.

*Happiness only real when shared*

Christopher McCandless

# Table of contents

<b>Introduction</b> .....	<b>1</b>
<b>1. The eye</b> .....	<b>1</b>
The human retina: an overview of the organization.....	2
The vertical pathway.....	5
Photoreceptor cells.....	5
Bipolar cells.....	8
Ganglion cells.....	9
Retinal development.....	9
<b>2. Inherited retinal dystrophies</b> .....	<b>15</b>
Clinical Examinations.....	15
ITM2B-related peculiar retinal dystrophy (RD).....	19
<b>3. ITM2B and related disorders</b> .....	<b>21</b>
Amyloid diseases, ITM2B-associated pathologies and dementia.....	21
Alzheimer disease (AD).....	21
The Familial British Dementia.....	24
The Familial Danish Dementia.....	25
Current knowledge about ITM2B.....	28
ITM2B animal models.....	34
<b>4. Human stem cells</b> .....	<b>36</b>
Stem cell definition and properties.....	36
Embryonic Stem cells.....	37
Induced Pluripotent Stem Cells (iPSCs).....	38
<b>5. Retinal organoids and disease modeling</b> .....	<b>43</b>
Controlling cellular differentiation and retinal induction.....	43
Retinal organoids.....	45
Drawbacks and improvements.....	49
Retinal disease modeling with organoids.....	50
<b>Aims</b> .....	<b>54</b>
Deep phenotyping of the ITM2B-related RD.....	54
Physiology of ITM2B in the retina in normal condition.....	54
Physiopathology and pathological mechanisms involved in the RD.....	54
<b>Results</b> .....	<b>56</b>
1. Development of the disease, follow-up.....	57
2. Identification of the ITM2B protein interactome in the human retina.....	89
3. Generation of human induced pluripotent stem cell lines from a patient with ITM2B-related retinal dystrophy and a non mutated brother.....	158
4. Disease modeling of ITM2B related retinal dystrophy.....	164
5. Complementary results.....	193
<b>Discussion and Perspectives</b> .....	<b>200</b>
<b>Conclusions</b> .....	<b>212</b>
<b>Bibliography</b> .....	<b>213</b>

# List of figures

Figure 1. The organization of the eye. ....	1
Figure 2. Scheme of the organization of the retina. ....	3
Figure 3. Schematic representation of the two types of photoreceptor cells: cone and rod. ..	6
Figure 4. Distribution of rod and cone photoreceptors at the surface of the human retina. ...	7
Figure 5. Eye field patterning and RPE/ Neural retina specification by extrinsic signals.....	10
Figure 6. The embryonic development of the eye.....	11
Figure 7. Development of human retinal cell types overtime. ....	12
Figure 8. Transitional cell populations along the retinal development. ....	14
Figure 9. Functional alterations of the retina with the Electroretinogram (ERG). ....	16
Figure 10. Fundus imaging. ....	17
Figure 11. Spectral domain optical coherence tomography (SD-OCT) imaging. ....	18
Figure 12. Family pedigree of the RD family. ....	19
Figure 13. APP processing through non-amyloidogenic and amyloidogenic pathway.....	23
Figure 14. ITM2B processing and the different mutations in ITM2B.....	30
Figure 15. ITM2B-BRICHOS activity is determined by its quaternary structure. ....	33
Figure 16. Evolution of potency over cell development. ....	37
Figure 17. Overview of different protocols to generate retinal organoids.....	48
Figure 18 Generation of iPSC lines from skin fibroblasts of one affected subject and one unaffected sibling.....	164

# List of Tables

Table 1. Mutations reported in ITM2B.....	28
---	----

# List of abbreviations

2D: Two dimensional  
3D: Three dimensional  
AD: Alzheimer disease  
ADAM: A disintegrin and metalloproteinase  
AICD: APP intracellular domain  
AMD: Age-related macular degeneration  
AMD: Age-related macular degeneration  
APP: Amyloid precursor protein  
APPL1/2: Amyloid precursor protein related protein 1/2  
A $\beta$ :  $\beta$ -Amyloid  
BMP: Bone morphogenetic protein  
DDK1: Dickkopf-1  
EBs: Embryoid bodies  
EF: Eye field  
ELM: External limiting membrane  
ERG: Electroretinogram  
ESCs: Embryonic stem cells  
FAI: Fundus autofluorescence imaging  
FBD: Familial British dementia  
FBS: Fetal bovine serum  
FDD: Familial Danish dementia  
FGF: Fibroblast growth factors  
FGF-2: Fibroblast growth factor 2  
GABA:  $\gamma$ -aminobutyric acid  
GCL: Ganglion cell layer  
hESCs: Human embryonic stem cells  
hiPSCs: Human induced pluripotent stem cells  
ICD: Intracellular domain  
IGF: insulin-like growth factors  
ILM: Inner limiting membrane  
INL: Inner nuclear layer  
IPL: Inner plexiform layer  
iPSCs: Induced pluripotent stem cells  
IRDs: Inherited retinal dystrophies  
ITM2A: Integral membrane protein 2 A  
ITM2B: Integral membrane protein 2 B  
ITM2Bm: ITM2B mature  
ITM2C: Integral membrane protein 2 C

KSR: Knockout serum replacement  
LCA: Leber congenital amaurosis  
LGN: Lateral geniculate nucleus  
NFT: Neurofibrillary tangles  
NGS: Next generation sequencing  
OCT-A: Optical coherence tomography angiography  
ONL: Outer nuclear layer  
OPL: Outer plexiform layer  
pGlu-A $\beta$ : A $\beta$  Pyroglutamate modified  
PSCs: Pluripotent stem cells  
RD: Retinal dystrophy  
RDGCA: Retinal dysfunction and ganglion cell abnormalities  
RGCs: Retinal ganglion cells  
RNA-Seq: RNA sequencing  
RPCs: Retinal progenitors cells  
RPE: Retinal pigment epithelium  
scRNA-Seq: Single cell RNA sequencing  
SD-OCT: spectral domain optical coherence tomography  
SHH: Sonic hedgehog  
SPPL2a/b: Signal peptide peptidase-like 2a/b  
TRPM1: Transient receptor potential cation channel subfamily member 1  
UV: Ultraviolet  
WES: Whole exome sequencing  
WGS: Whole genome sequencing

# Introduction

## 1. The eye

The eye, the sensory part of the visual pathway, is able to detect light from the environment and convert it into an electrical signal. This electrical signal is then processed and modified before reaching the cortical visual areas where images are formed. The sclera, the choroid and the retina are the three tissues composing the eye. The outermost layer, the sclera, is a fibrous protective tissue supporting the choroid which is the vascular layer of the eye. The retina is a light-sensitive tissue located at the inner surface of the eye (**Figure 1**).

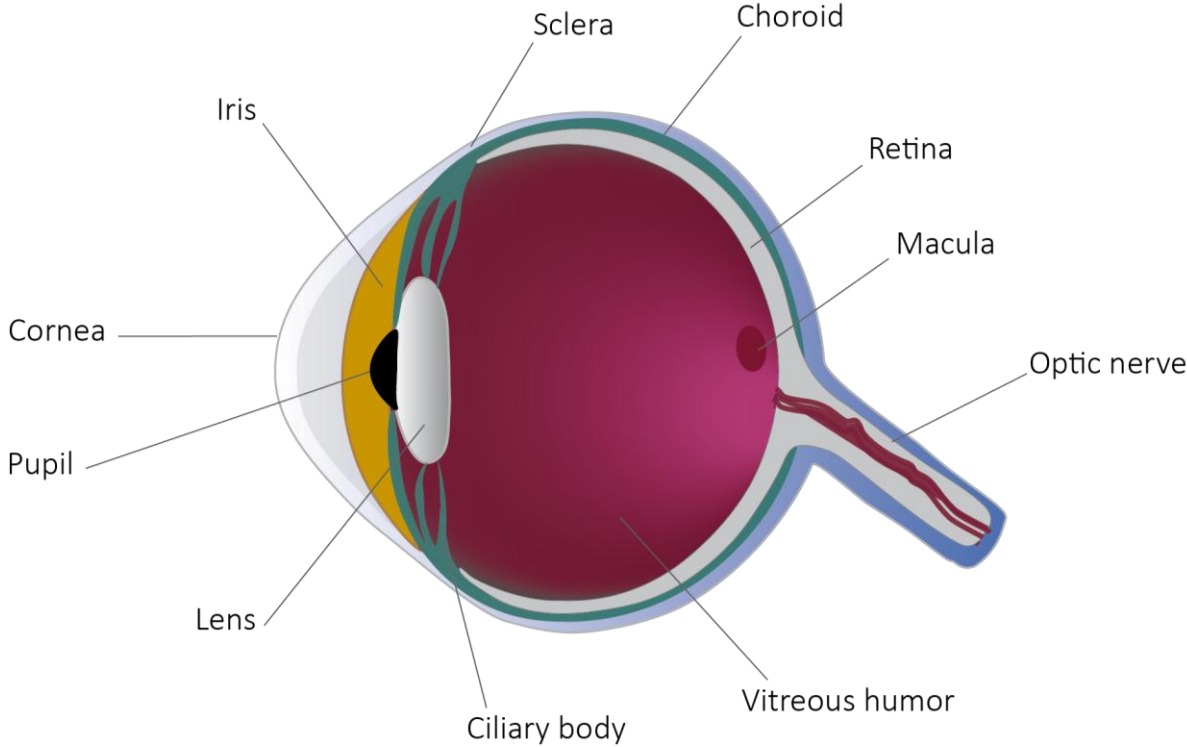


**Figure 1. The organization of the eye.**  
Scheme of a section of the eye.

In normal conditions, the light crosses all the transparent anterior media of the eye before reaching the retina. The first one, the cornea, is transparent and has a protective role against pathogens and damaging ultraviolet (UV). The second one, the crystalline lens, is transparent as well but also has the specificity to be soft, allowing its deformation, by contraction of the ciliary muscles. Images can be focused on the retina thanks to a mechanism called accommodation by which the lens has the ability to change shape. Past the crystalline lens, light crosses the posterior chamber of the eye filled with vitreous humor, an aqueous fluid, and finally reaches the innermost retinal layer.

## **The human retina: an overview of the organization**

The retina is a highly specialized and multistratified tissue composed of different cell types of specific functions (**Figure 2**). Visual stimuli are processed through these different layers before being sent to the cortical visual centers, generating the final images. The light must then pass through all layers of the retina to reach the first actors of the visual processing: the photoreceptors. Nuclei of the photoreceptors, of which two types exist: rods for dim light vision and cones for day light, are present in the outer nuclear layer (ONL). The phototransduction cascade, which is the process to convert light into a chemical signal, begins upon photon absorption allowing conformational change of the photopigment in the photoreceptors. All rods contain the same light-sensitive pigment, rhodopsin, and each cone contains one of the three opsins present in the human retina. The three opsins have a different spectral absorption to allow for color vision. Both rods and cones respond to light by hyperpolarizing which leads to a modulation of the glutamate release between photoreceptors and bipolar cells at the next synapse, in the outer plexiform layer (OPL).

Bipolar cells contact all different cell types in the retina and transmit the signal from the photoreceptors to the retinal ganglion cells (RGCs). Their nuclei are central in the retina, located in the inner nuclear layer (INL), allowing the connection between the inner and the outer retina. More than ten different types of bipolar cells have been distinguished in the mammalian retina, among which, only one type is connected to rods whereas all the other types are connected to cones (1). Differences in morphology and synaptic stratification in the inner plexiform layer (IPL) underlay this diversity. Bipolar cells may also be classified by their functional response following glutamate release: ON-bipolar cells depolarize and OFF-

bipolar cells hyperpolarize upon visual signal transmission (1). Upon activation, bipolar cells modulate the release of glutamate at the next synapse, with the RGCs, at the IPL. Nuclei of RGCs are present in the ganglion cell layer (GCL) and the convergence of all the axons of the RGCs form the optic nerve. After formation, the optic nerve leaves the back of the eye forming the optic disc and projects to the lateral geniculate nucleus before reaching the visual areas in the brain, which makes RGCs the final output neurons of the retina. RGCs are able to convert a chemical signal from neurotransmitter release into electrical signal and thus generate action potentials.

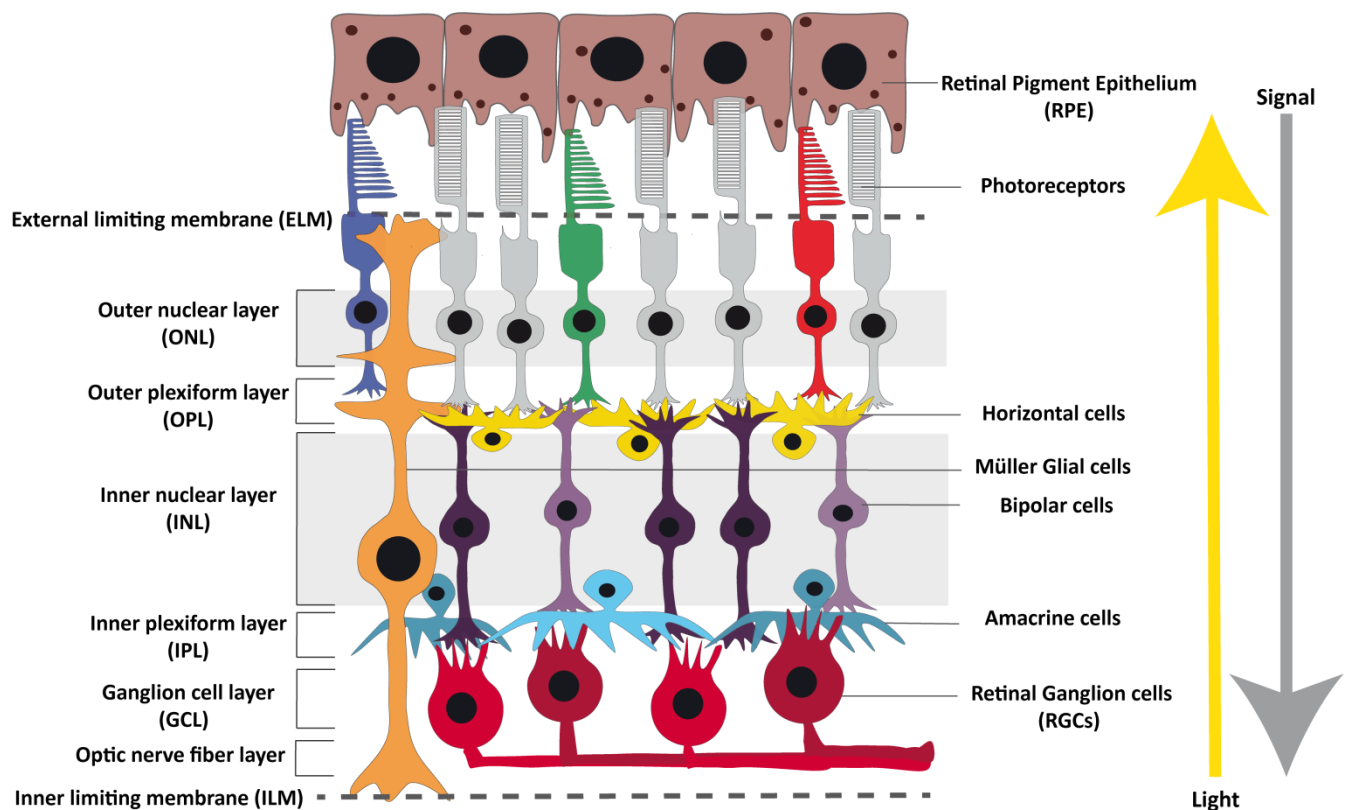


**Figure 2. Scheme of the organization of the retina.**

Light goes through all retinal layers to reach the photoreceptors (rods and cones). Three different types of rods are present (trichromatic vision). The signal is then transmitted to the bipolar cells in the inner nuclear layer (INL) and to the retinal ganglion cells (RGCs) in the ganglion cell layer (GCL). The axons of the RGCs regroup and form the optic nerve fiber layer before subsequently form the optic nerve. Horizontal cells and Amacrine cells are inhibitory cells which shape the signal, respectively in the outer plexiform layer (OPL) and in the inner plexiform layer (IPL). Müller cells are glial cells. They span the entire retina from the external limiting membrane (ELM) to the inner limiting membrane (ILM). Dark and light colors represent the diversity of each cell type.

The vertically-oriented pathway composed of the signal transmission between photoreceptors, bipolar cells and RGCs, interacts with two types of interneurons: the amacrine cells and the horizontal cells. These two cell types are inhibitory cells; they integrate and modulate the signal for better spatial and temporal coding as well as color contrast perception.

Horizontal cells shape the signal between photoreceptors and bipolar cells, providing an inhibitory feedback to the photoreceptors, probably through the  $\gamma$ -aminobutyric acid (GABA) neurotransmitter. The nuclei of the horizontal cells are present in the INL whereas synaptic processes occur in the OPL. Horizontal cells are interconnected with each other through gap junctions (2). The links between horizontal cells create a lateral network perpendicular to the direct pathway described above. The specific function of horizontal cells is still unclear, but their role in color contrast perception has been established.

Amacrine cells are the second type of interneuron in the retina. In the IPL, they modulate the signal delivered to the RGCs through two different mechanisms of action: either a feed-forward inhibition connecting directly with RGCs dendrites or a feedback inhibition via terminal axons of the bipolar cells. Amacrine cell inhibition is mainly generated by two neurotransmitters: GABA and glycine.

In addition to the previous, Müller cells are the most common type of retinal glial cells. Their nuclei are found in the INL but their extensions cross almost the whole thickness of the retina, delimitating two barriers: the external limiting membrane (ELM) and the inner limiting membrane (ILM). The ELM is formed by the contact, via adherens junctions, between the feet of the Müller cells and the photoreceptors. At the opposite end, the ILM barrier is delimited by the border of the retina and the vitreous humor. This specific organization contributes to the retinal structural integrity in which Müller cells are required (3-5). Müller cells play a role in the formation and the maintenance of the inner blood-retinal barrier and act as a trophic support for the other retinal cells. They also participate to retinal homeostasis by uptaking and metabolizing the neurotransmitter released into the synaptic cleft (6).

All of the previous elements compose what is called the neural retina, from the photoreceptors layer to the GCL, but other elements constitute the retina, such as the retinal pigment epithelium (RPE). The RPE is a monocellular layer connected by tight

junctions creating a hermetic barrier between the neural retina and the choroid tissue participating to the outer blood-retinal barrier. All exchanges between blood vessels from the choroid and the photoreceptors are tightly regulated by the RPE. This specific organization contributes to the immune privilege of the eye which is a combination of mechanisms limiting the inflammation, and immune system response after foreign antigen detection. As indicated by its name, the RPE contains pigment granules, or melanosomes, which catch the scattered light. The RPE is also important for maintaining functionality and homeostasis of the photoreceptors. Indeed, photoreceptor homeostasis is ensured by RPEs phagocytizing the light sensitive outer segment of the photoreceptors and by recycling some metabolites through the visual cycle (will be further discussed).

## **The vertical pathway**

### **Photoreceptor cells**

Photoreceptors are the photosensitive neurons of the retina and act as photon detectors. The two types of photoreceptor cells, the rod and the cone photoreceptors, have different morphologies but share common anatomical organization (**Figure 3**). Indeed, they are both composed of five compartments: 1) an outer segment containing stacked discs with the light-sensitive pigments, 2) an inner segment containing all cellular organelles, 3) the soma, 4) the axon and 5) the synaptic terminal process where connections with bipolar and horizontal cells occur in the OPL (7).

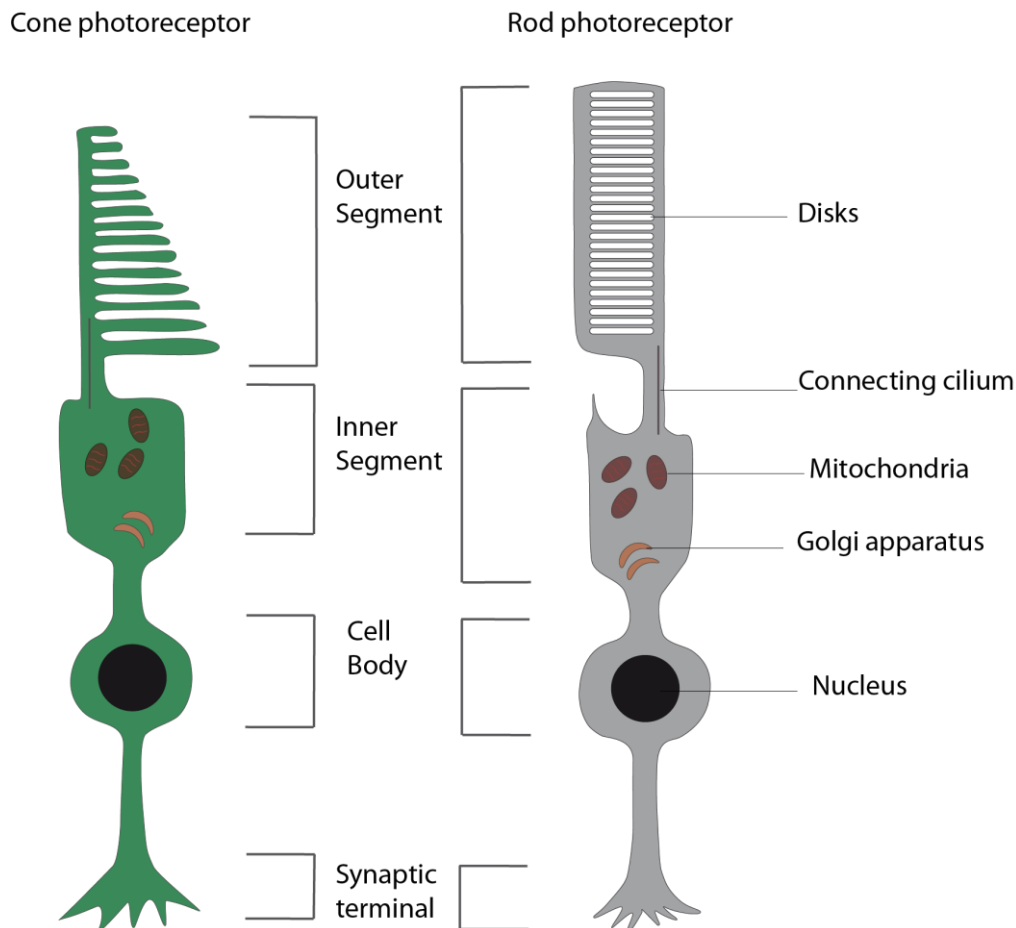


**Figure 3. Schematic representation of the two types of photoreceptor cells: cone and rod.**

Photoreceptors contain five compartments: an outer segment where the phototransduction happens, an inner segment containing different cellular organelles such as the mitochondria and the Golgi apparatus, a cell body comprising the nucleus, and finally a synaptic terminal process.

Cone and rod cells can nevertheless be distinguished by the shape of their outer segments, the type of light sensitive pigment contained within them, their spatial distribution in the retina, as well as their synaptic connections at the OPL. The long outer segment of rods is composed of individualized discs, in the membrane of which is located the rhodopsin photopigment. Rods are extremely sensitive to light and the circuitry underlying message delivery to the RGCs contributes to dim light vision (scotopic vision). On the contrary, cones have a shorter conic outer segment with evaginations of the cytoplasmic membrane forming stacked discs. Compared to rod cells, cone photoreceptors are less sensitive to light but respond faster following trigger of the phototransduction cascade. Cones are involved in day-light vision (photopic vision) and in color vision which is trichromatic in primates (8, 9). In humans and other primates, the three different types of cones, short, medium and long-wavelength sensitive, namely S, M and L, each contain a specific photopigment, opsin, each

having a distinct absorption peak spanning the visible spectrum. S, M, and L cones are sometimes called blue, green and red cones. The three types of photoreceptors are unequally distributed at the surface of the retina. L- and M-cone photoreceptors are the only photoreceptor types present at the very center of the retina, the fovea, and their high density is responsible for high visual acuity. At this location, only cones are present and other inner retinal cells are rejected at the border of the fovea, their synaptic connections with cone photoreceptors forming a slope around the foveal pit (10). The density of rod photoreceptors increases rapidly, outnumbering the cones, at the periphery of the fovea, being the most numerous photoreceptor types within the macula, the center of the retina. The density of rod photoreceptors decreases in the peripheral retina while cone density remains low and stable until it reaches the nasal periphery where it moderately increases again (Figure 4).

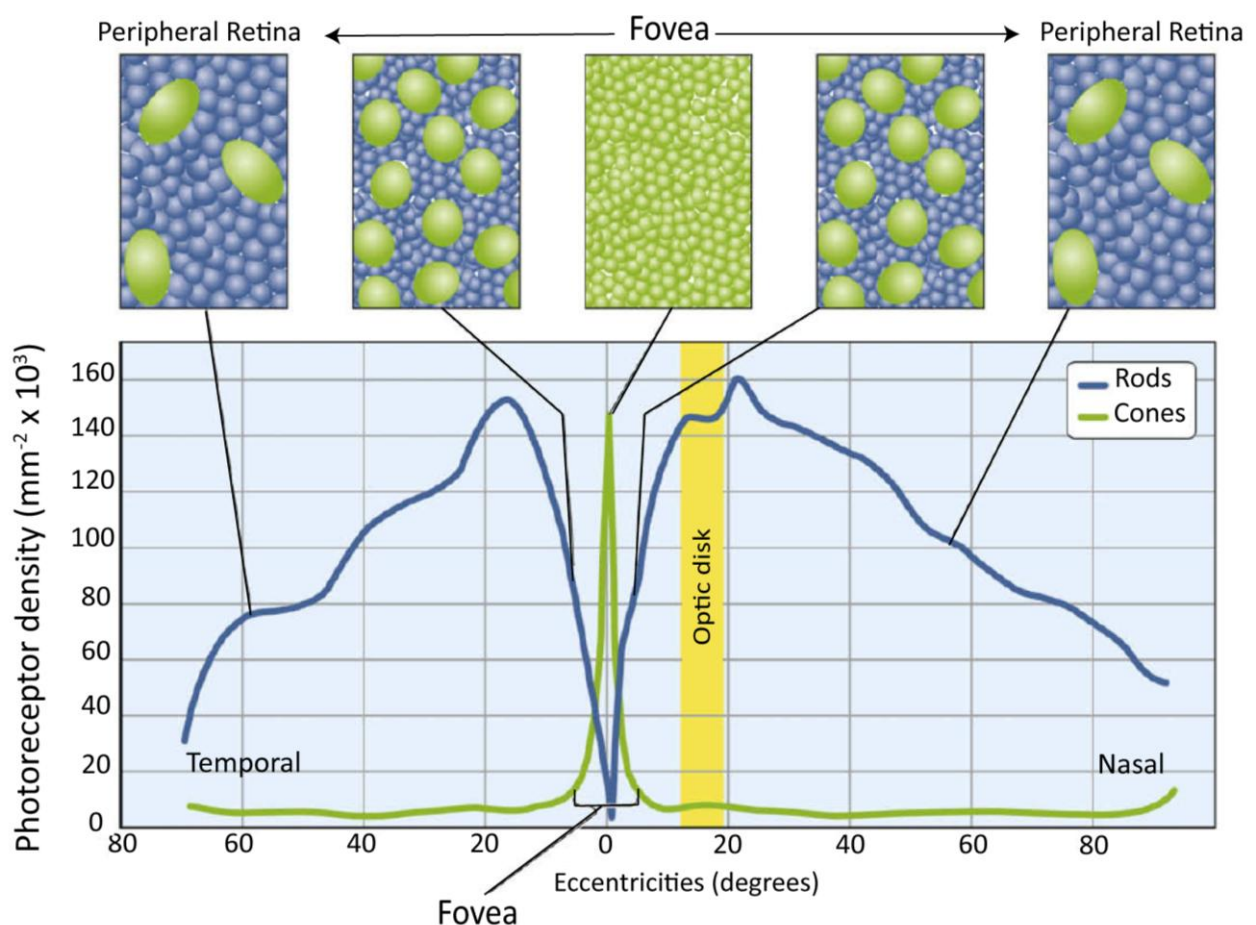


**Figure 4. Distribution of rod and cone photoreceptors at the surface of the human retina.** Cones photoreceptors are the only photoreceptors present in the fovea correlated with high visual acuity. In the periphery, rods outnumber cones. Adapted from (Mustafi *et al.*; 2009)(8).

Photoreceptors are the first initiators of the visual process, and transform light stimuli into an electrical signal through the phototransduction process. This mechanism involves the same molecular basis in the outer segments of both rods and cones. Basically, photoreceptors hyperpolarize upon light activation and depolarize in dark conditions (8). More specifically, under dark conditions also called resting conditions, a constant cationic influx goes through the cGMP-gated channels located at the plasma membrane of the outer segment. This dark current leads to the depolarization of the photoreceptors resulting in a continuous release of glutamate at the next synapse. On the contrary, the phototransduction cascade is triggered upon activation by light and results in the closure of the cGMP-gated channels and, therefore, into the modulation of the membrane potential. Finally, the hyperpolarization of the photoreceptors decreases the rate of glutamate release at the next synapse, between photoreceptors and bipolar cells, at the OPL.

### **Bipolar cells**

As their name suggests, bipolar cells have two extensions, thus linking the outer and inner retina. At the “upper” stage, bipolar cells connect to photoreceptors. Among the diversity of bipolar cells, distinctions are made based on their functional response after glutamate release. Under scotopic conditions, glutamate is continuously released by rods and cones and then captured by bipolar cells: ON-bipolar cells depolarize and OFF-bipolar cells hyperpolarize upon visual signal transmission (1). Rods only form synapses with ON-bipolar cells whereas cones connect with both ON- and OFF-bipolar cells (1).

Distinct glutamate receptors are localized on dendrites of the ON- and OFF-bipolar cells, underlying the opposite responses after the glutamatergic input. OFF-bipolar cells contain AMPA- or kainate- ionotropic receptors which function as cationic channels themselves. On the opposite, ON-bipolar cells express the metabotropic glutamate receptor 6 (mGluR6) which belongs to the G protein-coupled receptor family. The activation of mGluR6 triggers a second messenger cascade resulting in the closure of the transient receptor potential cation channel subfamily member 1 (TRPM1) (11, 12). At their terminal axons, bipolar cells receive inhibitory inputs from the amacrine cells before shaping the signal to the RGCs.

## Ganglion cells

RGCs are the last and only output neurons of the retina. Their axons converge to form the optic nerve leaving the back of the eye by forming the optic disc. Then, in humans, the axons connect to the lateral geniculate nucleus (LGN) with other neurons projecting to the primary visual cortex and the accessory visual areas. As mentioned, the RGCs are the only cells able to trigger action potentials in the retina. So far, more than twenty different RGCs cell types have been described, and all are excitatory glutamatergic neurons. To simplify, three categories of RGCs can be distinguished by their receptive field: ON-, OFF- and ON-/OFF-types. RGCs strongly respond to a set of stimuli in the center of their receptive field, and produce an antagonist answer to a stimulus in the periphery of the same receptive field. For instance, ON-RGCs increase the action potential frequency upon light activation in the center of their receptive field. At the opposite, the frequency of action potential is amplified in the absence of light in the center of the OFF-RGC receptive field and this frequency is lower or null in the presence of light. The answer to ON-/OFF RGCs is more complex, and combines the two previous answers. They also encode for direction stimuli having a directional selectivity. Of note, some RGCs are able to express a photopigment called melanopsin and thus participate to the non-visual perceptions (13).

## Retinal development

In vertebrates, the eye develops from different embryonic germ layers. The neural retina and the RPE originate from the neural ectoderm, the cornea and the lens originate from the surface ectoderm and, finally, the sclera derives from the mesoderm. Briefly, we will expose the main events leading to the development of the eye during mammalian embryogenesis. The eye field (EF) territory is a specific zone of the anterior medial neural plate which is induced during the gastrulation. The exact mechanisms involved in this process are still unclear. However, it has been demonstrated that extrinsic signals regulate the EF patterning. Indeed, Fibroblast Growth Factor (FGF) and Insulin-like Growth Factor (IGF) have been shown to promote the latter, whereas Bone Morphogenetic Protein (BMP) and Wingless Integration site (Wnt) repress the EF formation (**Figure 5**) (14). Moreover, the EF territory is characterized by the coordinated expression of at least six intrinsic signals: RX, LHX2, PAX6, SIX3, SIX6 and OTX2 (15, 16). These factors called EFTFs, for eye field transcription factors,

are highly conserved in vertebrates (17). They shape and maintain EF specification by a self-regulating feedback (16). During formation of the midline, SIX3 regulates the expression of SHH (Sonic hedgehog) which generates the split of the single territory, forming two bilateral optic pits (18). Any disruption of the EF division leads to the formation of one single eye called cyclopia.

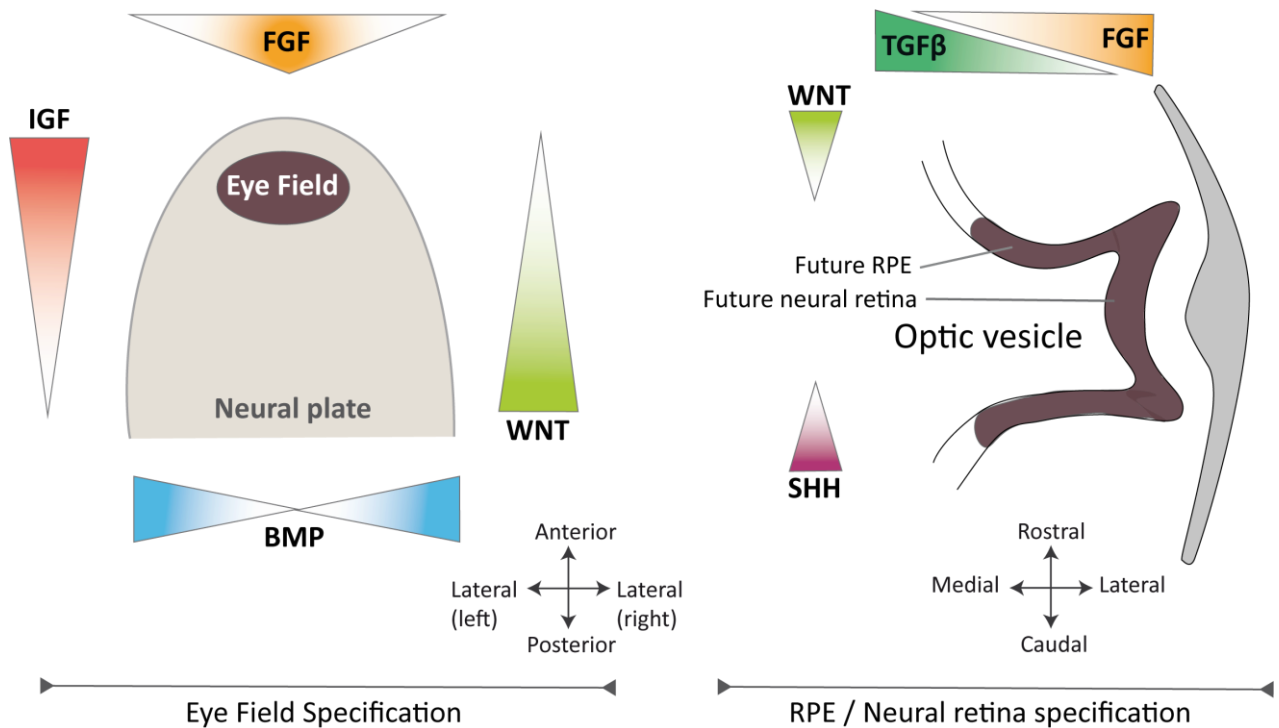


**Figure 5. Eye field patterning and RPE/ Neural retina specification by extrinsic signals.** Gradient of extrinsic signals are presented. Modified from (Gagliardi *et al.*, 2019)(14).

Evagination of the optic pits represents the first step of the eye morphogenesis which leads to the formation of two bilateral optical vesicles (**Figure 6**). This morphogenetic movement brings the optical vesicles in the vicinity of the surface ectoderm. The close interaction between the two tissues generates the formation of the lens placode by the thickening of the surface ectoderm (19). At the same time, under the influence of MITF, PAX2 and VSX2, the optic vesicle is regionalized in three distinct zones: the RPE, the optic stalk, which further becomes the optic nerve, and the future neural retina respectively. Reciprocal regulation between transcription factors, through repression pathways, allows shaping and delimiting each territory. Furthermore, the transition between optic vesicles to optic cups is mediated

by different factors; among them the LHX2 seems to play an important role in the dorso-ventral patterning regionalisation, as nicely demonstrated by Yun *et al.*, (20).

Later, the lens placode invaginates and detaches from the surface ectoderm thus forming the lens vesicles (19). The future corneal epithelium is subsequently formed by the surface ectoderm now covering the lens vesicles. Similarly, the optic vesicles invaginate and become bi-layered optic cups. The iris and ciliary body derive from the edge of the optic cups, in the zone where it comes close to the lens vesicle. During the differentiation of the optic cups, the RPE develops from the outer layer and the neural retina from the inner layer.

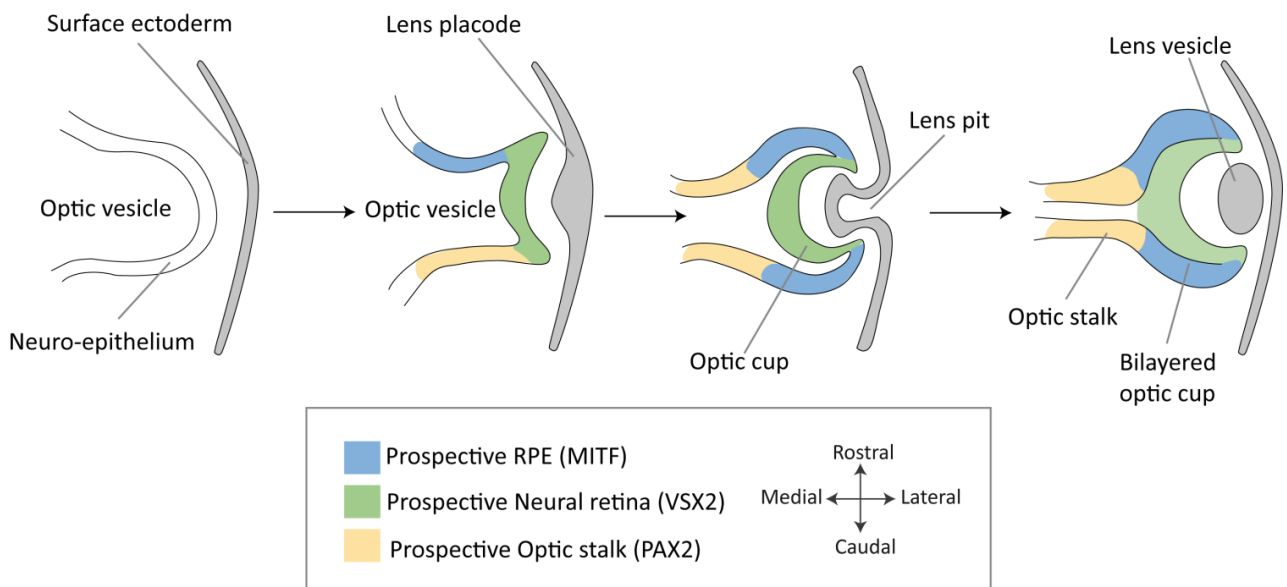


**Figure 6. The embryonic development of the eye.**

Formation of the optic vesicle after evagination of the neuro-epithelium. The interaction between the surface ectoderm and the neuro-epithelium induces the formation of the lens placode by thickening of the surface ectoderm meanwhile a regionalization of the optic vesicle occurs. The lens placode invaginates leading to the formation of the lens vesicle. This movement produces the invagination of the optic cup as well, generating bi-layered optic cups.

As previously mentioned, the neural retina is composed of different cell types which all derive from a common pool of retinal progenitor cells (RPCs) expressing specific markers (SOX2, PAX6). RPCs start to proliferate and differentiate before exiting the cell cycle. In humans, the differentiation process is initiated around 47 days and continues until the 8th month of gestation (19). During this time, the central retina develops and matures more rapidly than the peripheral retina (21). The seven retinal cell types are generated in a

sequential manner and this process is evolutionarily conserved. Usually, RGCs, horizontal cell, cone photoreceptors, and amacrine cells are the first cells generated whereas rod photoreceptors, bipolar and Müller cells appear at a later stage (**Figure 7**) (22). Of note, the apparition of the different cell types overlaps with each other overtime. Different hypotheses about retinal cell's fate and differentiation have been proposed to explain how this cell diversity can be produced from a common progenitor. So far, the competence model proposed by Livesey and Cepko is the most widely accepted hypothesis (23). According to this model, RPCs acquire different competence states overtime and generate specific cell types during a limited period of time. The process would be regulated by both extrinsic and intrinsic signals. However, this model relies on intrinsic mechanisms and, more specifically, relies on a hierarchy of transcription factors which evolve during the retinogenesis and drive the RPCs differentiation.

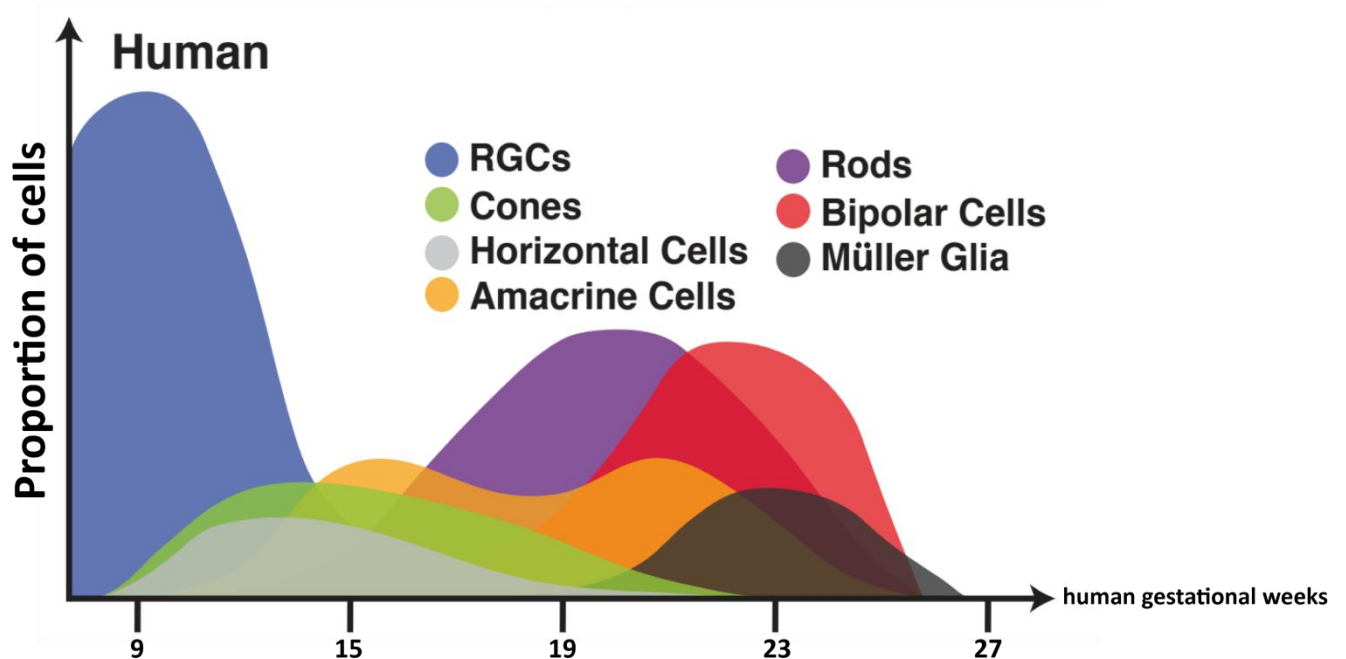


**Figure 7. Development of human retinal cell types overtime.**

Results obtained with single cell RNA sequencing (scRNA-Seq) on developing human retina. Figure from (Lu *et al.*, 2019) (24).

Overtime, and with advanced technologies, other studies allowed to refine the previous model and added a probabilistic component. According to those studies, proliferation and cell fate determination could be partially explained by a stochastic model (25). Following the addition of this hypothesis to the previous model, RPCs can generate different cell types at any time, even though the change of competence is restricted overtime and, therefore, follows a unique direction (26, 27).

Recently, new advances in sequencing technologies, combined with computational tools, allowed for a better understanding of retinal cell development and cell fate determination. For example, gene expression changes at different stages of the human fetal retinogenesis are now demonstrated, thanks to transcriptomic data analysis obtained from RNA-sequencing technology (RNA-Seq) (28, 29). The association between RNA-Seq and single-cell technologies (scRNA-Seq) constitutes a powerful tool which correlates transcriptomic data with cellular resolution (30-32). Applied to human fetal retina or developing retina from other species, this technology brought new insights on cell fate specification during the retinogenesis. Furthermore, comparing collected data shed light on conservative and divergent mechanisms controlling cell fate determination among species (24).

In 2020, Sridhar *et al.*, identified transitional cell populations during human retinal development using scRNA-Seq (33). Interestingly, cells composing these populations have already exited the cell cycle and are characterized by the expression of low levels of progenitor markers and high levels of cell fate-determining genes like *ATOH7*. Indeed, *Atoh7* is expressed in progenitor cells and previous studies reported its role in RGCs cell fate determination (34, 35). Transitional cell populations do not yet express a cell-specific profile. Chronologically, these cells stand between progenitor and mature cell types. The first transitional cell cluster named T1 is highly present after 59 days of the fetal development (D59). At that time, cells from this cluster express a high level of *ATOH7* and give rise to two different lineages: RGCs and amacrine/horizontal cells. At D82, two additional transitional cell clusters can be identified, respectively T2 and T3, which probably originate from the less mature T1 cluster. Cells from the T2 cluster develop into amacrine cells whereas T3 gives rise to photoreceptors and bipolar cells. T1, T2 and T3 represent intermediate states of the retinal development and are characterized by specific sets of gene expression (**Figure 8**).

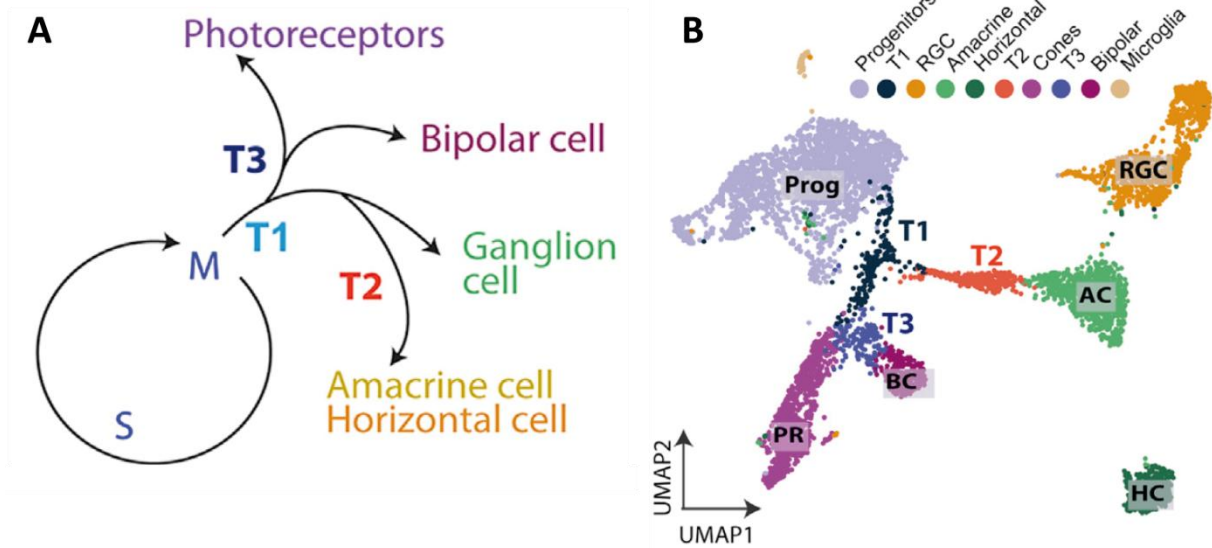


**Figure 8. Transitional cell populations along the retinal development.** (A) Scheme of the different transitional cell populations and their derivative cell population (B) Uniform Manifold Approximation and Projection (UMAP) plot data obtained with single cell RNA sequencing (sc-RNA-Seq) on human fetal retina after 82 fetal days of development. Data from (Sridhar *et al.*, 2020) (33).

As developed above, the retina is a well-organized tissue composed of different layers containing multiple cell types each with a dedicated role. This precise organization enables the first steps of the visual process, filters the damaging light and pathogens, transforms the light stimulus first into a chemical signal, then into an electrical one, encodes the visual stimulus and transmits it to the LGN then to the cortical areas specialized in vision. However, this complex system is fragile and pathologies can compromise its integrity.

## 2. Inherited retinal dystrophies

Inherited retinal dystrophies (IRDs) represent a heterogeneous group of disorders caused by one or more gene defects. Diseases can be restricted to the retina or affect other organs (syndromic disease). Inherited retinal dystrophies may be stationary or progressive with subsequent degeneration and loss of retinal cells. For instance, Congenital Stationary Night Blindness is a non-progressive disorder whereas retinitis pigmentosa is a degenerative disorder primarily affecting photoreceptors. Limited therapeutic options are available for these disorders which lead to progressive visual dysfunction and severe handicap sometimes reaching blindness. A better understanding in pathologic mechanisms is essential to establish new therapies for these yet incurable conditions.

The first step to diagnose such disease is ophthalmic examination. Several clinical exams, assessing both the function and the structure of the retina, and making part of a larger panel, will further be explained.

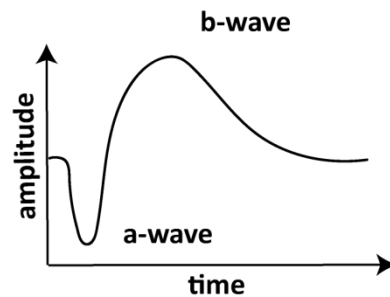
### Clinical Examinations

Visual acuity measurement and color vision testing allow indirect estimation of foveal cones function. Retinal sensitivity can be evaluated by assessing the visual field. This exam can help to determine where the visual stimuli are perceived in a field of vision of a subject. The function of the retina can be tested and recorded objectively by the **full-field electroretinogram (ERG)**. The ERG is an indirect measure of the modification of membrane potentials in response to light flashes in different lightning environments and at different light intensities. This clinical exam may be performed under dark (scotopic) or light (photopic) adapted conditions allowing to test the rod and the cone retinal pathways individually. The recorded signal is mainly generated by photoreceptors and bipolar cells. Other cell types contribute to shape the signal but their contribution is less significant **(Figure 9)**.

**The eye fundus examination** is a non-invasive clinical exam. Following pupil dilatation with mydriatic drops, clinicians can have access to different regions of the eye using an ophthalmoscope. This exam allows the assessment of different features of the eye such as the optic nerve head, the retinal blood vessels and some aspects of the retina.

**A**

Basic waveform of the ERG on scotopic conditions



**B**

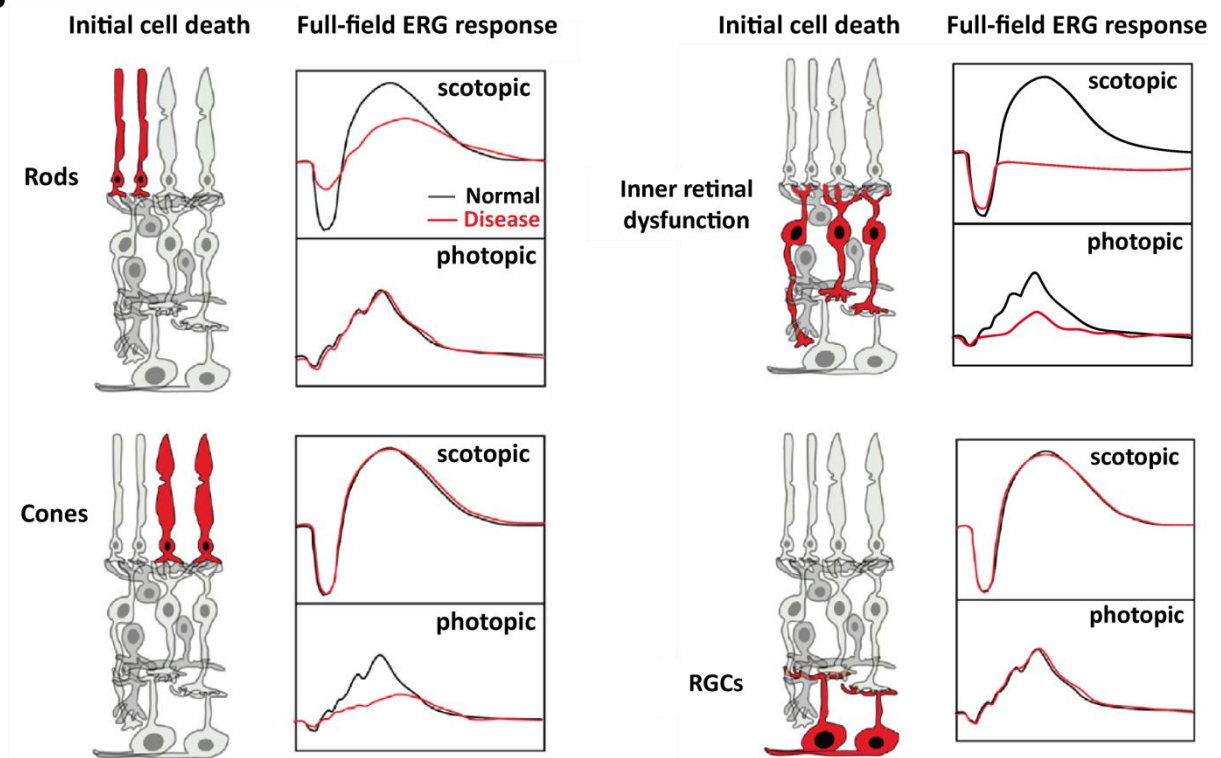


**Figure 9. Functional alterations of the retina with the Electroretinogram (ERG).**

(A) ERG in scotopic conditions with the a-wave and the b-wave. (B) Panels of ERGs after retinal cell death. Modified from (Hoon *et al.*, 2014) (36).

**Fundus autofluorescence imaging (FAI)** allows testing RPE integrity (**Figure 10**). The exam relies on the lipofuscin pigment which is naturally fluorescent upon excitation by specific wavelength light. Lipofuscin is the by-product of photoreceptors outer segment phagocytosis and incomplete digestion by the RPE, which increases over time. Usually, two wavelengths are used in clinical practice: a short wavelength (blue auto fluorescence) and one near

infrared. An increase in autofluorescence translates into either RPE dysfunction or photoreceptor outer segment instability. Any decrease or loss of the autofluorescence may represent a manifestation of RPE or photoreceptor cell death (37).

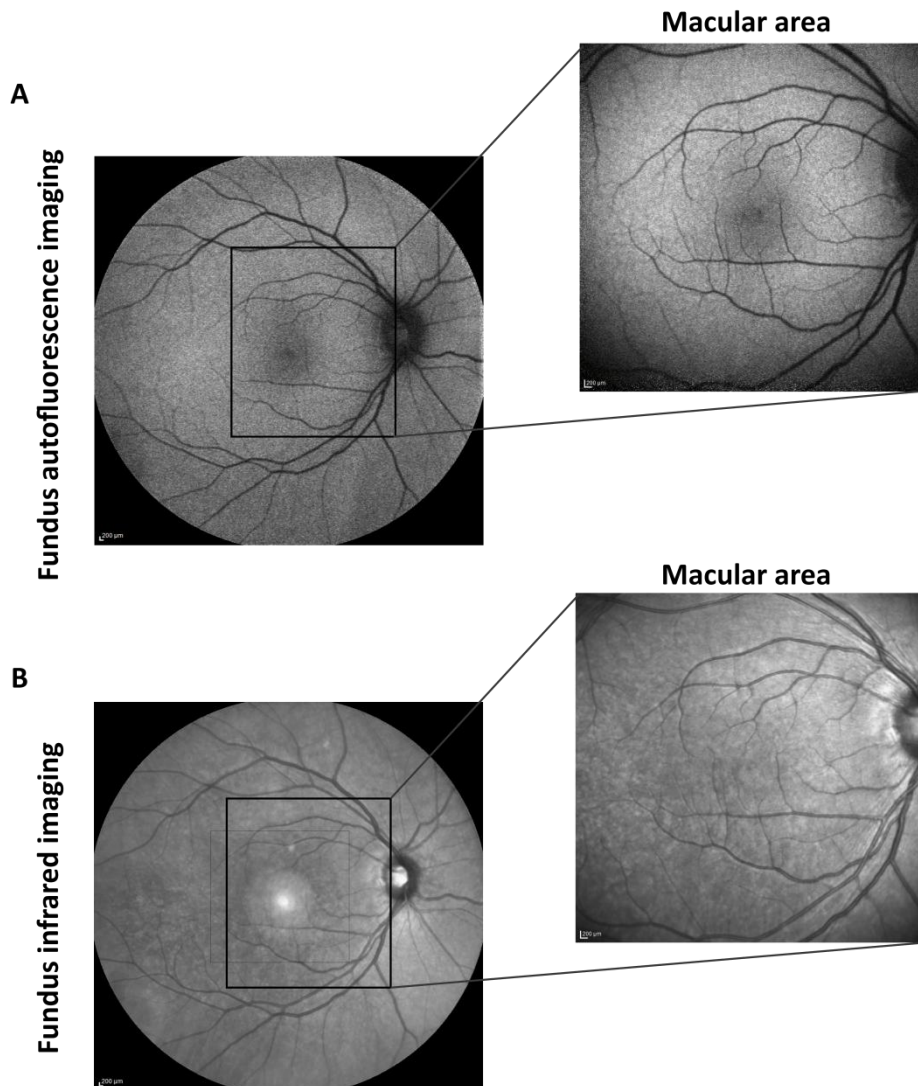


**Figure 10. Fundus imaging.**

(A) Fundus autofluorescence imaging with a zoom on the macular area (B) Fundus infrared reflectance imaging with zoom on the macular area. Image obtained with the courtesy of Dr Marco Nassisi.

Other more invasive techniques may also be used to assess the status of the retina but have now been replaced by FAI, SD-OCT and OCT-A (see below) in the diagnosis and management of IRDs. These include fluorescein angiography, which consists of injecting a fluorescent dye to follow its diffusion in retinal vessels thus indirectly assessing retinal atrophy through

window defect. The specific structure of the retina can be evaluated by **spectral domain optical coherence tomography (SD-OCT) (Figure 11)**. The different layers can be observed as a horizontal section with this imaging method. Conventionally the RPE cell layer is placed down and RGCs in the upper layer (which is different from all the previous schemes). Retinal cell integrity can therefore be assessed precisely. In addition, SD-OCT allows detection of sub-retinal structures like deposits or pigment accumulation. More recently, a new non-invasive technique called **OCT-Angiography (OCT-A)** has been developed to analyze vascular flow and assess retinal vascular integrity more precisely.

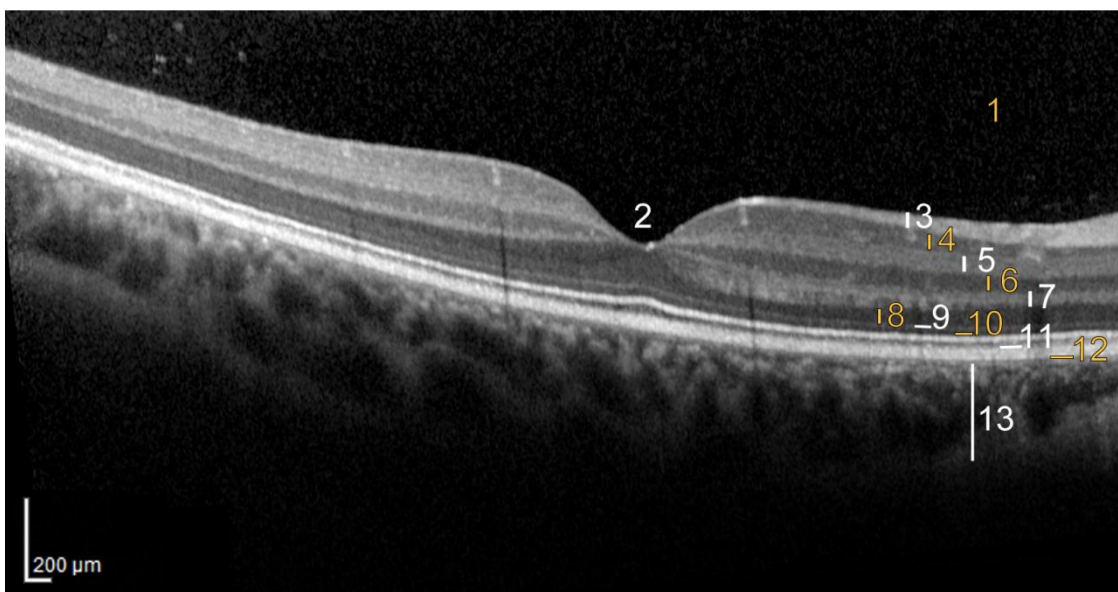


**Figure 11. Spectral domain optical coherence tomography (SD-OCT) imaging.**

(1) vitreous cavity (2) fovea; (3) nerve fiber layer; (4) GCL; (5) IPL; (6) INL; (7) OPL; (8) ONL; (9) external limiting membrane; (10) ellipsoid zone; (11) interdigitation zone; (12) RPE/Bruch membrane complex; (13) choroid. Image obtained with the courtesy of Dr Marco Nassisi.

Upon correlation with a precise and detailed clinical diagnosis, laboratory techniques based on DNA sequencing enable identification of an underlying gene defect. Several strategies can be followed in order to rapidly achieve this goal. Up until the past decade, a “candidate gene” approach was an efficient strategy. This technique, suggested by Dryja in 1990, proposes sequencing of all genes already known to play a role in the retinal physiology (38). Nevertheless, most of the IRDs are genetically heterogeneous with more than 200 genes implicated in these disorders (listed in the RetNet website: <https://sph.uth.edu/retnet/>). The advent of high throughput Next Generation Sequencing (NGS) offered a more efficient tool

to encompass this genetic heterogeneity. This approach may be targeted towards a list of genes known to be implicated in the disease of interest or may be broader and unbiased with Whole Exome and Whole Genome Sequencing (WES and WGS respectively). However, although giving the possibility to identify new genes and mutations involved in inherited retinal dystrophies (39), the latter generate a massive amount of data which need to be filtered and analyzed to extract significant results. In this respect, functional studies and disease modeling constitute an essential addition to validate and better understand the underlying pathologic mechanisms associated with a new genetic pathway.

### ITM2B-related peculiar retinal dystrophy (RD)

In our study, all patients from a family affected with this unusual retinal dystrophy (RD) were clinically examined at the Quinze-Vingts hospital in Paris.

Affected subjects have a very peculiar retinal degeneration combining inner retinal dysfunction, RGCs abnormalities and progressive cone degeneration (MIM#616079; retinal dystrophy with inner retinal dysfunction and ganglion cell abnormalities; RDGCA) (40). This atypical clinical presentation does not correspond to any inherited dystrophies already known and described thus far in the literature. The disease starts around thirty years of age with increased light-sensitivity (termed photophobia). The disease slowly progresses into a decreased central vision but with preservation of the peripheral visual field. In 2014, fourteen patients spanning three generations were affected in the same family (**Figure 12**).

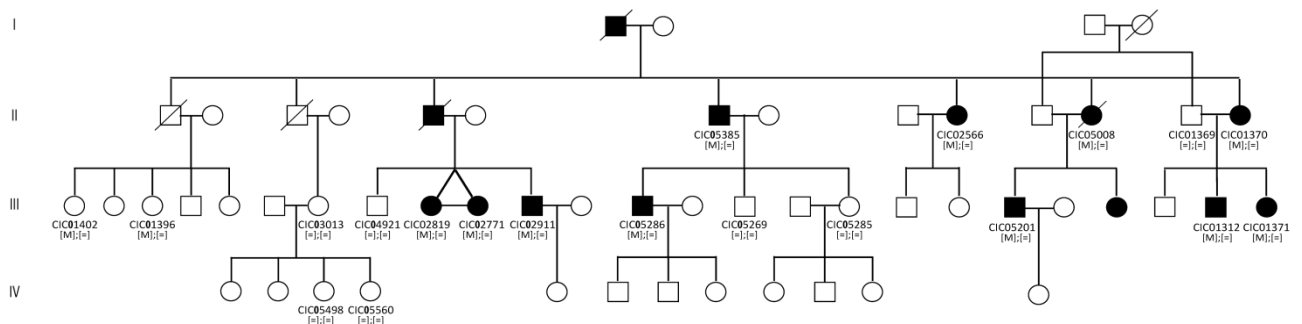


**Figure 12. Family pedigree of the RD family.**

The pedigree reveals an autosomal dominant segregation of the RD disease.

Fundus examination and retinal imaging reveal optic disc pallor. Full-field ERG shows an absence or a reduced b-wave in all affected subjects under scotopic conditions. However, in

the same conditions, the a-wave is maintained indicating a preserved photoreceptor, mainly rod, function and an inner retinal dysfunction. Cone system responses, generated mainly at the level of the inner retina on ERG, have also been tested under photopic conditions appearing to be normal in younger subjects but showing some abnormalities in older patients. In summary, this specific waveform of the full-field ERG reflects a transmission defect between the photoreceptors and bipolar cells. Structurally, all affected subjects display retinal abnormalities with distinct features on SD-OCT, including a hyper reflectivity of the IPL and the RGC layer, with severe thinning of the optic nerve fiber layer. An irregular reflectivity is also found within the ONL at the fovea in some subjects. Furthermore, abnormal macular autofluorescence (decrease of the autofluorescence) has been observed with autofluorescence imaging.

Some features of this peculiar RD are also found in other disorders: for instance, the absence of b-wave under scotopic conditions is a characteristic of several disorders including the Schubert-Bornschein types of congenital stationary night blindness, and the X-linked retinoschisis, but may also be acquired in disorders such as central artery occlusion or inflammatory disorders (e.g. Birdshot chorioretinopathy) (41). On the other hand, retinal degeneration with photophobia is found in cone-rod dystrophies. In addition, RGCs abnormalities and optic disc pallor can be found in inherited optic neuropathies. The persistent hyper reflective material seen on SD-OCT is however quite unique.

All the previous information lead I. Audo and C. Zeitz to identify, through whole exome sequencing, a new missense mutation (c.782A>C, p.Glu261Ala) in *ITM2B* in a large family affected with an unusual autosomal dominant retinal dystrophy (RD) (40). The subtle change of a glutamine for an alanine residue due to mutation is the starting point of our study and of my PhD.

Interestingly, two previous mutations in *ITM2B* affecting two distinct families have also been reported in the literature: the familial British dementia (FBD) and the familial Danish dementia (FDD) (42, 43). These two different neurodegenerative diseases share some clinical and physiopathological features with Alzheimer disease. Of note, no neurological disorders have been reported in the RD family. A description of these three different neurodegenerative diseases (Alzheimer disease, FBD, FDD) follows, thus helping to understand the link between *ITM2B*, Alzheimer disease and dementia.

### 3. ITM2B and related disorders

#### **Amyloid diseases, ITM2B-associated pathologies and dementia**

The amyloid term refers to an extracellular abnormal protein assembly. Amyloid is insoluble and depositions usually adopt a  $\beta$ -sheet structure (44). Amyloid deposits are present in several disorders, such as Parkinson or Huntington diseases. Among them, Alzheimer disease is probably the most documented. Of note, different dyes stain amyloid proteins: Thioflavin T is a basic staining method for any amyloid proteins whereas Congo red is specific to the  $\beta$ -cross structure and displays green birefringence under polarized light.

#### **Alzheimer disease (AD)**

Alzheimer disease (AD) is the most common neurodegenerative disease worldwide. Since its discovery by Alois Alzheimer more than one century ago (1906), lots of scientists and clinicians have investigated mechanisms involved in this disorder. Even if the etiology is still unknown, and available drugs only limit symptoms and do not cure the disease, major advances in the field have been achieved.

Symptoms start with memory loss often associated with confusion, and continue on with cognitive impairment which gradually worsens overtime and finally reaches severe dementia. Distinction should be made between sporadic and familial cases which are rarer. Sporadic cases have a late onset and involve a mix of genetic and non-genetic factors whereas familial cases are of early onset (before 65 years of age) and are usually associated with a genetic mutation often in a dominant manner. AD is a complex disease triggered by multiple factors among which aging is the most significant.

Definitive diagnostic is made after death from postmortem brain tissue examination. Indeed, AD is characterized by two neuropathological hallmarks: intracellular neurofibrillary tangles (NTF), and extracellular senile plaques. Briefly, NTF are formed by paired helical filaments and consist of abnormal insoluble aggregates mainly composed by the hyper-phosphorylated form of the microtubule associated protein Tau (45, 46). In normal conditions, Tau interacts and stabilizes microtubules, which allows cytoskeleton reorganization (47). In pathological conditions, the hyper-phosphorylated Tau has little affinity for its substrate and binds to the normal Tau instead, leading, along with other mechanisms, to microtubules breakdown (48). Regarding senile plaques, they are mainly

composed of  $\beta$ -amyloid ( $A\beta$ ) accumulation, a 39-43 amino acid peptide, which results from cleavage of the Amyloid Precursor Protein (APP) (49). Interestingly, only the hyperphosphorylation of Tau and not the amyloid plaques correlates with neuronal loss in AD (50). Nevertheless, only senile plaques are specific of AD while NTF are present in a variety of neurodegenerative diseases such as Huntington and Parkinson diseases.

APP is a type I integral membrane protein with one domain spanning the cellular membrane. In mammals, two other members are composing this protein family: the APP-related proteins 1 and 2 (APPL1, APPL2) (51). Of note, in this family, only APP is able to generate an amyloid peptide (52). Several alternative splice variants lead to produce different APP isoforms, among which APP695 is the most abundant in the brain (53). The specific function of APP is still unclear. Several studies have shown its role in neurogenesis, neurite outgrowth and axonal guidance. Moreover, APP could regulate synaptic function. However, APP peptides generated after enzyme cleavage can each have a different role, thus increasing the functions of the protein. Indeed, APP can be processed via two distinct pathways, resulting in different peptides production: non-amyloidogenic or amyloidogenic (53). The two different pathways involve sequential APP cleavages and the first process determines the following pathway. In the non-amyloidogenic pathway, APP is initially cleaved at the C-terminus by an  $\alpha$ -secretase enzyme, releasing the sAPP $\alpha$  peptide and generating a membrane-bound fragment of 83 residues (C83). This process is mediated by the ADAM (a disintegrin and metalloproteinase) family in which ADAM10 appears to be the main  $\alpha$ -secretase. After this first step, APP is cleaved intramembranously by a  $\gamma$ -secretase, generating the APP intracellular domain (AICD) and the P3 fragment, which does not form aggregates. The amyloidogenic pathway starts by the action of the  $\beta$ -secretase at the APP C-terminus which leads to the production of sAPP $\beta$  ectodomain and a remaining membrane-bound fragment composed by 99 amino acid residues (C99). After this first step, the C99 fragment can be cleaved inside the plasma membrane by the  $\gamma$ -secretase generating the AICD with the release of the  $A\beta$  peptide which is the major component of the senile plaques (53) (**Figure 13**). Although,  $A\beta_{40}$  is the most abundant peptide,  $A\beta_{42}$  is more prone to form oligomers and thus is the most toxic peptide (54, 55).

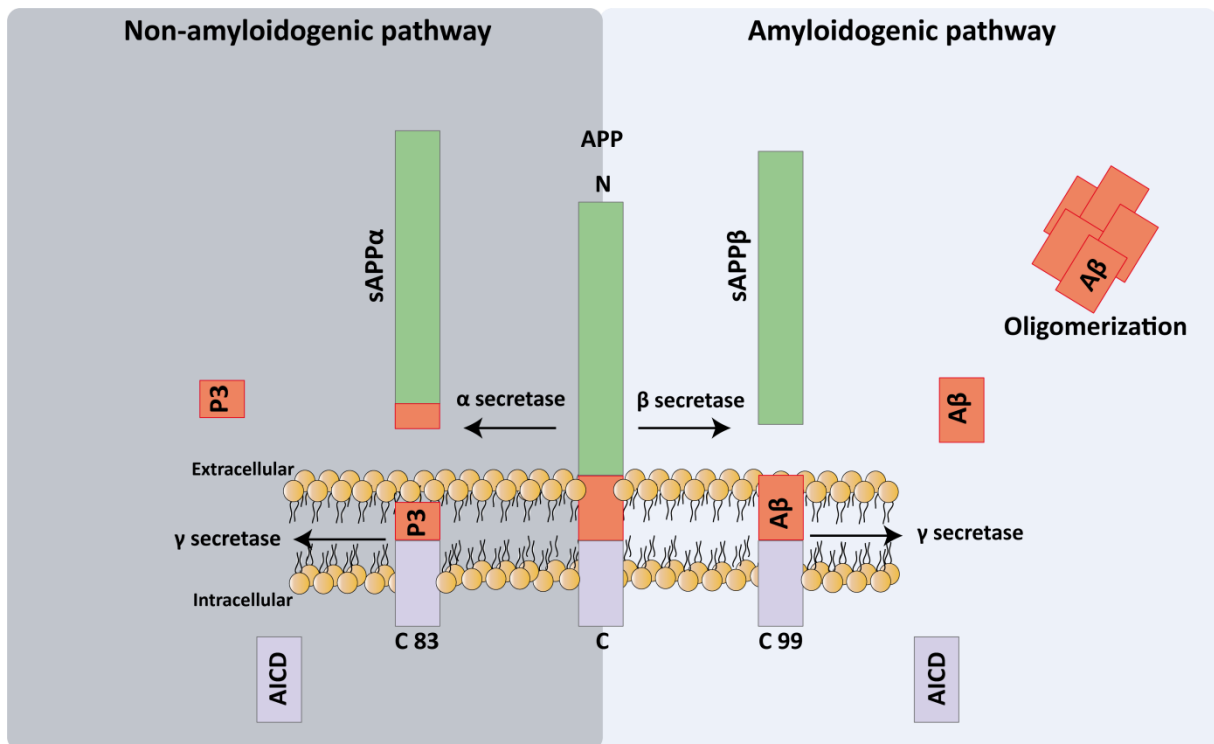


**Figure 13. APP processing through non-amyloidogenic and amyloidogenic pathway.**

APP undergoes several cleavages. A $\beta$  peptide is generated through cleavage by  $\beta$ -secretase and  $\gamma$ -secretase following the amyloidogenic pathway. After  $\beta$ -secretase cleavage, sAPP $\beta$  is released and the remaining membrane bound fragment (C99) is then cleaved intramembranously by the  $\gamma$ -secretase releasing the A $\beta$  peptide and the APP intra cellular domain (AICD) (53). Following the non-amyloidogenic pathway, P3 is generated through cleavage by  $\alpha$ -secretase and  $\gamma$ -secretase. After the first  $\alpha$ -secretase cleavage, sAPP $\alpha$  is released and the remaining membrane bound fragment (C83) is then cleaved inside the membrane by the  $\gamma$ -secretase (53).

A $\beta$  peptides can regroup and self-assemble into different forms: oligomers, profibrils and amyloid fibrils. Oligomers result from the spontaneous association of A $\beta$  monomers. Low molecular weight oligomers are soluble and might diffuse into the brain of affected subjects. The association of fibrils generates the amyloid plaques also named neuritic or senile plaques. Fibrils are characterized by cross- $\beta$  structure which are basically stacked  $\beta$ -sheet perpendicular to the long axis of the fibers. Different studies showed that the major neurotoxic effect contributing to neuronal cell death results from the soluble oligomers more than the senile plaques (56). The link between toxic oligomers, profibrils and amyloid has remained unknown for a long time. Other proteins, such as actin, have the capacity to self-assemble. In this case, its mechanism and kinetics leading to actin filament formation have been well defined as primary nucleation and elongation (57). This model, however, does not fit with A $\beta$  aggregation from A $\beta$  monomers. The process leading to protein

aggregation is a much more complex system. In 2013, Cohen and collaborators showed that, when a threshold of A $\beta$ <sub>42</sub> fibrils is reached, toxic oligomers are generated by a phenomenon which is called secondary nucleation; this process is enabled and amplified only by the presence of already formed A $\beta$ <sub>42</sub> fibrils (58). According to them, the secondary nucleation has no impact on the first nucleation and the two events happen at the same time but on different sides of the fibrils; elongation occurs at the extremities of the fibrils whereas secondary nucleation would appear along the fibril side. At one point, secondary nucleation will overtake slow primary nucleation and toxic oligomers will appear exponentially via the catalytic surface provided by the already formed A $\beta$ <sub>42</sub> fibrils (59). This discovery has an immense impact since the major part of neurotoxic oligomer production originates from the secondary nucleation. Thus, specific inhibitors of the secondary nucleation would stop toxic aggregated oligomers accumulation (further discuss p 31).

As previously mentioned, amyloid deposits are a feature shared by different disorders. In the literature, two families presenting mutations in *ITM2B* and suffering from Alzheimer-like dementia have already been described. These two families have common clinical features with AD-like amyloid deposits as well as other features which will further be exposed below.

### **The Familial British Dementia**

In 1933, Worster-Drought reported a family affected with an autosomal dominant neurodegenerative disease, characterized by progressive dementia, spastic paraparesis and cerebellar ataxia with onset in the fifth decade (60, 61). Affected subjects mostly die within 10 years after the first symptoms. In 1982, Griffiths mentioned two siblings who shared the same clinical features (62). Finally, it was proven that the two families have a common ancestor (63).

Histopathological features show severe amyloid angiopathy affecting the brain, the cerebellum and the spinal cord. Pathological features also include neurofibrillary tangles (NTF), amyloid plaques, cerebellar and white matter degeneration (63). Three different types of amyloid plaques have been observed with electron microscopy in affected subjects: perivascular plaques around capillaries, plaques with a large diameter around 150  $\mu$ m composed of a dense central core and peripheral spicules, small plaques with a same dense central core but without peripheral spicules and of a much smaller diameter (30  $\mu$ m) (63,

64). In the hippocampus, the majority of amyloid plaques found are small plaques first termed “non-neuritic” plaques because of the absence of positive Congo red staining compared to neuritic plaques. Further investigations with electron microscopy proved that neuritic plaques, then termed fibrillar plaques, arranged in a  $\beta$ -sheet conformation and co-localized with microglia and reactive astrocytes. On the contrary, non-neuritic plaques, also referred as non-fibrillary or pre-amyloid plaques do not organize into  $\beta$ -sheets and do not co-localize with other cells (65).

The disease was first called “familial cerebral amyloid angiopathy with non-neuritic plaque formation” and it is now recognized as the Familial British Dementia (FBD) (42, 63). The authors wanted to emphasize the fact that the hippocampal amyloid and pre-amyloid plaques coincide with neuritic changes and neuron loss. Similarly to AD, this disease is primarily a type of dementia and hippocampal lesions are independent of the vascular involvement (66). The exact composition of the amyloid plaques has been revealed following the discovery of the gene defect underlying FBD.

The mutation involved in the disease is a single base substitution in *ITM2B* stop codon, resulting in a longer protein product (MIM# 176500, FBD mutant: c.799T>A; p.Stop267Argext\*11) (**Table 1**) (42). ABri peptides are composed by the last 34 amino acid residues of the ITM2B-FBD mutant form, and accumulate *in vitro* into irregular short fibrils composing the amyloid plaques (42, 67). Systemic ABri amyloid deposits have been found in different organs of affected subjects such as the pancreas, adrenal glands, myocardium and skeletal muscles (68).

### **The Familial Danish Dementia**

Familial Danish Dementia (FDD), also called hereditary ophthalmic-otitic-encephalic, is an early onset autosomal dominant neurodegenerative disease discovered by E. Strömberg and collaborators in 1970 (69). Nine cases of a five generations family originating from Denmark were reported in this study. The disease starts with the development of ocular disorders like cataract (clouding of the crystalline lens) and ocular hemorrhages in patients under 30 years of age. The disease rapidly progresses with hearing loss ten to twenty years later. Cerebral symptoms come later with ataxia often associated with paranoid reactions. The death appears around 60 years of age for most of the patients (69).

Neuropathologically, the disease is characterized by widespread cerebral amyloid angiopathy, parenchymal lesions and neurofibrillary tangles (NTF) (70). Only little information about the clinical retinal features is present in the literature and is resumed in the next lines. Cataract is the first symptom to appear but most FDD patients also develop vitreous hemorrhages originating from pre-retinal neovascularisation (71). In the retina of FDD patients, photoreceptors outer and inner segments are reported as totally absent. The inner retina is disorganized with macrophage infiltration and astrocyte activation. Retinal vessels are often occluded or contain ADan (i.e. mutant peptide) deposits. Finally the optic nerve is severely affected with axonal loss and other ongoing damages such as swollen axons (70).

FDD is due to a 10-nucleotide duplication (MIM# 117300, FDD mutant: c.795-796insTTTAATTTGT; p.Ser266Pheext\*11) in *ITM2B* (**Table 1**) (43). This mutation leads to a change in the reading frame, removing the *ITM2B* last stop codon (codon 266) resulting in a longer protein product. The last 34 amino acid residues of this *ITM2B* mutated form have been identified as the ADan peptide and accumulate in the form of amyloid fibrils in different regions of the brain, mostly limbic structures. Interestingly, amyloid deposits in the hippocampus are mainly Congo-red negative suggesting that the aggregation has a non-fibrillary structure comparable to those found in the FBD (43). Interestingly, the different lesions are composed by a mixture of ADan and A $\beta$  peptides (70, 72).

ADan as ABri peptides contains a vast majority a pyroglutamate at the N-terminal position (43, 68). This modification is frequently observed in some hormones or neuropeptides as well as in AD with a pyroglutamate modified A $\beta$  (pGlu-A $\beta$ ) (73-75). In mice, it has been demonstrated that pGlu-A $\beta$  could initiate A $\beta$  plaque formation (76). Different studies demonstrate the influence of the pyroglutamate modification on the solubility of ABri and ADan and the amyloid plaque formation (77). Indeed, in FBD most of the amyloid plaques are composed of pyroglutamate modified peptides (68). This led to the hypothesis that pyroglutamation occurs before plaque formation. However, ABri and ADan also present in a soluble form which surprisingly does not contain any pyroglutamate modification (68, 72). This would suggest that the N-terminal modification occurs after amyloid deposition.

A specific antibody (named AB77) recognizing the N-terminal pyroglutamate and the first 22 amino acid residues common to ABri and ADan has been generated by Saul *et al.*, in 2012 (78).

FBD and FDD have a lot in common. Mutations underlying these disorders are present in *ITM2B* and generate an 11-amino acid residue longer protein product in both cases. The mode of inheritance is autosomal dominant and both are neurodegenerative diseases with severe amyloid angiopathy. Neurofibrillary tangles and amyloid plaques have been found in affected subjects from the two families. The insoluble form of the Tau protein has the same western-blot profile in both conditions and is also similar in AD (70). However, some differences between the FBD and FDD should be emphasized. In FDD, the first alteration to appear is cataract whereas no ocular damages have been reported in FBD. The two amyloidogenic peptides, ABri and ADan, have the first 22 residues in common but the next 12 amino acid residues differ. In both cases, amyloid plaques are composed of ABri or ADan, but only ADan co-localizes with A $\beta$  peptide (70, 72). Moreover, the ADan peptide seems to accumulate mostly in intracellular compartments compared to ABri peptide (79). These findings support the hypothesis that the pathological mechanisms involved are different although mutations affect the same gene.

Of note, other mutations in *ITM2B* have recently been reported (**Table 1**). A probably new pathogenic variant (c.751A>G, p.(Ile251Val)) has been described by Giannocaro *et al.* in one patient from a large pedigree affected by autosomal dominant amyotrophic lateral sclerosis (ALS) and frontotemporal dementia (FTD) (80). Interestingly, this patient presents a complex phenotype combining schizophrenia, deafness, optic and cortical atrophy. Furthermore, the optic atrophy is only present in this patient and this clinical feature has not been reported for any other affected member of the family (80). In another study, Bartoletti-Stella *et al.*, applied NGS on 246 well-characterized patients affected with different forms of dementia. In their cohort, they found a new potential *ITM2B* pathogenic variant in one patient (c.758A>G p.(His253Arg)) (81). Further functional studies and population replicates will be needed to support the implication of *ITM2B* in these cases.

**Table 1. Mutations reported in ITM2B.**

Mutations	Exon	Associated Diseases
c.799T>A; p.Stop267Argext*11 – 2	6	Familial British Dementia (FBD) (42)
c.795-796insTTTAATTTGT; p.Ser266Pheext*11	6	Familial Danish Dementia (FDD) (43)
c.782A>C, p.Glu261Ala	6	Retinal Dystrophy (RD) (40)
c.751A>G, p.(Ile251Val)	6	Probably pathogenic; one patient with a complex phenotype (80)
c.758A>G p.(His253Arg)	6	Behavioral variant of frontotemporal (81)

## Current knowledge about ITM2B

ITM2B, for Integral Membrane Protein 2 B also called BRI2, is a type II protein with still an unclear role (67, 82). Two additional members belong to the ITM family: ITM2A and ITM2C (BRI1 and BRI3 respectively). Each member has its own expression pattern: ITM2B is ubiquitous whereas ITM2A is mostly expressed in chondro- and osteogenic tissues and ITM2C is principally expressed in the brain (83, 84). ITM2B mRNA is found in high concentrations in the brain, placenta, kidney, and pancreas (42). More recently, it has also been found highly expressed in the retina (40). ITM2B is broadly expressed in the brain, but the hippocampal and cerebellar regions present a more abundant expression compared to the other cortical areas (85). This distribution of *ITM2B* expression is in accordance with the phenotypes observed in FBD and FDD.

*ITM2B* is located on 13q14.2, comprises 6 exons and encodes a 266-amino acid protein. It is an integral membrane protein composed by only one domain spanning the plasma membrane. Unlike a type I protein like APP, ITM2B C-terminus faces the extracellular space when binding to the plasma membrane. The protein is cleaved by different enzymes at three different locations. A furin or furin-like protease cleaves the protein between amino acid residues 243 and 244 releasing a soluble 23-amino acid peptide, termed BRI23 (67, 79). The remaining membrane-bound fragment corresponds to the mature form of ITM2B (ITM2Bm) which is then processed in the *cis*-or-medial Golgi apparatus (86). The furin-mediated cleavage is maintained in FBD and FDD leading to the secretion of ABri and ADan respectively (67, 79). Noteworthy, all the mutations (RD, FBD and FDD) are present in

ITM2B's last exon which encodes for the part released after the furin cleavage. ITM2Bm can then be shed by ADAM10 which leads to the release of the ectodomain containing the BRICHOS domain (amino acid residues 137-231) (87, 88). ADAM 10 belongs to a metallopeptidase family of enzyme which specifically cleaves membrane proteins at the cellular surface. Of note, ADAM10 has already been mentioned above as the main  $\alpha$ -secretase implicated in the APP non-amyloid pathway. Like APP, ITM2B is proteolysed within the membrane but unlike APP this action is not mediated by the  $\gamma$ -secretase but rather by different families of enzyme specific to type II proteins: Signal Peptide Peptidase-Like 2a/b (SPPL2a, SPPL2b). Although not required, intramembrane proteolysis is however facilitated by previous ADAM10 mediated-shedding (89). This process generates two fragments: the intracellular domain (ICD) in the cytosol and a small extracellular secreted peptide (89, 90) **(Figure 14)**. SPPL2b is highly expressed in the endosome and lysosome.

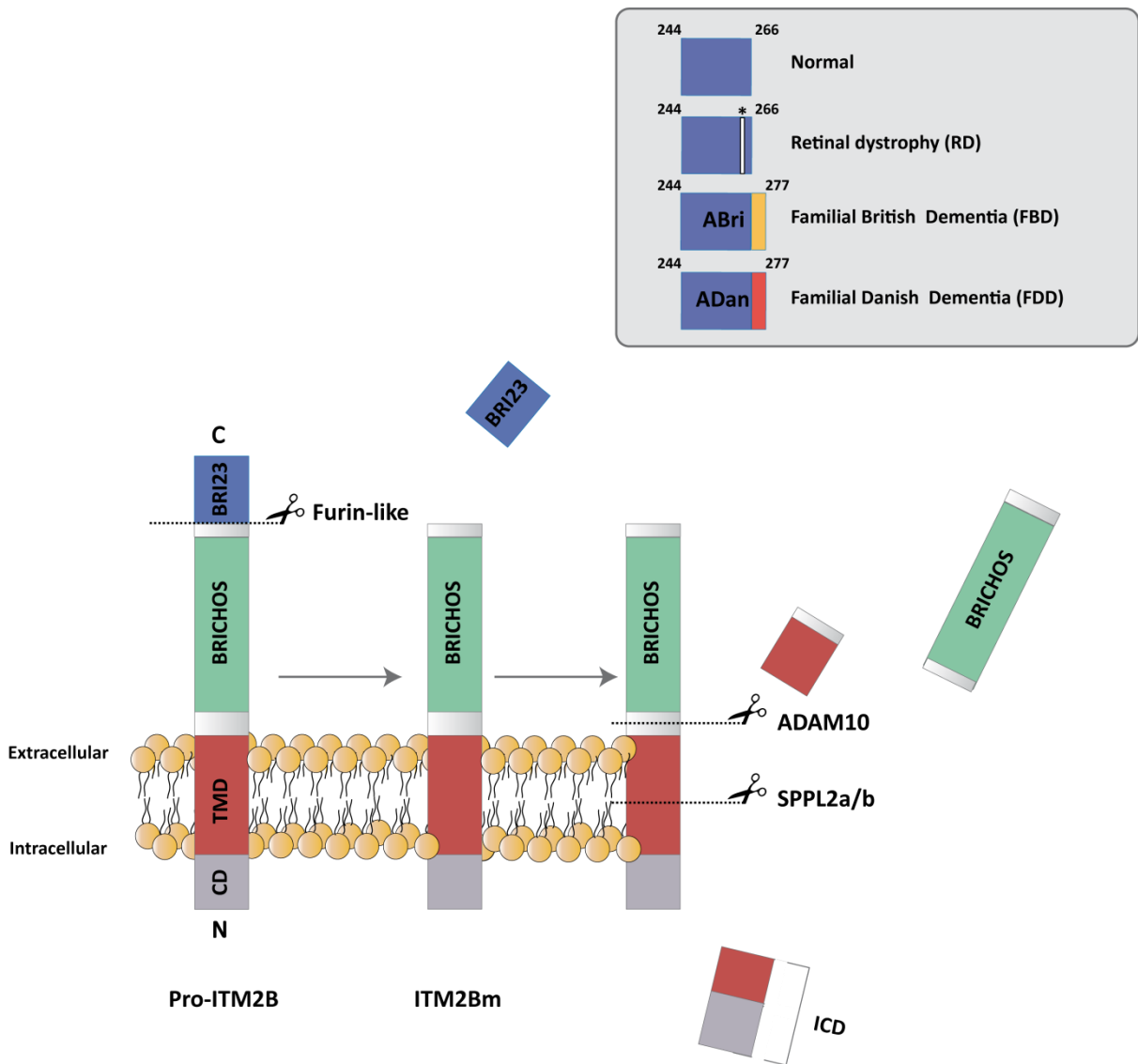


**Figure 14. ITM2B processing and the different mutations in ITM2B.**

ITM2B is composed of different domains; CD: cytosolic domain, TMD: transmembrane domain, BRICHOS, BRI23 and two linker domains (in light grey). In normal conditions, ITM2B is cleaved by a furin-like protease releasing BRI23 and generates the mature form of ITM2B (ITM2Bm). The RD, FBD and FDD mutations present in the C-terminal part of ITM2B generate two longer fragments for FBD and FDD (ABri and ADan respectively) after the furin cleavage. ITM2B is then cleaved by ADAM10 releasing the BRICHOS domain and is subsequently proteolysed intramembranously by SPPL2a/b generating two fragments: the intracellular domain (ICD) and a small extracellular fragment.

In the brain and in overexpressing systems, ITM2B interacts with APP to modulate its processing. Both proteins interact at the plasma membrane and in endocytic vesicles, probably in a *cis* rather than in *trans* fashion. This hypothesis is supported by the fact that the main parts of their extracellular domains are not required for the interaction process (91-93). Indeed, the ITM2B specific region between 46-106 amino acid residues

(corresponding to the transmembrane domain and a small part of the linker domain) seems to be sufficient for its interaction with APP (91). It has been demonstrated that ITM2B interacts with APP and more specifically C99 but, surprisingly, not with C83 (C99 and C83 are APP fragments, see Figure 13). Moreover, ITM2B over-expression increases C99 stabilization (92). In accordance with these results, ITM2B would inhibit the action of the  $\alpha$ ,  $\beta$  and  $\gamma$ -secretases when it can bind to their substrate (e.g. APP full length or C99) (92). In this respect, *ITM2B* is called an “Anti-AD gene” because it would specifically inhibit A $\beta$  release, thus preventing APP to access the different secretases (94). It has also been demonstrated that virus-mediated ITM2B transfer reduces A $\beta$  deposits in an AD mouse model. This anti-amyloidogenic effect seems to be mediated by the BRI23 peptide secreted after furin cleavage. Indeed, the same experiment without BRI23 does not show any effect on amyloid deposition (95). Interestingly, other one part of ITM2B seems to play a role in A $\beta$  aggregation (see below).

Originally discovered in various proteins like BRI2 (ITM2B), chondromodulin-1 and lung surfactant protein C (SP-C/pro-SP-C), the BRICHOS domain is a small (about 100 residues) evolutionary conserved domain which is now found in twelve different protein families (including the ITM family) (96). All the BRICHOS-containing proteins have a similar structure and are prone to aggregation with a high tendency to form amyloid deposits (97). In most cases, this fragment is found in the C-terminal part of the protein. For instance, in ITM2B, BRI23 peptide corresponds to the fragment predicted to form  $\beta$ -sheets. Interestingly, BRI23 peptide binds the ITM2B BRICHOS domain (98). From there, it has been suggested that the BRICHOS domain could act as an intramolecular chaperone, preventing misfolding of a fragment originating from the same pro-protein (88). However, the BRICHOS domain does not only have one substrate. It is also able to inhibit A $\beta_{40}$  and A $\beta_{42}$  aggregate formation *in vitro*, through a yet-unknown mechanism (99). S.I.A Cohen *et al.*, demonstrated that the BRICHOS domain inhibits the second nucleation of A $\beta_{42}$  (100) (see p 24). According to their study, this specific action role is mediated by the direct interaction between the BRICHOS domain and the fibrillar surface but not with A $\beta_{42}$  monomers. Through inhibition of the secondary nucleation, the BRICHOS chaperone is able to almost entirely prevent the generation of toxic oligomers present in AD, without any impact on the primary nucleation and, therefore, the fibrillar elongation. It is important to note that these experiments were

performed with the proSP-C BRICHOS domain and not with ITM2B. Nonetheless, the chaperone-mediated role of ITM2B-BRICHOS domain has been assessed, both *in vitro* and *in vivo*, in the central nervous system and in the eyes of *Drosophila melanogaster*, in order to test the longevity and locomotor activity of this model after A $\beta$ <sub>42</sub> mediated toxicity (101). The ITM2B-BRICHOS domain is more efficient than the proSP-C-BRICHOS domain in inhibiting A $\beta$ <sub>42</sub> toxicity *in vivo* (101). For instance, the ITM2B-BRICHOS domain alone inhibits A $\beta$ <sub>42</sub> induced malformations in the eyes, more specifically within the rhabdomeres which correspond to the mammalian photoreceptors. Also, unlike the proSP-C-BRICHOS domain, ITM2B-BRICHOS not only represses A $\beta$ <sub>42</sub> secondary nucleation, but also has an impact on fibril elongation (102). The BRICHOS domain acts through different modes of action, influencing the kinetics of amyloid formation in order to suppress amyloid formation (101). A subsequent study confirmed the previous results and brought some new information on the specific mechanisms underlying ITM2B-BRICHOS inhibitory properties. The BRICHOS domain behaviors are mediated through different multimeric assemblies which regulate specific aspects of protein misfolding. Monomeric ITM2B-BRICHOS domains are able to spontaneously self-assemble and form dimers or oligomers. Each self-assembly regulates a specific chaperon function. Briefly, oligomers composed of 20-30 subunits are efficient to suppress non-fibrillar aggregation whereas monomers inhibit the A $\beta$ <sub>42</sub>-associated neurotoxicity. Dimers repress A $\beta$ <sub>42</sub> fibrillization through inhibition of the secondary nucleation and fibrillar elongation (103) (**Figure 15**).

Altogether, these data on ITM2B suggest that this protein acts to prevent and limit AD development through several actions: inhibiting A $\beta$  formation, preventing APP to access secretases, and inhibiting A $\beta$  aggregation with its chaperone BRICHOS domain. ITM2B has also been associated with neuronal functions where it could have a role in neurite outgrowth (86). Although ITM2B peptides have been associated with different anti-amyloidogenic functions, the exact role of the proteins is still unclear.

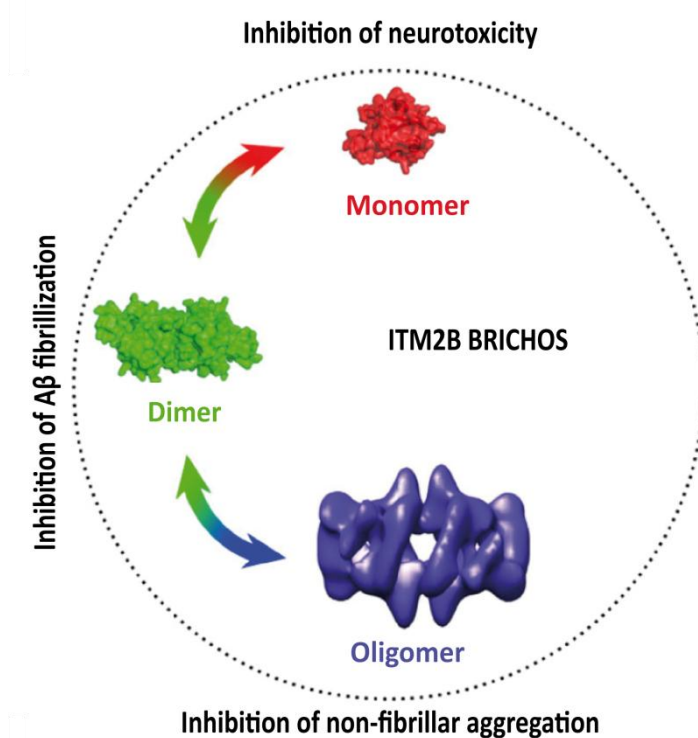


**Figure 15. ITM2B-BRICHOS activity is determined by its quaternary structure.**  
 Modified from (Chen *et al.*, 2017) (103).

More recently, ITM2B has been shown to facilitate glutamate signaling in the rodent brain via both presynaptic and postsynaptic mechanisms (104). Furthermore, other proteomic studies in rodent brains demonstrate that ITM2B interacts with APP and APLP2 forming a complex which links to the heterodimeric metabotropic GABA<sub>b</sub> receptors (105). Several distinct multiprotein complexes have been reported and could each mediate different processes. However, in this specific nano-architecture, APP would interact with the sushi domains of GB1a subunit, which are necessary for the localization and stability of the receptor. Further proteomic analyses demonstrate that GABA<sub>b</sub> anterograde trafficking to the axon is mediated by APP. Indeed, through vesicles trafficking, APP would constitute the link between adaptor proteins and their receptors. However, the interaction between APP and GABA<sub>b</sub> receptors appears to be labile and seems to be made possible only during the trafficking phase, and not at the plasma membrane. Therefore, ITM2B seems to be involved in axonal trafficking and amyloidogenic processing via its interaction with APP.

Along with *in vitro* assays with several cell types and in order to gain further insight into the protein function, different groups chose to develop *in vivo* studies. Indeed, animal models are useful tools to better understand the physiology and the physiopathology of human diseases. Several animal models carrying the FBD or the FDD mutations have been generated in order to investigate the role of ITM2B, mostly in the brain.

## **ITM2B animal models**

Among all different species, the mouse is undoubtedly the most widely used animal model. Different reasons explain this choice. Housing is convenient and can be relatively easily managed for a laboratory. Breeding is rapid compared to some species, even humans. Moreover, the mouse genome is well annotated so as to allow genetic modifications. Finally, and maybe the most important, mice are mammalian and their physiology is close to humans. For all these reasons, several rodent mutants of FBD and FDD have been developed in order to try to mimic the diseases and better understand the physiology and physiopathology of ITM2B. The aim of using animal models for a neurodegenerative disease is also to document the progression of a disorder.

The first generation of FBD mouse models genetically over-expressed mutant ITM2B-FBD under the brain mouse prion or Thy-1.2 promoter. This model does not contain amyloid deposits but rather an intracellular accumulation of the FBD mutant, and does not present any change in behavioral phenotype (106). On the opposite, FDD models, using the same genetic approach with the expression of the ITM2B-FDD mutant (Tg-FDD and ADanPP7), developed FDD features. Indeed, Tg-FDD and ADanPP7 models exhibit amyloid angiopathy, parenchymal diffuse ADan deposits, as well as amyloid deposition in the brain associated with microglial and astrocytic activation (107, 108). Nevertheless, no behavioral deficits were observed in the Tg-FDD model unlike in ADanPP7 mice which present an anxiety phenotype. Deficits in spatial learning and memory were assessed with the Morris water maze experiment. ADanPP7 mice were able to swim longer to find a hidden platform compared with age matched non transgenic controls. However, they did not swim as fast as the control mice, leading to believe that the previous results could have been due to motion impairment more than a memory deficit (108).

Using a different approach and with the progress of genetic tools, new models were created such as the FBD and FDD knock-in models (respectively FBD<sub>KI</sub> and FDD<sub>KI</sub>). In these models, one of the alleles of the *mITM2B* was replaced by the human mutant form, better reflecting the disease mechanisms compared to the previous over-expressing systems. In addition, an haploinsufficiency mouse model (BRI<sup>+/-</sup>) was also generated, expressing only one of the two *mITM2B* alleles. Interestingly, FBD<sub>KI</sub>, FDD<sub>KI</sub> and BRI<sup>+/-</sup> mice did not present any of the histopathological FBD or FDD features but were similar to wild type mice (109, 110). However, they presented with severe memory deficits (110, 111).

Differences in phenotype among the different mouse models bring two pathological hypotheses: one being the role of the amyloid cascade, or the other, the loss of function of ITM2B. The first hypothesis focuses on the toxic effect of the mutation. In this theory, ABri and ADan have a deleterious effect and act as a trigger for a cascade of events leading to the disease. Of note, the amyloid cascade theory with A $\beta$  peptide has been broadly used in order to try to explain AD physiopathological mechanisms and is still the most popular hypothesis to this day. The second hypothesis proposes that the diseases are due to ITM2B loss of function. In this case, amyloid deposits would not induce FBD or FDD but rather result from the neurodegenerative process. The role of protein aggregation on neurodegenerative diseases has been actively debated for a long time for all disorders involving amyloid plaques, such as Alzheimer's, Parkinson's and Huntington's diseases (112).

Each of the different animal models has its own advantages and has been very valuable to help in providing new insights into FBD and FDD. Nevertheless, it is important to note that none of those animal models fully summarizes the hallmarks of neither FBD nor FDD. As well, no current AD mouse model encompasses the entire spectrum of the disease either (113). To date, there is no animal model available for the RD mutant. Not all FBD and FDD characteristics are present in the developed rodent models and, considering the differences between human and mouse biology; rodents do not seem to be the best option to model ITM2B-related disorders.

In our case, another major obstacle to better understand the physiopathological mechanisms involved in RD consists in the absence of access to diseased tissues. However, another option has recently been made available for disease modeling. Indeed, the past years have seen stem cell research emerging not only as a treatment option or as a

preclinical screening tool for therapeutic interventions, but also for disease modeling. The next part will focus on the advances in the field of stem cells and their utilization as a tool to better understand the RD physiopathology.

## **4. Human stem cells**

### **Stem cell definition and properties**

Stem cells have two fundamental properties. First, they have the capability of self-renewal. Indeed, during the division process, stem cells renew themselves while also producing a daughter cell. Thus, the asymmetric division maintains the stem cell population. Secondly, stem cells have the capacity to differentiate into different cell types, meaning they can specialize and acquire specific characteristics of a certain cell type; criteria called cell potency. Four different types of cell potency can be distinguished: totipotency, pluripotency, multipotency and unipotency (**Figure 16**). Totipotent cells are only found during the early steps of the development following fertilization, and before the inner cell mass formation into a blastocyst. Totipotent cells can differentiate into embryonic and extra embryonic cells. According to the stringiest definition of totipotent cells, one isolated totipotent cell is able to produce an entire organism from the maternal tissues for its proper development (114). Pluripotent cells appear later during embryonic development. In fact, pluripotent cells can be isolated from the inner cell mass during the blastocyst stages and can give rise to all the cell types composing the three embryonic germ layers: ectoderm, mesoderm and endoderm. As for them, multipotent cells have a limited differentiation capacity and generate a restricted number of cell types, usually cells related to a same lineage. For instance, retinal progenitor cells (RPCs) are multipotent cells during retinogenesis (see retinal development p9). Finally, unipotent cells are able to differentiate only into one specific cell type such as the satellite cells in the adult skeletal muscles which can only differentiate into myofibers (115).

Stem cells may also be classified into either embryonic or adult stem cells. Embryonic stem cells (ESCs) are pluripotent whereas adult stem cells are multi or unipotent. Adult stem cells reside within specialized microenvironments of adult tissues termed niche (116). Upon specific stimulations, adult stem cells renew themselves and give rise to a daughter cell

which further differentiates into a specific cell type depending on the needs of the tissues. Otherwise, adult stem cells rest in a quiescent stage. Adult stem cells have been identified in many different organs such as the liver and the intestine. Adult stem cells play a role in tissue regeneration and homeostasis. For instance, hematopoietic stem cells enable constant blood cell production.

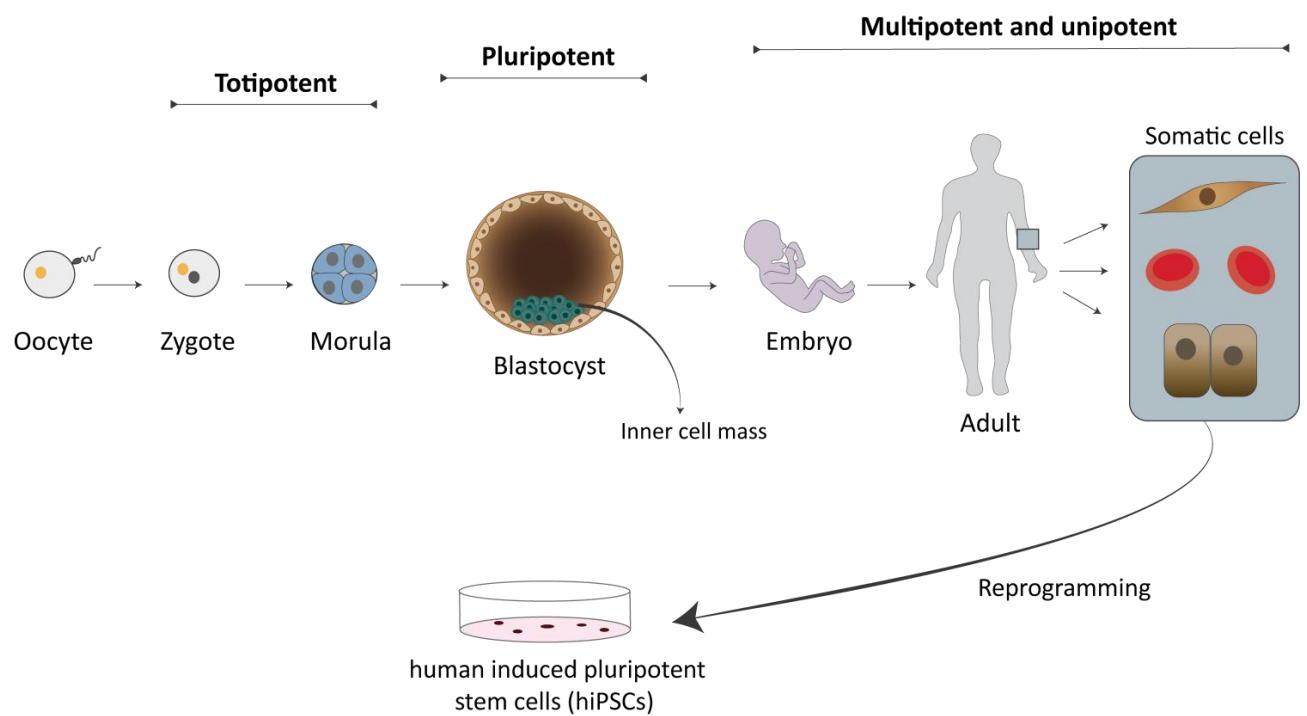


**Figure 16. Evolution of potency over cell development.**

After fertilization, cells remain totipotent from the zygote to the morula stages. Then, embryonic stem cells originating from the inner cell mass of the blastocyst are pluripotent. Throughout development of the embryo, cells lose their pluripotency to become multipotent and unipotent during the adult stage. Several types of somatic cells can be reprogrammed into human induced pluripotent stem cells (hiPSCs) using different factors.

## Embryonic Stem cells

As described above, embryonic stem cells (ESCs) are pluripotent and have the ability to differentiate into the three embryonic germ layers. Pluripotency is not a permanent state *in vivo*; the more the embryo develops, the more this ability is lost because of cell fate specification. *In vitro*, the pluripotent state can be artificially maintained under specific culture conditions. However, finding the right cell culture conditions to cultivate and maintain ESCs has been a long journey. In 1981, M. J. Evans and collaborators isolated the first ESCs line from a mouse embryo (117). Almost twenty years later, the protocol was

adapted, allowing the isolation of human embryonic stem cells (hESCs) from a human blastocyst (118). This major breakthrough brought hope and ESCs appeared as an unlimited source of undifferentiated cells which could further be used for regenerative medicine, drug screening and disease modeling. ESCs also represent a powerful tool to study human embryonic development and related diseases, as well as cell fate control. Following the rapid evolution in the field, several clinical trials with ESCs have already been conducted in different countries. For instance, in 2011 two clinical trials started with hESC-derived RPE cells for different retinal dystrophies (ClinicalTrial.gov Identifiers: NCT01344993 and NCT01345006) (119). Moreover a clinical trial is currently ongoing in France for patients affected with retinitis pigmentosa linked to mutations in a gene specifically expressed in the RPE (ClinicalTrial.gov Identifier: NCT03963154). Human ESCs that have differentiated into RPE cells can grow on an amniotic membrane thus forming a cell patch. The patch is then surgically introduced into the subretinal space in patients. Because of the relative immune privilege which diminishes the risk of rejection, the subretinal space appears as an ideal environment for cell therapy testing.

As mentioned above, human embryonic stem cells (hESCs) originate from the inner cell mass of the blastocyst, which subsequently forms the human embryo. For this reason, hESCs access and use for research and medicine have been limited and strictly regulated (depending on the country legislation). Indeed, the exploitation of derived cells from “potential developing being” has raised ethical, political and religious issues. In addition, hESCs utilization for transplantation can cause tissue rejection because of the differences in the donor and the recipient immune systems. In this context, researchers had to find alternatives for pluripotent stem cell sources. One way to overcome all the ESCs issues is to generate pluripotent cells directly from a patient.

## **Induced Pluripotent Stem Cells (iPSCs)**

Different strategies allow the induction of somatic cells into pluripotent cells. One of them, the somatic cell nuclear transfer, consists in introducing the nucleus of a somatic cell into an enucleated oocyte. First demonstrated with *Xenopus* oocytes, this technique has later been adapted to mammalian cells and has led to the birth of Dolly, the first mammal cloned in

1997 (120, 121). In 2011, the technology was adapted to human oocytes (122). Although somatic nuclear transfer raised ethical issues because of the use of human oocytes and the potential abuses related to cloning, this technique has brought the idea that pluripotency can be induced by factors present inside an unfertilized egg. In 2006, based on that concept, Kazutoshi Takahashi and Shinya Yamanaka demonstrated how, with the addition of only four transcription factors, mouse fibroblasts can be reprogrammed into ES-like cells named iPSCs for induced pluripotent stem cells (123). They started with a pool of 24 candidate genes which had already been reported to have a role in ESC pluripotency, phenotype or morphology. They designed a strategy where any combination of factors that could reactivate the ESCs specific locus *Fbx15* could be isolated after antibiotic selection. Factors were delivered by a retroviral vector and removed one by one to finally find the good combination. At the end, surprisingly, only four factors, Oct3/4, Sox2, c-Myc, and Klf4, were necessary and sufficient to obtain iPSCs from mice. In addition, mouse iPSCs injected into a host blastocyst were able to generate an adult mouse by tetraploid complementation assays (124). Essentially, at the two-cell development stage of a mouse embryo, nuclei of somatic cells are fused forming tetraploid cells which are then forced to differentiate into extraembryonic tissues. In order to test their pluripotent potential, cells are injected during the blastocyst stage of the newly formed tetraploid embryo. If the injected cells are indeed pluripotent, they will therefore be able to form an entire organism supplemented by the extra embryonic tissues (generated by the tetraploid cells). This test is considered as the most stringent for pluripotency (125). Following the same reprogramming strategy, Yamanaka's team induced human pluripotent stem cells (hiPSCs) derived from human dermal fibroblast only one year after the mouse iPSCs experiment (126). The same year, Thomson's group reported the reprogramming of human fibroblasts using a different set of factors, Oct4, Nanog, Sox2 and Lin28, which were delivered by a lentiviral system (127). For this stunning discovery, Shinya Yamanaka received the 2012 Nobel Prize in Physiology or Medicine jointly with John Gurdon for his work on somatic cell nuclear transfer in *Xenopus*.

The first reprogramming methods involved viral vectors, such as a retrovirus or a lentivirus, which can integrate into the host genome (126, 127). The potential risk of mutagenesis in the iPSCs genome was a big concern for further clinical applications. To solve this problem, different non-integrative techniques using an adenovirus, the Sendai virus, synthesized

RNAs, plasmids, proteins and small molecules were developed (128-133). Today, plasmids and Sendai viruses are the most routinely used in laboratories. Another aspect of the first protocol has evolved over time: dermal fibroblasts were the first cell type used for reprogramming but it is now possible to use different somatic cell sources, such as keratinocytes (hair follicles), peripheral blood cells, or even cells present in urine (134-136).

As described above, protocols have evolved for hiPSCs generation including some with animal-free components for potential clinical applications. Almost every laboratory has its own adapted reprogramming protocol and culture conditions. One way to guarantee best practices is to perform an exhaustive reproducible and rigorous characterization of every newly generated iPSC or ESCs lines (125). The following quality control criteria are from ESCs characterization and can therefore be extended to iPSCs to demonstrate their pluripotent ability and the absence of significant chromosomal aberrations. For clarity, the term pluripotent stem cells (PSCs) will be used in the following paragraph, as it regroups ESCs and iPSCs. All different characterization steps were nicely reviewed by Martí *et al.*, and will be further exposed below (137). The morphology of PSCs is really specific; these cells harbor a round shape colony organization. PSCs show high alkaline phosphatase activity and are characterized by the expression of different markers: the cell surface markers TRA-1-60, TRA-1-81 (keratin sulfate antigens) and SSEA4 (glycolipid antigens), and the nuclear transcription factor markers NANOG, OCTO4 and SOX2. The next step for the characterization is to prove that the cells can differentiate and give rise to cells from the three primitive germ layers. During this test, stem cells are injected *in vivo* into an immunodeficient rodent host where they form spontaneous teratomas containing cells from the three embryonic germ layers. Nonetheless, the relevance of this *in vivo* experiment has been highly debated, especially in the context of the "three Rs" concept in animal research: replacement, reduction, refinement. In parallel, an *in vitro* alternative has emerged and is currently sufficient to register a pluripotent stem cell line. Cells are cultured in suspension where they form small aggregates called embryoid bodies (EBs) (138). If the cells are pluripotent, EBs should contain cells from the endoderm, mesoderm and ectoderm. Another critical step in PSCs characterization is the maintenance of genome integrity. Reprogramming and even extensive passages can produce alterations in the genome. Genomic lesions have often been reported to map to loci commonly mutated in cancer cells

(especially in iPSC lines) (139). Moreover, genomic instability is also associated with cancer cells and, for this reason, presents a high concern in the stem cell field mainly for their safe use in regenerative medicine. Karyotypic analysis has been extensively and routinely used for stem cell line characterization. This technique, even though easy and cheap, has some limitation. Large genomic alterations like chromosome aberrations (loss, translocation, inversion) can be detected by karyotyping. However, smaller abnormalities such as copy number variations and single nucleotide variants are not identified by karyotyping. Nowadays, techniques with better resolution and sensitivity are available including microarray techniques such as SNP, NGS, and comparative genomic hybridization (139).

The number of reports concerning genetic instabilities in PSC lines has increased these last years. The gain of 20q11.21 is one of the most recurrent chromosomal aberrations reported in PSC lines and is, for instance, observed in more than 20% of the cell lines over the world (140-142). In this context, it has been proposed to monitor PSC genome quality after derivation and every 12 passages, which represents a balance between the cost and laboratory constraints related to experiments (143). However, this objective is still not reach and most teams only perform karyotyping once, mostly because of cost issues. Other cheaper alternatives are emerging, and consist of using droplet digital PCR approach which allows the detection of more than 90% of the recurrent abnormalities (144).

Although iPSCs are highly similar to ESCs, molecular and functional differences are significant. iPSCs are generated from differentiated mature tissues and are “forced” to adopt a pluripotent fate by the expression of the four transcription factors. Different studies have shown that iPSCs keep an epigenetic memory from their original tissue (145, 146). During the reprogramming process, DNA demethylation is not complete and therefore iPSCs retain vestiges of methylation which are characteristics of their original tissue (147). Thus, iPSCs would be more prone to differentiate into cells of their own origin (145, 148). In addition, it has recently been demonstrated that cells from older patients harbor epigenetic characteristics linked to the age compared to young donor (149). However, anomalies seem to be lost or highly reduced with passaging (146). Of note, the epigenetic memory was not observed with PSCs obtained from the somatic nuclear transfer technique (148). In addition, differences are not only observed between iPSCs and ESCs but also between different iPSC

lines (and ESCs). Variability in laboratory practices entails the long characterization process required before stem cell lines can be registered.

It must be borne in mind that stem cells, and more specifically iPSC, research is a relatively young field and genomic and epigenetic alterations during reprogramming or prolonged passages are still under investigation. If some alterations are unacceptable, other modifications such as epigenetics or polymorphisms are more difficult to categorize. No current standardized guidelines, or international consensus, is available, and for this reason, fixing a threshold of what should or should not be tolerated in terms of anomalies is still ambiguous and mostly depends on the future use of the cells (150). Recent studies seem to focus on the methylome analysis, which is only a part of epigenetics (151). Methylome analysis might be the future crucial interest in the stem cell community, and may one day become a part of the characterization process.

Although ESCs are still the “gold standard” for pluripotency, the iPSC technology created a revolution in the field since it bypasses a lot of ethical issues. Today a lot of protocols are available for differentiation of various cell types. However, the major interest of the iPSCs is that they use a genetic copy of the donor and therefore represent a source of cells for personalized cell therapy. In a short period of use, iPSCs have already demonstrated their utility in different diseases. In 2017, almost ten years after the discovery of Yamanaka, Masayo Takahashi reported the first autologous transplantation of iPSCs-derived RPE in subject affected with wet age-related macular degeneration (AMD) (152, 153). This pathology is one of the most prevalent diseases affecting vision in the elderly. Of note, out of two patients, only one has been transplanted, as copy number alterations in iPSCs prevented transplantation in the second patient. In Japan in October 2018, Jun Takahashi and colleagues started the first clinical trial for Parkinson disease. They implanted iPSCs from an allogenic donor into the brain of a first patient (154). This accomplishment was possible because the disease etiology was already known, which is not always the possible.

The ultimate goal when studying a specific disease is to find a treatment to cure the affected subjects. Unfortunately, the journey could be long and the first step is always to get an understanding of the pathological mechanisms involved in the disease. In this perspective, since PSCs consist of genetic copies of the donor, they represent a powerful tool for disease

modeling; especially when the disorder is rare and either no model is available, or the model does not accurately summarize the disease. Moreover, cell types previously inaccessible (like cardiomyocytes or retinal cells), can now be generated after specific PSCs differentiation. In the context of disease modeling, hiPSCs have the benefit to be derived from the patient and can, therefore, be better adapted to summarize a specific disease than hESCs. This allows for much more precision in the practice of medicine (155).

## **5. Retinal organoids and disease modeling**

As mentioned above, studying pathological mechanisms may be hampered by the lack of access to disease tissue and relevant animal models. This is particularly true for IRDs where retinal biopsies are not possible for ethical issues. In addition, histological studies are rarely available and mostly, only performed on post-mortem specimens. The latter often carry end stage diseases and are subject to artifacts linked to the time delay between death and sample handling. Performing disease modeling using patient-derived iPSCs which can be differentiated in retinal cells, and present great similarity with the original retinal tissue, offers a valuable tool to investigate disease mechanisms along with other cellular or animal models. The challenge however is to find the right culture conditions which allow PSCs differentiation into retinal cells in two-dimensional (2D) or three-dimensional (3D) culture. Protocols were developed and adjusted over time to achieve this goal.

### **Controlling cellular differentiation and retinal induction**

In 2002, Zhao *et al.*, provided the first evidence of a potential for retinal differentiation in mouse ESCs (156). Mouse-derived neural progenitors were treated with FGF2 and iTSFn (medium supplemented with insulin, transferrin, selenium and fibronectin (157)) in a neural induction medium and few cells expressed retinal progenitor markers. However, this protocol was not really efficient to induce retinal progenitors. Thereafter, Sasai's group developed an *in vitro* system based on a serum-free culture of suspended EBs aggregates (SFEB culture) to differentiate mouse ESCs into neural precursors (158). They then combined the SFEB culture method with the addition of two extrinsic signals; Dickkopf-1 (DDK1) and Lefty-A, respectively Wnt and Nodal antagonist, allowing a rostral specification of the

progenitors. Finally, before plating the cells, treatment with Activin-A and serum significantly induced PAX6/RAX co-expression in the cells, thus demonstrating the differentiation of mouse ESCs into neural retinal precursors (159). One year later, retinal cells were generated from hESCs following the same concept of sequential differentiation: neural induction followed by retinal differentiation (160). Nevertheless, several aspects differed from the previous protocol in particular the treatment with a combination of Noggin (BMP antagonist), DDK1 and IGF-1 factors. The EBs were also coated onto matrigel or laminin and maintained in a proneural medium supplemented with fibroblast growth factor 2 (FGF-2), B27 and N2. Of note, this protocol does not properly recapitulate the timing of normal human retinal development and but rather accelerates the induction of neural retinal cells. In 2009, Meyer *et al.*, developed a protocol based on a passive strategy for the neural induction, without using exogenous BMP and Wnt antagonists (161). This strategy based on the “default model” of neural induction proposes that BMP signaling inhibition leads to neural induction in the embryonic ectoderm (162). The passive neural induction was possible with this protocol because of the endogenous upregulation of DDK1 and Noggin during the eye field specification. The investigators reported the expression of PAX6 and RAX by more than 95% of the cell population after 16 days of differentiation. Furthermore, the developmental timing seems to be consistent with the normal human retinal development. Interestingly, this protocol was also tested on iPSCs and showed some variability depending on the type of cell line tested.

However, even if the 2D culture system is more convenient, it still does not entirely encompass the aspect present *in vivo*, such as cell architecture and cell-cell interactions.

In the quest for the most accurate and complex model, the organoid technology has been a major progress in the stem cell field, not only to recapitulate a specific disease but also for drug screening. Historically, roots can be traced back to the experiments of Wilson in 1907 in which cells dissociated from sponge can recreate whole sponges (163). Organoids or “organ in a dish”, are 3D *in vitro* structures generated from self-organizing pluripotent or multipotent stem cells which mimic the *in vivo* development of an organ (164). According to the criteria exposed by Lancaster and Knoblich in 2014: 1) organoids are composed of different cell types, 2) these cells exhibit the rudimental organization resembling the whole organ 3) the system displays some functions specific to the organ itself (165). Under specific

culture conditions, organoids have been developed for a diversity of organs such as kidney, intestine, brain, lung and retina (166-170). In the next part, I will focus on several protocols leading to retinal organoid formation, sometimes called optic cups, optic vesicles or vesicle-like structures, depending on the authors and protocols. Each protocol contributed to what retinal organoids are today and each has advantages and disadvantages.

## **Retinal organoids**

The advent of retinal organoids is associated with the sophisticated work developed by Sasai's team in Japan. By improving their previous SFEB culture system (now called SFEBq), they demonstrated the self-organization of mouse ESCs into polarized cortical tissue. Moreover, the newly formed structures recapitulate the early *in vivo* cortical development and are composed of the different layers each containing specific neurons (171). This major step paves the way for the development of retinal organoids by modifying the previous SFEBq protocol and finds the culture conditions suitable for retinal morphogenesis. Two main changes were essential to obtain 3D self-organizing optic-cup from mouse ESCs; first they added matrigel which contains extracellular-matrix components allowing RPE formation, and second, they drastically decreased the knockout serum replacement concentration (KSR: from 10% to 1.5%) (172). The resulting bi-layered structure remarkably mimics the *in vivo* patterning of the eye formation with evagination of the optic vesicle followed by invagination of the optic cup (see Figure 6). One of the most striking aspect of their work is the fact that 3D self-organization occurs spontaneously guided by intrinsic signals. Inside the optic cup, cells in the inner layer express neural retinal markers such as PAX6, RAX and VSX2 whereas cells in the outer layer express RPE markers (PAX6, MITF). Importantly, generated retinal progenitors are able to differentiate into retinal cells and thus follow a temporal sequence similar to the mouse retinogenesis. Moreover, excised optic cups cultured in a floating medium for 10 extra days, presented stratified neural retina containing all retinal cell types. One year later, in 2012, the same team extended and adapted the protocol to hESCs (**Figure 17**) (170). Contrary to mouse ESCs, hESCs are not able to form retinal epithelium with a low Knockout serum replacement (KSR) concentration. However, increasing KSR concentrations cause a caudalization of the neural progenitors (KSR 20 %). To solve this problem, a treatment with a Wnt inhibitor was used. Furthermore, 10%

of fetal bovine serum (FBS) and a treatment with SHH were also added in order to promote retinal differentiation. Due to specie specificity, several differences were observed between optic cups generated from mouse ESCs and hESCs; such as developmental time frame, size, and thickness. All these parameters are increased with hESCs compared to the use of mouse ESCs. Nevertheless, the formation of optic cups was much less frequent with hESCs. In 2015, the protocol was again improved by the same team; in this new version, the “step-wise induction-reversal method”, allows the co-formation of neural retina and adjacent RPE from hESCs. Interestingly, the interaction between the two tissues recreates a growth zone containing a stem cell niche (173). An early treatment with BMP4 improved the differentiation of cells into RPCs (173).

In parallel, other teams developed distinct protocols with the goal of generating retinal organoids. In 2011, Meyer *et al.*, added an adherent intermediate culture stage in order to select neuroepithelial structures, later forming “optic-vesicle like structures” (3D/2D/3D culture) (174). After the formation of EBs from hESCs and hiPSCs, 3D aggregates were coated onto laminin to enhance neural differentiation. Generated 2D neural clusters were then mechanically isolated and transferred to floating cultures with retinal differentiation medium allowing the formation of new 3D structures. Progenitor cells in these optic vesicle-like structures were able to differentiate into retinal cell types following stages of the normal retinal development. Few years later, Zhong *et al.*, modified the protocol and observed two major improvements: the production of laminated 3D retinal cups which turned out to contain functional photoreceptors (175). The key to this improvement was the addition of 10% FBS (serum), taurine and retinoic acid at a specific time during the formation of the 3D retinal cups. Using this protocol, investigators reported functional photoreceptors containing outer segment discs after 180 days of differentiation (**Figure 17**). For the first time, by patch-clamp recordings, they demonstrated that some retinal organoids hiPSCs-derived photoreceptors are able to respond to light stimuli.

However, all previous protocols required the addition of exogenous factors, like serum or matrigel for cell culture. Although, this would not preclude their use as a therapy in humans providing that these animal-based products are appropriately monitored, their use is not optimal with further therapeutic applications. In order to deliver a more define cell culture

system which is safer for clinical applications, Reichman *et al.*, from our institute, established a 2D/3D culture protocol bypassing the formation of EBs as well as omitting the use of any substrates or exogenous molecules (**Figure 17**) (176). Of note, in order to be completely xeno-free (i.e. without any animal component in the culture medium), the protocol was adapted to feeder-free conditions (177). The authors demonstrated that withdrawal of FGF2 from the medium induces the endogenous expression of DDK1 and Noggin and, along with the presence of N2 supplement, allows the self-formation of “neural-like structures” (176). After 28 days in 2D culture, retinal organoids were manually picked and put in a floating medium containing B27 supplement and FGF2 (177). Retinal organoids subsequently generated contain all retinal cell types, appearing in a sequential manner consistent with the normal retinal development. Interestingly, organoids are not laminated but rather contain rosette structures where the retinal cells appear and mature. This non-laminated organization is probably due to the absence of serum. Robin Ali’s team then established a protocol combining the protocols from Zhong *et al.* and Reichman *et al* protocols (178). Similarly, the first 2D culture stage occurs as previously mentioned by Reichman *et al.*, in absence of FGF2 and with the addition of N2 supplement to induce neural differentiation (177). However, the second 3D culture part is closer to the protocol from Zhong *et al.* protocol with a retinal differentiation medium containing FBS, RA and taurine enabling the formation of laminated organoids (175). Their protocol is efficient in generating photoreceptor cells with outer segments and presynaptic structures.

More recently, the 2D/3D protocol from Reichman *et al.* was adapted at our institute to generate laminated retinal organoids by adding FBS and glutamax during the floating part. This protocol promotes cone differentiation without the addition of retinoic acid (179).

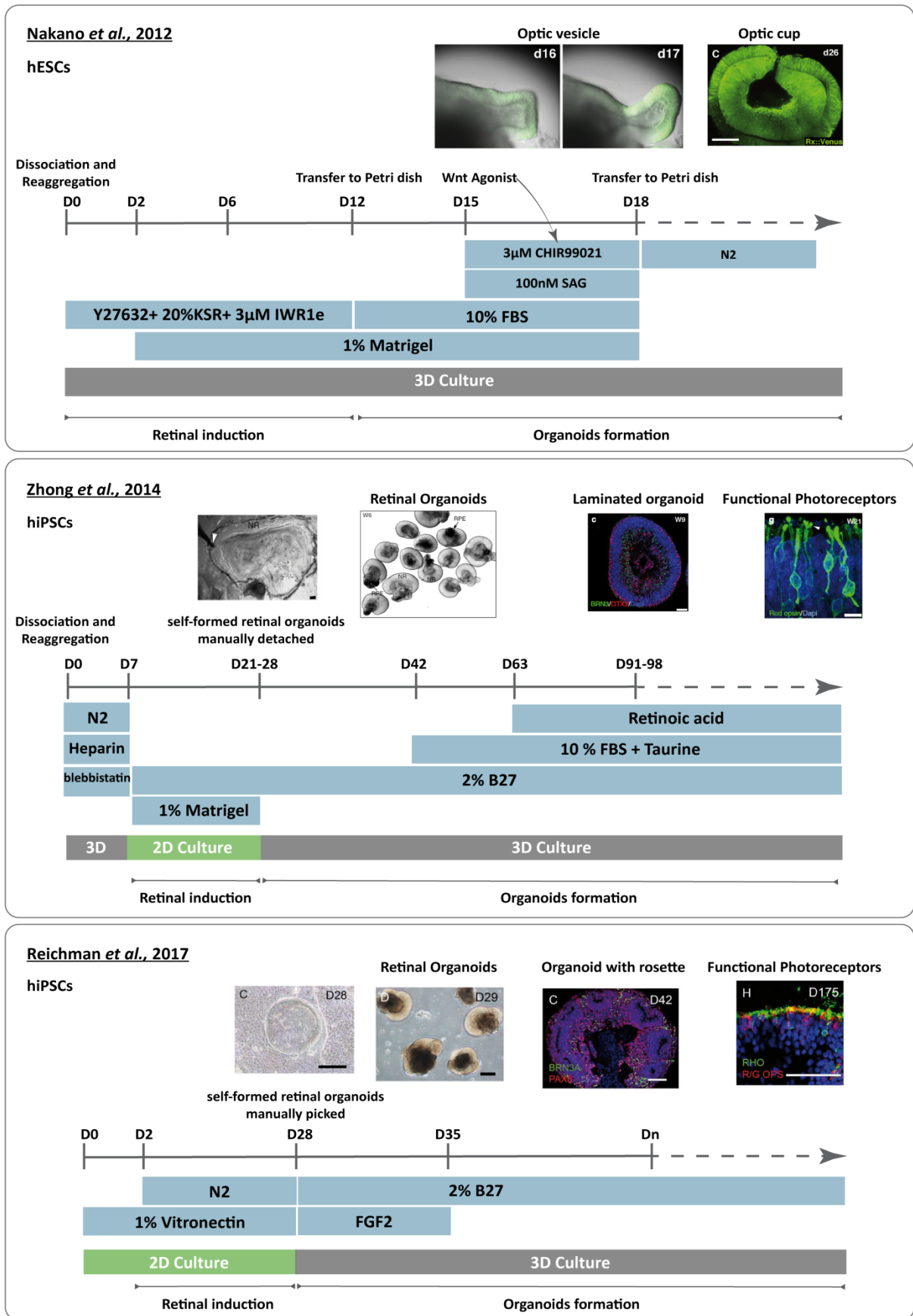


**Figure 17. Overview of different protocols to generate retinal organoids.**

Three different examples of differentiating protocols used to obtain 3D retinal organoids from hESCs (Nakano et al., 2012) (170) or hiPSC (Zhong et al., 2014) (175) (Reichman et al., 2017) (177).

## Drawbacks and improvements

After exposing different protocols to obtain PSCs and retinal organoids, the first obvious limitation of the system is the reproducibility among generated structures. A lack of uniformity in size, shape, or maturity, among retinal organoids has been observed even using one PSC line (178). In this context, multiplying the number of cell lines could also increase the variability into retinal organoid cultures due to genetic and epigenetic differences.

Organoids from a same batch do not all develop exactly the same; different developmental stages can be observed in a culture, making the comparison difficult (180). This difference in organoid maturity may be partially explained by both the relative lack of oxygen and nutriment diffusion, which impact on their development and enhance the diversity in a classical static suspension culture. Therefore, the recent development of spinning bioreactors, which improve fluid convection, helped to improve culture conditions. This system has proven its efficiency by accelerating organoid maturation compared to static culture, as well as generating larger organoids with a better preservation of the lamination (181, 182). However, this strategy is not compatible with the maturation of the outer segment of the photoreceptors over time (182). Recently, another strategy has been proposed in order to limit biases imposed by culture conditions. The staging method consists of bypassing temporal criteria and sorting the organoids according to their morphology (180).

In a really interesting study conducted by Reh's team, hiPSCs-derived retinal organoids have been compared to fetal retina using RNA-seq combined with single-cell techniques (see p13) (33). Of note, their protocol of differentiation is mostly based on the protocol from Zhong *et al.*, with some variations. In the light of this study, retinal organoids faithfully recapitulate normal human retinal development in terms of cellular composition and gene expression when analyzed at equivalent developmental time points. However, retinal organoids present a disrupted inner retinal organization. Interestingly, culture conditions do not seem to have an impact on the maintenance of the inner retinal architecture (33).

Despite the spectacular progression in the retinal organoids' field, some shortcomings persist (using any of the protocols available to date) such as the absence of inner retinal organization or the degeneration of the RGCs over time. Regarding this last issue, the

absence of a neural target and/or metabolic support could explain the progressive loss. In addition, the lack of interaction between the outer segment of the photoreceptors and the RPE is also one of the main current issues in retinal organoids, limiting the maturation of photoreceptors derived-PSCs. Emergence of engineering approaches like organ-on-a-chip systems and, notably, retina-on-a-chip demonstrated their potential recreating the physiological interaction between photoreceptors and RPE cells *in vitro* (183). The apposition between the two cell types is a key feature of the visual cycle and enables phagocytosis of the photoreceptor outer segments by the RPE cells which subsequently impacts on the improvement of the OS formation in organoids.

Furthermore, retinal organoids present a modest heterogeneity of cells in accordance with the absence of microglia and astrocytes, which normally compose the retina in normal conditions. Another limitation of current retinal organoids is the absence of vascularization and endothelial cells. Recent advances in the organoids' field have led to the generation of human blood vessel organoids from hiPSCs and hESCs (184). Once transplanted into the kidney capsule of immunodeficient mice, these fascinating formations, composed of vessel-like structures, can create anastomoses with the host vascular tree system (185). However, this technique has not been integrated into a tissue specific organoid yet. For this last part, several emerging approaches such as 3D bioprinting or incorporation of endothelial cells, are promising and tend to fill the gap with the complexities of the human retina.

Retinal organoids is a relative young field in constant evolution. Development of strategies mixing different fields like physics or engineering will push forward the current limitations. As a matter of fact, this year, winners of the "3D retinal organoid" challenge sponsored by the National Institute of Health, will be announced, highlighting new strategies to improve retinal organoids.

## **Retinal disease modeling with organoids**

Recent advances in the field of retinal organoids (described above) combined with the emergence of hiPSCs have enabled the development of disease modeling. As it is now possible to reprogram patient's somatic cells into iPSCs from a simple skin biopsy, and subsequently use these cells to generate mini-organs in a dish, pathological mechanisms

involved in several diseases can be more easily studied. This is particularly interesting for IRDs since access to tissue is not always possible and animal models often fail to summarize all the hallmarks of the disease. I will now focus on disease modeling through several examples of IRDs modeled with retinal organoids. However, the following list is not exhaustive and more examples are present in the literature(186).

One of the best examples for disease modeling involves autosomal dominant mutations in *PRPF31* which leads to retinitis pigmentosa type 11 (187). Interestingly, pre-mRNA processing factors (PRPFs) are ubiquitously expressed; however, monoallelic mutations in *PRPF31* lead to a disorder with a phenotype restricted to the retina. Disease modeling showed that due to specific splicing program, mutations only impact on retinal cells and more specifically on photoreceptors and RPE cells. In consequence, mutations in *PRPF31* particularly affect transcripts coding for components of the primary cilia (187). Subsequently, both photoreceptor outer segments and RPE cells derived from patient-specific iPSCs present abnormal morphologies, notably defects in the ciliary structure of the photoreceptors on one side as well as RPE alterations including shorter microvilli, loss of polarity, reduced barrier function and defective phagocytosis. Furthermore, the investigators showed that the CRISPR-Cas9 technology allows correcting the mutation and restoring the normal phenotype *in vitro* with iPSCs (187).

Other mutations affecting cilia proteins have been modeled using retinal organoids. For instance, Leber congenital amaurosis (LCA) consists of an autosomal recessive type of IRD which affects the photoreceptors and/or the RPE and is characterized by an early onset profound visual loss in infancy. Mutations in *CEP290* coding for a ciliary protein involved in protein trafficking are a major cause of LCA (188). However, distinct mutations in *CEP290* can either lead to a retina-restricted phenotype or to syndromic disorders including Joubert syndrome and Senior-Loken syndrome (188). Of particular interest is the deep intronic variant, c.2991+1665A>G responsible for missplicing leading to a truncated protein product (p.C998\*), which account for 86% of CEP290-related LCA cases (189). This variant is responsible for a retina-restricted disease. Of note, *in vitro* assays performed on mutant patients' fibroblasts revealed a residual full-length transcript as high as 50% of normal transcript in control fibroblasts (189, 190). The underlying mechanisms involved in the photoreceptor-restricted phenotype in association with this deep intronic variant as well as

the phenotype/genotype correlations associated with the retina-restricted phenotype vs. the syndromic phenotype retina were still unclear. Two studies modeled the disease with the aid of retinal organoids using iPSCs derived from subjects carrying mutations in *CEP290* (191, 192). Parfitt *et al.*, demonstrated that photoreceptor differentiation in retinal organoids homozygous for the frequent deep intronic mutation was associated with a higher level of aberrant transcripts compared to mutant fibroblasts or RPE cells, and profound cilia defect (191). This cellular phenotype was rescued by the use of specific oligoantisense nucleotides silencing the mutation. This study outlines the photoreceptor specific splicing machinery involved in disease process and served basis of treatment development. In the second study, Shimada *et al.*, analyzed cells derived from subjects affected with CEP290-related Joubert syndrome and CEP290-related LCA. They demonstrated a profound cilia dysgenesis in fibroblasts of Joubert patients with a compromised protein which was only mildly affected in fibroblasts from LCA patients whereas ciliogenesis was affected in optic cups of LCA patients. (191, 192).

Finally, X-linked juvenile retinoschisis is a congenital retinal dystrophy associated with mutations in *RS1*. The pathology appears during childhood and affects cell-cell retinal adhesion. *RS1* encodes for a secreted protein called retinoschisin forming homo-octameric complexes which plays a role in proper protein localization to the cell membrane and cell-cell adhesion (193). Most of the mutations are located in the discoid domain and lead to a misfolding of the mutant protein retained within the endoplasmic reticulum (193). *RS1* is localized in the inner segment of the photoreceptors, in bipolar cells and in the two different plexiform layers (IPL and OPL). Its proper expression is necessary for a normal lamination of the retina. iPSCs derived from affected subjects have recently been used to generate an *in vitro* model of the disease with retinal organoids (194). Interestingly, this new model summarizes all features of the disorder and demonstrates that retinoschisin is required for a normal retinal organization. Indeed, the mutation leads to disruption of the retinal integrity in retinal organoids (194).

As a matter of fact, most of the current literature on disease modeling focuses on monogenic diseases. Additionally, retinal disorders modeled with iPSCs often affect either

photoreceptors or RPE cells, as those are the most advanced cell types in morphology and functionality obtained with iPSCs (see drawbacks and improvement p49).

In a recent study, Saini *et al.*, generated iPSCs-derived RPE cells from age-related macular degeneration (AMD) patients carrying the common ARMS2/HTRA1 risk alleles (195). Disease modeling of this multi-factorial disorder demonstrated upregulation of AMD biomarkers. This result tends to demonstrate that more complex retinal disorders can also be modeled with hiPSCs. In the next years, improvement in retinal organoid architecture combined with new omics tools, such as genomics and proteomics, will develop the applicability of disease modeling with retinal organoids.

# Aims

Patients from the same family affected with a peculiar retinal dystrophy have been diagnosed and followed at the rare disease center of XV-XX hospital (Paris). After several clinical exams to better characterize the disease, it appeared that their dystrophy did not correspond to any of the previously reported inherited dystrophies. In 2014, applying WES, our group identified a mutation in *ITM2B* which is at the center of my PhD project. The function of ITM2B is largely unknown and little information was available. However, other mutations had already been identified in ITM2B, in two families affected with Alzheimer-like dementia (FBD and FDD). The only information concerning ITM2B was its link with APP, a major component of Alzheimer disease.

From this starting point, the aim of my PhD thesis was to better understand the role of ITM2B in the retina. Two axes were of particular interest to us:

1. the physiology of ITM2B in the retina in normal condition
2. the physiopathology and the pathological mechanisms involved in the RD

## **Deep phenotyping of the ITM2B-related RD**

For this aspect of my work, we decided to better characterize the phenotype of the affected RD patients. After several years of clinical follow-up, the progression of this rare disease gave us some new insights in the clinical aspects of the ITM2B-related RD (**Results 1**).

## **Physiology of ITM2B in the retina in normal condition**

For this part of my thesis, we decided to focus on the function of ITM2B in the normal retina. For that purpose, we conducted proteomic experiments on normal human retina in order to identify the ITM2B interactome in the retina (**Results 2**).

## **Physiopathology and pathological mechanisms involved in the RD**

In order to better approach physiopathological mechanisms, we developed hiPSC lines from one affected subject as well as from one unaffected sibling, as a cellular model for the disease. This part of our project was conducted in collaboration with Dr O. Goureau's lab

(Department of development, Institut de la Vision). The characterization of the different cell lines is presented in **Results 3**. The corresponding hiPSC lines were then differentiated into retinal organoids in order to explore the pathological mechanisms involved in RD (**Results 4**).

# Results

## 1. Development of the disease, follow-up

This first manuscript presents a more detailed phenotypic characterization of the ITM2B-related retinopathy than the original paper published by the group in 2014. It also documents disease progression over a ten-year period. This manuscript confirms the unique presentation of the disease which includes ganglion cell alterations, inner retinal dysfunction, progressive cone-system dysfunction and an hyperreflectivity of inner retinal layers. Optical coherence tomography angiography performed in three subjects ruled out a specific microangiopathy as seen in FDD, and revealed mostly vascular changes secondary to retinal disease. Disease progression is slow and better documented by functional (i.e. visual acuity, visual field and electroretinogram) than structural tests. Additional testing performed in three siblings revealed mild hearing loss in high frequencies which needs to be confirmed on other affected subjects. Normal cerebral magnetic resonance imaging in these three subjects combined with the absence of historical report of Alzheimer-like dementia in this family outline the unique features of the disease. We also discussed the impact of a mutation which does not induce missplicing but most likely leads to a misfolding of the mutant BRI23. Finally, further cellular immunolabeling coupled with RNA *in situ* hybridization suggest that *Itm2b* is expressed ubiquitously in the mouse retina at least in all inner retinal cells.

*This work is in press in Retina, the journal of retinal and vitreous disease.*

# Deep-phenotyping and further insights in *ITM2B*-related retinal dystrophy

Marco Nassisi<sup>1,2,\*</sup>, Juliette Wohlschlegel<sup>1,\*</sup>, Bingqian Liu<sup>1</sup>, Camille Letellier<sup>1</sup>, Christelle Michiels<sup>1</sup>, Anne Audois<sup>2</sup>, Saddek Mohand-Said<sup>1,2</sup>, Christophe Habas<sup>3</sup>, José-Alain Sahel<sup>1,2,4,5,6</sup>, Christina Zeitz<sup>1</sup>, Isabelle Audo<sup>1,2,7</sup>.

<sup>1</sup> Sorbonne Université, INSERM, CNRS, Institut de la Vision, 17 rue Moreau, F-75012 Paris, France

<sup>2</sup> CHNO des Quinze-Vingts, DHU Sight Restore, INSERM-DGOS CIC1423, 28 rue de Charenton, F-75012 Paris, France

<sup>3</sup> Neuroradiology, CHNO des Quinze-Vingts, 28 rue de Charenton, F-75012 Paris, France

<sup>4</sup> Fondation Ophtalmologique Adolphe de Rothschild, F-75019 Paris, France.

<sup>5</sup> Department of Ophthalmology, University of Pittsburgh Medical School, Pittsburgh, PA 15213, USA

<sup>6</sup> Académie des Sciences-Institut de France, F-75006 Paris, France

<sup>7</sup> Institute of Ophthalmology, University College of London, London, EC1V 9EL, United Kingdom

**\* These authors contributed equally to this work**

**Corresponding author:** Isabelle Audo, MD, PhD, Institut de la Vision, 17 Rue Moreau, Paris, France, 75012. Mail: [isabelle.audo@inserm.fr](mailto:isabelle.audo@inserm.fr)

**Conflict of Interest Disclosures:** None reported.

**Funding/Support:** LABEX LIFESENSES [reference ANR-10-LABX-65] supported by French state funds managed by the Agence Nationale de la Recherche within the Investissements d'Avenir program [ANR-11-IDEX-0004-0]; RHU-Light4deaf (MN). IHU FOReSIGHT [ANR-18-IAHU-0001] supported by French state funds managed by the Agence Nationale de la Recherche within the Investissements d'Avenir program; Foundation Fighting Blindness center grant [C-CMM-0907-0428-INSERM04] and fellowship award (MN) [CD-CL-0619-0759-INSERM]. FFB-CG1-ASS-001 and FFB-CG2-ASS-000. Retina France. UNADEV (Union Nationale des Aveugles et Déficiants Visuels) in partnership with ITMO NNP / AVIESAN (alliance nationale pour les sciences de la vie et de la santé) for research in visual disorders. J. Wohlschlegel was supported by Fondation de France (Berthe Fouassier-Maladies de l'Oeil) PhD fellowship.

**Role of the Funder/Sponsor:** The funders had no role in the design and conduct of the study; collection, management, analysis, or interpretation of the data; preparation, review, or approval of the manuscript; nor in the decision to submit the manuscript for publication.

**Short title:** *ITM2B*-related retinal dystrophy insights and phenotype

**Keywords:** *ITM2B*; Integral Membrane Protein 2B; *ITM2B*-related retinal dystrophy; Retinal dystrophy with inner retinal dysfunction and ganglion cell abnormalities.

**Brief summary:** The *ITM2B*-related retinal dystrophy is a progressive disease with symptoms starting in early adulthood and is characterized by retinal ganglion cell abnormalities, inner retinal and cone dysfunctions. Functional exams (ff-ERG and VA) can accurately monitor the slow progression of the disease.

## Abstract

**Purpose:** to reappraise the presentation and the course of the *ITM2B*-related retinal dystrophy (RD) and give further insights on *ITM2B* expression in the retina.

**Methods:** Clinical data of nine subjects with *ITM2B*-related RD were retrospectively reviewed. The genetic mutation was assessed for its influence on splicing in cultured fibroblasts. Cellular expression of *ITM2B* within the inner retina was investigated in wild-type mice through mRNA in-situ hybridization.

**Results:** all patients complained of decreased vision and mild photophobia around their twenties-thirties. They also shared a peculiar feature: hyperreflective material on optical coherence tomography within the inner retina and the central outer nuclear layer with thinning of the retinal nerve fiber layer. While retinal imaging revealed very mild or no changes over the years, the VA slowly decreased of about one ETDRS letter per year. Finally, full-field electroretinography (ff-ERG) showed a mildly progressive inner retinal and cone dysfunction. *ITM2B* mRNA is expressed in all cellular types of the inner retina. Disease mechanism most likely involves mutant protein misfolding and/or modified protein interaction rather than misplicing.

**Conclusions:** *ITM2B*-related RD is a peculiar, rare, slowly progressive retinal degeneration. Functional exams (ff-ERG and VA) seem more accurate in monitoring the progression in these patients, as imaging tends to be stable over the years.

## Introduction

The Integral Membrane Protein 2B (ITM2B) is an ubiquitous transmembrane protein processed at the C-terminus by furin or furin-like proteases to produce a small secreted peptide (BRI23)<sup>1-3</sup>. The remaining membrane-bound fragment corresponds to the mature form of ITM2B.<sup>4</sup> In the brain, ITM2B interacts with Amyloid Precursor Protein (APP) and acts as a modulator of its processing<sup>5-7</sup>. Alterations of *ITM2B* (MIM\*603904, chromosome 13q14.3) have been associated with an autosomal dominant Alzheimer-like form of dementia, characterized by cerebral amyloid deposits with two reported mutations: (1) c.799T>A; p.(\*267Argext\*11), leading to the Familial British Dementia (FBD, MIM# 176500)<sup>8</sup> and (2) c.787\_796dup; p.(Ser266Phefs\*13), leading to the Familial Danish Dementia (FDD, MIM# 117300)<sup>9</sup>. Both mutations cause an extension of the C-terminal end of the protein, thereby increasing the size of the secreted peptide which forms aggregates, leading to cellular death.<sup>8,9</sup> While initial reports on FBD did not mention any ocular manifestations, FDD mostly presents with early onset cataract, retinal microangiopathy and neovascular complications<sup>10</sup>.

In 2014, our group identified a novel autosomal dominant retinal dystrophy (MIM#616079) associated with a missense mutation in *ITM2B*, c.782A>C p.(Glu261Ala), in a large three-generation-French family with 14 affected members (Fig. 1).<sup>11</sup>

This mutation is located within the last 23 bases of the last exon of *ITM2B* and it is still unknown whether it impacts on the conformation of BRI23 and/or on the overall protein, disturbing its interactions with APP or other unknown partners. Giannoccaro et al., also suggested an alteration in splicing after *in silico* predictions with the creation of a novel splice donor site at position c.780 and a higher chance of exon skipping as the possible pathogenic mechanism.<sup>12</sup> Interestingly, the phenotype of the subjects carrying this heterozygous missense change seems to be restricted to the retina. Both *ITM2B* mRNA and the respective protein are present in the inner nuclear layer (INL) and ganglion cell layer (GCL) within mouse retina.<sup>11</sup> This suits well with the phenotype of the disease mainly characterized by inner retinal dysfunction with evident thinning of the GCL on optical coherence tomography (OCT). Nevertheless, many aspects of the disease remain unknown including the exact retinal cell type(s) expressing *ITM2B* in the inner retina, as well as course of the disease. In order to shed further light on the pathogenicity of the *ITM2B* variant and on the expression of the gene within the inner retina, we performed expression analyses on

patients' derived fibroblasts and wild-type mouse retinal sections. Furthermore, the presentation, course and pathophysiology of *ITM2B*-related retinal dystrophy (IRRD) were revisited in light of the new genetic insights, further clinical investigations and available follow-up.

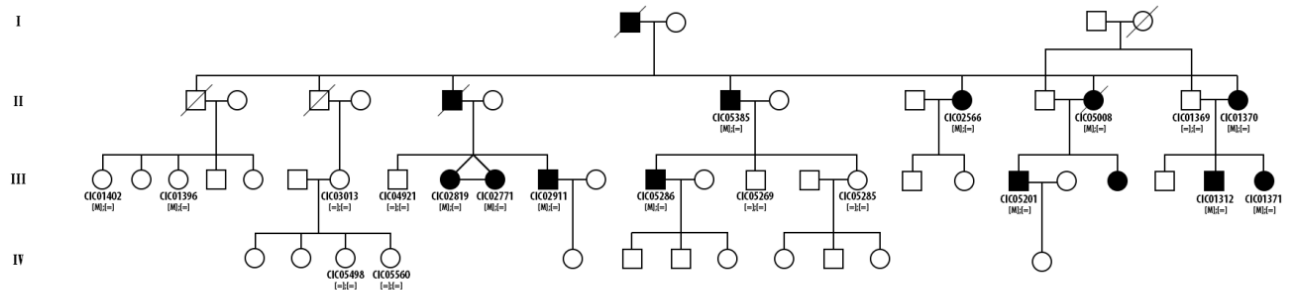


**Fig.1 Pedigree of the family with isolated autosomal dominant retinal dystrophy associated with a missense mutation in *ITM2B*.** [M]: allele c.782A>C p.(Glu261Ala) ; [=]: reference sequence.

## Material and methods

### Clinical Investigation

The charts and the clinical exams of the patients with IRRD were retrospectively reviewed. Patients were investigated at the National Reference Center for Rare Diseases of Quinze-Vingts Hospital, Paris, France. Ophthalmic examination was performed as previously described.<sup>13,14</sup> Further details are provided in the supplementary material. Neurological and audiological data were also collected when available. All quantitative data are presented as mean  $\pm$  standard deviation (SD).

### Genetic Analysis and *in-vitro* Splicing assay

Informed consent was obtained from all patients and their family members for both clinical and genetic analysis. The study protocol was in accordance with the tenets of the Declaration of Helsinki and was approved by a national ethics committee (CPP Ile de France V, Project number 06693, N<sup>o</sup>EUDRACT 2006-A00347-44, 11 December 2006). The genetic analysis was performed at the Institut de la Vision, Paris, France, as previously reported.<sup>11</sup> To document the possible misplicing effect of the [c.782A>C p.(Glu261Ala)] mutation, total mRNA was extracted from human fibroblasts of affected subject CIC05286 and his

unaffected sibling (CIC05269) followed by reverse transcriptase – PCR (RT-PCR). Details of the analysis are available in the supplementary material.

### **RNA in-situ hybridization (ISH) and immunohistology**

Wild-type C57BL/6J mouse retinal sections were used for this study.<sup>15</sup> Further details about the protocols are provided in the supplementary material.

### **Mutant protein modeling**

Structural predictions for the reference and mutated forms of the 23-aminoacid secreted peptide were established using a software (QUARK, available at <https://zhanglab.ccmb.med.umich.edu/QUARK/>).

The comparison between the two models was performed using another software (PyMOL Molecular Graphics System, Version 2.0 Schrödinger, LLCA).

## **Results**

### **Functional clinical data**

Upon clinical examination, fourteen patients were affected, while 8 subjects had no functional or structural alterations. Clinical data were available for 9 affected subjects (5 females). The overall results are presented in Table 1.

**Table1. Summary of clinical characteristics of patients with ITM2B-related retinal dystrophy**

	<i>ITM2B</i>
Female (n)	5/9 (55.56%)
Decade of onset (n)	
21-30 years	2/9 (22.22%)
31-40 years	7/9 (77.78%)
Symptoms at onset (n)	
Decreased Vision	9/9 (100%)
Mild photophobia	9/9 (100%)
Night blindness	2/9 (22.22%)
Age at first visit (years; Mean $\pm$ SD, [range])	n=9 53.33 $\pm$ 11.03 [45-73]
Follow-up for BCVA (n)	Range: 0-11 years
Only one visit	4
Range 1-5 years	1
Range 6-10 years	3
Range 10-15 years	1
BCVA at first visit (LogMAR; Mean $\pm$ SD, [Snellen equivalent])	n=9
RE	0.56 $\pm$ 0.27 [20/63]
LE	0.7 $\pm$ 0.31 [20/100]
Annual rate of BCVA decline (LogMAR/year; Mean $\pm$ SD)	
RE	0.02 $\pm$ 0.01
LE	0.02 $\pm$ 0.01
Binocular normal color vision at baseline	5/9 (55.56%)

Abbreviations - BCVA: Best Corrected Visual Acuity; SD: Standard deviation; RE: Right Eye; LE: Left Eye.

The mean age at the first examination was 53.33  $\pm$  11.03 years (median: 49 years, range: 45-73 years). All subjects referred reported an onset of symptoms around their late twenties and late thirties complaining of decreased vision (9 subjects, 100%), associated with mild photophobia (9 subjects, 100%) and night blindness (2 subjects, 22.2%). The mean best corrected visual acuity (BCVA) was 0.56  $\pm$  0.27 LogMAR (about 20/63 Snellen) and 0.7  $\pm$  0.31 LogMAR (about 20/100 Snellen) for the right and left eyes respectively (overall median 20/80 Snellen; range: 20/400 – 20/25 Snellen). Interestingly, seven patients had no more than one Early Treatment Diabetic Retinopathy Study (ETDRS) line of difference between both eyes while the other two (CIC05008, CIC05286) showed a higher asymmetry. Longitudinal follow-up on BCVA was available for five patients (range of follow-up: 5-11 years). Overall, there was a slow decrease in BCVA in all subjects, with an annual decline rate

of 1 ETDRS letter per year in both eyes. Color vision was impaired in at least one eye in four subjects: two presented a deuteranopia, one showed a tritanopia, and one had no preferential axis. The remaining five subjects had normal color vision in both eyes at presentation. Among them, CIC01312 and CIC02819 developed a dyschromatopsia of deutan axis after 11 and 3 years respectively, while CIC02911 kept a normal colour vision after 8 years of follow-up. No longitudinal data was available for the other two subjects with normal color vision.

Kinetic perimetry showed decreased central retinal sensitivity with an intact peripheral field. In the five patients who attended multiple visits (range of follow-up: 5-11 years), this central relative scotoma increased in depth and size, but never became absolute.

Full-field ERGs (ff-ERGs) showed a marked inner retinal dysfunction: all affected subjects had an electronegative waveform (b-wave/a-wave ratio  $< 1$ ) in response to a bright flash (3 and 10  $\text{cd}\cdot\text{s}\cdot\text{m}^{-2}$ ) under scotopic conditions. Photopic responses were better preserved in younger patients, while older affected subjects showed reduced amplitudes and delayed implicit time. The tendency of a progressive worsening of the ff-ERGs responses was further confirmed by longitudinal data (available for four patients, range of follow-up: 8-11 years). All subjects demonstrated a progressive reduction in amplitude and increased delay of the photopic responses (Fig. 2).

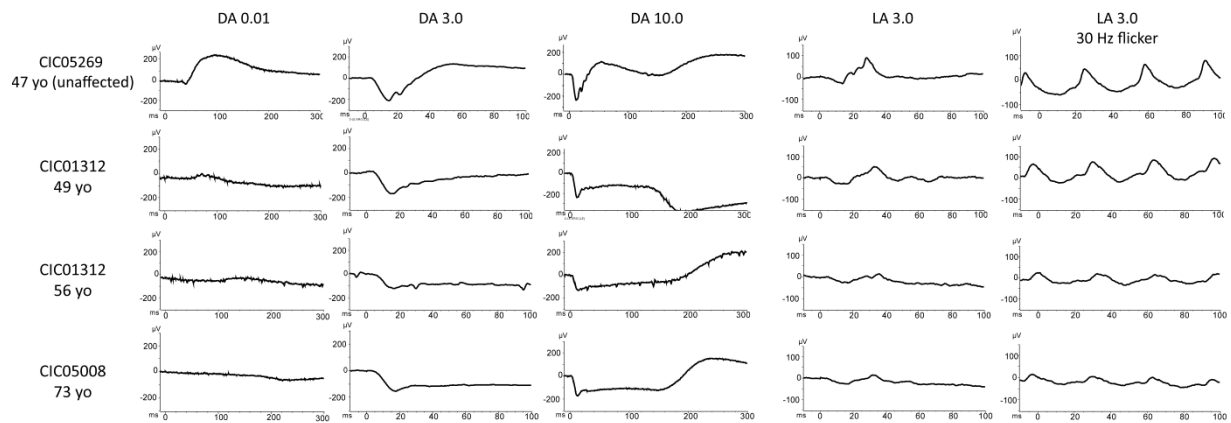


**Fig.2 Full-field electroretinography of two patients with *ITM2B*-related retinal dystrophy (CIC01312 and CIC05008) compared to a healthy control from the same family (CIC05269).** The affected subjects showed a typical electronegative waveform (b-wave/a-wave ratio < 1) after stimulation with a bright flash under scotopic conditions. As for the photopic responses, they tended to be better preserved in the younger subject (CIC01312), while CIC05008 showed markedly reduced amplitudes and delayed implicit time. However, after 7 years, CIC01312 showed a worsening of the ff-ERG responses.

### Structural clinical data

All affected subjects showed very mild changes on fundus examination, mostly presenting only pallor of the optic disc (Fig. 3). However, short-wavelength fundus autofluorescence (SW-FAF) demonstrated a subtle ring of increased autofluorescence around the fovea (Fig. 3). Only one patient (CIC05286) had more obvious alterations showing focal areas of grainy hypofluorescence surrounding the central macula. The peculiar feature of this dystrophy consists of hyperreflectivity of the inner plexiform layer (IPL) on OCT, with a subtle shadowing effect on the underlying outer retinal layers. Highly hyperreflective material was also present in the outer nuclear layer (ONL) at the fovea (Fig. 3). In addition, the retinal nerve fiber layer (RNFL) and the GCL were significantly thinner. The ellipsoid zone (EZ) was preserved at the center, in younger patients; however, a grainy hyporeflective appearance was obvious at the level of the hyperautofluorescent halo on SW-FAF suggestive of a “window defect”. The two elder patients (CIC01370 and CIC05008) presented more severe central EZ alterations, with additional subfoveal drusenoid lesions in CIC05008.

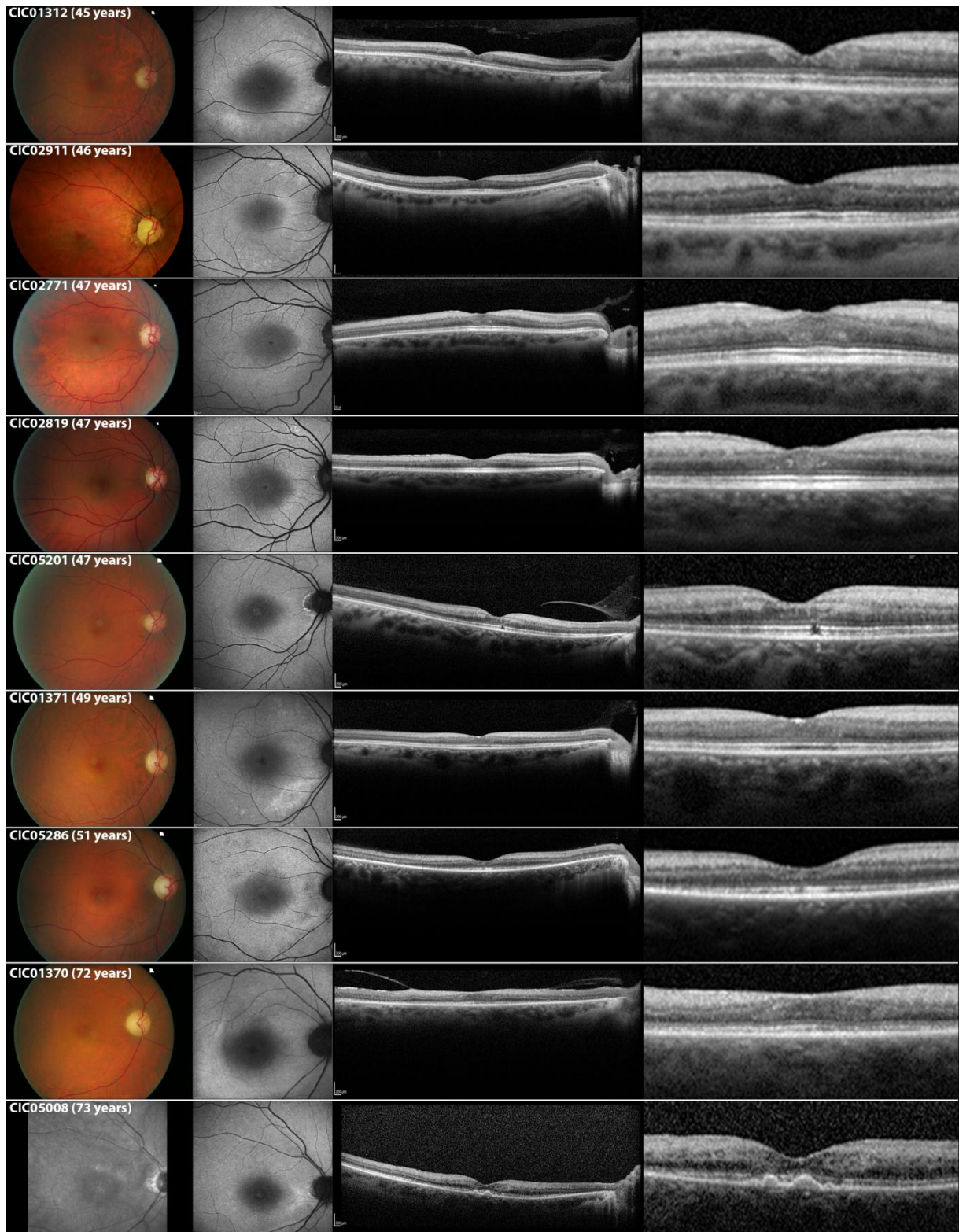


**Fig.3 Phenotype of all affected subjects at baseline.** Each row represents findings in the right eye of a single subject: a fundus photograph or an infrared reflectance image (left), a short wavelength fundus autofluorescence image (middle) and the central horizontal B-scan on optical coherence tomography (OCT; right) with a magnified view of the fovea are displayed. All patients show pallor of the optic nerve on fundus photos and a circular halo of increased autofluorescence around the center of the macula. Only patient CIC05286 also had

focal areas of grainy hypo/hyperautofluorescence at the posterior pole. On OCT, all subjects showed thinning of the retinal nerve fiber layers and the ganglion cell layers, while the inner plexiform layer appear hyperreflective, mainly in the para- and perifovea. Some irregular hyperreflective material may also be seen at the level of the outer nuclear layer, within the fovea.

Follow-up images were available for five subjects (range of follow-up: 5-11 years). Overall, retinal alterations remained stable over time except for CIC05286 whose peripheral outer retinal atrophy visibly progressed towards the center (Fig. 4 and 5). Furthermore, another patient (CIC02911) developed cystoid macular edema in one eye (Fig. 4).

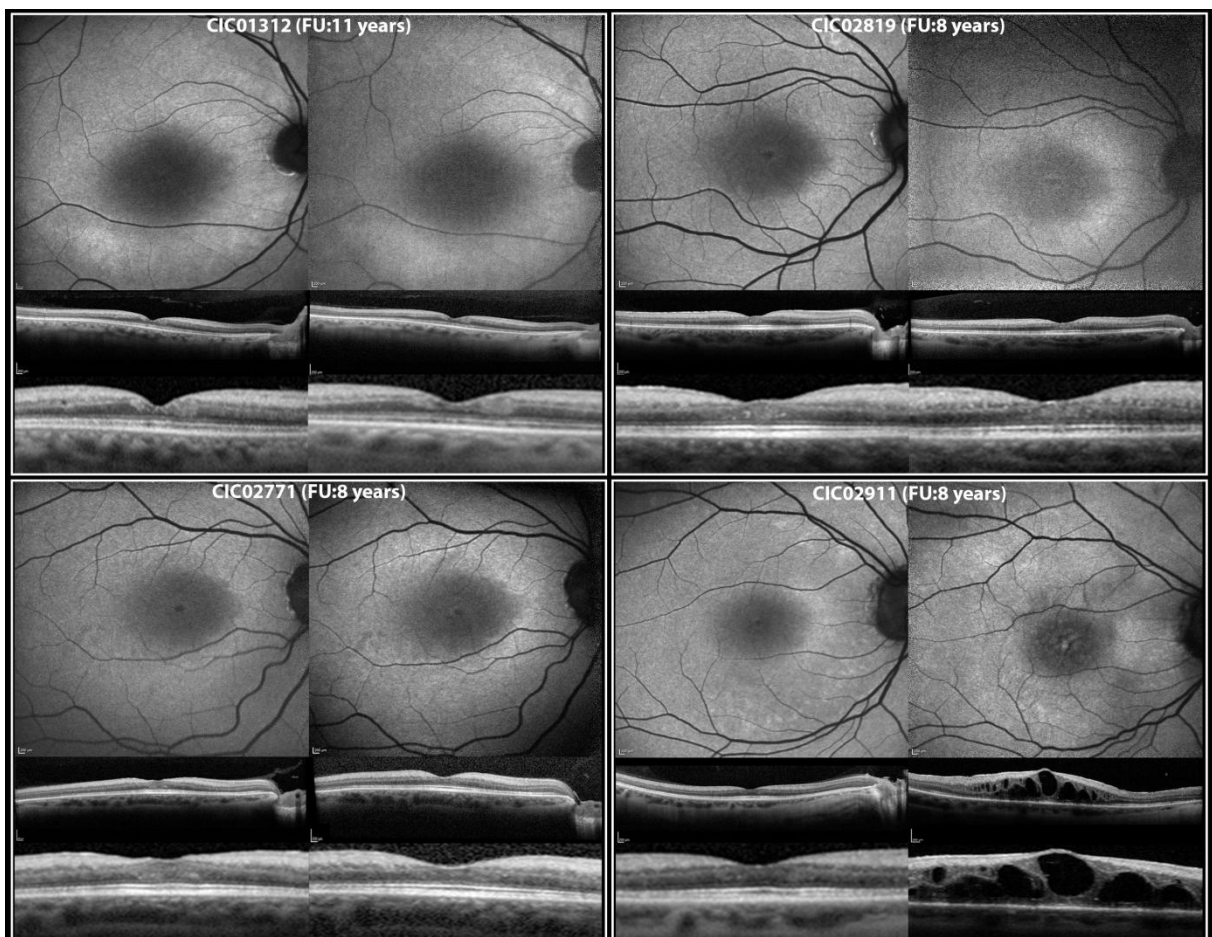


**Fig.4 Follow-up of the right eye of four patients affected with *ITM2B*-related retinal dystrophy.** For each subject the short-wavelength fundus autofluorescence (top) and the central B-scan on optical coherence tomography (bottom) with a close-up of the fovea, are shown for both baseline (left) and follow-up (right) visits. After several years, all patients present very mild/no changes on both imaging modalities. Only CIC02911 developed a unilateral cystoid macular edema.

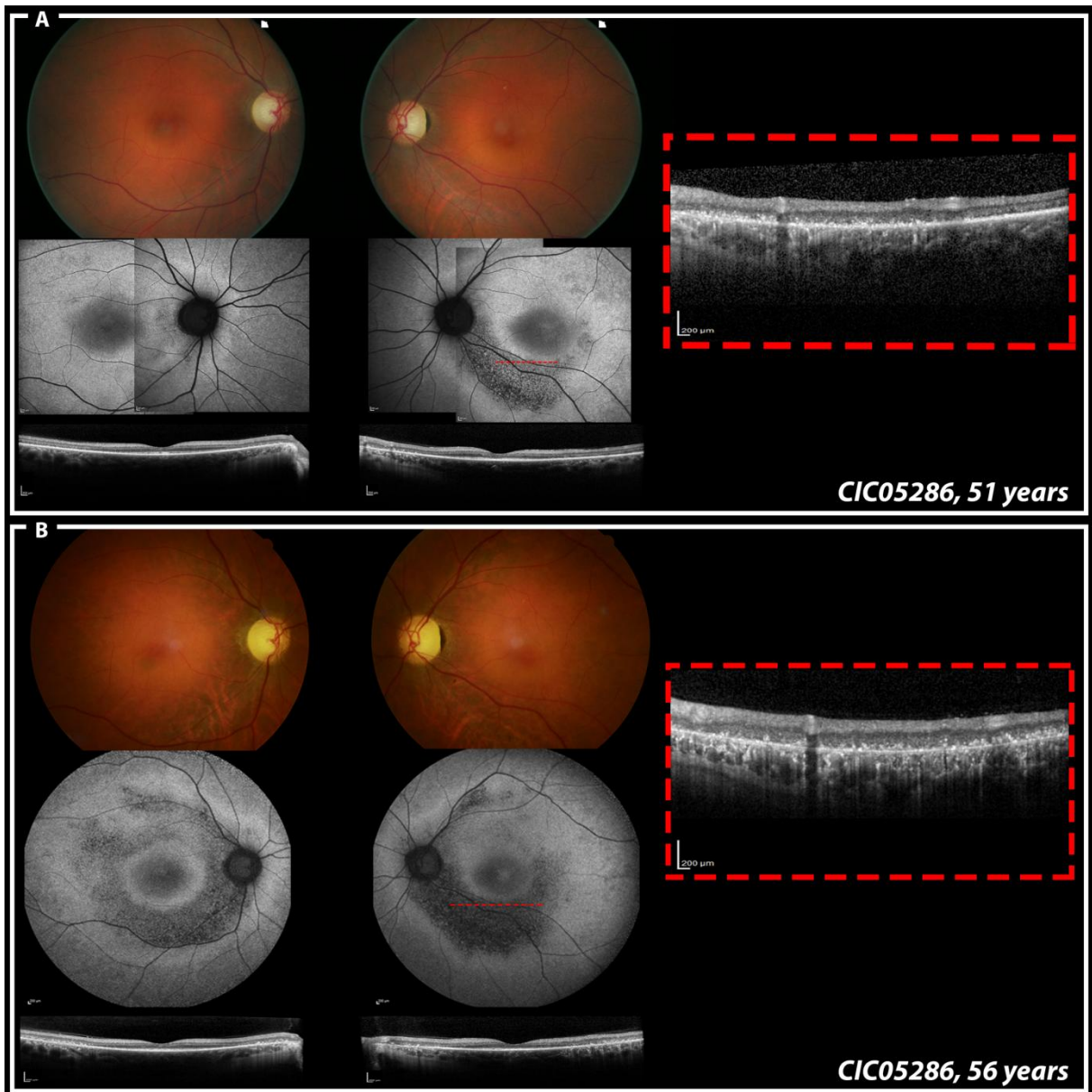


**Fig.5 Clinical follow-up of patient CIC05286.** Fundus photographs (top), short-wavelength fundus autofluorescence (middle) and the central B-scan on optical coherence tomography (OCT, bottom) are shown for both baseline (A) and follow-up (5 years later, B) visits. At baseline (A), the patient shows a large area of hyperautofluorescence which surrounded the optic nerve and the posterior pole with some focal areas of grainy hypo/hyperautofluorescence. The latter changes are particularly obvious in the left eye where they extend from the optic nerve, along the inferior temporal vascular arcade around the macula. On OCT (image in the red box), these areas correspond to outer retinal atrophy with a multitude of intraretinal hyperreflective foci. Of note, these foci did not correspond to pigmented changes on fundus photos. After five years (B), this pattern of hypoautofluorescence was more obvious and expanded circumferentially in both eyes surrounding the central macular region.

The three siblings CIC02819, CIC02771 and CIC02911 also underwent OCT-angiography (OCTA) examination during their last visit. Compared to an age-matched control, the density of all retinal vascular plexa looked reduced; the radial peripapillary capillary (RPCP) and the superficial capillary (SCP) plexa seem the most severely affected (Fig. 6). Furthermore, the physiologic architecture of the deep capillary plexus (DCP) looked altered, i.e. the vessels were more tortuous and the typical capillary vortices were more difficult to recognize. Finally, the choriocapillaris (CC) looked unaltered compared to age-matched controls.

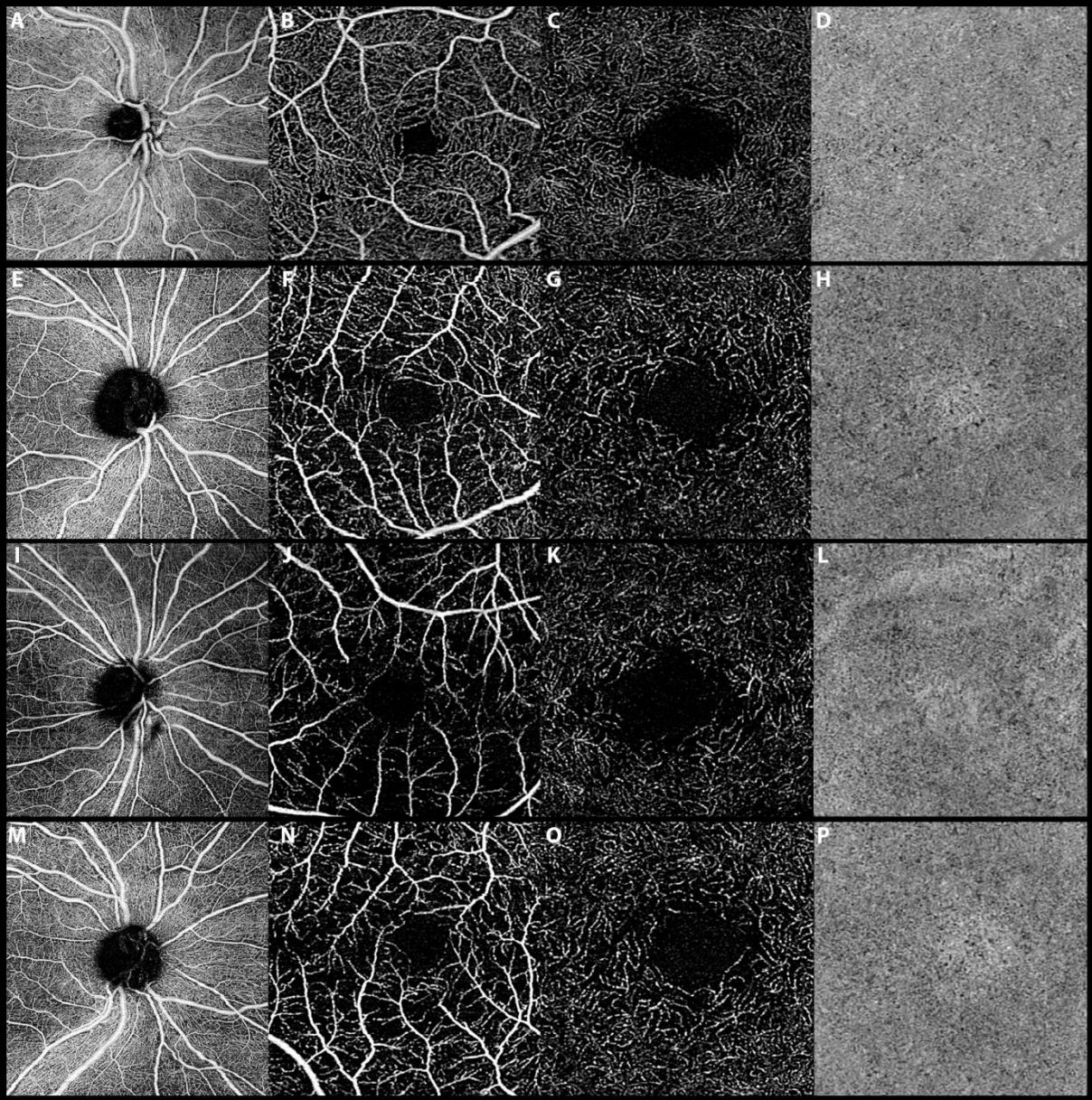


**Fig.6 Optical coherence tomography angiography (OCTA) acquisitions of a healthy subject (A-D) and patients CIC02771 (E-H), CIC02911 (I-L), and CIC02819 (M-P) affected with *ITM2B*-related retinal dystrophy. (A, E, I, M) A 6x6mm angiogram of the optic nerve region, allowed the visualization of a marked reduction of the radial peripapillary capillary plexus in**

the three patients compared to the control. (B-D, F-H, J-L, N-P) A 3x3mm acquisition centered on the fovea allowed the analysis of the superficial capillary plexus (SCP; B, F, J, N), the deep capillary plexus (DCP; C, G, K, O) and the choriocapillaris (CC; D, H, L, P). All three patients showed a reduction of both SCP and DCP (SCP>DCP). The structure of the DCP also look altered with more tortuous vessels. Finally, the CC looked unaltered compared to age-matched controls.

### **Neurological and ENT findings**

Three affected subjects (CIC02819 [55 years], CIC02771 [55 years] and CIC02911 [54 years]) underwent further neurological examination through brain magnetic resonance imaging (MRI) which did not reveal any alterations at the level of the cerebral cortex, cerebellar cortex or hippocampus (Supplementary Fig. S1). Furthermore, optic nerves showed a normal thickness along their course (Supplementary Fig. S1). A multi-subject Independent Component Analysis allowed visualization of resting-state networks common to the three subjects. The main intrinsically connected networks were observed, including: visual, motor, default-mode, dorsal attentional and central executive networks (Supplementary Fig. S2). Finally, an audiogram performed on the same three affected subjects revealed hearing loss in high frequencies with no reported history of trauma.

### **Genetic findings and *in silico* studies.**

All affected subjects carried the heterozygous mutation c.782A>C p.(Glu261Ala) in *ITM2B* which was absent in clinically unaffected subjects.

The mutation was absent in common databases and the amino acid change was predicted to be pathogenic (Supplementary table S1). Furthermore, the glutamic acid in position p.261 is highly conserved among all species for which the sequence data is available on UCSC genome browser (last checked on 1<sup>st</sup> April 2020, Supplementary table S2). As the mutation affects one of the 23-amino acid residues of the peptide secreted following the action of furin or furin-like proteases, we modeled the wild-type and mutated sequences and checked for any differences in structure (Supplementary Fig. S3). Both models show that the structure of the 23-amino acid peptide arranged as two consecutive  $\beta$ -strands in a spiral conformation. However, in the mutated form, the two  $\beta$ -strands look more parallel and more distant from each other (Supplementary Fig. S3A). This is likely related to the interaction between the altered p.261 residue and the arginine (positively charged) at

position 252: while the glutamic acid of the reference protein is negatively charged and “attracts” the arginine located on the opposite  $\beta$ -strand, the alanine, in the mutant peptide, is neutral and “releases” the arginine, opening the conformation of the peptide (Supplementary Fig. S3B). In addition, RNA extraction and RT-PCR analysis performed from skin fibroblasts of the affected subject CIC05286 compared with a control did not confirm the predicted missplicing (Supplementary table S2 and Fig. S4).

### ***ITM2B* cellular localization in wild-type mouse retina**

Experiments of co-*ITM2B* ISH/immunostaining, using several antibodies reacting towards markers specific of each cell types present in the inner retina revealed that *ITM2B* is ubiquitously expressed in the inner retina of the mouse including the ganglion cells, amacrine cells, horizontal cells, Müller cells and bipolar cells (Supplementary Fig. S5).

## **Discussion**

The IRRD is a peculiar rare disorder, with a unique phenotype characterized by inner retinal dysfunction and structural alterations predominantly within the inner retina. It appears to be a slowly progressive disease: over about 10 years, very mild structural changes difficult to detect on SW-FAF and OCT (Fig. 4) are seen. Evidence of progression is more noticeable on functional tests which may be better at monitoring IRRD overtime: BCVA and photopic responses on ff-ERGs slowly but steadily decrease. Since photopic responses are driven by cones but generated at the inner retinal level<sup>16</sup>, this progression may represent either progressive primary cone and/or inner retinal degeneration. The latter correlates with the predominant alterations of inner retinal layers on OCT and fits the expression profile of *ITM2B* in mouse retina (Supplementary Fig. S5). Nevertheless, all subjects showed hyperreflective material within the foveal ONL (Fig. 3), EZ alterations on OCT in the periphery of the macula as well as marked outer retinal alterations in one subject (CIC05986, Fig. 5), suggestive of additional progressive photoreceptor degeneration. The two most striking features of IRRD are the electronegative waveform of the scotopic ERG and the hyperreflectivity of the inner retina on OCT. The electronegative ERG is a common feature in diseases involving the inner retinal layers including ischemic vascular disorders, synaptic disorders (e.g. congenital stationary night blindness), disorders with inner retinal

inflammation, deposits or degeneration, and syndromic metabolic disorders (e.g. Batten disease or mucopolipidosis IV)<sup>17</sup>. Most of them have distinct ophthalmic abnormalities and several of the rare diseases are dominated by systemic alterations. The inner retinal dysfunction associated with IRRD may have several explanations: altered ITM2B may affect either synaptogenesis or postreceptoral visual transduction, either directly or indirectly through protein partners<sup>4,18-20</sup>. Several studies provide evidence for both hypotheses. Interestingly, the stable expression of the wild-type or Alzheimer-related mutants of ITM2B in neuronal cells devoid of endogenous expression of ITM2B stimulates neurite outgrowth<sup>4</sup>. ITM2B may interact with GABA<sub>B</sub> receptors after forming a complex with APP, linking axonal trafficking to amyloidogenic processing<sup>19,20</sup>. ITM2B seems to facilitate glutamate signaling in the rodent brain via both presynaptic and postsynaptic mechanisms<sup>18</sup>. It may also be the case in the retina either at the photoreceptor synapses or at the dendritic tips of bipolar cells which may be impaired in the case of the RD mutation, leading to an absent b-wave. Alternatively, the hyperreflective material seen on SD-OCT may preclude proper visual signal transmission within the inner retinal layers as it is the case with inflammation associated with Birdshot chorioretinopathy<sup>21</sup>.

The nature of this hyperreflective material on OCT in IRRD remains unknown. Of note, acute ischemic changes in the retina are also characterized by transient hyperreflectivity of the inner layers unlike in IRRD where it is a constant sign, persisting even in advanced stages, at least until 73 years (oldest case examined). Our investigations through co-*ITM2B* ISH/immunostaining revealed that *ITM2B* mRNA is present in all cellular types in the inner retina (Supplementary Fig. S5) which may support a cellular origin to the hyperreflective material rather than a secondary ischemic effect. We hypothesize that these inner retinal changes might represent the aggregation of the mutated BRI23. Considering the two families previously reported with *ITM2B*-related Alzheimer-like dementia, i.e. FBD and FDD<sup>8,9</sup>, the respective mutations lead to a longer ITM2B product and generated two amyloidogenic 34-amino acid peptides named ABri and ADan, respectively. These longer peptides accumulate in the brain, playing a major role in neurodegeneration<sup>8,9</sup>. In our IRRD cases, the missense mutation c.782A>C, p.(Glu261Ala) does not affect the length of BRI23 as *in vitro* experiments showed no effect on splicing. However, the conformation of mutant BRI23 is predicted to change in favor of a more opened structure where the two  $\beta$  strands are more parallel and distant (Supplementary Fig. S3). This might favor the aggregation of the mutant peptide or

modify its interaction with APP, leading to its accumulation as documented in the brain<sup>22</sup>, hence explaining the presence of hyperreflective material on OCT. Interestingly, the only histological study performed on postmortem retinal sections of a FDD patient revealed photoreceptor degeneration, severe astrocytosis and infiltration by activated microglial cells<sup>23</sup>. Similarly, intravitreal injection of  $\beta$ -amyloid produced photoreceptor cell death in mice<sup>24</sup>. These reports would support a direct toxicity of the deposits with photoreceptors and/or inner retinal cells degeneration.

Contrary to FDD patients, none of the patients with IRRD presented with retinal microangiopathy and neovascular complications as reported in FDD<sup>10</sup>. In addition, the analysis of the OCTA performed on three affected subjects excludes a vascular etiology to the outer layer degeneration, as the CC looks preserved (Fig. 6). Indeed, the main alterations on OCTA concern the RCPC, SCP, and (mildly) DCP, and this seems coherent with the thinning of the RNFL and GCL as seen in patients with Alzheimer disease (AD) or primary open angle glaucoma (POAG)<sup>25,26</sup>. Interestingly, when comparing OCTA results of AD and POAG patients, the latter showed a higher impairment in the RCPC and SCP (RNFL-GCL thinning), whereas in AD, the DCP looks more affected (GCL-IPL thinning)<sup>26</sup>. In our case, IPL is not thin; nevertheless, the DCP looks mildly compromised and disorganized probably as a consequence of the deposits lying in the IPL. Whether this alteration is due to primary amyloid microangiopathy, or is secondary to the retinal abnormalities, will require further investigations. However, the intact CC suggests that the vascular changes would be secondary to retinal modifications.

IRRD does not seem to be associated with cerebral alterations. In fact, none of our IRRD patients showed signs of Alzheimer-like dementia when neurologically tested with mini-mental test (data previously reported)<sup>11</sup> and no case of Alzheimer disease was reported in the family history in previous generations, including CIC05008 who recently passed away at 80. Furthermore, the brain MRI of 3 affected subjects was normal (Supplementary Fig. S1). The mechanism for this retinal restricted phenotype remains unknown and may be related to a retinal-specific isoform of the enzyme responsible for the cleavage of ITM2B and the release of BRI23.

In addition, we report here high frequency hearing loss in three siblings. Interestingly, FDD is also clinically associated with the development of hearing impairment 10–20 years after the onset of ocular symptoms<sup>23</sup>. Further audiology testing in the IRRD family will determine

whether high frequency hearing loss is a common feature also associated with the retinal degeneration.

In conclusion, IRRD consists of a peculiar slowly progressive retinal degeneration involving ganglion cells, inner retinal and photoreceptor alterations suggesting a specific role of ITM2B in the retina in addition with its implication in Alzheimer-like dementia. The physiological role of ITM2B remains largely unknown. Recently, our group successfully generated human induced pluripotent stem cell lines (hiPSCs) from dermal fibroblasts of an IRRD patient and from an healthy control of the same family<sup>27</sup>. Disease modeling on organoids derived from these hiPSCs will shed further light into physiopathological mechanisms associated with ITM2B<sup>27</sup>.

## References

1. Kim SH, Wang R, Gordon DJ, et al. Furin mediates enhanced production of fibrillogenic ABri peptides in familial British dementia. *Nat Neurosci.* 1999;2(11):984-988. doi:10.1038/14783
2. Kim S-H, Creemers JWM, Chu S, Thinakaran G, Sisodia SS. Proteolytic processing of familial British dementia-associated BRI variants: evidence for enhanced intracellular accumulation of amyloidogenic peptides. *J Biol Chem.* 2002;277(3):1872-1877. doi:10.1074/jbc.M108739200
3. Pittois K, Deleersnijder W, Merregaert J. cDNA sequence analysis, chromosomal assignment and expression pattern of the gene coding for integral membrane protein 2B. *Gene.* 1998;217(1-2):141-149. doi:10.1016/s0378-1119(98)00354-0
4. Choi S-I, Vidal R, Frangione B, Levy E. Axonal transport of British and Danish amyloid peptides via secretory vesicles. *FASEB J.* 2004;18(2):373-375. doi:10.1096/fj.03-0730fje
5. Fotinopoulou A, Tsachaki M, Vlavaki M, et al. BRI2 interacts with amyloid precursor protein (APP) and regulates amyloid beta (Abeta) production. *J Biol Chem.* 2005;280(35):30768-30772. doi:10.1074/jbc.C500231200
6. Matsuda S, Giliberto L, Matsuda Y, et al. The familial dementia BRI2 gene binds the Alzheimer gene amyloid-beta precursor protein and inhibits amyloid-beta production. *J Biol Chem.* 2005;280(32):28912-28916. doi:10.1074/jbc.C500217200
7. Matsuda S, Matsuda Y, Snapp EL, D'Adamio L. Maturation of BRI2 generates a specific inhibitor that reduces APP processing at the plasma membrane and in endocytic vesicles. *Neurobiol Aging.* 2011;32(8):1400-1408. doi:10.1016/j.neurobiolaging.2009.08.005
8. Vidal R, Frangione B, Rostagno A, et al. A stop-codon mutation in the BRI gene associated with familial British dementia. *Nature.* 1999;399(6738):776-781. doi:10.1038/21637
9. Vidal R, Revesz T, Rostagno A, et al. A decamer duplication in the 3' region of the BRI gene originates an amyloid peptide that is associated with dementia in a Danish kindred. *Proc Natl Acad Sci USA.* 2000;97(9):4920-4925. doi:10.1073/pnas.080076097
10. Bek T. Ocular changes in heredo-oto-ophthalmo-encephalopathy. *Br J Ophthalmol.* 2000;84(11):1298-1302. doi:10.1136/bjo.84.11.1298
11. Audo I, Bujakowska K, Orhan E, et al. The familial dementia gene revisited: a missense mutation revealed by whole-exome sequencing identifies ITM2B as a candidate gene underlying a novel autosomal dominant retinal dystrophy in a large family. *Hum Mol Genet.* 2014;23(2):491-501. doi:10.1093/hmg/ddt439
12. Giannoccaro MP, Bartoletti-Stella A, Piras S, et al. The First Historically Reported Italian Family with FTD/ALS Teaches a Lesson on C9orf72 RE: Clinical Heterogeneity and Oligogenic Inheritance. *J Alzheimers Dis.* 2018;62(2):687-697. doi:10.3233/JAD-170913
13. Nassisi M, Mohand-Saïd S, Dhaenens C-M, et al. Expanding the Mutation Spectrum in ABCA4: Sixty Novel Disease Causing Variants and Their Associated Phenotype in a Large French Stargardt Cohort. *Int J Mol Sci.* 2018;19(8). doi:10.3390/ijms19082196
14. Khateb S, Mohand-Saïd S, Nassisi M, et al. PHENOTYPIC CHARACTERISTICS OF ROD-CONE DYSTROPHY ASSOCIATED WITH MYO7A MUTATIONS IN A LARGE FRENCH COHORT. *Retina (Philadelphia, Pa).* Published online August 29, 2019. doi:10.1097/IAE.0000000000002636
15. Keane TM, Goodstadt L, Danecek P, et al. Mouse genomic variation and its effect on phenotypes and gene regulation. *Nature.* 2011;477(7364):289-294. doi:10.1038/nature10413

16. Sieving PA, Murayama K, Naarendorp F. Push-pull model of the primate photopic electroretinogram: a role for hyperpolarizing neurons in shaping the b-wave. *Vis Neurosci.* 1994;11(3):519-532. doi:10.1017/s0952523800002431
17. Audo I, Robson AG, Holder GE, Moore AT. The negative ERG: clinical phenotypes and disease mechanisms of inner retinal dysfunction. *Surv Ophthalmol.* 2008;53(1):16-40. doi:10.1016/j.survophthal.2007.10.010
18. Yao W, Yin T, Tambini MD, D'Adamio L. The Familial dementia gene ITM2b/BRI2 facilitates glutamate transmission via both presynaptic and postsynaptic mechanisms. *Sci Rep.* 2019;9(1):4862. doi:10.1038/s41598-019-41340-9
19. Schwenk J, Pérez-Garci E, Schneider A, et al. Modular composition and dynamics of native GABAB receptors identified by high-resolution proteomics. *Nat Neurosci.* 2016;19(2):233-242. doi:10.1038/nn.4198
20. Dinamarca MC, Raveh A, Schneider A, et al. Complex formation of APP with GABAB receptors links axonal trafficking to amyloidogenic processing. *Nat Commun.* 2019;10(1):1331. doi:10.1038/s41467-019-09164-3
21. Holder GE, Robson AG, Pavesio C, Graham EM. Electrophysiological characterisation and monitoring in the management of birdshot chorioretinopathy. *Br J Ophthalmol.* 2005;89(6):709-718. doi:10.1136/bjo.2004.047837
22. Kim J, Miller VM, Levites Y, et al. BRI2 (ITM2b) inhibits Abeta deposition in vivo. *J Neurosci.* 2008;28(23):6030-6036. doi:10.1523/JNEUROSCI.0891-08.2008
23. Holton JL, Lashley T, Ghiso J, et al. Familial Danish dementia: a novel form of cerebral amyloidosis associated with deposition of both amyloid-Dan and amyloid-beta. *J Neuropathol Exp Neurol.* 2002;61(3):254-267. doi:10.1093/jnen/61.3.254
24. Jen LS, Hart AJ, Jen A, et al. Alzheimer's peptide kills cells of retina in vivo. *Nature.* 1998;392(6672):140-141. doi:10.1038/32327
25. Asanad S, Ross-Cisneros FN, Nassisi M, Barron E, Karanjia R, Sadun AA. The Retina in Alzheimer's Disease: Histomorphometric Analysis of an Ophthalmologic Biomarker. *Invest Ophthalmol Vis Sci.* 2019;60(5):1491-1500. doi:10.1167/iovs.18-25966
26. Zabel P, Kaluzny JJ, Wilkosc-Debczynska M, et al. Comparison of Retinal Microvasculature in Patients With Alzheimer's Disease and Primary Open-Angle Glaucoma by Optical Coherence Tomography Angiography. *Invest Ophthalmol Vis Sci.* 2019;60(10):3447-3455. doi:10.1167/iovs.19-27028
27. Wohlschlegel J, Letellier C, Liu B, et al. Generation of human induced pluripotent stem cell lines from a patient with ITM2B-related retinal dystrophy and a non mutated brother. *Stem Cell Res.* 2019;41:101625. doi:10.1016/j.scr.2019.101625

## Deep-phenotyping and further insights in *itm2b*-related retinal dystrophy

### Supplemental Material

#### Materials and Methods

##### Clinical examination

The following exams and images were included in the analysis when available: best corrected visual acuity (BCVA) with early treatment diabetic retinopathy study (ETDRS) chart, Goldmann visual field, fundus photos (Topcon, Tokyo, Japan), OCT (Spectralis HRA+OCT; Heidelberg Engineering, Dossenheim, Germany), OCT angiography (OCTA, PLEX Elite 9000 device, Carl Zeiss Meditec, Dublin, California, USA) and fundus autofluorescence (FAF, Heidelberg retina angiograph [HRA] II). Full-field electroretinography (ff-ERG) incorporated the minimum standards of the International Society for Clinical of Electrophysiology of Vision (Espion E2; for full field ERG; Diagnosys, Lowell, MA, USA).<sup>1</sup>

##### Genetic analysis

Whole-exome sequencing (WES) and subsequent haplotype analysis allowed the identification of the missense mutation in *ITM2B*, c.782A>C p.(Glu261Ala), which co-segregated with the disease in the family. The presence of the mutation was confirmed by Sanger sequencing of the coding and flanking exonic regions of *ITM2B* in all available family members (RefSeq NM\_021999.4, primer sequences and Polymerase chain reaction [PCR] conditions available upon request). The frequency of the variant was checked using the Genome Aggregation Database (gnomAD, v.2.1.1, <https://gnomad.broadinstitute.org/>).

*In silico* predictions were performed using Alamut Visual software v. 2.7.1 where the following predictive algorithms are implemented: PolyPhen2 (Polymorphism Phenotyping, <http://genetics.bwh.harvard.edu/pph2/>),<sup>2</sup> SIFT (Sorting Intolerant from Tolerant; <http://sift.bii.a-star.edu.sg/>),<sup>3</sup> Mutation Taster (<http://www.mutationtaster.org/>),<sup>4</sup> MaxEntScan ([http://genes.mit.edu/burgelab/maxent/Xmaxentscan\\_scoreseq.html](http://genes.mit.edu/burgelab/maxent/Xmaxentscan_scoreseq.html)),<sup>5</sup> Splice site prediction by neural network (NNSplice, [https://www.fruitfly.org/seq\\_tools/splice.html](https://www.fruitfly.org/seq_tools/splice.html)),<sup>6</sup> human splicing finder v 3.0 (<http://www.umd.be/HSF3/>),<sup>7</sup> and EX-SKIP (<https://ex-skip.img.cas.cz/>)<sup>8</sup>. Evolutionary

conservation was investigated using the Vertebrate Multiz Alignment and Conservation of the University of California Santa Cruz (UCSC) genome browser (<http://genome.ucsc.edu/>).<sup>9</sup>

### ***In-vitro* Spicing assay**

Total mRNA was isolated using a kit (RNeasy Mini Kit, Qiagen, Hilden, Germany), and 500 ng were used to synthesize cDNA with a reverse transcriptase (SuperScript®II, Invitrogen, Carlsbad, Czech Republic), according to the manufacturer's recommendations. Specific primers were designed in exon 4 (forward - F) and in the 3'UTR region (reverse – R) of *ITM2B* (Refseq: NM\_021999.4; F: 5'ccctctgaacacttcattg 3'; R: 5'ccctgttgctacttacatg 3'). The specificity of all PCR products was first verified by electrophoresis on 1% agarose gel and subsequently by Sanger sequencing.

### **RNA in-situ hybridization and immunohistology**

#### ***Animal preparation***

Dissected eyes of adult, 6-13 week old C57BL/6J wild-type mice were used in this study.<sup>10</sup> All procedures were carried out according to the guidelines on the ethical use of animals from the European community council directive (86/609/EEC). Mice were killed with anesthesia. Eyeballs were enucleated and positioned in phosphate buffered saline (PBS) under a stereo microscope. A hole was pierced near the ora serrata, which allows a better diffusion of the fixative with 4% Paraformaldehyde (PFA) for 1h. Then eyes were incubated in PBS, 10% Sucrose for 1h at 4°C followed by PBS, 30% Sucrose for overnight at 4°C. Eyes were embedded in PGS (0.12M PBS, 7.5% Gelatin and 10% Sucrose) and frozen at -40°C in isopentane. Ten-micrometer-thick cryo-sections were collected (8 sections by a slide, Microm HM 560 Microtome Cryostat (Thermo Fisher Scientific, Waltham, MA USA).

#### ***Digoxigenin (DIG)-labeled RNA probes synthesis***

Plasmid type pBluescript II SK (+) was used to clone exon 2 to exon 6 of the *ITM2B* mouse mRNA (RefSeq NM\_008410.2) (GeneCust, Boynes, France). The 12 µg pBluscripII SK *ITM2B* plasmid was linearized by 100000 U *NotI* and *KpnI* enzymes (New England Biolabs, Ipswich, MA, USA). After verification by gel migration, linearized plasmids were purified using kits (Promega Wizard SV Gel & PCR clean-up system, Promega, Madison, WI, USA or QIAquick PCR Purification Kit, Qiagen, Hilden, Germany) according to manufacture recommendations.

RNA probes (sense and antisense) were synthesized as previously partially reported<sup>11</sup>; briefly RNA polymerases, T7 and T3 (Roche, France) respectively, were used and labeled with DIG. After precipitated with absolute ethanol (overnight, -20°C), washed by 4°C 70% ethanol and verified by electrophoresis – Ethidium bromide method, RNA probes were obtained and stored at -80°C.

#### *Co-RNA in situ Hybridization (ISH) / Fluorescent Immunohistochemistry (Fr-IHC)*

Co-ISH/IHC was performed with non-perfused animal. Slides were fixed with 4% PFA, without permeabilisation with proteinase K, incubated together with probes (72°C, overnight) then with anti-DIG and primary antibodies (RT, ON), followed by incubation with corresponding secondary antibodies, and finally stained by using NBT/BCIP (Roche Diagnostics, Basel, Switzerland) according to manufacturer recommendations.

The following primary antibodies were used (supplemental table S3): mouse anti-ITM2B (Sigma 1/100), rabbit anti-ITM2B (Sigma 1/100), mouse anti-myc (Roche 1/500), mouse anti-brn3a (Millipore, France 1/400), rabbit anti-GAD65 (Millipore 1/1000), mouse anti-glutamine synthetase (Millipore 1/2000), rabbit anti-calbindin D-28k (Swant, France 1/5000), mouse anti-Go $\alpha$  (Millipore 1/200), and rabbit anti-chx10 (Santa Cruz, France 1/2000). The following secondary antibodies were used: Alexa Fluor<sup>®</sup> 488 AffiniPure Donkey Anti-Mouse or Rabbit IgG (H+L), Cy<sup>™</sup>3 AffiniPure donkey anti-mouse or rabbit IgG (H+L), Cy<sup>™</sup>3 AffiniPure bovine Anti-Goat IgG (H+L) (Jackson ImmunoResearch, France). A HAMAMATSU Nanozoomer Digital Pathology (NDP) 2.0 HT and an inverted Olympus confocal microscope were used for image acquisition. The cellular specificities of each antibody used in the study are listed in table S1.

**Table S1.** *In silico* analysis performed on the *ITM2B* variant c.782A>C. PhyloP range: -14.1;6.4. Grantham score range: 0;215.

Genomic start position (hg19)	Exon	cDNA (NM_021999)	Protein change	rs#; gnomAD: frequency (allele count/total alleles/number of homozygous)	PhyloP <sup>1</sup> <sub>2</sub>	Grantham score <sup>13</sup>	Pathogenic prediction for missense changes			Effect on splicing prediction			
							SIFT <sup>3</sup> (score)	MutationTaster <sup>4</sup> (prob)	PolyPhen2 <sup>2</sup> (score)	MaxEnt Scan <sup>5</sup>	NNSplice <sup>6</sup>	HSF <sup>7</sup>	EX-SKIP <sup>8</sup>
48835341	6	c.782A>C	p.(Glu261Ala)	rs606231283; gnomAD: absent	4.48	107	Tolerated (0.29)	Disease Causing (1)	Probably Damaging (1)	No modifications	No modifications	New donor site in position c.780 (score 73.57)	The mutated allele has a higher chance of exon skipping than allele wild-type

**Table S2.** Conservation analysis of the variant c.782A>C on *ITM2B*, described in the study. The interested residue is highlighted in bold and red. Data for conservation were collected using the Vertebrate Multiz Alignment and Conservation of the University of California Santa Cruz (UCSC) genome browser (<http://genome.ucsc.edu/>)<sup>9</sup>.

Nucleotide genomic position (hg19)	48835341	Nucleotide genomic position (hg19)	48835341	Nucleotide genomic position (hg19)	48835341
AA position	782	AA position	782	AA position	782
Altered residue	A	Altered residue	A	Altered residue	A
Human	NKFAV <b>ETL</b> ICS	Domestic goat	NKFAV <b>ETL</b> ICS	Tibetan ground jay	NKFAM <b>ETL</b> I--
Chimp	NKFAV <b>ETL</b> ICS	Horse	NKFAV <b>ETL</b> ICS	Budgerigar	SRFAM <b>ETL</b> I--
Gorilla	NKFAV <b>ETL</b> ICS	White rhinoceros	NKFAV <b>ETL</b> ICS	Parrot	SRFAM <b>ETL</b> I--
Orangutan	NKFAV <b>ETL</b> ICS	Cat	NKFAV <b>ETV</b> ICP	Scarlet macaw	SRFAM <b>ETL</b> I--
Gibbon	NKFAV <b>ETL</b> ICS	Dog	NKFAV <b>ETV</b> ICP	Rock pigeon	NRFAM <b>ETL</b> I--
Rhesus	NKFAV <b>ETL</b> ICS	Ferret	NKFAV <b>ETV</b> ICP	Mallard duck	NRFAM <b>ETL</b> I--
Crab-eating Macaque	NKFAV <b>ETL</b> ICS	Panda	NKFAV <b>ETV</b> ICP	Chicken	NRFAM <b>ETL</b> I--
Baboon	NKFAV <b>ETL</b> ICS	Pacific walrus	NKFAV <b>ETV</b> ICP	Turkey	NRFAM <b>ETL</b> I--
Green Monkey	NKFAV <b>ETL</b> ICS	Weddell seal	NKFAV <b>ETV</b> ICP	American alligator	NRFAM <b>ETL</b> I--
Marmoset	NKFAV <b>ETL</b> ICS	Black flying-fox	NKFAV <b>ETL</b> ICS	Green seaturtle	NWFAI <b>ETL</b> I--
Squirrel Monkey	NKFAV <b>ETL</b> ICS	Megabat	NKFAV <b>ETL</b> ICS	Painted turtle	NRFAI <b>ETL</b> I--
Bushbaby	NIFAV <b>ETL</b> ICS	David's myotis (bat)	NKFAV <b>ETL</b> ICS	Chinese softshell turtle	NRFAM <b>ETL</b> I--
Chinese tree shrew	NKFAV <b>ETL</b> ICS	Microbat	NKFAV <b>ETL</b> ICS	Cpiny softshell turtle	NRFAM <b>ETL</b> I--
Squirrel Monkey	NKFAV <b>ETL</b> ICS	Big brown bat	NKFAV <b>ETL</b> ICS	Lizard	NRFV <b>ETV</b> I--
Egyptian jerboa	NKFAV <b>ETL</b> ICS	Hedgehog	NKFAV <b>ETL</b> ICS	X_tropicalis	NRFV <b>ETQ</b> I--
Prairie	NKFV <b>ETS</b> ICS	Shrew	NKFAV <b>ETL</b> ICP	Coelacanth	SKD <b>VV</b> ETL I--
Chinese hamster	NSFV <b>ETS</b> ICS	Star-nosed mole	NKFAV <b>ETL</b> ICS	Tetraodon	-----
Golden hamster	NKFV <b>ETS</b> ICS	Elephant	NKFAV <b>ETL</b> ICS	Fugu	SHV <b>VV</b> ETQIC-
Mouse	NKFAV <b>ETL</b> ICS	Cape elephant shrew	NKFV <b>ETL</b> ICS	Yellowbelly pufferfish	-----
Rat	NKFAV <b>ETL</b> ICS	Manatee	NKFAV <b>ETL</b> ICS	Nile tilapia	SQFV <b>ETL</b> IC-
Naked mole-rat	NKFAV <b>ETL</b> ICS	Cape golden mole	NKFAV <b>ETL</b> ICS	Princess of Burundi	SQFV <b>ETL</b> IC-
Guinea pig	NKFAV <b>ETV</b> ICS	Tenrec	SRV <b>AV</b> ETLICS	Burton's mouthbreeder	SQFV <b>ETL</b> IC-
Chinchilla	NKFAV <b>ETS</b> ICS	Aardvark	NKFAV <b>ETL</b> ICS	Zebra mbuna	SQFV <b>ETL</b> IC-
Brush-tailed rat	NKFAV <b>ETL</b> ICS	Armadillo	NKFAV <b>ETL</b> ICS	Pundamilia nyererei	SQFV <b>ETL</b> IC-
Rabbit	NKFAV <b>ETL</b> ICS	Opossum	NKFAV <b>ETR</b> ICA	Medaka	NNFV <b>ETQ</b> I--
Pika	NKFAV <b>ETL</b> ICS	Tasmanian devil	NKFAV <b>ETR</b> ICA	Southern platyfish	NKFV <b>ETL</b> I--
Pig	NKFAV <b>ETL</b> ICS	Wallaby	NKFAV <b>ETR</b> ICA	Stickleback	NKFV <b>ETL</b> I--
Alpaca	NKFAV <b>ETL</b> ICS	Platypus	NRFAM <b>ETL</b> I--	Atlantic cod	-----
Bactrian camel	NKFAV <b>ETL</b> ICS	Saker falcon	NRFAM <b>ETV</b> I--	Zebrafish	NKFV <b>ETL</b> I--
Dolphin	NKFAV <b>ETL</b> ICS	Peregrine falcon	NRFAM <b>ETV</b> I--	Mexican tetra (cavefish)	NKFV <b>ETL</b> I--
Killer whale	NKFAV <b>ETL</b> ICS	Collared flycatcher	NKFAM <b>ETL</b> I--	Spotted gar	NKFV <b>ETL</b> I--
Tibetan antelope	NRFV <b>AV</b> ETLICS	White-throated sparrow	NKFAM <b>ETL</b> I--	Lamprey	-----
Cow	NRFV <b>AV</b> ETL ICP	Medium ground finch	NKFAM <b>ETL</b> I--		
Sheep	NKFAV <b>ETL</b> ICS	Zebra finch	NKFAM <b>ETL</b> I--		

**Table S3.** Retinal cells specificity of the antibodies used for Co-RNA *in situ* Hybridization / Fluorescent Immunohistochemistry.

Antibody	Cell type	References
Mouse anti-brn3a	Ganglion cells	Xiang et al. <sup>14</sup>
Mouse anti-glutamine synthetase	Müller cells	Haverkamp and Wässle <sup>15</sup>
Rabbit anti-calbindin D	Horizontal cells; Amacrine cells	Peichl and González-Soriano <sup>16</sup>
Rabbit anti-GAD65	Amacrine cells	Haverkamp and Wässle <sup>15</sup>
Mouse anti-Goa	Bipolar cells	Vardi et al. <sup>17</sup>

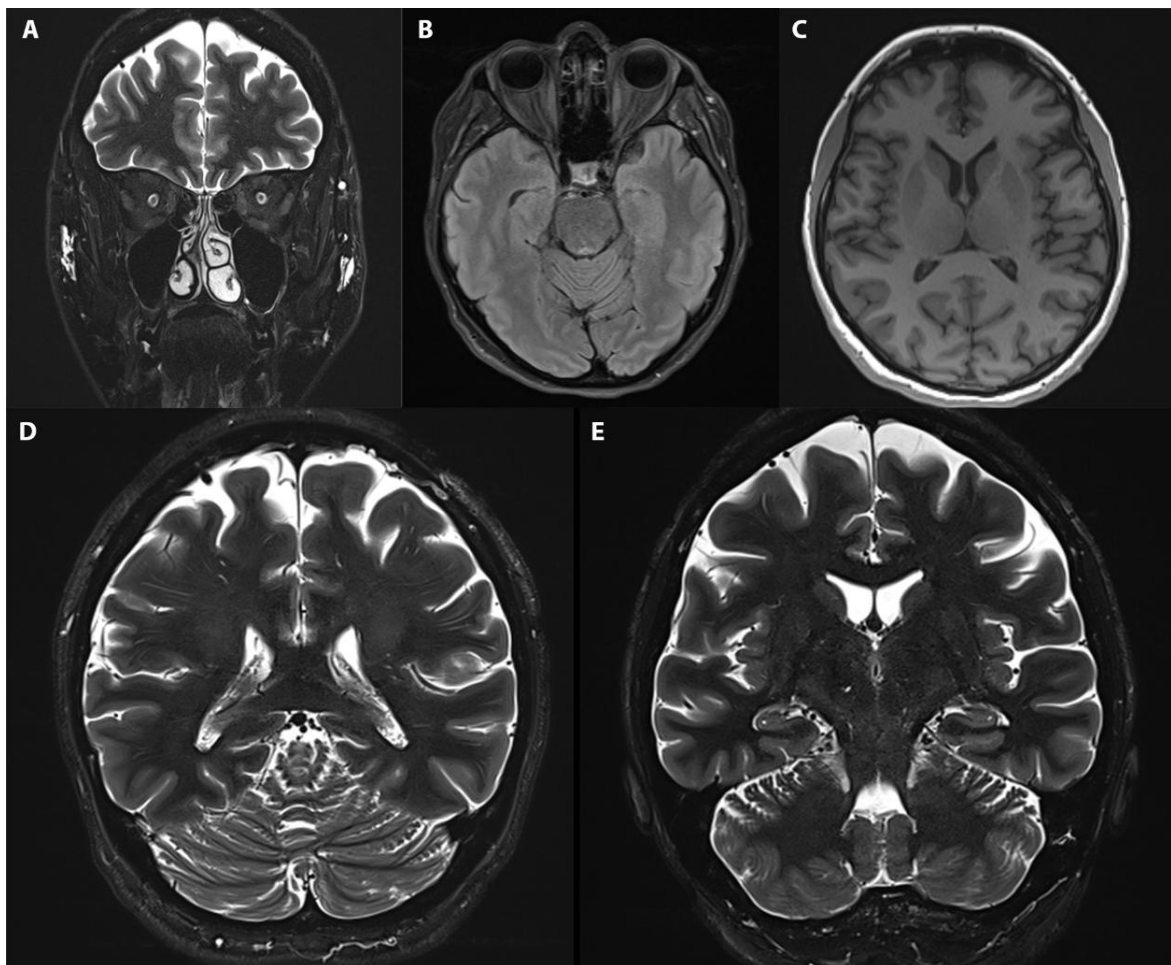


**Fig. S1** Magnetic Resonance Imaging (MRI) of the brain of an affected patient (CIC02771) (3 T SIEMENS Skyra MRI with a 64-channel head coil). In coronal contrast-inverted short-T1 inversion-recovery (STIR) images passing through the prefrontal lobe and the orbits (A) and in the fluid-attenuated inversion recuperation (FLAIR) axial section passing through the pons (B); the optic nerves show normal thickness and signal within the orbit. The T1 weighted gradient-echo (MPRAGE) axial section (C) shows a normal white and grey matter of the cerebral cortex, thalami, lenticular and caudate nuclei. In the STIR coronal-oblique sections passing through the cerebellum (D-E), the cerebellar cortex (D) and the hippocampi (E) display no morphological nor signal alterations.

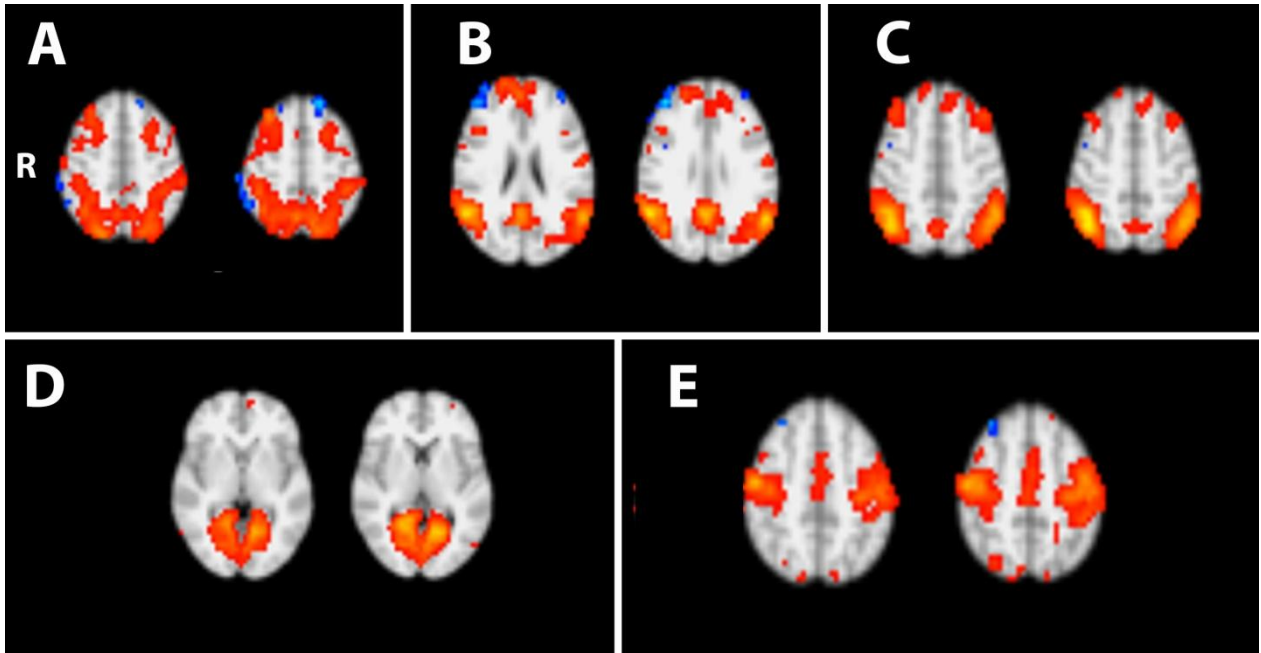


**Fig. S2 Axial slices of the brain showing fMRI resting-state networks common to the three subjects, using multi-subject Independent Component Analysis (ICA).** A group (N = 3) ICA with 20 components using temporal concatenation with spatial ICA maps thresholded at 0.7; Multivariate Exploratory Linear Optimized Decomposition into Independent Components (MELODIC) option of Functional Magnetic Resonance Imaging of the Brain (FMRIB) Software Library ((FSL) software version 6.0.1, <https://fsl.fmrib.ox.ac.uk/fsl/fslwiki/MELODIC>) was applied to resting-state echo-planar imaging (EPI) images of each subject (300 volumes, spatial resolution : 2.5x2.5x2.5x mm). (A) Dorsal attentional network. (B) Default-mode network (C) Central executive network (D) Medial visual network (E) (pre-) motor network. R; Right.

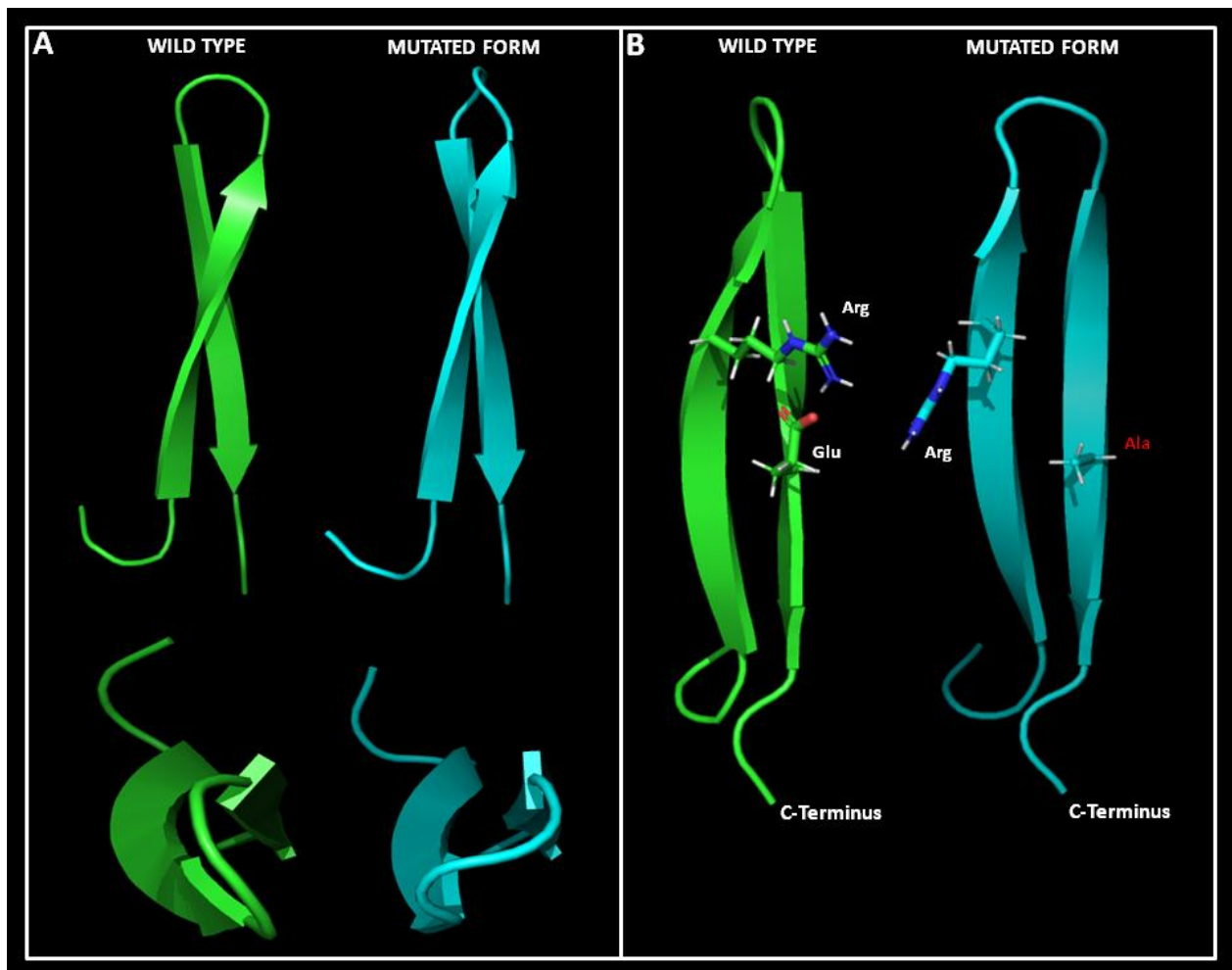


**Fig.S3** *In silico* predictions of the 23-aminoacids peptide at the C-terminus of the *ITM2B* protein using the software QUARK (available at <https://zhanglab.ccmb.med.umich.edu/QUARK/>)<sup>18</sup>. The mutated form (A, top right) has an Alanine (Ala) in position 261 at the place of a glutamic acid (Glu) in the wild-type form (B, top left). The two forms are slightly different as the two  $\beta$ -strands look more parallel and distant in the mutated form than the wild-type. This is particularly evident from a top view of the peptides (A, bottom left for the wild-type and bottom right for the mutated form). This change in conformation is probably due to different interaction between altered amino acid in position 261 and Arginine (Arg, positively charged) in position 252, as the glutamic acid (Glu) in the wild-type is negatively charged, while the Alanine (Ala) is neutral.

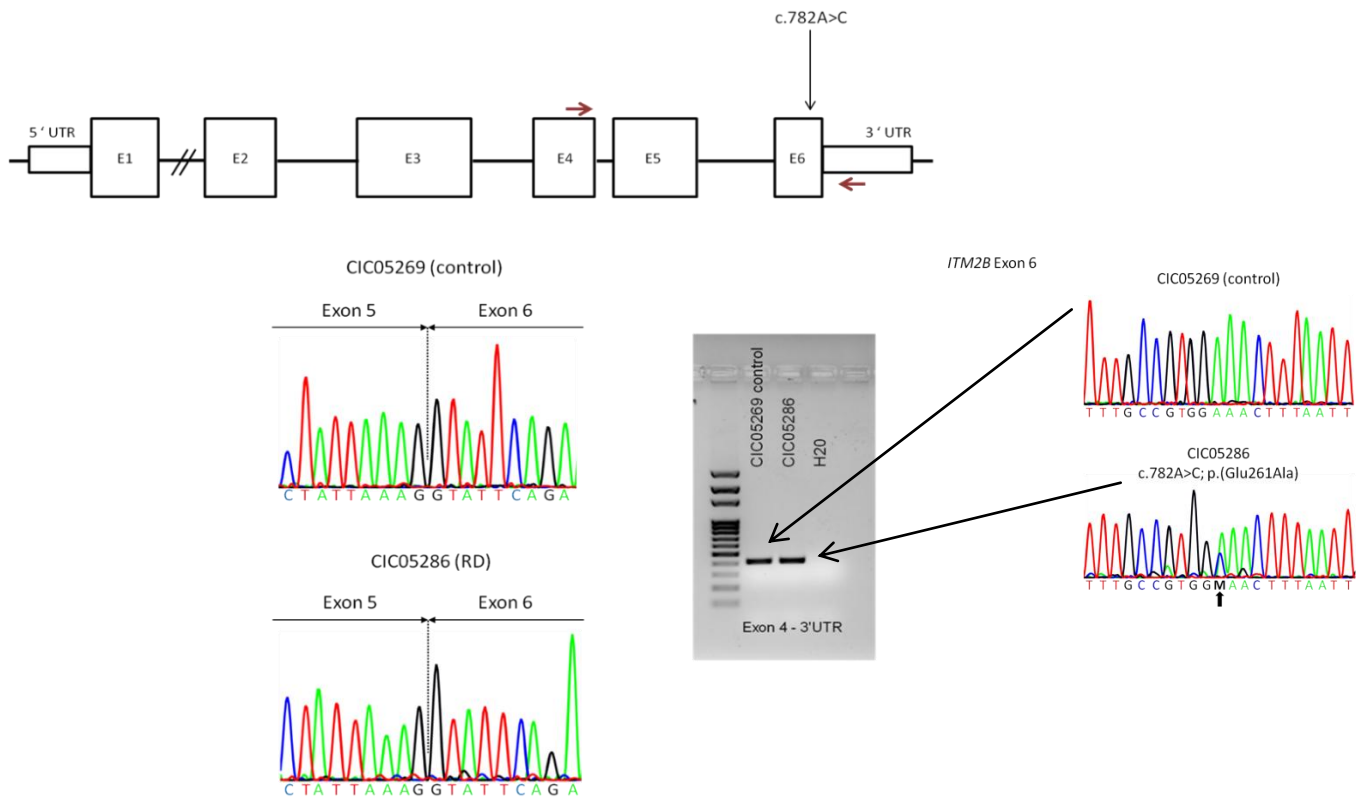


**Fig.S4 Reverse Transcription –Protein Chain Reaction (RT-PCR) and Sanger Sequencing performed on the fibroblasts derived from an affected patient (CIC05286) and a control (CIC05269).** (Top) cDNA structure of *ITM2B* with the localization of the variant c.782A>C and the designed primers (top red arrow: primer forward; bottom red arrow: primer reverse). (Bottom) The RT-PCR fragments from the mutant and the unaffected control were the same after migration on a 1% agarose gel. This finding was further confirmed through Sanger sequencing.

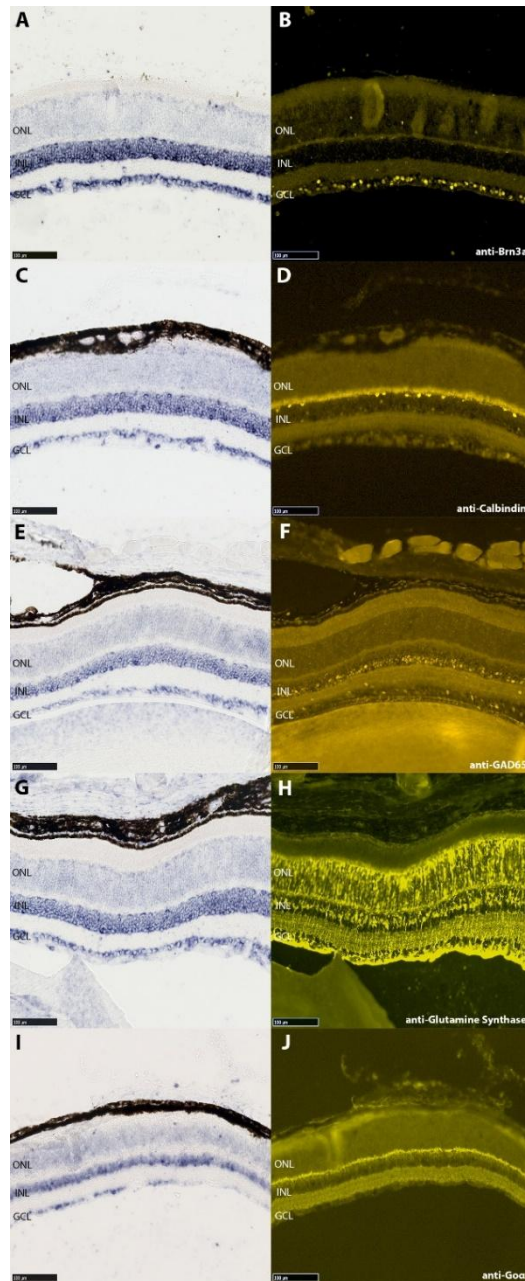


**Fig.S5 Results of the Co-RNA *in situ* Hybridization (IHS) / Fluorescent immunohistochemistry studies.** Immunostaining against *ITM2B* is sparse (A,C,E,G,I), hence it was impossible to precisely document co-localization through co-immunostaining. Therefore, we analyzed *ITM2B* expression in the inner retina using specific retinal cell markers. (A-B) Co-IHS of *ITM2B* (purple in A) with mouse anti-Brn3a antibody (yellow in B) for ganglion cells; (C-D) Co-IHS of *ITM2B* (purple in C) with rabbit anti-calbindin D antibody (yellow in D) for horizontal and amacrine cells; (E-F) Co-IHS of *ITM2B* (purple in E) with rabbit anti-GAD65 antibody (yellow in F) for amacrine cells; (G-H) Co-IHS of *ITM2B* (purple in G) with mouse anti-glutamine synthetase antibody (yellow in H) for Müller cells; (I-J) Co-IHS of *ITM2B* (purple in I) with mouse anti-Goa (yellow in J) for bipolar cells.

## References

1. McCulloch DL, Marmor MF, Brigell MG, et al. ISCEV Standard for full-field clinical electroretinography (2015 update). *Doc Ophthalmol*. 2015;130(1):1-12. doi:10.1007/s10633-014-9473-7
2. Adzhubei IA, Schmidt S, Peshkin L, et al. A method and server for predicting damaging missense mutations. *Nat Methods*. 2010;7(4):248-249. doi:10.1038/nmeth0410-248
3. Sim N-L, Kumar P, Hu J, Henikoff S, Schneider G, Ng PC. SIFT web server: predicting effects of amino acid substitutions on proteins. *Nucleic Acids Res*. 2012;40(Web Server issue):W452-457. doi:10.1093/nar/gks539
4. Schwarz JM, Cooper DN, Schuelke M, Seelow D. MutationTaster2: mutation prediction for the deep-sequencing age. *Nat Methods*. 2014;11(4):361-362. doi:10.1038/nmeth.2890
5. Yeo G, Burge CB. Maximum entropy modeling of short sequence motifs with applications to RNA splicing signals. *J Comput Biol*. 2004;11(2-3):377-394. doi:10.1089/1066527041410418
6. Reese MG, Eeckman FH, Kulp D, Haussler D. Improved splice site detection in Genie. *J Comput Biol*. 1997;4(3):311-323. doi:10.1089/cmb.1997.4.311
7. Desmet F-O, Hamroun D, Lalande M, Collod-Bérout G, Claustres M, Bérout C. Human Splicing Finder: an online bioinformatics tool to predict splicing signals. *Nucleic Acids Res*. 2009;37(9):e67. doi:10.1093/nar/gkp215
8. Raponi M, Kralovicova J, Copson E, et al. Prediction of single-nucleotide substitutions that result in exon skipping: identification of a splicing silencer in BRCA1 exon 6. *Hum Mutat*. 2011;32(4):436-444. doi:10.1002/humu.21458
9. Kent WJ, Sugnet CW, Furey TS, et al. The human genome browser at UCSC. *Genome Res*. 2002;12(6):996-1006. doi:10.1101/gr.229102
10. Keane TM, Goodstadt L, Danecek P, et al. Mouse genomic variation and its effect on phenotypes and gene regulation. *Nature*. 2011;477(7364):289-294. doi:10.1038/nature10413
11. Orhan E, Prézeau L, El Shamieh S, et al. Further insights into GPR179: expression, localization, and associated pathogenic mechanisms leading to complete congenital stationary night blindness. *Invest Ophthalmol Vis Sci*. 2013;54(13):8041-8050. doi:10.1167/iovs.13-12610
12. Pollard KS, Hubisz MJ, Rosenbloom KR, Siepel A. Detection of nonneutral substitution rates on mammalian phylogenies. *Genome Res*. 2010;20(1):110-121. doi:10.1101/gr.097857.109
13. Grantham R. Amino acid difference formula to help explain protein evolution. *Science*. 1974;185(4154):862-864. doi:10.1126/science.185.4154.862
14. Xiang M, Zhou L, Macke JP, et al. The Brn-3 family of POU-domain factors: primary structure, binding specificity, and expression in subsets of retinal ganglion cells and somatosensory neurons. *J Neurosci*. 1995;15(7 Pt 1):4762-4785.
15. Haverkamp S, Wässle H. Immunocytochemical analysis of the mouse retina. *J Comp Neurol*. 2000;424(1):1-23.
16. Peichl L, González-Soriano J. Morphological types of horizontal cell in rodent retinae: a comparison of rat, mouse, gerbil, and guinea pig. *Vis Neurosci*. 1994;11(3):501-517. doi:10.1017/s095252380000242x
17. Vardi N, Matesic DF, Manning DR, Liebman PA, Sterling P. Identification of a G-protein in depolarizing rod bipolar cells. *Vis Neurosci*. 1993;10(3):473-478. doi:10.1017/s0952523800004697

18. Xu D, Zhang Y. Ab initio protein structure assembly using continuous structure fragments and optimized knowledge-based force field. *Proteins*. 2012;80(7):1715-1735. doi:10.1002/prot.24065

## **2. Identification of the ITM2B protein interactome in the human retina**

In this second work, we performed proteomic analyses to characterize the ITM2B interactome in the human retina. This study allowed us to identify ITM2B interactors in the retina, compared them to previous work on rat brain and shed light on functional retinal pathways in which ITM2B may be involved. More specifically, ITM2B interactors are present in all the retinal cell types suggesting a ubiquitous role of ITM2B in this tissue. We documented for the first time the interaction between ITM2B and APP as well as with APLP2 in the retina. Moreover, we identified common ITM2B interactors previously reported in the rat brain. Our work also suggests a unique role of ITM2B in mitochondrial homeostasis in the retina.

This first proteomic study of the ITM2B interactome in the retina represents a valuable resource for the scientific community.

*This work has been submitted for publication.*

## **First identification of ITM2B interactome in the human retina**

J. Wohlschlegel<sup>1</sup>, M. Argentini<sup>1</sup>, V. Forster<sup>1</sup>, C. Condroyer<sup>1</sup>, Z. He<sup>2</sup>, G. Thuret<sup>2,3</sup>, C. Zeitz<sup>1</sup>, T. Léger<sup>4,5</sup>, I. Audo<sup>1,6,7\*</sup>

1. Sorbonne Université, INSERM, CNRS, Institut de la Vision, 17 rue Moreau, F-75012 Paris, France

2. Corneal Graft Biology, Engineering and Imaging Laboratory, Health Innovation Campus, Faculty of Medicine, Jean Monnet University, Saint-Etienne, France.

3. Department of Ophthalmology, University Hospital, Saint-Etienne, France.

4. Mass Spectrometry Laboratory, Institut Jacques Monod, UMR 7592, Université Paris Diderot, CNRS, Sorbonne Paris Cité, F-75205 Paris, France.

5. Univ Rennes, Inserm, EHESP, Irset (Institut de recherche en santé, environnement et travail) – UMR\_S 1085, F-35000 Rennes, France

6. CHNO des Quinze-Vingts, INSERM-DGOS CIC 1423, 28 rue de Charenton, F-75012 Paris, France

**7. Department of Genetics, UCL-Institute of Ophthalmology, 11–43 Bath Street, London EC1V 9EL, UK**

**Corresponding author:** Isabelle Audo, MD, PhD, Institut de la Vision, 17 Rue Moreau, Paris, France, 75012. Mail: [isabelle.audo@inserm.fr](mailto:isabelle.audo@inserm.fr)

## Abstract

Integral Membrane Protein 2 B (ITM2B) is a type II ubiquitous transmembrane protein which role remains unclear. *ITM2B* mutations have been associated with different disorders: mutations leading to longer mutant proteins have been reported in two distinct Alzheimer-like autosomal dominant disorders with early-onset progressive dementia and cerebellar ataxia. Both disorders share neurological features including severe cerebral amyloid angiopathy, non-neuritic plaques, and fibrillary tangles as in Alzheimer Disease. Our group reported a missense mutation in *ITM2B*, in an unusual retinal dystrophy with no dementia. This finding suggests a specific role of ITM2B in the retina. As the identification of retinal-specific ITM2B partners could bring new insights into the cellular functions of ITM2B, we performed quantitative proteomics of ITM2B interactome of the human retina. Overall, 457 ITM2B partners were identified with 8 of them involved in visual transduction. In addition, bulk Gene Ontology analyses showed that many ITM2B partners are involved in several other biological functions, such as microtubule organization, protein translation and interestingly, mitochondrial homeostasis. These data represent the first report of the ITM2B interactome in the human retina and may serve as a valuable inventory of new potential ITM2B partners for future investigations of ITM2B physiological functions and dysfunctions.

## Introduction

ITM2B (Integral membrane protein 2b also called BRI2, MIM#603904) is a single pass type II ubiquitous protein which function is still unclear. ITM2B is cleaved by different enzymes, furin or furin-like proteases, at its C-terminus, releasing a 23-amino acid peptide, called Bri23.<sup>1,2</sup> ITM2B is highly expressed in the brain and the retina<sup>3,4</sup>. Mutations in this gene lead to different disorders in humans. *ITM2B* mutations leading to a longer protein product are responsible for two distinct autosomal dominant neurodegenerative disorders: the Familial British Dementia (FBD, MIM#176500)<sup>5-7</sup> and the Familial Danish Dementia (FDD, MIM#117300)<sup>8</sup>. The diseases consist mainly of early-onset forms of progressive dementia with cerebellar ataxia and spasticity. FDD is also known as hereditary ophthalmoto-encephalica<sup>9</sup> with the first symptoms being the development of cataract and progressive deafness. Both FBD and FDD share neurological features including severe cerebral amyloid angiopathy, non-neuritic plaques<sup>7</sup>, and fibrillary tangles as in Alzheimer Disease (AD). The respective mutations lead to a longer protein at the C-terminus the cleavage of which releases, instead of Bri23, a 34-amino acid peptide named ADan in FDD and ABri in FBD. ADan<sup>8</sup> and ABri<sup>5</sup> are the major components of insoluble aggregates in the brain of affected subjects. More recently, another autosomal dominant mutation in *ITM2B* (c.782A>C, p.Glu261Ala) has been reported in an unusual retinal dystrophy associated with retinal ganglion cell abnormalities, inner retinal and cone dysfunctions. Furthermore, the phenotype is only restricted to the retina (MIM#616079)<sup>3,10</sup> and none of the affected subjects present dementia, suggesting that ITM2B play a specific role in the retina. Interestingly, the mutation identified in the retinal dystrophy<sup>3</sup> is also located within the 23-amino acid C-terminal cleaved peptide, outlining the functional importance of this peptide. In normal conditions, the furin or furin-like cleavage generates the mature form of ITM2B which is processed in the cis-Golgi apparatus. ITM2B may also be cleaved by ADAM10<sup>11</sup> releasing an evolutionary conserved domain called the BRICHOS domain. Then, the remaining membrane-bound peptide is intramembranously proteolysed by Signal Peptidase-Like 2B (SPPL2B) releasing one intracellular domain in the cytosol and a small extracellular secreted peptide<sup>12,13</sup>.

In the brain, ITM2B interacts with A $\beta$ PP (Amyloid  $\beta$  Precursor Protein) acting as an inhibitor of Amyloid  $\beta$  (A $\beta$ ) oligomerization<sup>12-14</sup>, a major component of amyloid plaques in AD and AD-like diseases. ITM2B has also been involved in neuronal functions and in particular in neurite

outgrowth<sup>15</sup>. Recently, ITM2B has been shown to interact with APLP2 (APP-related protein 2), a protein belonging to the APP family<sup>16</sup>. Interestingly APP, APLP2 and ITM2B were found to form a complex interacting with GABA<sub>b</sub> receptors in rodent brains.<sup>17,18</sup>

Despite these published data, the molecular function of ITM2B remains mostly unknown and has never been studied in the retina. To address this issue, we performed quantitative proteomics of immunopurified ITM2B complexes isolated from normal human retinal protein extracts. We used two distinct anti-ITM2B antibodies recognizing different epitopes of the protein in order to immunopurify as many ITM2B partners as possible. Gene ontology annotation with *in silico tools* enabled to shed light on new functional retinal pathways in which ITM2B may be involved. Interestingly, besides common protein partners purified with both antibodies, two distinct clusters of ITM2B protein interactors were identified for each of the two antibodies. To our knowledge, ITM2B interactome has only been described in rodent brains<sup>19</sup>, not in the retina and never in human tissues. Our findings support a specific role for ITM2B in the retina and might suggest a role in the mitochondrial homeostasis.

## Results

### *Identification of ITM2B retinal interactome by quantitative proteomics*

In order to gain insight into the role of ITM2B in the retina we applied quantitative mass spectrometry-based proteomics to identify ITM2B partners. Whole proteins from an unaffected human post-mortem retina were extracted, separated in three equal samples and subjected to three independent immunoprecipitations (IP) with two anti-ITM2B antibodies raised against different epitopes of the protein and one IgG unspecific antibody. The mouse anti-ITM2B antibody binds a specific site encompassing the N-terminal 1-54 aminoacidic region of the protein, whereas the rabbit anti-ITM2B antibody binds the 15-264 aminoacidic region of ITM2B. This experimental strategy was chosen to identify as many as possible specific and functionally relevant ITM2B partners. We performed three independent experiments with one human retina (see Methods). Immunopurified protein complexes from each retinal sample were analyzed using LC-MS/MS in triplicates. This proteomic analysis provides the first dataset of the ITM2B interactome in the retina. The workflow of the experience is depicted in Figure 1.

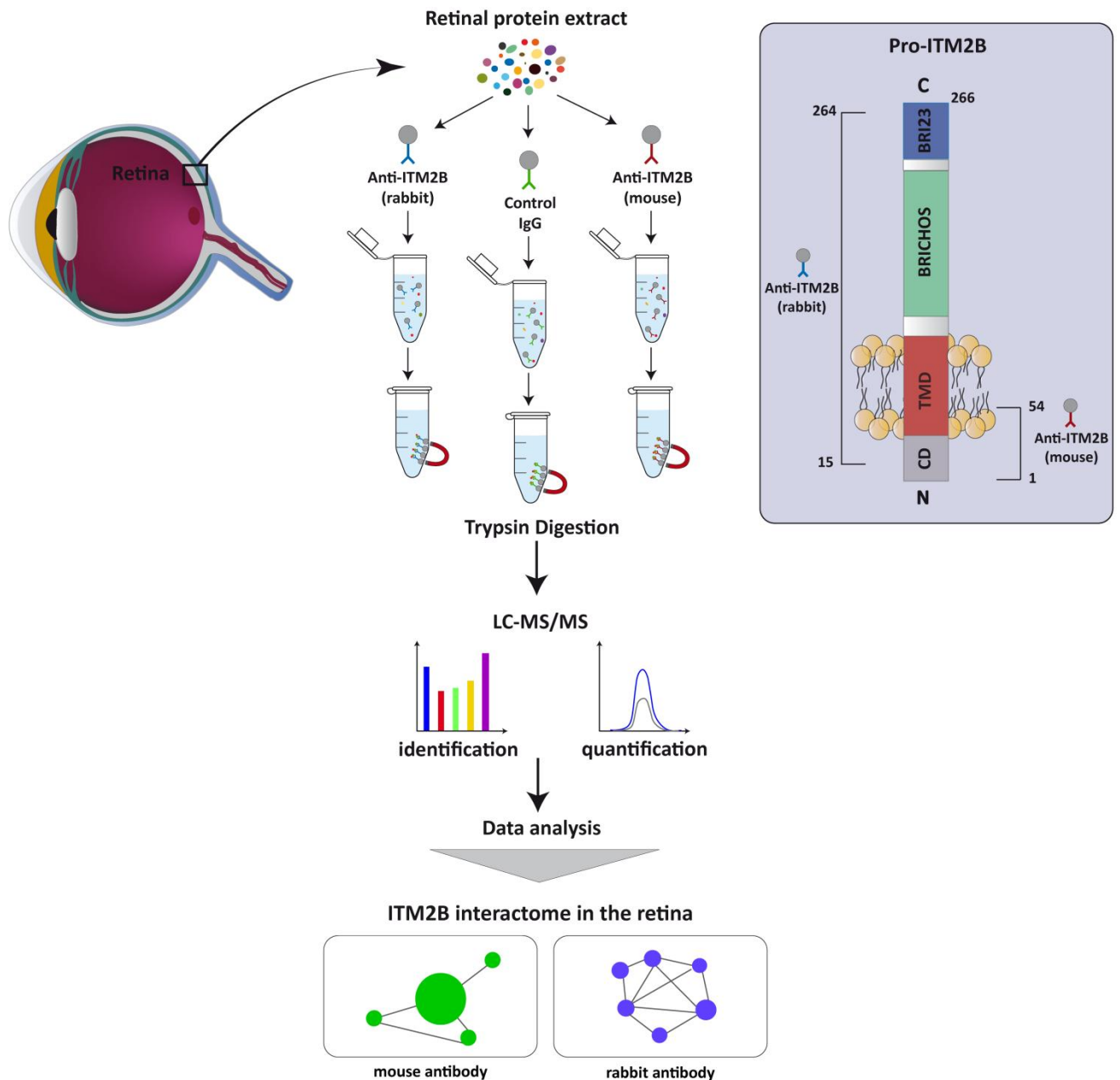


**Figure 1.** Experimental design. ITM2B is composed of several domains: CD: cytosolic domain, TMD: transmembrane domain, BRICHOS, Bri23 and two linker domains (in light grey). Two distinct anti-ITM2B antibodies were used for immunoprecipitation. The first antibody is a rabbit polyclonal antibody raised against the 15-264 aminoacidic region of ITM2B and the second antibody is a mouse monoclonal antibody raised against the N-terminal 1-54 aminoacidic region of the protein. A third unspecific IgG mouse antibody was used as negative control. After ITM2B immunoprecipitation, protein complexes were digested with trypsin and peptide mixtures were analyzed by LC-MS/MS. A label-free quantitative proteomic analysis was then performed to identify and quantify ITM2B partners.

Stringent filtering identified a total of 1102 proteins from immunopurified ITM2B complexes with the two anti-ITM2B antibodies. To concentrate only on specific interactors, only ITM2B protein partners with a fold change  $>2$  ( $FC>2$ ) compared to the negative control and a  $p$ -value  $<0.01$  were retained. Considering only specific interactors, ( $FC >2$  and  $p$ -values  $<0.01$ ) a total of 457 putative ITM2B interactors were identified in the human retina (Supplementary Table S1).

The vast majority of the identified proteins are not reported as specifically expressed in the retina. Indeed, we compared our dataset with a Human Protein Atlas database list of 310 proteins highly expressed in the retina compared to other tissues. Among the 457 putative ITM2B interactors, only 9 proteins are highly expressed in the retina (Supplementary Table S2). These proteins are almost all exclusively expressed in photoreceptor cells and their associated biological processes are visual perception and photoreceptor development (Supplementary Table S3). However, we also identified interactors localized in all retinal cell types. Indeed, among 457 ITM2B potential interactors, we found tubulin beta-3 class III (TUBB3) and the neurofilament light polypeptide (NEFL) both highly expressed in retinal ganglion cells<sup>20,21</sup>. In addition, the well-known marker for Müller glial cells, Dickkopf-related protein 3 (DKK3)<sup>22</sup>, was also identified. Likewise, other proteins such as the sodium/potassium-transporting ATPase subunit beta-1 (ATP1B1)<sup>23</sup> specific to amacrine cells and the septin-4 (SEPT4)<sup>24</sup> specific to horizontal cells were also found ( $p$ -value  $<0.05$ ). Interestingly, we also found key proteins of the vesicular trafficking and exocytose pathways such as syntaxin binding protein 1 (STXBP1), synaptotagmin-11 (SYT11), the trafficking protein particle complex subunit 2-like protein (TRAPPC2L), Kinesin-like protein KIF21A (KIF21A) and vesicle-trafficking protein SEC22b (SEC22B). This result reinforces previous studies that reported the anterograde transport of ITM2B in the nerve terminals<sup>15,19</sup>.

To exhaustively identify known molecular pathways in which ITM2B may be involved, we apply gene ontology (GO) analysis to the 457 ITM2B interactors. Cellular component (GO-CC) annotations revealed protein interactome associated with organelle inner membrane, and other GO-CC terms associated more specifically with the mitochondria such as mitochondrial inner membrane, inner mitochondrial membrane protein complex, mitochondrial respirasome and mitochondrial respiratory chain complex I (Supplementary Fig. S1, Supplementary Table S4). Gene ontology biological process (GO-BP) identified interesting biological pathways such as oxidative phosphorylation and GO-BP terms associated with

mitochondrial processes (cellular respiration, respiratory electron transport chain, mitochondrial respiratory chain complex I assembly, mitochondrial ATP synthesis coupled electron transport, mitochondrial electron transport, NADH to ubiquinone, NADH dehydrogenase activity) (Supplementary Fig. S1, Supplementary Table S4). These results suggest a possible involvement of ITM2B in mitochondrial functions, in particular in cellular respiration.

### ***Differential interactomes identified by the anti-ITM2B mouse versus the rabbit antibody***

We first focused on the common ITM2B partners immunopurified with both antibodies. Indeed, 254 and 360 proteins were identified respectively with the mouse and rabbit anti-ITM2B antibody (Fig. 2a). Among them, a total of 140 proteins were immunopurified with both antibodies (Fig.2a, Supplementary Table S5). GO-CC analysis of these 140 common interactors showed proteins involved in supramolecular fiber, polymeric cytoskeletal fiber and microtubule (Supplementary Fig. S2, Supplementary Table S6). A subsequent network analysis shows an association between polymeric cytoskeletal fiber and the two other annotations (i.e. supramolecular fiber, microtubule). Only one significantly enriched GO-BP term was found: organelle localization by membrane tethering. We thus concluded that proteins with GO-BP or CC terms associated with the mitochondria were purified with only one of the two antibodies. To describe more precisely the protein complexes immunopurified by each antibody we analyzed ITM2B interactors with unsupervised hierarchical clustering. We then established a heatmap of identified proteins according to the antibodies used for protein complex purification (Fig. 2b). Beside the 140 common proteins, we also found two distinct clusters of 114 and 220 proteins specifically purified with the mouse and rabbit anti-ITM2B antibody respectively (Fig. 2b). To better characterize these two specific clusters, each data set was studied separately.

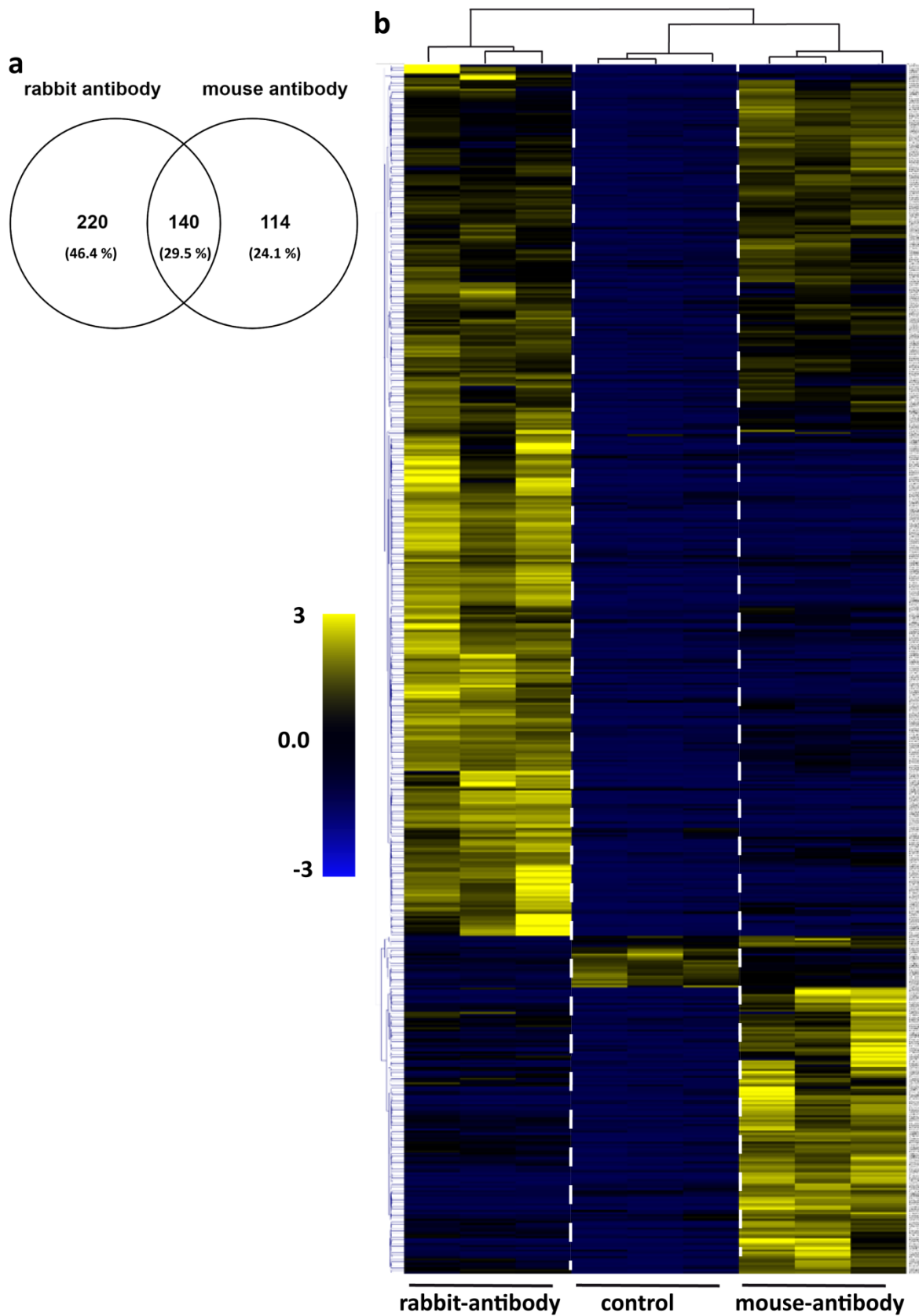


**Figure 2.** (a) Venn diagram showing the number of proteins purified respectively with the rabbit and the mouse antibodies. (b) Unsupervised hierarchical clustering and heatmap overview showing the protein abundance patterns using the two different antibodies.

### ***ITM2B interactome purified specifically with the mouse anti-ITM2B antibody***

We analyzed the cluster of proteins specifically purified with the mouse antibody. A total of 440 significantly enriched proteins ( $FC > 2$  and  $p\text{-value} < 0.05$ ) were identified and are represented in the top right panel of the volcano plot (Fig. 3). Among them, 254 statistically significant proteins were identified using a  $p\text{-value} < 0.01$  (Fig. 3). The specificity of the mouse anti-ITM2B antibody was rather high as illustrated by the low number of significantly enriched proteins identified by the mouse IgG unspecific antibody (top left panel). Among the significantly enriched proteins purified with the mouse anti-ITM2B antibody, we found APP and APLP2 proteins which have been previously described as ITM2B partners, notably playing a role in GABA<sub>b</sub> signaling in rodent brains<sup>17,18</sup>. Surprisingly, no protein belonging to the GABA<sub>b</sub> receptor family were identified in our study, which might suggest a different role of the ITM2B-APP-APLP2 complex in the retina. We performed co-immunoprecipitation and immunoblotting experiments from human retinal protein extracts to confirm these proteomic data (Fig. 3b). To our knowledge, this is the first time that interactions between ITM2B and APP, and ITM2B and APLP2 are shown in the human retina (Fig. 3b).

As expected from the previous analyses, GO-CC annotation of the 254 specific proteins ( $p\text{-value} < 0.01$ ), revealed proteins associated with microtubule (Fig. 4, Supplementary Table S7). Besides, GO analysis of ITM2B retinal interactome identified three other interesting functional pathways: organonitrogen compound biosynthetic process, peptide metabolic process and translation (Supplementary Table S7). Subsequent network analysis shows common interactions between these last three GO-BP terms (Fig. 4a).

We then compared this proteomic dataset with the previously reported ITM2B interactome purified with the same mouse antibody from rat brains<sup>19</sup>. Overall, 124 proteins are in common between our dataset and the 511 rat cerebral proteins<sup>19</sup> (Supplementary Table S8). The majority of these common proteins are involved in translation process including the eukaryotic translation elongation factor 1 alpha 1 (EEF1A), the ribosomal protein L12 (RPL12) and the solute carrier family 25 member 11 (SCL25A11) or involved in microtubule processes such as tubulin beta 2A (TUBB2A), tubulin beta 2B (TUBB2B) and tubulin beta-3 class III TUBB3 (Supplementary Table S8). This comparative analysis strongly suggests that some functions of ITM2B are similar in the brain and the retina.

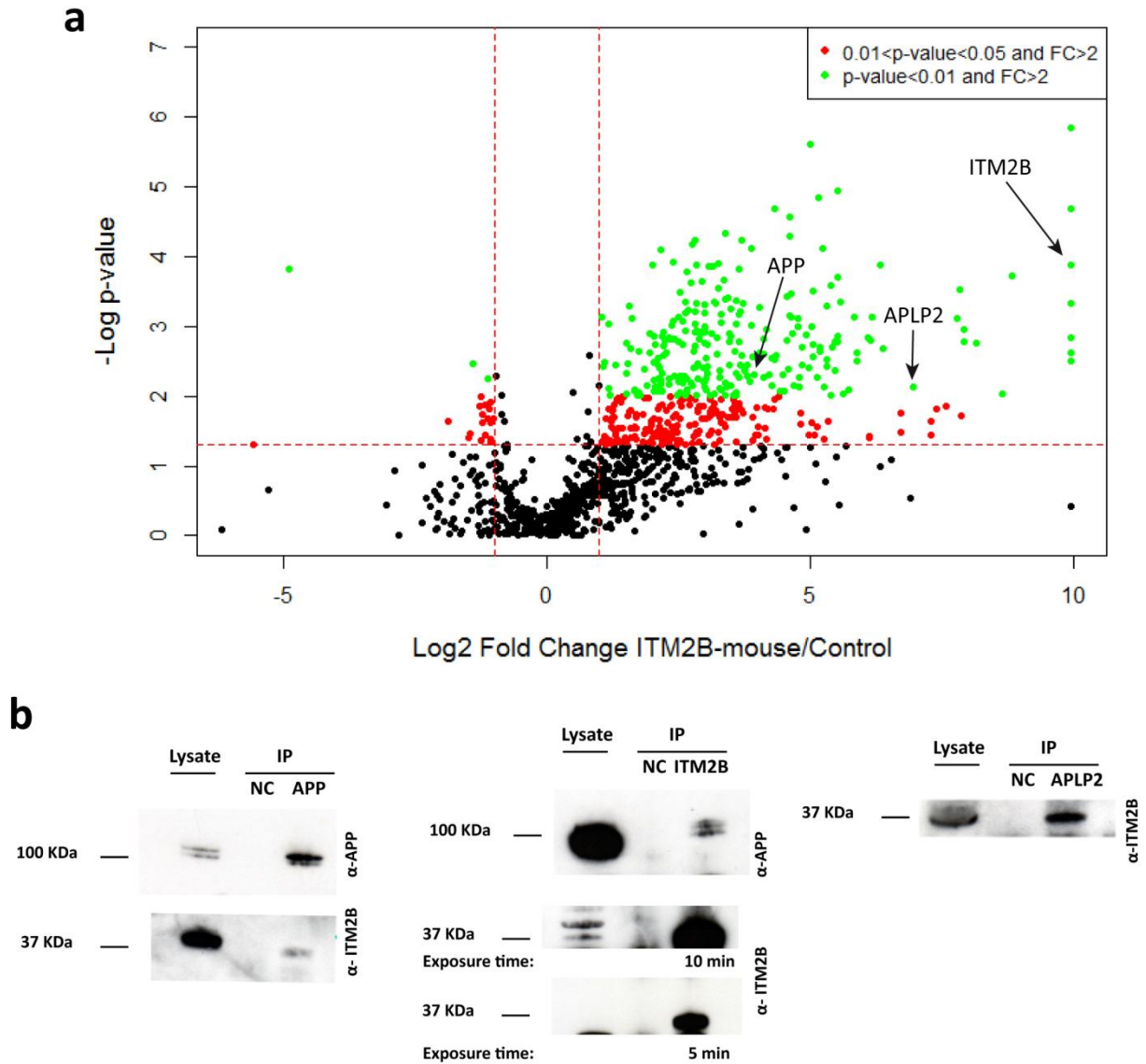


**Figure 3.** (a) Volcano plots with  $-\log_{10} p\text{-value}$  vs.  $\log_2 \text{FC}$  (mouse anti-ITM2B/unspecific antibody). Each point represents an identified protein. Proteins with significantly different abundances (in red  $0.01 < p\text{-value} < 0.05$ , in green  $p\text{-value} < 0.01$ ) are above the horizontal red line. On the right side are the proteins enriched with the mouse anti-ITM2B antibody with a  $\text{FC} > 2$  while on the left side are the proteins enriched with the unspecific antibody with  $\text{FC} > 2$ . (b) Co-immunoprecipitation of APP and APLP2 from the human retina. The IP for negative controls (NC) was performed using Dynabeads and mouse IgG (isotypic control). Full-length blots are presented in Supplementary Figure S4.

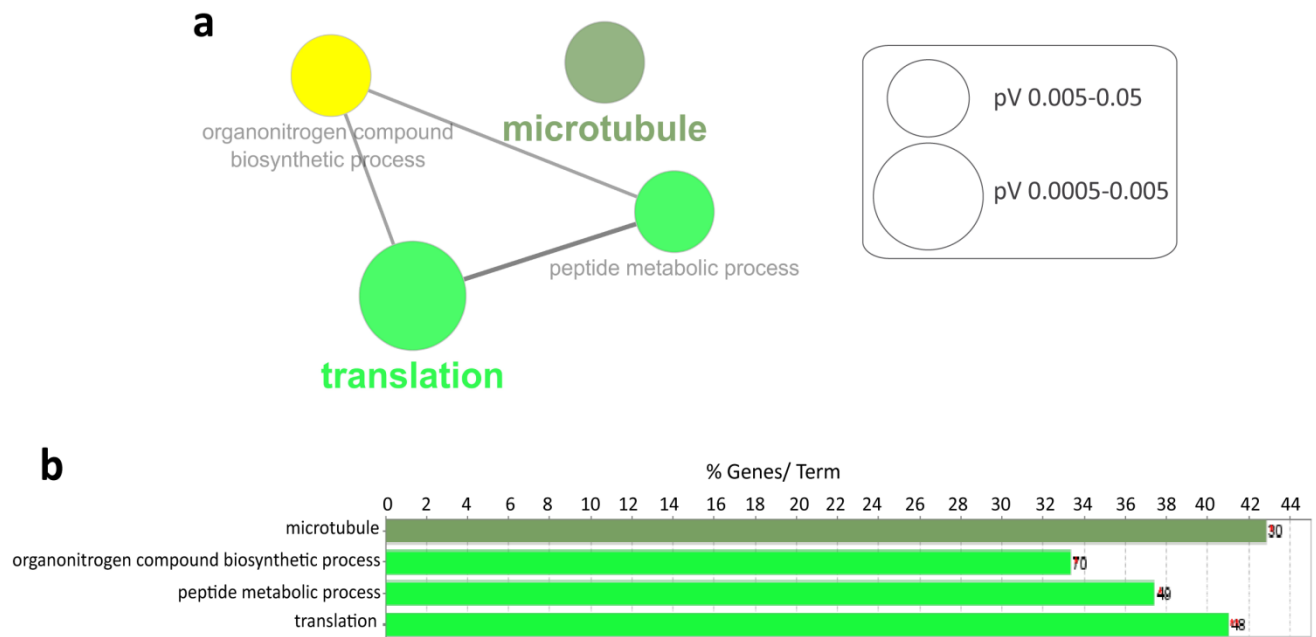


**Figure 4.** ITM2B interactome in the retina with the 254 proteins purified with the mouse antibody (FC>2 and p-value<0.01). (a) GO-term network analysis. (b) Functional clusters and pathways enriched within the ITM2B interactors. %Genes/Term corresponds to the proportion of genes enriched in the functional clusters. Bars with the same color belong to the same functional cluster.

### ***ITM2B interactome purified specifically with the rabbit anti-ITM2B antibody***

We then analyzed the cluster of proteins specifically purified by the rabbit anti-ITM2B antibody. We found a total of 615 enriched proteins ( $FC > 2$  and  $p\text{-value} < 0.05$ ). Among these proteins, 360 were identified with a  $p\text{-value} < 0.01$  and are shown in the top right panel of the volcano plot (Figure 5). We performed GO analysis on these proteins and the main biological pathways that we found are involved in mitochondrial processes, such as oxidative phosphorylation, electron transfer activity, cellular respiration, mitochondrial respiratory chain complex I assembly, mitochondrial ATP synthesis coupled electron transport, mitochondrial electron transport, NADH to ubiquinone and NADH dehydrogenase activity (Fig. 6, Supplementary Table S9). Furthermore, GO-CC annotations refer to mitochondria including mitochondrion, mitochondrial matrix, mitochondrial protein complex, and mitochondrial envelope (Figure 6, Table S9). These annotations have never been reported before and suggest a new unsuspected function of ITM2B associated with the mitochondria. Additionally, GO-CC terms revealed significantly enriched proteins in the myosin complex related to the cytoskeleton, distinct from the microtubule GO-BP annotation found with the mouse anti-ITM2B antibody (Fig 6, Supplementary Table S9).

Unlike the mouse anti-ITM2B antibody, the rabbit anti-ITM2B has never been used before for affinity-purification-MS experiments (AP-MS). However, the cluster of specific proteins purified with the rabbit anti-ITM2B antibody was also compared with the rat cerebral ITM2B interactome. Among the 150 proteins found in common, we observed proteins associated with the cytoskeleton organization including the adducing 1 (ADD1), the plectin (PLEC) and the vimentin (VIM) (Supplementary Table S10). This comparative analysis supports the reliability of the ITM2B interactome identified with the rabbit antibody.

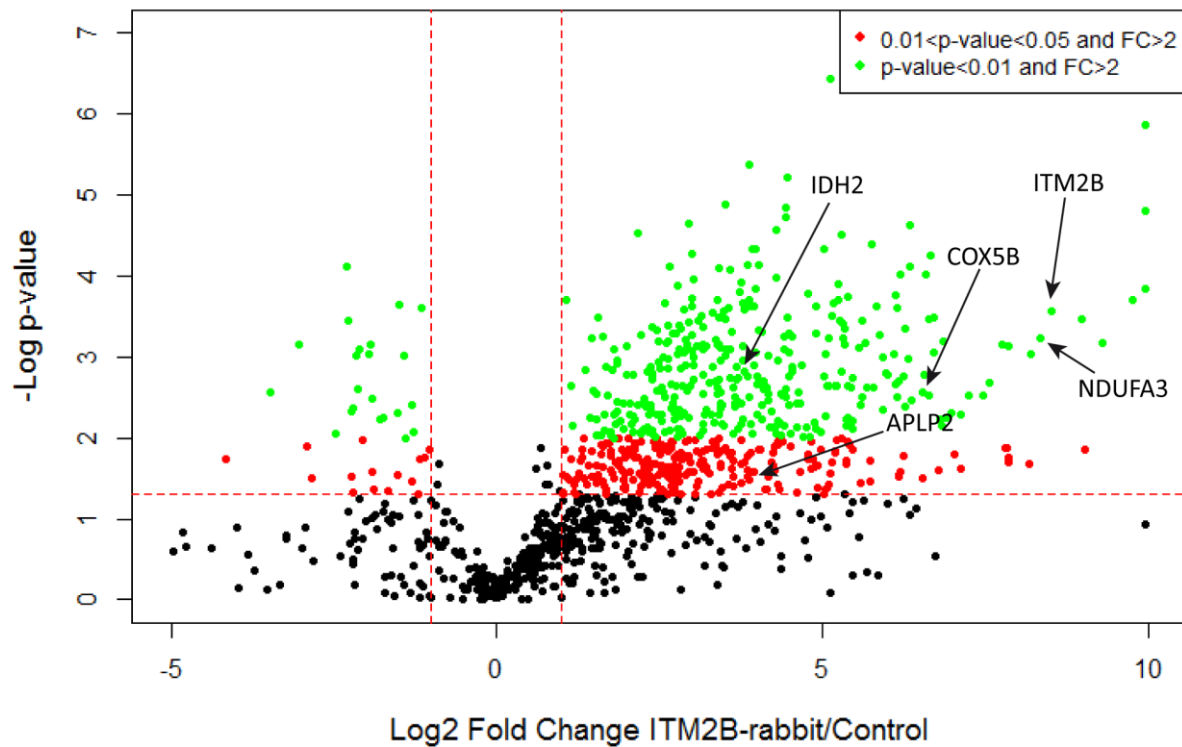


**Figure 5.** Volcano plots with  $-\log_{10}$  p-value vs.  $\log_2$  FC (rabbit anti-ITM2B/unspecific antibody). Each point represents an identified protein. Proteins with significantly different abundances (in red  $0.01 < p\text{-value} < 0.05$ , in green  $p\text{-value} < 0.01$ ) are above the horizontal red line. On the right side are the proteins enriched with the rabbit anti-ITM2B antibody with  $FC > 2$  while on the left side are the proteins enriched with the unspecific antibody with  $FC > 2$ .

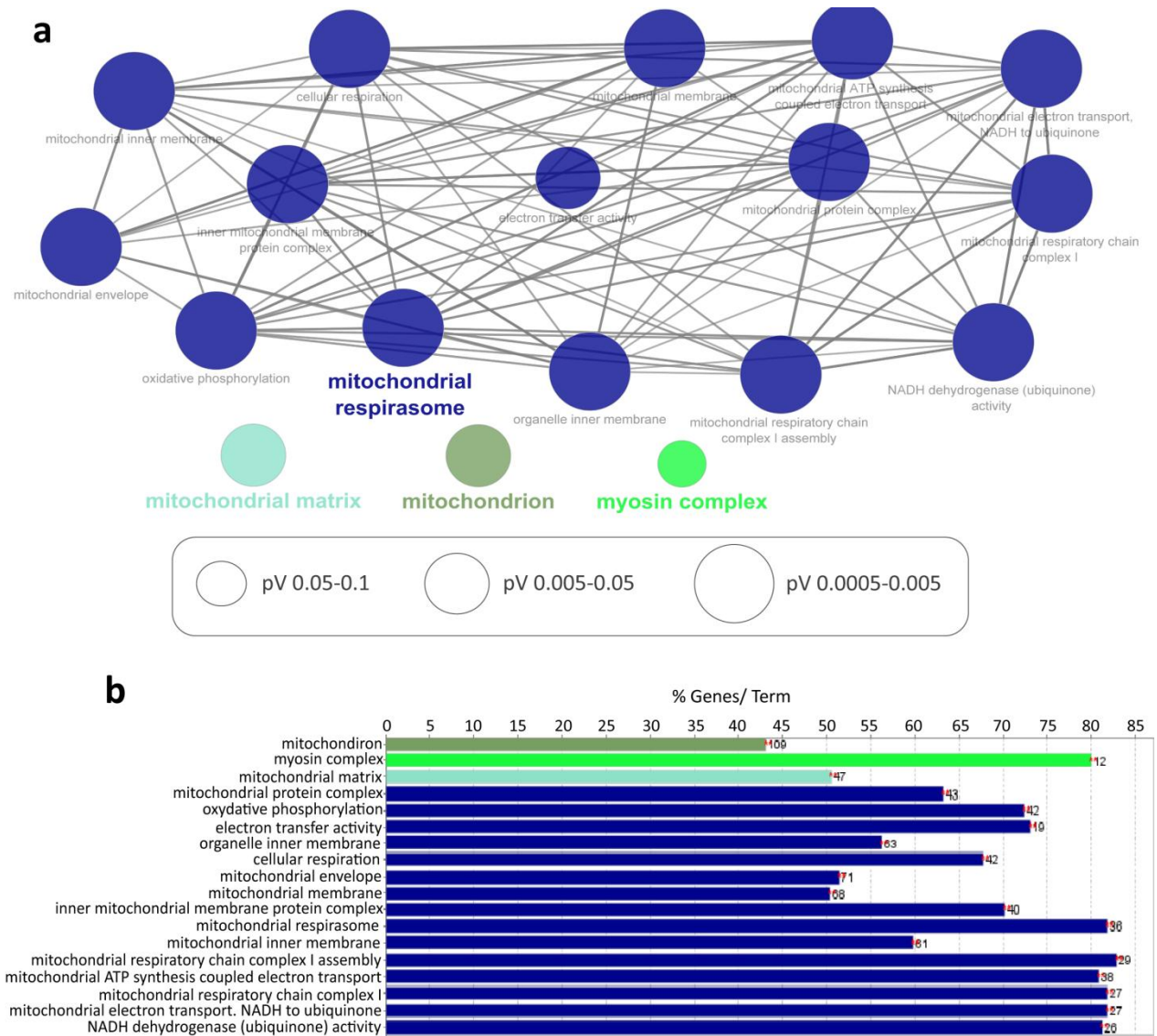


**Figure 6.** . ITM2B interactome in the retina with the 360 proteins purified with the rabbit antibody (FC>2 and p-value<0.01). (a) GO-term network analysis. (b) Functional clusters and pathways identified with enriched proteins. %Genes/Term corresponds to the proportion of genes enriched in the functional clusters. Bars with the same color belong to the same functional cluster.

### ***Different ITM2B transcripts are expressed in the human retina***

As described before, common interactors as well as distinct clusters of proteins were identified using the two antibodies. One possible explanation to these distinct clusters is given by the difference in the epitopes against which each antibody was raised (Fig. 1). Interestingly, in humans, a new ITM2B alternative transcript was recently annotated in Ensembl (ENST00000649266.1). This transcript harbors a translation initiation codon in exon 2 and is predicted to generate a shorter ITM2B protein (210 amino acids). For the rest of this manuscript, this isoform will be named short form whereas the canonical 266-amino acid protein will be the long form (transcript ENST00000647800.2). Based on the distinct epitopes used to generate the antibodies, the rabbit anti-ITM2B antibody would recognize both the short and the long forms whereas the mouse anti-ITM2B antibody would recognize only the long one. To check the expression of both transcripts in the human retina, we performed PCR experiments on human retinal cDNA using specific primers for each isoform followed by Sanger sequencing. Both *ITM2B* transcripts were identified in human retina (Fig. 7). We thus speculate that the different ITM2B interactomes isolated by each of the two antibodies might be the consequence of the unique ability of the rabbit anti-ITM2B antibody to immunopurify the long as well as the short isoform of ITM2B. Indeed, as shown in Figure 7, the rabbit anti-ITM2B antibody, while detecting the canonical 266-amino acid protein as the mouse antibody, also recognizes at least three other proteins in total human retinal proteic lysate.

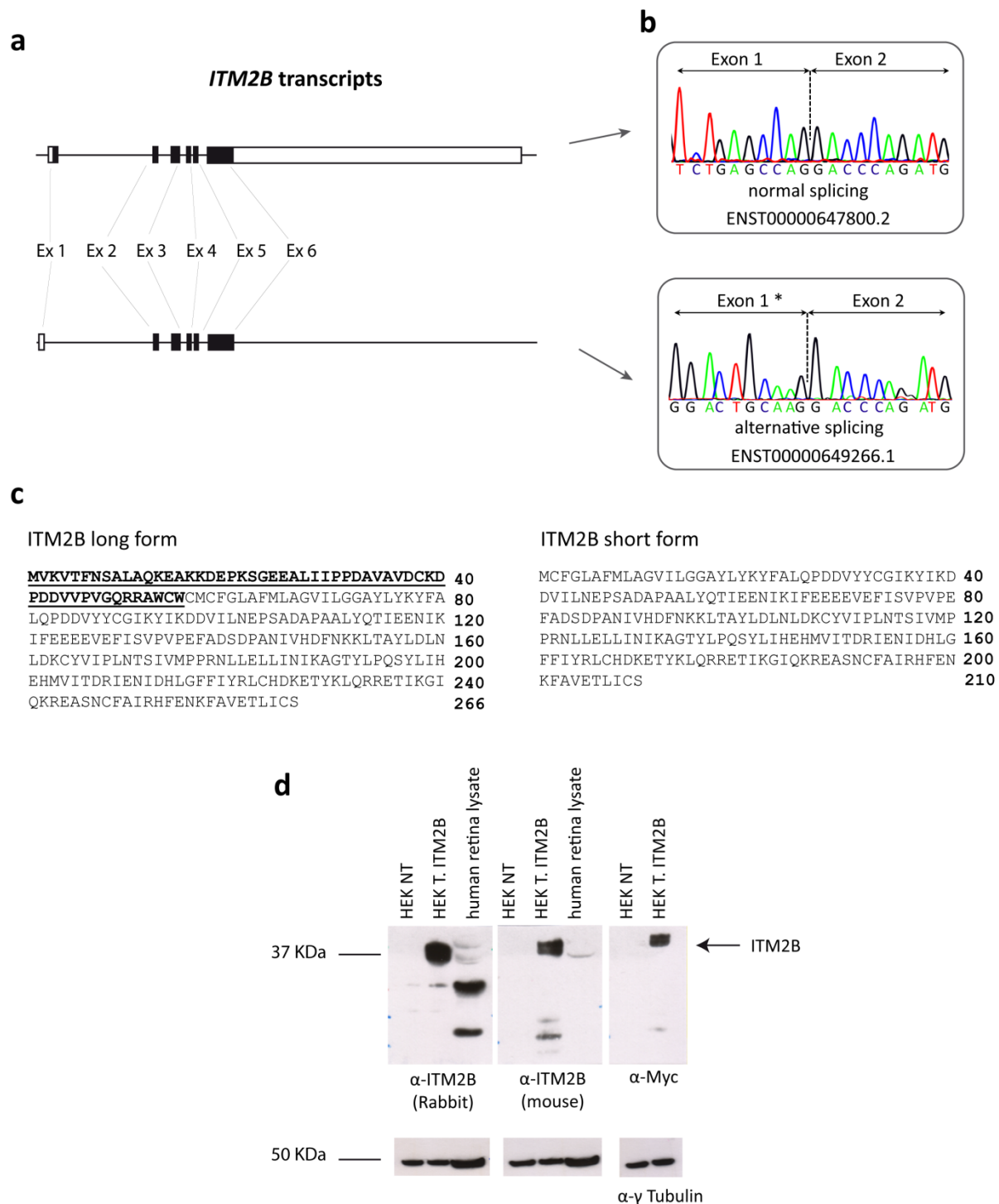


**Figure 7.** Identification of ITM2B alternative transcripts in the human retina. (a) Different ITM2B splice variants. (b) Identification of ITM2B alternative splicing in the human retina. (c) Amino acid sequence for ITM2B long isoform and predicted amino acid sequence for ITM2B short isoform. (d) Western blotting on HEK 293 cells and retinal protein extract, NT: non transfected, T.ITM2B: transfected with ITM2B, anti-  $\gamma$ -Tubulin is used as a loading control. Full-length blots are presented in Supplementary Figure S5.

## Discussion

ITM2B is an intriguing protein involved in different cerebral and retinal disorders. Three distinct autosomal dominant mutations in this gene are associated with two different early onset severe forms of dementia (FBD and FDD)<sup>5,8</sup> and with one peculiar retinal dystrophy<sup>3,10</sup>. Interestingly, there is no report of retinal degeneration in patients affected with ITM2B-related dementia but early onset cataract and a microangiopathy (FDD)<sup>23</sup> and reciprocally patients carrying the mutation leading to the retinal dystrophy do not develop dementia. These clinical data support the idea that ITM2B could have different roles in the brain and in the retina. All previous studies focused on ITM2B functions in the brain. More specifically, ITM2B is known to interact with APP and plays a role in A $\beta$  cerebral metabolism. In addition, ITM2B has been involved in GABA<sub>b</sub> and glutamate receptor signaling pathways and neurite outgrowth.<sup>15,17,18,24</sup> In this study we aimed at identifying the ITM2B interactome in the retina to unravel new biological pathways of ITM2B.

A total of 457 proteins were identified by quantitative proteomics of human retinal immunopurified ITM2B complexes (Supplementary Table S1). Among them, different retinal cell markers were identified suggesting that ITM2B acts ubiquitously in retinal tissue. Furthermore, our group previously showed that *ITM2B* is expressed in different retinal cells of the inner nuclear layer and in retinal ganglion cells<sup>3,10</sup>. The proteomic analysis identified 8 proteins highly expressed in photoreceptor cells and specific of these cells among the ITM2B interactors. Since photoreceptors are a major cell type in the retina, there may be a possibility that highly abundant photoreceptor proteins are being nonspecifically captured. On the other hand, this finding may also indicate that ITM2B is present in photoreceptor cells. This is supported by transcriptomic data which suggests the ubiquitous expression of ITM2B in human retina<sup>25</sup>.

Interestingly, APP and APLP2 previously reported to interact with ITM2B in the brain<sup>17,18</sup> were also found in our retinal dataset.<sup>17,18</sup> APLP2 is particularly interesting since its deletion in the mouse retina induces a phenotype similar to the retinal dystrophy observed in subjects carrying the ITM2B c.782A>C, p.Glu261Ala mutation notably with similar electroretinogram alterations.<sup>3,26</sup> Furthermore, more than 40% of the ITM2B interactors were also identified in the previous rat cerebral ITM2B interactome<sup>19</sup>. All these data indicate that ITM2B has overlapping but also specific functions in the brain and in the retina.

Gene Ontology analyses of the whole retinal interactome revealed several terms associated to cytoskeleton, translation and more surprisingly mitochondria. While the functional involvement of ITM2B in cytoskeleton and vesicular trafficking processes has already been demonstrated<sup>17-19</sup>, the link between ITM2B and mitochondrial functions has never been reported so far.

The human retinal ITM2B interactome was identified by combining the protein complexes isolated using two different anti-ITM2B antibodies. GO-BP analysis of the ITM2B interactome specifically purified with the mouse antibody revealed that beyond microtubule association, most functional pathways are linked to protein translation, organonitrogen compound biosynthetic process and peptide metabolism. These two last functional annotations were found neither in the whole dataset analysis nor in the previous published rat cerebral interactome. ITM2B has never been associated with metabolic processes and this result might suggest a new and specific role of ITM2B in the retina. We next analyzed the ITM2B specific interactome isolated with the rabbit antibody. Most of the GO-BP terms indicate that ITM2B might be involved in mitochondrial functions. While this annotation did not emerge in the previous published proteomic analysis, several mitochondrial proteins were also identified in the ITM2B interactome purified with the mouse antibody (Supplementary Fig. S3). This result strengthens the reliability of these new data. The putative role of ITM2B in the retinal mitochondrial homeostasis is of particular interest while studying pathogenic mechanisms associated with ITM2B mutations. Indeed, among other retinal abnormalities, affected subjects carrying the retinal dystrophy-related ITM2B missense mutation exhibit an early onset ganglion cell loss<sup>3,27</sup>. Mitochondrial dysfunction is a common mechanism underlying optic nerve diseases including primary ganglion cell disorders<sup>28</sup>. Therefore this new identified role of ITM2B in the mitochondria may shed light to the early ganglion cell loss in case of the missense mutation. To date we do not know if the link between ITM2B and the mitochondria is specific to the retina since the rabbit anti-ITM2B antibody was never used in previous proteomic studies. Therefore, we cannot rule out the possible involvement of ITM2B in cerebral mitochondrial homeostasis. Indeed, several mitochondrial proteins, such as the cytochrome c oxidase subunit 5B (cox5b), the cytochrome c oxidase subunit 7A-related protein (cox7a2l), the mitochondrial 2-oxoglutarate/malate carrier protein (slc25a11) and the phosphate carrier protein (slc25a3) have been reported in the rat cerebral cortex

ITM2B interactome<sup>19</sup> and were also identified in our dataset with both antibodies (Supplementary Fig. S3).

The diversity of GO-BP terms associated to the ITM2B interactomes may reflect a difference in the biochemical nature of the protein complexes immunopurified with each antibody. Indeed, ITM2B undergoes proteolytic cleavages and each antibody could preferentially bind to different fragments of the protein and purify distinct complexes. For instance, ITM2B is cleaved at amino acid 243 by a furin-like protease releasing Bri23, a 23-amino acid peptide. Bri23 is potentially immunopurified only by the rabbit antibody and could represent the mitochondrial-specific ITM2B bait. Alternatively, the two antibodies could purify different protein isoforms with different functions. Of note, a new human ITM2B alternative transcript was recently annotated. Its predicted coding sequence would generate a 210-amino acid protein which would not be recognized by the mouse antibody and could represent, as for Bri23, the mitochondrial-specific ITM2B bait. Interestingly, in a murine T cell line, a shorter form of ITM2B (ITM2Bs) involved in the mitochondria homeostasis was previously reported<sup>29</sup>. This shorter form corresponds to the one recently annotated in human and would have a pro-apoptotic effect by interacting with Bcl-2. Interestingly, Bcl-2-associated transcription factor 1 (BCLAF1) was also found in the human retinal ITM2B interactome. To date, we were able to show that the transcript of this shorter isoform is present in the human retina. Unfortunately it will be very difficult to study this isoform at the protein level due to the lack of specific antibody. Taken together, these data show that the use of antibodies directed against distinct epitopes of a protein may allow the identification of different protein interactors helping to unveil still unknown cellular functions.

Recently, our group generated induced pluripotent stem cell lines (iPSCs) from a subject affected with the ITM2B-related retinal dystrophy and his unaffected sibling<sup>30</sup>. Further investigations using retinal organoids derived from these iPSCs will help to better characterize the ITM2B interactome during the retinal cell development and the impact of the ITM2B-retinal dystrophy mutation on protein interactors. Moreover, it will give new insights into the role of ITM2B in mitochondrial homeostasis.

## **Material and Methods**

### ***Preparation of human retina samples***

Postmortem human ocular globes from donors were acquired from the School of Surgery (Ecole de Chirurgie, Assistance Publique Hôpitaux de Paris, Paris, France) and from the Laboratory of Anatomy, (Faculty of Medicine of St-Etienne, France). Experiments on postmortem human retina were performed according to the National regulations, as well as the guidelines of the Declaration of Helsinki. The protocol was approved by the IRBs of the School of Surgery and Faculty of Medicine of St-Etienne. The authorization for the use of human samples for research at the Institut de la Vision is registered as CODECOH DC-2015-2400.

One post-mortem human retina was obtained from an 85-year old man with no apparent history of ophthalmic disorder. The entire retina without the macula was put in liquid nitrogen and conserved in -80°C. Total proteins were extracted from the human retina using 1.8 ml lysis buffer (50 mM Tris pH 7.5 , 150 mM NaCl, 1% Triton 100 X) containing protease and phosphatase inhibitors (1% Phosphatase inhibitor cocktail 2 and 3 Sigma, 1% Protease inhibitor cocktail Merck, Darmstadt, Germany). The mix of lysis buffer and human retina was kept on ice during 30 min with vortexing every 10 min. After centrifugation 13 000 rpm 10 min, the supernatant containing the proteins was transferred to a new tube. All the proteins extracted were used for immunoprecipitation.

Extracted proteins from other normal post-mortem human retinas respectively obtained from a 97-year old man, an 84-year old woman and a 90-year old man were used in order to validate ITM2B interactions with its partners (see Interaction validation by immunoblotting).

### ***Immunoprecipitation***

We used Dynabead protein G (Thermo Fisher Scientific, Waltham, USA) to perform immunoprecipitation. We chose two different anti-ITM2B antibodies: one raised in rabbit (14.88 µg; PA531441 Thermo Fisher Scientific, Waltham, USA), the other raised in mouse (6 µg; SC-374362 Santa Cruz Biotechnology, Dallas, USA) and one mouse IgG (6 µg; G3A1, Cell Signaling Technology, Leiden, Netherlands) as a control. The procedure below was performed three independent times to obtain triplicates. A volume of 50 µl of beads solution were incubated with the 3 different antibodies and 600 µl PBS 1X 0.02 % Tween 20 for each antibody for 1.30 hour at 4°C under shaking. After one wash with 500 µl PBS 0.02 % Tween

20, 190  $\mu$ l of human retina protein extract were applied to the antibody-Dynabeads mix and incubated overnight at 4°C under shaking (for each condition). The protein immunoprecipitates were then washed twice with 500  $\mu$ l of PBS 0.02 % Tween 20 and one last time with 500  $\mu$ l of PBS 1X.

### ***LC-MS/MS analyses***

Proteins on beads from 3 experimental conditions (control, mouse antibody, rabbit antibody) were digested in biological triplicates overnight at 37°C by sequencing grade trypsin (12,5  $\mu$ g/ml ; Promega Madison, WI, USA) in 20  $\mu$ l of 25 mM  $\text{NH}_4\text{HCO}_3$ . Peptides were desalted using ZipTip  $\mu$ -C18 Pipette Tips (ThermoFisher Scientific). Peptide mixtures were analyzed by a Q-Exactive Plus coupled to a Nano-LC Proxeon 1000 (both from ThermoFisher Scientific). Peptides were separated by chromatography with the following parameters: Acclaim PepMap100 C18 pre-column (2 cm, 75  $\mu$ m i.d., 3  $\mu$ m, 100 Å), Pepmap-RSLC Proxeon C18 column (50 cm, 75  $\mu$ m i.d., 2  $\mu$ m, 100 Å), 300 nl/min flow rate, a 98 min gradient from 95 % solvent A (water, 0.1 % formic acid) to 35 % solvent B (100 % acetonitrile, 0.1% formic acid). Peptides were analyzed in the Orbitrap cell, at a resolution of 70,000, with a mass range of  $m/z$  375-1500. Fragments were obtained by higher-energy collisional dissociation (HCD) activation with a collisional energy of 28 %. MS/MS data were acquired in the Orbitrap cell in a Top20 mode, at a resolution of 17,500.

### ***Quantification of protein abundance variations***

Label-free relative quantification was performed in a Between-Subject Study Design using Progenesis-Qi software 4.1 (Nonlinear Dynamics Ltd, Newcastle, UK). For the identification step, all MS and MS/MS data were processed with the Proteome Discoverer software (ThermoFisher Scientific, version 2.2) coupled to the Mascot search engine (Matrix Science, version 2.5.1). The mass tolerance was set to 7 ppm for precursor ions and 0.05 Da for fragments. The maximum number of missed cleavages was limited to two for the trypsin protease. The following variable modifications were allowed: oxidation (Met), phosphorylation (Ser, Thr, and Tyr), acetylation (Protein N-term). The SwissProt database (02/2017) with the *Homo sapiens* taxonomy was used for the MS/MS identification step. Peptide identifications were validated using a 1% FDR (False Discovery Rate) threshold calculated with the Percolator algorithm. Protein identifications were validated if at least

two unique peptides per protein were identified. Protein abundance measurements were calculated according to the Hi-3 label-free quantification method. Protein variations were validated if their calculated p-values were under 0.01.

### ***In silico analyses and statistics***

The list of the 310 proteins highly expressed in the human retina was obtained from the Human Protein Atlas (available online: [www.proteinatlas.org](http://www.proteinatlas.org)). Venn Diagrams were generated using Venny online tool<sup>31</sup> (version 2.1). Hierarchical clustering and heatmap were performed by the MEV (Multiple Experiment Viewer software) software (version 4.9) with a Pearson correlation<sup>32</sup> and the average linkage clustering method. Ontology term enrichment and visualization were obtained using the ClueGo plug-in (Version 2.5.6)<sup>33</sup> within the Cytoscape software (version 3.7.1). The following parameters were used for the GO term enrichment analyses: (i) right sided hypergeometric test with a Benjamini-Hochberg correction with a minimum p-value threshold of 0.01, (ii) reference set with all identified proteins in concerned proteomic experiments with at least 2 unique identified peptides, (iii) GO tree interval from 4 to 8, (iv) GO term fusion activated, (v) GO terms process, function and component from EBI, UniProt and GOA. Volcano plots representing protein abundance variations between control condition and specific antibodies according to p-values were generated with R (version 3.6.1).

### ***Interaction validation by immunoblotting***

To validate the interaction between ITM2B and its partners we performed co-immunoprecipitation and westernblotting experiments using protein extracts from normal human retinas. Proteins from human retinal lysate and eluted from the co-immunoprecipitation assays were resolved on 4-12% gradient SDS-PAGE and transferred onto nitrocellulose membranes. Additional co-immunoprecipitation assays were performed using other antibodies (see Table 1). After transfer, membranes were incubated with blocking buffer PBST (PBS 1X, 0.05% Tween20) with 5% non-fat powder milk and incubated with the primary antibodies (Table 1) overnight at 4°C with shaking. The membranes were then washed three times for 10 minutes with PBST and incubated for 1 h at room temperature with horseradish peroxidase (HRP)-linked secondary antibodies (Table 1). Finally, the membranes were washed three times for 10 minutes with PBST and enhanced

chemiluminescence-based system (ECL Plus, ThermoFisher Scientific) was used for protein detection.

**Table 1:** List of primary and secondary antibodies

Antigen	Species	Dilution	Source
ITM2B	Mouse	IP : 6 µg ; WB: 1/500	Santa Cruz (sc-374362)
	Rabbit	WB : 1/1000	Thermo Fisher (PA531441)
APP	Rabbit	IP : 5 µg ; WB: 1/1000	Merk (HPA001462)
	Mouse	WB : 1/500	Merck (MAB348)
APLP2	Mouse	IP : 10 µg WB : 1/500	Merck (SAB1410669-100UG)
Myc	Mouse	WB : 1/500	Roche (11667149001)
γ Tubulin	Mouse	WB : 1/10 000	Merck (T6557)
IgG Isotype Control	Mouse	According to the specific antibody used	Cell Signaling (#5415)
IgG Isotype Control	Rabbit	According to the specific antibody used	Cell Signaling (#3900)
Mouse HRP	Donkey	WB : 1/20 000	Jackson ImmunoResearch (715-035-150)
Rabbit HRP	Donkey	WB : 1/20 000	Jackson ImmunoResearch (111-035-003)

*IP: immuno-precipitation, WB: westernblot, HR: horseradish peroxidase*

### ***HEK transfection***

The GripTite™ 293 MSR Cells (Thermo Fisher Scientific) were transfected with a ITM2B expression vector (pBudCE4\_1ITM2B plasmid<sup>3</sup>) using lipofectamine 2000 as transfection reagent (Invitrogen) following the standard manufacturer's protocol. The expression vector generates a fusion protein of ITM2B with a Myc-tag sequence placed after the ATG initial codon of the cDNA. The ITM2B sequence integrated in the plasmid corresponds to the human wild-type cDNA sequence (Refseq NM\_021999.4)

### ***PCR and Sanger sequencing***

Specific forward and reverse primers were designed for both forms (1shortF: 5'gagcttctccacattggctc3' and 1shortR: 5'caattgtctgtagagagcag3'; longF: 5'tgacgttcaactccgctctg3' and longR: 5'catcatctgggtccttgctg3'), (ENST00000649266.1). PCR was performed using Human Retina QUICK-Clone cDNA (TAKARA, Kusastu, Japan) and Q5<sup>®</sup> High-Fidelity 2X Master Mix (New England Biolabs, Ipswich, USA) (Supplementary Table S11 and Supplementary Table S12). Specificity of all PCR products was first verified by electrophoresis on 1% agarose gel and subsequently by Sanger sequencing. Purification of PCR products was done on agarose gel for the short form using PCR clean-up Gel extraction (Macherey-Nagel) following manufacturer's recommendations.

### ***Data availability***

The mass spectrometry proteomic data have been deposited to the ProteomeXchange Consortium via the PRIDE<sup>34</sup> partner repository with the dataset identifier PXD020088. All other data generated or analysed during this study are included in this published article (and its Supplementary Information files).

## References

- 1 Kim, S. H., Creemers, J. W., Chu, S., Thinakaran, G. & Sisodia, S. S. Proteolytic processing of familial British dementia-associated BRI variants: evidence for enhanced intracellular accumulation of amyloidogenic peptides. *The Journal of biological chemistry* **277**, 1872-1877, doi:10.1074/jbc.M108739200 (2002).
- 2 Kim, S. H. *et al.* Furin mediates enhanced production of fibrillogenic ABri peptides in familial British dementia. *Nature neuroscience* **2**, 984-988, doi:10.1038/14783 (1999).
- 3 Audo, I. *et al.* The familial dementia gene revisited: a missense mutation revealed by whole-exome sequencing identifies ITM2B as a candidate gene underlying a novel autosomal dominant retinal dystrophy in a large family. *Human molecular genetics* **23**, 491-501, doi:10.1093/hmg/ddt439 (2014).
- 4 Akiyama, H. *et al.* Expression of BRI, the normal precursor of the amyloid protein of familial British dementia, in human brain. *Acta neuropathologica* **107**, 53-58, doi:10.1007/s00401-003-0783-1 (2004).
- 5 Vidal, R. *et al.* A stop-codon mutation in the BRI gene associated with familial British dementia. *Nature* **399**, 776-781, doi:10.1038/21637 (1999).
- 6 Ghiso, J., Plant, G. T., Revesz, T., Wisniewski, T. & Frangione, B. Familial cerebral amyloid angiopathy (British type) with nonneuritic amyloid plaque formation may be due to a novel amyloid protein. *Journal of the neurological sciences* **129**, 74-75 (1995).
- 7 Plant, G. T., Revesz, T., Barnard, R. O., Harding, A. E. & Gautier-Smith, P. C. Familial cerebral amyloid angiopathy with nonneuritic amyloid plaque formation. *Brain : a journal of neurology* **113 ( Pt 3)**, 721-747, doi:10.1093/brain/113.3.721 (1990).
- 8 Vidal, R. *et al.* A decamer duplication in the 3' region of the BRI gene originates an amyloid peptide that is associated with dementia in a Danish kindred. *Proceedings of the National Academy of Sciences of the United States of America* **97**, 4920-4925, doi:10.1073/pnas.080076097 (2000).
- 9 Stromgren, E., Dalby, A., Dalby, M. A. & Ranheim, B. Cataract, deafness, cerebellar ataxia, psychosis and dementia--a new syndrome. *Acta neurologica Scandinavica* **46**, 261-262 (1970).
- 10 Nassisi, M. *et al.* Deep-Phenotyping and Further Insights in Itm2b-Related Retinal Dystrophy. *Retina*, doi:10.1097/IAE.0000000000002953 (2020).
- 11 Martin, L. *et al.* Regulated intramembrane proteolysis of Bri2 (Itm2b) by ADAM10 and SPPL2a/SPPL2b. *The Journal of biological chemistry* **283**, 1644-1652, doi:10.1074/jbc.M706661200 (2008).
- 12 Fotinopoulou, A. *et al.* BRI2 interacts with amyloid precursor protein (APP) and regulates amyloid beta (Abeta) production. *The Journal of biological chemistry* **280**, 30768-30772, doi:10.1074/jbc.C500231200 (2005).
- 13 Matsuda, S. *et al.* The familial dementia BRI2 gene binds the Alzheimer gene amyloid-beta precursor protein and inhibits amyloid-beta production. *The Journal of biological chemistry* **280**, 28912-28916, doi:10.1074/jbc.C500217200 (2005).
- 14 Kim, J. *et al.* BRI2 (ITM2b) inhibits Abeta deposition in vivo. *The Journal of neuroscience : the official journal of the Society for Neuroscience* **28**, 6030-6036, doi:10.1523/JNEUROSCI.0891-08.2008 (2008).
- 15 Choi, S. I., Vidal, R., Frangione, B. & Levy, E. Axonal transport of British and Danish amyloid peptides via secretory vesicles. *FASEB journal : official publication of the*

- Federation of American Societies for Experimental Biology* **18**, 373-375, doi:10.1096/fj.03-0730fje (2004).
- 16 Coulson, E. J., Paliga, K., Beyreuther, K. & Masters, C. L. What the evolution of the amyloid protein precursor supergene family tells us about its function. *Neurochemistry international* **36**, 175-184, doi:10.1016/s0197-0186(99)00125-4 (2000).
- 17 Schwenk, J. *et al.* Modular composition and dynamics of native GABAB receptors identified by high-resolution proteomics. *Nature neuroscience* **19**, 233-242, doi:10.1038/nn.4198 (2016).
- 18 Dinamarca, M. C. *et al.* Complex formation of APP with GABAB receptors links axonal trafficking to amyloidogenic processing. *Nature communications* **10**, 1331, doi:10.1038/s41467-019-09164-3 (2019).
- 19 Martins, F. *et al.* Identification and characterization of the BRI2 interactome in the brain. *Scientific reports* **8**, 3548, doi:10.1038/s41598-018-21453-3 (2018).
- 20 Jiang, S. M. *et al.* beta-III-Tubulin: a reliable marker for retinal ganglion cell labeling in experimental models of glaucoma. *International journal of ophthalmology* **8**, 643-652, doi:10.3980/j.issn.2222-3959.2015.04.01 (2015).
- 21 Ruiz-Ederra, J., Garcia, M., Hicks, D. & Vecino, E. Comparative study of the three neurofilament subunits within pig and human retinal ganglion cells. *Molecular vision* **10**, 83-92 (2004).
- 22 Blackshaw, S. *et al.* Genomic analysis of mouse retinal development. *PLoS biology* **2**, E247, doi:10.1371/journal.pbio.0020247 (2004).
- 23 Bek, T. Ocular changes in heredo-oto-ophthalmo-encephalopathy. *The British journal of ophthalmology* **84**, 1298-1302, doi:10.1136/bjo.84.11.1298 (2000).
- 24 Yao, W., Yin, T., Tambini, M. D. & D'Adamio, L. The Familial dementia gene ITM2b/BRI2 facilitates glutamate transmission via both presynaptic and postsynaptic mechanisms. *Scientific reports* **9**, 4862, doi:10.1038/s41598-019-41340-9 (2019).
- 25 Yan, W. *et al.* Cell Atlas of The Human Fovea and Peripheral Retina. *Scientific reports* **10**, 9802, doi:10.1038/s41598-020-66092-9 (2020).
- 26 Dinet, V. *et al.* Amyloid Precursor-Like Protein 2 deletion-induced retinal synaptopathy related to congenital stationary night blindness: structural, functional and molecular characteristics. *Molecular brain* **9**, 64, doi:10.1186/s13041-016-0245-z (2016).
- 27 Nassisi\*, M. *et al.* Deep-phenotyping and further insights in itm2b-related retinal dystrophy. *Retina in press* (2020).
- 28 Yu-Wai-Man, P. & Newman, N. J. Inherited eye-related disorders due to mitochondrial dysfunction. *Human molecular genetics* **26**, R12-R20, doi:10.1093/hmg/ddx182 (2017).
- 29 Fleischer, A., Ayllon, V., Dumoutier, L., Renauld, J. C. & Rebollo, A. Proapoptotic activity of ITM2B(s), a BH3-only protein induced upon IL-2-deprivation which interacts with Bcl-2. *Oncogene* **21**, 3181-3189, doi:10.1038/sj.onc.1205464 (2002).
- 30 Wohlschlegel, J. *et al.* Generation of human induced pluripotent stem cell lines from a patient with ITM2B-related retinal dystrophy and a non mutated brother. *Stem cell research* **41**, 101625, doi:10.1016/j.scr.2019.101625 (2019).
- 31 Oliveros, J. Venny. An interactive tool for comparing lists with Venn's diagrams. *Online Available at <https://bioinfogp.cnb.csic.es/tools/venny/index.html>* (2007-2015).

- 32 Howe, E. A., Sinha, R., Schlauch, D. & Quackenbush, J. RNA-Seq analysis in MeV. *Bioinformatics* **27**, 3209-3210, doi:10.1093/bioinformatics/btr490 (2011).
- 33 Bindea, G. *et al.* ClueGO: a Cytoscape plug-in to decipher functionally grouped gene ontology and pathway annotation networks. *Bioinformatics* **25**, 1091-1093, doi:10.1093/bioinformatics/btp101 (2009).
- 34 Perez-Riverol, Y. *et al.* The PRIDE database and related tools and resources in 2019: improving support for quantification data. *Nucleic acids research* **47**, D442-D450, doi:10.1093/nar/gky1106 (2019).

## **Acknowledgments**

The authors gratefully acknowledge the technical support of the Institut Jacques Monod, UMR7592 Université Paris Diderot/CNRS.

## **Author contributions**

JW: study design, data collection, data analysis, drafting of the manuscript

MA: data analysis, critical review of the manuscript

VF: technical support, critical review of the manuscript

CC: technical support, critical review of the manuscript

ZH: technical support, critical review of the manuscript

GT: technical support, critical review of the manuscript

CZ: funding sources, critical review of the manuscript

TL: data analysis, drafting of the manuscript, critical review of the manuscript

IA: study design, supervision, funding sources, critical review of the manuscript

## **Additional information**

**Competing interests:** The authors declare no competing interests.

**Funding/Support:** LABEX LIFESENSES [reference ANR-10-LABX-65] supported by French state funds managed by the Agence Nationale de la Recherche within the Investissements d'Avenir program [ANR-11-IDEX-0004-0]; IHU FOReSIGHT [ANR-18-IAHU-0001] supported by French state funds managed by the Agence Nationale de la Recherche within the Investissements d'Avenir program. UNADEV (Union Nationale des Aveugles et Déficients Visuels) in partnership with ITMO NNP / AVIESAN (alliance nationale pour les sciences de la vie et de la santé) for research in visual disorders. Retina France. J. Wohlschlegel was supported by Fondation de France (Berthe Fouassier-Maladies de l'Oeil, PhD fellowship). Support of the Institut Jacques Monod, UMR7592 Université Paris Diderot/CNRS, and the region Ile de France.

**Role of the Funder/Sponsor:** The funders had no role in the design and conduct of the study; collection, management, analysis, and interpretation of the data; preparation, review, or approval of the manuscript; and decision to submit the manuscript for publication.

## Supplementary data

**Supplementary Table S1.** Curated list representing 457 proteins identified by LC-MS/MS and purified with the mouse and/or the rabbit anti-ITM2B antibodies (FC >2 and p-value < 0.01).

Uniprot accession	Gene name	Protein name
P01023	<i>A2M</i>	alpha-2-macroglobulin
P61221	<i>ABCE1</i>	ATP binding cassette subfamily E member 1
Q8NFV4	<i>ABHD11</i>	abhydrolase domain containing 11
Q9NYB9	<i>ABI2</i>	abl interactor 2
Q9H845	<i>ACAD9</i>	acyl-CoA dehydrogenase family member 9
P11310	<i>ACADM</i>	acyl-CoA dehydrogenase medium chain
P45954	<i>ACADSB</i>	acyl-CoA dehydrogenase short/branched chain
Q9UKV3	<i>ACIN1</i>	apoptotic chromatin condensation inducer 1
P24666	<i>ACP1</i>	acid phosphatase 1
Q4G176	<i>ACSF3</i>	acyl-CoA synthetase family member 3
O95573	<i>ACSL3</i>	acyl-CoA synthetase long chain family member 3
P60709	<i>ACTB</i>	actin beta
P68032	<i>ACTC1</i>	actin alpha cardiac muscle 1
P61160	<i>ACTR2</i>	actin related protein 2
Q08828	<i>ADCY1</i>	adenylate cyclase 1
P35611	<i>ADD1</i>	adducin 1
Q9UEY8	<i>ADD3</i>	adducin 3
Q9UPQ3	<i>AGAP1</i>	ArfGAP with GTPase domain, ankyrin repeat and PH domain 1
P23526	<i>AHCY</i>	adenosylhomocysteinase
P27144	<i>AK4</i>	adenylate kinase 4
P02768	<i>ALB</i>	albumin
P49418	<i>AMPH</i>	amphiphysin
Q12955	<i>ANK3</i>	ankyrin 3
O95782	<i>AP2A1</i>	adaptor related protein complex 2 subunit alpha 1
Q96CW1	<i>AP2M1</i>	adaptor related protein complex 2 subunit mu 1
Q06481	<i>APLP2</i>	amyloid beta precursor like protein 2
P05067	<i>APP</i>	amyloid beta precursor protein
P55087	<i>AQP4</i>	aquaporin 4
Q8N6H7	<i>ARFGAP2</i>	ADP ribosylation factor GTPase activating protein 2
Q15052	<i>ARHGEF6</i>	Rac/Cdc42 guanine nucleotide exchange factor 6
P40616	<i>ARL1</i>	ADP ribosylation factor like GTPase 1
P36404	<i>ARL2</i>	ADP ribosylation factor like GTPase 2
Q9NVJ2	<i>ARL8B</i>	ADP ribosylation factor like GTPase 8B
P59998	<i>ARPC4</i>	actin related protein 2/3 complex subunit 4
Q8NBU5	<i>ATAD1</i>	ATPase family AAA domain containing 1
Q9NVI7	<i>ATAD3A</i>	ATPase family AAA domain containing 3A
Q676U5	<i>ATG16L1</i>	autophagy related 16 like 1
P13637	<i>ATP1A3</i>	ATPase Na <sup>+</sup> /K <sup>+</sup> transporting subunit alpha 3

---

Q01814	<i>ATP2B2</i>	ATPase plasma membrane Ca <sup>2+</sup> transporting 2
P23634	<i>ATP2B4</i>	ATPase plasma membrane Ca <sup>2+</sup> transporting 4
P25705	<i>ATP5F1A</i>	ATP synthase F1 subunit alpha
P06576	<i>ATP5F1B</i>	ATP synthase F1 subunit beta
P36542	<i>ATP5F1C</i>	ATP synthase F1 subunit gamma
P18859	<i>ATP5PF</i>	ATP synthase peripheral stalk subunit F6
Q93050	<i>ATP6VOA1</i>	ATPase H <sup>+</sup> transporting V0 subunit a1
P61421	<i>ATP6VOD1</i>	ATPase H <sup>+</sup> transporting V0 subunit d1
P38606	<i>ATP6V1A</i>	ATPase H <sup>+</sup> transporting V1 subunit A
P21281	<i>ATP6V1B2</i>	ATPase H <sup>+</sup> transporting V1 subunit B2
Q9Y5K8	<i>ATP6V1D</i>	ATPase H <sup>+</sup> transporting V1 subunit D
O43505	<i>B4GAT1</i>	beta-1,4-glucuronyltransferase 1
Q9UL15	<i>BAG5</i>	BAG cochaperone 5
P46379	<i>BAG6</i>	BAG cochaperone 6
Q9NYF8	<i>BCLAF1</i>	BCL2 associated transcription factor 1
P38398	<i>BRCA1</i>	BRCA1 DNA repair associated
P35613	<i>BSG</i>	basigin (Ok blood group)
P30042	<i>C21orf33</i>	ES1 protein homolog, mitochondrial
Q9Y426	<i>C2CD2</i>	C2 calcium dependent domain containing 2
P01024	<i>C3</i>	complement C3
P0C0L4	<i>C4B</i>	complement C4B (Chido blood group)
P01031	<i>C5</i>	complement C5
P27708	<i>CAD</i>	carbamoyl-phosphate synthetase 2, aspartate transcarbamylase, and dihydroorotase
O43852	<i>CALU</i>	calumenin
Q8IU85	<i>CAMK1D</i>	calcium/calmodulin dependent protein kinase ID
Q9UQM7	<i>CAMK2A</i>	calcium/calmodulin dependent protein kinase II alpha
Q13557	<i>CAMK2D</i>	calcium/calmodulin dependent protein kinase II delta
Q14444	<i>CAPRIN1</i>	cell cycle associated protein 1
P47755	<i>CAPZA2</i>	capping actin protein of muscle Z-line subunit alpha 2
P47756	<i>CAPZB</i>	capping actin protein of muscle Z-line subunit beta
Q8N163	<i>CCAR2</i>	cell cycle and apoptosis regulator 2
Q96NT0	<i>CCDC115</i>	coiled-coil domain containing 115
P0CW27	<i>CCDC166</i>	coiled-coil domain containing 166
P49368	<i>CCT3</i>	chaperonin containing TCP1 subunit 3
P50991	<i>CCT4</i>	chaperonin containing TCP1 subunit 4
P48643	<i>CCT5</i>	chaperonin containing TCP1 subunit 5
Q99832	<i>CCT7</i>	chaperonin containing TCP1 subunit 7
P50990	<i>CCT8</i>	chaperonin containing TCP1 subunit 8
P10966	<i>CD8B</i>	CD8b molecule
P19022	<i>CDH2</i>	cadherin 2
Q96JP9	<i>CDHR1</i>	cadherin related family member 1
Q00535	<i>CDK5</i>	cyclin dependent kinase 5
Q96JB5	<i>CDK5RAP3</i>	CDK5 regulatory subunit associated protein 3
Q07065	<i>CKAP4</i>	cytoskeleton associated protein 4
Q14008	<i>CKAP5</i>	cytoskeleton associated protein 5

---

---

O75122	<i>CLASP2</i>	cytoplasmic linker associated protein 2
P51797	<i>CLCN6</i>	chloride voltage-gated channel 6
P09496	<i>CLTA</i>	clathrin light chain A
Q5SYC1	<i>CLVS2</i>	clavesin 2
P09543	<i>CNP</i>	2',3'-cyclic nucleotide 3' phosphodiesterase
P53621	<i>COPA</i>	COPI coat complex subunit alpha
O14579	<i>COPE</i>	COPI coat complex subunit epsilon
Q9Y678	<i>COPG1</i>	COPI coat complex subunit gamma 1
Q96D53	<i>COQ8B</i>	coenzyme Q8B
Q9UQ03	<i>CORO2B</i>	coronin 2B
P00403	<i>COX2</i>	cytochrome c oxidase subunit II
P13073	<i>COX4I1</i>	cytochrome c oxidase subunit 4I1
P20674	<i>COX5A</i>	cytochrome c oxidase subunit 5A
P10606	<i>COX5B</i>	cytochrome c oxidase subunit 5B
P09669	<i>COX6C</i>	cytochrome c oxidase subunit 6C
P14406	<i>COX7A2</i>	cytochrome c oxidase subunit 7A2
O14548	<i>COX7A2L</i>	cytochrome c oxidase subunit 7A2 like
P00450	<i>CP</i>	ceruloplasmin
P14384	<i>CPM</i>	carboxypeptidase M
P15169	<i>CPN1</i>	carboxypeptidase N subunit 1
O95741	<i>CPNE6</i>	copine 6
Q9NQ79	<i>CRTAC1</i>	cartilage acidic protein 1
P02511	<i>CRYAB</i>	crystallin alpha B
P56545	<i>CTBP2</i>	C-terminal binding protein 2
P35222	<i>CTNNB1</i>	catenin beta 1
O60716	<i>CTNND1</i>	catenin delta 1
Q93034	<i>CUL5</i>	cullin 5
Q02318	<i>CYP27A1</i>	cytochrome P450 family 27 subfamily A member 1
P14868	<i>DARS1</i>	aspartyl-tRNA synthetase 1
Q8WVC6	<i>DKAKD</i>	dephospho-CoA kinase domain containing
O15075	<i>DCLK1</i>	doublecortin like kinase 1
Q8N568	<i>DCLK2</i>	doublecortin like kinase 2
Q16531	<i>DDB1</i>	damage specific DNA binding protein 1
Q92841	<i>DDX17</i>	DEAD-box helicase 17
O15523	<i>DDX3Y</i>	DEAD-box helicase 3 Y-linked
P17844	<i>DDX5</i>	DEAD-box helicase 5
P17661	<i>DES</i>	desmin
P52429	<i>DGKE</i>	diacylglycerol kinase epsilon
Q9Y485	<i>DMXL1</i>	Dmx like 1
P31689	<i>DNAJA1</i>	DnaJ heat shock protein family (Hsp40) member A1
Q96EY1	<i>DNAJA3</i>	DnaJ heat shock protein family (Hsp40) member A3
P25685	<i>DNAJB1</i>	DnaJ heat shock protein family (Hsp40) member B1
O00429	<i>DNM1L</i>	dynamamin 1 like
Q9C005	<i>DPY30</i>	dpy-30 histone methyltransferase complex regulatory subunit
Q14195	<i>DPYSL3</i>	dihydropyrimidinase like 3
Q14204	<i>DYNC1H1</i>	dynein cytoplasmic 1 heavy chain 1

---

---

Q96EX3	<i>DYNC2I2</i>	dynein 2 intermediate chain 2
Q9NP97	<i>DYNLRB1</i>	dynein light chain roadblock-type 1
Q5JPH6	<i>EARS2</i>	glutamyl-tRNA synthetase 2, mitochondrial
P68104	<i>EEF1A1</i>	eukaryotic translation elongation factor 1 alpha 1
Q05639	<i>EEF1A2</i>	eukaryotic translation elongation factor 1 alpha 2
P29692	<i>EEF1D</i>	eukaryotic translation elongation factor 1 delta
P26641	<i>EEF1G</i>	eukaryotic translation elongation factor 1 gamma
P13639	<i>EEF2</i>	eukaryotic translation elongation factor 2
P60842	<i>EIF4A1</i>	eukaryotic translation initiation factor 4A1
Q8N336	<i>ELMOD1</i>	ELMO domain containing 1
Q15369	<i>ELOC</i>	elongin C
P50402	<i>EMD</i>	emerin
Q9Y2J2	<i>EPB41L3</i>	erythrocyte membrane protein band 4.1 like 3
Q7L775	<i>EPM2AIP1</i>	EPM2A interacting protein 1
O75477	<i>ERLIN1</i>	ER lipid raft associated 1
O94905	<i>ERLIN2</i>	ER lipid raft associated 2
B1AK53	<i>ESPN</i>	espin
Q9BSJ8	<i>ESYT1</i>	extended synaptotagmin 1
P00734	<i>F2</i>	coagulation factor II, thrombin
P12259	<i>F5</i>	coagulation factor V
Q96CS3	<i>FAF2</i>	Fas associated factor family member 2
Q9NZB2	<i>FAM120A</i>	family with sequence similarity 120A
Q96EK7	<i>FAM120B</i>	family with sequence similarity 120B
P23142	<i>FBLN1</i>	fibulin 1
Q9UBX5	<i>FBLN5</i>	fibulin 5
Q9UK22	<i>FBXO2</i>	F-box protein 2
Q9NVF7	<i>FBXO28</i>	F-box protein 28
Q86UX7	<i>FERMT3</i>	fermitin family member 3
Q14318	<i>FKBP8</i>	FKBP prolyl isomerase 8
Q13045	<i>FLII</i>	FLII actin remodeling protein
Q14254	<i>FLOT2</i>	flotillin 2
Q9H479	<i>FN3K</i>	fructosamine 3 kinase
Q96CU9	<i>FOXRED1</i>	FAD dependent oxidoreductase domain containing 1
Q96I24	<i>FUBP3</i>	far upstream element binding protein 3
P51114	<i>FXR1</i>	FMR1 autosomal homolog 1
Q13283	<i>G3BP1</i>	G3BP stress granule assembly factor 1
O14976	<i>GAK</i>	cyclin G associated kinase
Q969S9	<i>GFM2</i>	GTP dependent ribosome recycling factor mitochondrial 2
O94925	<i>GLS</i>	glutaminase
P29992	<i>GNA11</i>	G protein subunit alpha 11
P04899	<i>GNAI2</i>	G protein subunit alpha i2
Q5JWF2	<i>GNAS</i>	GNAS complex locus
P19086	<i>GNAZ</i>	G protein subunit alpha z
Q08379	<i>GOLGA2</i>	golgin A2
Q08378	<i>GOLGA3</i>	golgin A3
O75715	<i>GPX5</i>	glutathione peroxidase 5

---

---

Q4V328	<i>GRIPAP1</i>	GRIP1 associated protein 1
P06396	<i>GSN</i>	gelsolin
Q8N442	<i>GUF1</i>	GUF1 homolog, GTPase
P13807	<i>GYS1</i>	glycogen synthase 1
Q92522	<i>H1-10</i>	H1.10 linker histone
P40939	<i>HADHA</i>	hydroxyacyl-CoA dehydrogenase trifunctional multienzyme complex subunit alpha
P55084	<i>HADHB</i>	hydroxyacyl-CoA dehydrogenase trifunctional multienzyme complex subunit beta
O60741	<i>HCN1</i>	hyperpolarization activated cyclic nucleotide gated potassium channel 1
Q00341	<i>HDLBP</i>	high density lipoprotein binding protein
P52789	<i>HK2</i>	hexokinase 2
Q2TB90	<i>HKDC1</i>	hexokinase domain containing 1
P01892	<i>HLA-A</i>	HLA class I histocompatibility antigen, A-2 alpha chain
P01889	<i>HLA-B</i>	major histocompatibility complex, class I, B
P31943	<i>HNRNPH1</i>	heterogeneous nuclear ribonucleoprotein H1
Q9BUJ2	<i>HNRNPUL1</i>	heterogeneous nuclear ribonucleoprotein U like 1
Q53GQ0	<i>HSD17B12</i>	hydroxysteroid 17-beta dehydrogenase 12
O43301	<i>HSPA12A</i>	heat shock protein family A (Hsp70) member 12A
P54652	<i>HSPA2</i>	heat shock protein family A (Hsp70) member 2
P11142	<i>HSPA8</i>	heat shock protein family A (Hsp70) member 8
P10809	<i>HSPD1</i>	heat shock protein family D (Hsp60) member 1
Q9Y4L1	<i>HYOU1</i>	hypoxia up-regulated 1
Q9NSE4	<i>IARS2</i>	isoleucyl-tRNA synthetase 2, mitochondrial
O43837	<i>IDH3B</i>	isocitrate dehydrogenase (NAD(+)) 3 non-catalytic subunit beta
Q96ID5	<i>IGSF21</i>	immunoglobulin superfamily member 21
A1L0T0	<i>ILVBL</i>	ilvB acetolactate synthase like
Q16891	<i>IMMT</i>	inner membrane mitochondrial protein
P20839	<i>IMPDH1</i>	inosine monophosphate dehydrogenase 1
Q16352	<i>INA</i>	internexin neuronal intermediate filament protein alpha
Q6DN90	<i>IQSEC1</i>	IQ motif and Sec7 domain ArfGEF 1
Q06033	<i>ITIH3</i>	inter-alpha-trypsin inhibitor heavy chain 3
Q9Y287	<i>ITM2B</i>	integral membrane protein 2B
Q9NQX7	<i>ITM2C</i>	integral membrane protein 2C
Q14721	<i>KCNB1</i>	potassium voltage-gated channel subfamily B member 1
Q6ZWB6	<i>KCTD8</i>	potassium channel tetramerization domain containing 8
Q9ULH0	<i>KIDINS220</i>	kinase D interacting substrate 220
Q7Z4S6	<i>KIF21A</i>	kinesin family member 21A
O14686	<i>KMT2D</i>	lysine methyltransferase 2D
P32004	<i>L1CAM</i>	L1 cell adhesion molecule
A8MY62	<i>LACTBL1</i>	Putative beta-lactamase-like 1
Q9P2J5	<i>LARS1</i>	leucyl-tRNA synthetase 1
Q9BXB1	<i>LGR4</i>	leucine rich repeat containing G protein-coupled receptor 4
P49916	<i>LIG3</i>	DNA ligase 3
P49257	<i>LMAN1</i>	lectin, mannose binding 1

---

---

Q07954	<i>LRP1</i>	LDL receptor related protein 1
Q13449	<i>LSAMP</i>	limbic system associated membrane protein
Q3MHD2	<i>LSM12</i>	LSM12 homolog
O95372	<i>LYPLA2</i>	lysophospholipase 2
Q8WYG6	<i>MADD</i>	MAP kinase activating death domain
P46821	<i>MAP1B</i>	microtubule associated protein 1B
Q96JE9	<i>MAP6</i>	microtubule associated protein 6
Q14244	<i>MAP7</i>	microtubule associated protein 7
Q15555	<i>MAPRE2</i>	microtubule associated protein RP/EB family member 2
P56192	<i>MARS1</i>	methionyl-tRNA synthetase 1
Q96N66	<i>MBOAT7</i>	membrane bound O-acyltransferase domain containing 7
C9JLW8	<i>MCRIP1</i>	MAPK regulated corepressor interacting protein 1
P55083	<i>MFAP4</i>	microfibril associated protein 4
Q9GZY8	<i>MFF</i>	mitochondrial fission factor
Q15773	<i>MLF2</i>	myeloid leukemia factor 2
Q13015	<i>MLLT11</i>	MLLT11 transcription factor 7 cofactor
Q13724	<i>MOGS</i>	mannosyl-oligosaccharide glucosidase
Q14168	<i>MPP2</i>	membrane palmitoylated protein 2
O43347	<i>MSI1</i>	musashi RNA binding protein 1
Q96DH6	<i>MSI2</i>	musashi RNA binding protein 2
		methylenetetrahydrofolate dehydrogenase, cyclohydrolase and
P11586	<i>MTHFD1</i>	formyltetrahydrofolate synthetase 1
O75592	<i>MYCBP2</i>	MYC binding protein 2
P35580	<i>MYH10</i>	myosin heavy chain 10
O14950	<i>MYL12A</i>	myosin light chain 12A
P12829	<i>MYL4</i>	myosin light chain 4
P60660	<i>MYL6</i>	myosin light chain 6
P24844	<i>MYL9</i>	myosin light chain 9
Q92614	<i>MYO18A</i>	myosin XVIII A
O00159	<i>MYO1C</i>	myosin IC
Q9Y411	<i>MYO5A</i>	myosin VA
Q9ULV0	<i>MYO5B</i>	myosin VB
Q13402	<i>MYO7A</i>	myosin VIIA
P43490	<i>NAMPT</i>	nicotinamide phosphoribosyltransferase
P13591	<i>NCAM1</i>	neural cell adhesion molecule 1
P19338	<i>NCL</i>	nucleolin
O95299	<i>NDUFA10</i>	NADH:ubiquinone oxidoreductase subunit A10
Q9UI09	<i>NDUFA12</i>	NADH:ubiquinone oxidoreductase subunit A12
Q9P0J0	<i>NDUFA13</i>	NADH:ubiquinone oxidoreductase subunit A13
O43678	<i>NDUFA2</i>	NADH:ubiquinone oxidoreductase subunit A2
O95167	<i>NDUFA3</i>	NADH:ubiquinone oxidoreductase subunit A3
Q16718	<i>NDUFA5</i>	NADH:ubiquinone oxidoreductase subunit A5
P56556	<i>NDUFA6</i>	NADH:ubiquinone oxidoreductase subunit A6
O95182	<i>NDUFA7</i>	NADH:ubiquinone oxidoreductase subunit A7
Q16795	<i>NDUFA9</i>	NADH:ubiquinone oxidoreductase subunit A9
O96000	<i>NDUFB10</i>	NADH:ubiquinone oxidoreductase subunit B10

---

---

O95168	<i>NDUFB4</i>	NADH:ubiquinone oxidoreductase subunit B4
O43674	<i>NDUFB5</i>	NADH:ubiquinone oxidoreductase subunit B5
O95139	<i>NDUFB6</i>	NADH:ubiquinone oxidoreductase subunit B6
O95169	<i>NDUFB8</i>	NADH:ubiquinone oxidoreductase subunit B8
Q9Y6M9	<i>NDUFB9</i>	NADH:ubiquinone oxidoreductase subunit B9
P28331	<i>NDUFS1</i>	NADH:ubiquinone oxidoreductase core subunit S1
O75306	<i>NDUFS2</i>	NADH:ubiquinone oxidoreductase core subunit S2
O75489	<i>NDUFS3</i>	NADH:ubiquinone oxidoreductase core subunit S3
O43181	<i>NDUFS4</i>	NADH:ubiquinone oxidoreductase subunit S4
O43920	<i>NDUFS5</i>	NADH:ubiquinone oxidoreductase subunit S5
O75380	<i>NDUFS6</i>	NADH:ubiquinone oxidoreductase subunit S6
O75251	<i>NDUFS7</i>	NADH:ubiquinone oxidoreductase core subunit S7
O00217	<i>NDUFS8</i>	NADH:ubiquinone oxidoreductase core subunit S8
P49821	<i>NDUFV1</i>	NADH:ubiquinone oxidoreductase core subunit V1
P19404	<i>NDUFV2</i>	NADH:ubiquinone oxidoreductase core subunit V2
P56181	<i>NDUFV3</i>	NADH:ubiquinone oxidoreductase subunit V3
P12036	<i>NEFH</i>	neurofilament heavy
P07196	<i>NEFL</i>	neurofilament light
P07197	<i>NEFM</i>	neurofilament medium
P08651	<i>NFIC</i>	nuclear factor I C
Q9Y2X3	<i>NOP58</i>	NOP58 ribonucleoprotein
P46459	<i>NSF</i>	N-ethylmaleimide sensitive factor, vesicle fusing ATPase
Q8TB37	<i>NUBPL</i>	nucleotide binding protein like
Q9BRJ7	<i>NUDT16L1</i>	nudix hydrolase 16 like 1
P04181	<i>OAT</i>	ornithine aminotransferase
Q14982	<i>OPCML</i>	opioid binding protein/cell adhesion molecule like
Q9BZF1	<i>OSBPL8</i>	oxysterol binding protein like 8
Q9UQ80	<i>PA2G4</i>	proliferation-associated 2G4
P11940	<i>PABPC1</i>	poly(A) binding protein cytoplasmic 1
Q13310	<i>PABPC4</i>	poly(A) binding protein cytoplasmic 4
Q6VY07	<i>PACS1</i>	phosphofurin acidic cluster sorting protein 1
Q9Y2J8	<i>PADI2</i>	peptidyl arginine deiminase 2
O75781	<i>PALM</i>	paralemmin
Q96AQ6	<i>PBXIP1</i>	PBX homeobox interacting protein 1
P11498	<i>PC</i>	pyruvate carboxylase
Q15365	<i>PCBP1</i>	poly(rC) binding protein 1
O95206	<i>PCDH8</i>	protocadherin 8
Q9Y5F8	<i>PCDHGB7</i>	protocadherin gamma subfamily B, 7
P20941	<i>PDC</i>	phosducin
P16499	<i>PDE6A</i>	phosphodiesterase 6A
P11177	<i>PDHB</i>	pyruvate dehydrogenase E1 subunit beta
P17858	<i>PFKL</i>	phosphofructokinase, liver type
Q01813	<i>PFKP</i>	phosphofructokinase, platelet
P07737	<i>PFN1</i>	profilin 1
O00264	<i>PGRMC1</i>	progesterone receptor membrane component 1
P42356	<i>PI4KA</i>	phosphatidylinositol 4-kinase alpha

---

---

P78356	<i>PIP4K2B</i>	phosphatidylinositol-5-phosphate 4-kinase type 2 beta
Q99959	<i>PKP2</i>	plakophilin 2
Q99569	<i>PKP4</i>	plakophilin 4
Q15149	<i>PLEC</i>	plectin
P24928	<i>POLR2A</i>	RNA polymerase II subunit A
P50336	<i>PPOX</i>	protoporphyrinogen oxidase
Q6ZSY5	<i>PPP1R3F</i>	protein phosphatase 1 regulatory subunit 3F
P62714	<i>PPP2CB</i>	protein phosphatase 2 catalytic subunit beta
Q66LE6	<i>PPP2R2D</i>	protein phosphatase 2 regulatory subunit Bdelta
Q9HCU5	<i>PREB</i>	prolactin regulatory element binding
P51888	<i>PRELP</i>	proline and arginine rich end leucine rich repeat protein
P22694	<i>PRKACB</i>	protein kinase cAMP-activated catalytic subunit beta
P60891	<i>PRPS1</i>	phosphoribosyl pyrophosphate synthetase 1
P28066	<i>PSMA5</i>	proteasome 20S subunit alpha 5
P62191	<i>PSMC1</i>	proteasome 26S subunit, ATPase 1
P35998	<i>PSMC2</i>	proteasome 26S subunit, ATPase 2
P17980	<i>PSMC3</i>	proteasome 26S subunit, ATPase 3
P62333	<i>PSMC6</i>	proteasome 26S subunit, ATPase 6
Q99460	<i>PSMD1</i>	proteasome 26S subunit, non-ATPase 1
P10586	<i>PTPRF</i>	protein tyrosine phosphatase receptor type F
Q13332	<i>PTPRS</i>	protein tyrosine phosphatase receptor type S
Q96C36	<i>PYCR2</i>	pyrroline-5-carboxylate reductase 2
P11216	<i>PYGB</i>	glycogen phosphorylase B
P47897	<i>QARS1</i>	glutaminyl-tRNA synthetase 1
P63244	<i>RACK1</i>	receptor for activated C kinase 1
P62826	<i>RAN</i>	RAN, member RAS oncogene family
P54136	<i>RARS1</i>	arginyl-tRNA synthetase 1
Q15291	<i>RBBP5</i>	RB binding protein 5, histone lysine methyltransferase complex subunit
Q15293	<i>RCN1</i>	reticulocalbin 1
Q14257	<i>RCN2</i>	reticulocalbin 2
Q96NR8	<i>RDH12</i>	retinol dehydrogenase 12
Q8IXI1	<i>RHOT2</i>	ras homolog family member T2
Q6R327	<i>RICTOR</i>	RPTOR independent companion of MTOR complex 2
P62906	<i>RPL10A</i>	ribosomal protein L10a
P30050	<i>RPL12</i>	ribosomal protein L12
P40429	<i>RPL13A</i>	ribosomal protein L13a
P18621	<i>RPL17</i>	ribosomal protein L17
Q07020	<i>RPL18</i>	ribosomal protein L18
P84098	<i>RPL19</i>	ribosomal protein L19
P62829	<i>RPL23</i>	ribosomal protein L23
P61254	<i>RPL26</i>	ribosomal protein L26
P61353	<i>RPL27</i>	ribosomal protein L27
P46776	<i>RPL27A</i>	ribosomal protein L27a
P62888	<i>RPL30</i>	ribosomal protein L30
P36578	<i>RPL4</i>	ribosomal protein L4

---

---

P62424	<i>RPL7A</i>	ribosomal protein L7a
P05388	<i>RPLP0</i>	ribosomal protein lateral stalk subunit P0
P04843	<i>RPN1</i>	ribophorin I
P62277	<i>RPS13</i>	ribosomal protein S13
P62263	<i>RPS14</i>	ribosomal protein S14
P62249	<i>RPS16</i>	ribosomal protein S16
P62269	<i>RPS18</i>	ribosomal protein S18
P39019	<i>RPS19</i>	ribosomal protein S19
P15880	<i>RPS2</i>	ribosomal protein S2
P60866	<i>RPS20</i>	ribosomal protein S20
P62847	<i>RPS24</i>	ribosomal protein S24
P62979	<i>RPS27A</i>	ribosomal protein S27a
P62701	<i>RPS4X</i>	ribosomal protein S4 X-linked
Q8TD47	<i>RPS4Y2</i>	ribosomal protein S4 Y-linked 2
P62241	<i>RPS8</i>	ribosomal protein S8
P08865	<i>RPSA</i>	ribosomal protein SA
O00442	<i>RTCA</i>	RNA 3'-terminal phosphate cyclase
Q9Y310	<i>RTCB</i>	RNA 2',3'-cyclic phosphate and 5'-OH ligase
Q7L099	<i>RUFY3</i>	RUN and FYVE domain containing 3
Q9Y265	<i>RUVBL1</i>	RuvB like AAA ATPase 1
Q01118	<i>SCN7A</i>	sodium voltage-gated channel alpha subunit 7
P31040	<i>SDHA</i>	succinate dehydrogenase complex flavoprotein subunit A
P55735	<i>SEC13</i>	SEC13 homolog, nuclear pore and COPII coat complex component
O15027	<i>SEC16A</i>	SEC16 homolog A, endoplasmic reticulum export factor
O75396	<i>SEC22B</i>	SEC22 homolog B, vesicle trafficking protein
Q15393	<i>SF3B3</i>	splicing factor 3b subunit 3
Q9NR46	<i>SH3GLB2</i>	SH3 domain containing GRB2 like, endophilin B2
P55011	<i>SLC12A2</i>	solute carrier family 12 member 2
Q9H2X9	<i>SLC12A5</i>	solute carrier family 12 member 5
P53985	<i>SLC16A1</i>	solute carrier family 16 member 1
Q02978	<i>SLC25A11</i>	solute carrier family 25 member 11
O75746	<i>SLC25A12</i>	solute carrier family 25 member 12
Q00325	<i>SLC25A3</i>	solute carrier family 25 member 3
P12236	<i>SLC25A6</i>	solute carrier family 25 member 6
Q9Y2P4	<i>SLC27A6</i>	solute carrier family 27 member 6
P11166	<i>SLC2A1</i>	solute carrier family 2 member 1
Q6U841	<i>SLC4A10</i>	solute carrier family 4 member 10
Q2Y0W8	<i>SLC4A8</i>	solute carrier family 4 member 8
Q13884	<i>SNTB1</i>	syntrophin beta 1
Q13425	<i>SNTB2</i>	syntrophin beta 2
Q96PQ0	<i>SORCS2</i>	sortilin related VPS10 domain containing receptor 2
Q07889	<i>SOS1</i>	SOS Ras/Rac guanine nucleotide exchange factor 1
Q01082	<i>SPTBN1</i>	spectrin beta, non-erythrocytic 1
Q9C0H9	<i>SRCIN1</i>	SRC kinase signaling inhibitor 1
P19623	<i>SRM</i>	spermidine synthase
P37108	<i>SRP14</i>	signal recognition particle 14

---

---

P49458	<i>SRP9</i>	signal recognition particle 9
Q9UJZ1	<i>STOML2</i>	stomatin like 2
Q9UNE7	<i>STUB1</i>	STIP1 homology and U-box containing protein 1
P61764	<i>STXBP1</i>	syntaxin binding protein 1
Q9P2R7	<i>SUCLA2</i>	succinate-CoA ligase ADP-forming subunit beta
P53597	<i>SUCLG1</i>	succinate-CoA ligase GDP/ADP-forming subunit alpha
Q8IX01	<i>SUGP2</i>	SURP and G-patch domain containing 2
O15260	<i>SURF4</i>	surfeit 4
O60506	<i>SYNCRIP</i>	synaptotagmin binding cytoplasmic RNA interacting protein
O15061	<i>SYNM</i>	synemin
Q9BT88	<i>SYT11</i>	synaptotagmin 11
P26639	<i>TARS1</i>	threonyl-tRNA synthetase 1
A2RTX5	<i>TARS3</i>	threonyl-tRNA synthetase 3
P17987	<i>TCP1</i>	t-complex 1
Q9NZ01	<i>TECR</i>	trans-2,3-enoyl-CoA reductase
Q8IYQ7	<i>THNSL1</i>	threonine synthase like 1
Q9UKI8	<i>TLK1</i>	tousled like kinase 1
P49755	<i>TMED10</i>	transmembrane p24 trafficking protein 10
Q24JP5	<i>TMEM132A</i>	transmembrane protein 132A
Q8N511	<i>TMEM199</i>	transmembrane protein 199
Q96Q45	<i>TMEM237</i>	transmembrane protein 237
Q9NZR1	<i>TMOD2</i>	tropomodulin 2
Q92973	<i>TNPO1</i>	transportin 1
O60784	<i>TOM1</i>	target of myb1 membrane trafficking protein
Q6ZVM7	<i>TOM1L2</i>	target of myb1 like 2 membrane trafficking protein
Q9Y5R8	<i>TRAPPC1</i>	trafficking protein particle complex 1
Q9UL33	<i>TRAPPC2L</i>	trafficking protein particle complex 2 like
P14373	<i>TRIM27</i>	tripartite motif containing 27
Q71U36	<i>TUBA1A</i>	tubulin alpha 1a
P68366	<i>TUBA4A</i>	tubulin alpha 4a
A6NHL2	<i>TUBAL3</i>	tubulin alpha like 3
P07437	<i>TUBB</i>	tubulin beta class I
Q13885	<i>TUBB2A</i>	tubulin beta 2A class IIa
Q9BVA1	<i>TUBB2B</i>	tubulin beta 2B class IIb
Q13509	<i>TUBB3</i>	tubulin beta 3 class III
P04350	<i>TUBB4A</i>	tubulin beta 4A class IVa
P68371	<i>TUBB4B</i>	tubulin beta 4B class IVb
P23258	<i>TUBG1</i>	tubulin gamma 1
P49411	<i>TUFM</i>	Tu translation elongation factor, mitochondrial
O00294	<i>TULP1</i>	TUB like protein 1
Q14157	<i>UBAP2L</i>	ubiquitin associated protein 2 like
Q92900	<i>UPF1</i>	UPF1 RNA helicase and ATPase
P31930	<i>UQCRC1</i>	ubiquinol-cytochrome c reductase core protein 1
O14949	<i>UQCRQ</i>	ubiquinol-cytochrome c reductase complex III subunit VII
P45974	<i>USP5</i>	ubiquitin specific peptidase 5
Q93008	<i>USP9X</i>	ubiquitin specific peptidase 9 X-linked

---

---

Q08AM6	<i>VAC14</i>	VAC14 component of PIKFYVE complex
O95292	<i>VAPB</i>	VAMP associated protein B and C
P26640	<i>VAR51</i>	valyl-tRNA synthetase 1
P45880	<i>VDAC2</i>	voltage dependent anion channel 2
P08670	<i>VIM</i>	vimentin
Q9H269	<i>VPS16</i>	VPS16 core subunit of CORVET and HOPS complexes
Q9NP79	<i>VTA1</i>	vesicle trafficking 1
A3KMH1	<i>VWA8</i>	von Willebrand factor A domain containing 8
O94967	<i>WDR47</i>	WD repeat domain 47
Q9Y4E6	<i>WDR7</i>	WD repeat domain 7
P27348	<i>YWHAQ</i>	tyrosine 3-monooxygenase/tryptophan 5-monooxygenase activation protein theta

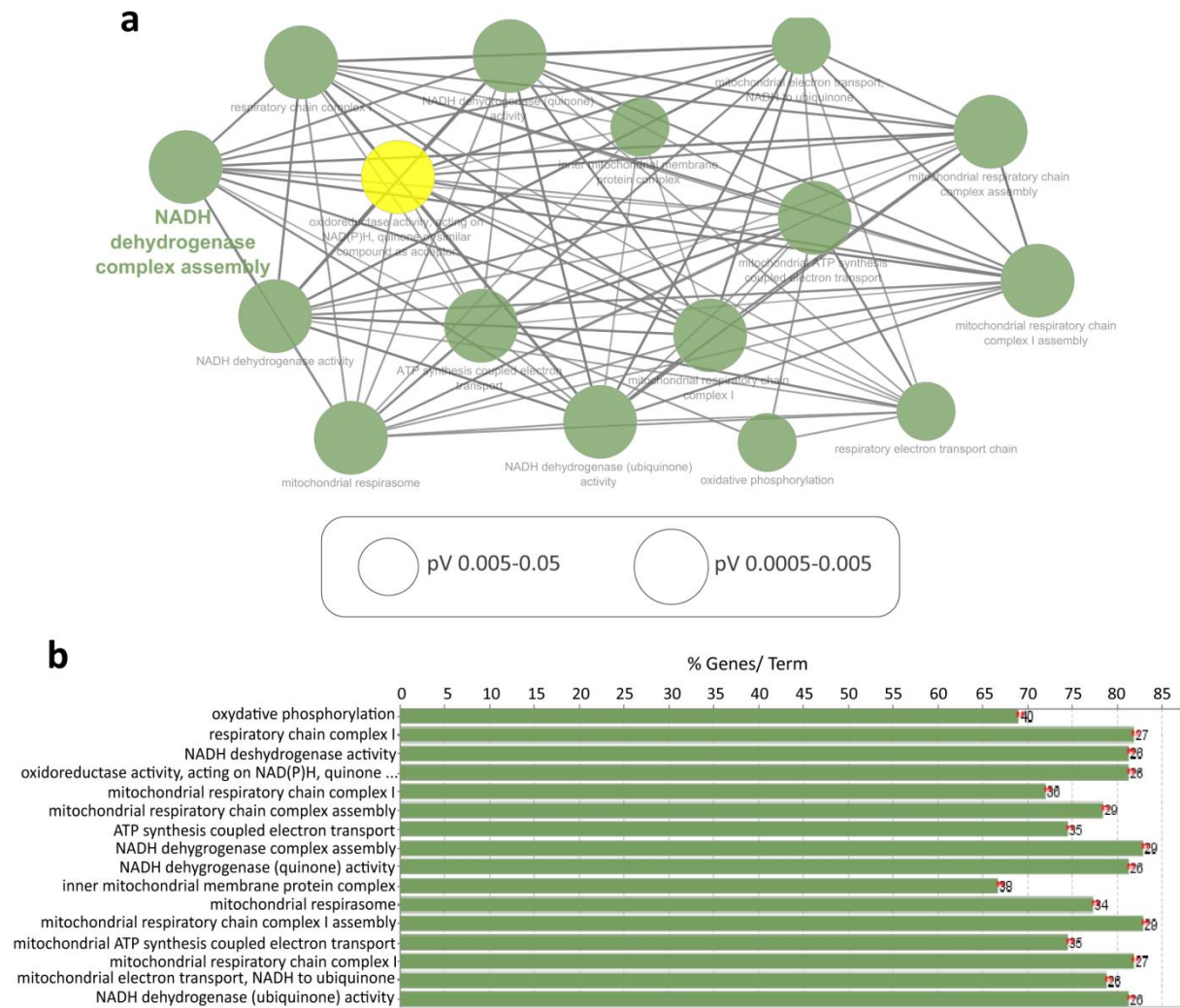
---

**Supplementary Table S2:** Proteins identified in this study and highly enriched in the retina (data obtained from the Human Atlas Protein (available online: [www.proteinatlas.org](http://www.proteinatlas.org))).

Uniprot accession	Gene name	Protein name	Expression in the retina
O60741	<i>HCN1</i>	Potassium/sodium hyperpolarization-activated cyclic nucleotide-gated channel 1	Photoreceptors
Q14721	<i>KCNB1</i>	Potassium voltage-gated channel subfamily B member 1	Photoreceptors
Q96JP9	<i>CDHR1</i>	Cadherin-related family member	Photoreceptors
Q9NQ79	<i>CRTAC1</i>	Cartilage acidic protein	N.A
O43347	<i>MSI1</i>	RNA-binding protein Musashi homolog 1	Photoreceptors
O00294	<i>TULP1</i>	Tubby-related protein 1	Photoreceptors
Q13402	<i>MYO7A</i>	Unconventional myosin-VIIa	Photoreceptors
P20941	<i>PDC</i>	Phosducin	Photoreceptors
P16499	<i>PDE6A</i>	Rod cGMP-specific 3',5'-cyclic phosphodiesterase subunit alpha	Photoreceptors

**Supplementary Table S3.** GO-Terms enrichment analysis of the 9 proteins identified in our study and highly enriched in the retinal tissue (Supplementary Table S2). Analysis obtained using DAVID online database (version 6.8). Enriched categories identified are those with p-value < 0.05.

GO-Term	p-value	Number of proteins	Associated proteins
Visual perception	1.4 E -4	4	MYO7A ,PDC, PDE6A, TULP1
Eye photoreceptor cell development	3.7E-2	2	MYO7A, TULP1



**Supplementary Figure S1.** ITM2B interactome in the retina. (a) GO-term network analysis (b) Functional clusters and pathway enriched by enriched proteins. %Genes/Term corresponds to the proportion of genes enriched in the functional clusters. Bars with the same color belong to the same functional cluster.

**Supplementary Table S4.** GO-Terms enrichment analysis of the ITM2B retinal interactome (457 proteins).

GO-Term	% Associated Genes	Nr Genes	Associated Proteins
oxidative phosphorylation	68,97	40,00	ATP5F1A, ATP5F1B, ATP5F1C, ATP5PF, COX2, COX4I1, COX5A, COX5B, COX6C, COX7A2L, NDUFA10, NDUFA12, NDUFA13, NDUFA2, NDUFA3, NDUFA5, NDUFA6, NDUFA7, NDUFA9, NDUFB10, NDUFB4, NDUFB5, NDUFB6, NDUFB8, NDUFB9, NDUF1, NDUF2, NDUF3, NDUF4, NDUF5, NDUF6, NDUF7, NDUF8, NDUFV1, NDUFV2, NDUFV3, SDHA, STOML2, UQCRC1, UQCRCQ
respiratory chain complex I	81,82	27,00	FOXRED1, NDUFA10, NDUFA12, NDUFA13, NDUFA2, NDUFA3, NDUFA5, NDUFA6, NDUFA7, NDUFA9, NDUFB10, NDUFB4, NDUFB5, NDUFB6, NDUFB8, NDUFB9, NDUF1, NDUF2, NDUF3, NDUF4, NDUF5, NDUF6, NDUF7, NDUF8, NDUFV1, NDUFV2, NDUFV3
NADH dehydrogenase activity	81,25	26,00	NDUFA10, NDUFA12, NDUFA13, NDUFA2, NDUFA3, NDUFA5, NDUFA6, NDUFA7, NDUFA9, NDUFB10, NDUFB4, NDUFB5, NDUFB6, NDUFB8, NDUFB9, NDUF1, NDUF2, NDUF3,
oxidoreductase activity, acting on NAD(P)H, quinone or similar compound as acceptor	81,25	26,00	NDUFA10, NDUFA12, NDUFA13, NDUFA2, NDUFA3, NDUFA5, NDUFA6, NDUFA7, NDUFA9, NDUFB10, NDUFB4, NDUFB5, NDUFB6, NDUFB8, NDUFB9, NDUF1, NDUF2, NDUF3,
respiratory electron transport chain	72,00	36,00	COX2, COX4I1, COX5A, COX5B, COX6C, COX7A2L, NDUFA10, NDUFA12, NDUFA13, NDUFA2, NDUFA3, NDUFA5, NDUFA6, NDUFA7, NDUFA9, NDUFB10, NDUFB4, NDUFB5,
mitochondrial respiratory chain complex assembly	78,38	29,00	ACAD9, FOXRED1, NDUFA10, NDUFA12, NDUFA13, NDUFA2, NDUFA3, NDUFA5, NDUFA6, NDUFA7, NDUFA9, NDUFB10, NDUFB4, NDUFB5, NDUFB6, NDUFB8, NDUFB9, NDUF1, NDUF2, NDUF3, NDUF4, NDUF5, NDUF6, NDUF7, NDUF8, NDUFV1, NDUFV2, NDUFV3, NUBPL

ATP synthesis coupled electron transport	74,47	35,00	COX2, COX4I1, COX5A, COX5B, COX6C, COX7A2L, NDUFA10, NDUFA12, NDUFA13, NDUFA2, NDUFA3, NDUFA5, NDUFA6, NDUFA7, NDUFA9, NDUFB10, NDUFB4, NDUFB5, NDUFB6, NDUFB8, NDUFB9, NDUFS1, NDUFS2, NDUFS3, NDUFS4, NDUFS5, NDUFS6, NDUFS7, NDUFS8, NDUFV1, NDUFV2, NDUFV3, SDHA, UQCRC1, UQCRQ
NADH dehydrogenase complex assembly	82,86	29,00	ACAD9, FOXRED1, NDUFA10, NDUFA12, NDUFA13, NDUFA2, NDUFA3, NDUFA5, NDUFA6, NDUFA7, NDUFA9, NDUFB10, NDUFB4, NDUFB5, NDUFB6, NDUFB8, NDUFB9, NDUFS1,
NADH dehydrogenase (quinone) activity	81,25	26,00	NDUFA10, NDUFA12, NDUFA13, NDUFA2, NDUFA3, NDUFA5, NDUFA6, NDUFA7, NDUFA9, NDUFB10, NDUFB4, NDUFB5, NDUFB6, NDUFB8, NDUFB9, NDUFS1, NDUFS2, NDUFS3,
inner mitochondrial membrane protein complex	66,67	38,00	ATP5F1A, ATP5F1B, ATP5F1C, ATP5PF, COX4I1, COX5A, FOXRED1, IMMT, NDUFA10, NDUFA12, NDUFA13, NDUFA2, NDUFA3, NDUFA5, NDUFA6, NDUFA7, NDUFA9, NDUFB10, NDUFB4, NDUFB5, NDUFB6, NDUFB8, NDUFB9, NDUFS1, NDUFS2, NDUFS3, NDUFS4, NDUFS5, NDUFS6, NDUFS7, NDUFS8, NDUFV1, NDUFV2, NDUFV3, SDHA, SLC25A6, UQCRC1, UQCRQ]
mitochondrial respirasome	77,27	34,00	COX4I1, COX5A, COX7A2, COX7A2L, FOXRED1, NDUFA10, NDUFA12, NDUFA13, NDUFA2, NDUFA3, NDUFA5, NDUFA6, NDUFA7, NDUFA9, NDUFB10, NDUFB4, NDUFB5, NDUFB6,
mitochondrial respiratory chain complex I assembly	82,86	29,00	ACAD9, FOXRED1, NDUFA10, NDUFA12, NDUFA13, NDUFA2, NDUFA3, NDUFA5, NDUFA6, NDUFA7, NDUFA9, NDUFB10, NDUFB4, NDUFB5, NDUFB6, NDUFB8, NDUFB9, NDUFS1,
mitochondrial ATP synthesis coupled electron transport	74,47	35,00	COX2, COX4I1, COX5A, COX5B, COX6C, COX7A2L, NDUFA10, NDUFA12, NDUFA13, NDUFA2, NDUFA3, NDUFA5, NDUFA6, NDUFA7, NDUFA9, NDUFB10, NDUFB4, NDUFB5, NDUFB6, NDUFB8, NDUFB9, NDUFS1,

			NDUFS2, NDUFS3, NDUFS4, NDUFS5, NDUFS6, NDUFS7, NDUFS8, NDUFV1, NDUFV2, NDUFV3, SDHA, UQCRC1, UQCRCQ
mitochondrial respiratory chain complex I	81,82	27,00	FOXRED1, NDUFA10, NDUFA12, NDUFA13, NDUFA2, NDUFA3, NDUFA5, NDUFA6, NDUFA7, NDUFA9, NDUFB10, NDUFB4, NDUFB5, NDUFB6, NDUFB8, NDUFB9, NDUFS1, NDUFS2, NDUFS3, NDUFS4, NDUFS5, NDUFS6, NDUFS7, NDUFS8, NDUFV1, NDUFV2, NDUFV3
mitochondrial electron transport, NADH to ubiquinone	78,79	26,00	NDUFA10, NDUFA12, NDUFA13, NDUFA2, NDUFA3, NDUFA5, NDUFA6, NDUFA7, NDUFA9, NDUFB10, NDUFB4, NDUFB5, NDUFB6, NDUFB8, NDUFB9, NDUFS1, NDUFS2, NDUFS3, NDUFS4, NDUFS5, NDUFS6, NDUFS7, NDUFS8, NDUFV1, NDUFV2, NDUFV3
NADH dehydrogenase (ubiquinone) activity	81,25	26,00	NDUFA10, NDUFA12, NDUFA13, NDUFA2, NDUFA3, NDUFA5, NDUFA6, NDUFA7, NDUFA9, NDUFB10, NDUFB4, NDUFB5, NDUFB6, NDUFB8, NDUFB9, NDUFS1, NDUFS2, NDUFS3, NDUFS4, NDUFS5, NDUFS6, NDUFS7, NDUFS8, NDUFV1, NDUFV2, NDUFV3

**Supplementary Table S5.** Curated list representing 140 proteins identified by LC-MS/MS and purified with the mouse and rabbit anti-ITM2B antibodies (FC >2 and p-value < 0.01).

<b>Uniprot accession</b>	<b>Gene name</b>	<b>Protein name</b>
P01023	<i>A2M</i>	alpha-2-macroglobulin
P61221	<i>ABCE1</i>	ATP binding cassette subfamily E member 1
P24666	<i>ACP1</i>	acid phosphatase 1
P60709	<i>ACTB</i>	actin beta
P68032	<i>ACTC1</i>	actin alpha cardiac muscle 1
P61160	<i>ACTR2</i>	actin related protein 2
P02768	<i>ALB</i>	albumin
O95782	<i>AP2A1</i>	adaptor related protein complex 2 subunit alpha 1
Q8N6H7	<i>ARFGAP2</i>	ADP ribosylation factor GTPase activating protein 2
P40616	<i>ARL1</i>	ADP ribosylation factor like GTPase 1
P59998	<i>ARPC4</i>	actin related protein 2/3 complex subunit 4
Q676U5	<i>ATG16L1</i>	autophagy related 16 like 1
Q01814	<i>ATP2B2</i>	ATPase plasma membrane Ca <sup>2+</sup> transporting 2
Q9UL15	<i>BAG5</i>	BAG cochaperone 5
P27708	<i>CAD</i>	carbamoyl-phosphate synthetase 2, aspartate transcarbamylase, and dihydroorotase
Q9UQM7	<i>CAMK2A</i>	calcium/calmodulin dependent protein kinase II alpha
Q13557	<i>CAMK2D</i>	calcium/calmodulin dependent protein kinase II delta
Q14444	<i>CAPRIN1</i>	cell cycle associated protein 1
Q96JP9	<i>CDHR1</i>	cadherin related family member 1
Q00535	<i>CDK5</i>	cyclin dependent kinase 5
O75122	<i>CLASP2</i>	cytoplasmic linker associated protein 2
P09543	<i>CNP</i>	2',3'-cyclic nucleotide 3' phosphodiesterase
O14579	<i>COPE</i>	COPI coat complex subunit epsilon
Q8N568	<i>DCLK2</i>	doublecortin like kinase 2
Q9NP97	<i>DYNLRB1</i>	dynein light chain roadblock-type 1
Q5JPH6	<i>EARS2</i>	glutamyl-tRNA synthetase 2, mitochondrial
P68104	<i>EEF1A1</i>	eukaryotic translation elongation factor 1 alpha 1
Q8N336	<i>ELMOD1</i>	ELMO domain containing 1
Q15369	<i>ELOC</i>	elongin C

---

P50402	<i>EMD</i>	emerin
O75477	<i>ERLIN1</i>	ER lipid raft associated 1
O94905	<i>ERLIN2</i>	ER lipid raft associated 2
Q9BSJ8	<i>ESYT1</i>	extended synaptotagmin 1
Q9NZB2	<i>FAM120A</i>	family with sequence similarity 120A
Q9NVF7	<i>FBXO28</i>	F-box protein 28
Q86UX7	<i>FERMT3</i>	fermitin family member 3
Q14318	<i>FKBP8</i>	FKBP prolyl isomerase 8
Q13045	<i>FLII</i>	FLII actin remodeling protein
Q96I24	<i>FUBP3</i>	far upstream element binding protein 3
P51114	<i>FXR1</i>	FMR1 autosomal homolog 1
O94925	<i>GLS</i>	glutaminase
P29992	<i>GNA11</i>	G protein subunit alpha 11
Q5JWF2	<i>GNAS</i>	GNAS complex locus
P19086	<i>GNAZ</i>	G protein subunit alpha z
O60741	<i>HCN1</i>	hyperpolarization activated cyclic nucleotide gated potassium channel 1
P52789	<i>HK2</i>	hexokinase 2
Q2TB90	<i>HKDC1</i>	hexokinase domain containing 1
P01892	<i>HLA-A</i>	HLA class I histocompatibility antigen, A alpha chain
P31943	<i>HNRNPH1</i>	heterogeneous nuclear ribonucleoprotein H1
Q9BUJ2	<i>HNRNPUL1</i>	heterogeneous nuclear ribonucleoprotein U like 1
Q53GQ0	<i>HSD17B12</i>	hydroxysteroid 17-beta dehydrogenase 12
O43301	<i>HSPA12A</i>	heat shock protein family A (Hsp70) member 12A
Q9Y4L1	<i>HYOU1</i>	hypoxia up-regulated 1
A1L0T0	<i>ILVBL</i>	ilvB acetolactate synthase like
P20839	<i>IMPDH1</i>	inosine monophosphate dehydrogenase 1
Q6DN90	<i>IQSEC1</i>	IQ motif and Sec7 domain ArfGEF 1
Q06033	<i>ITIH3</i>	inter-alpha-trypsin inhibitor heavy chain 3
Q9Y287	<i>ITM2B</i>	integral membrane protein 2B
Q9NQX7	<i>ITM2C</i>	integral membrane protein 2C
Q14721	<i>KCNB1</i>	potassium voltage-gated channel subfamily B member 1
Q7Z4S6	<i>KIF21A</i>	kinesin family member 21A
P32004	<i>L1CAM</i>	L1 cell adhesion molecule
Q9BXB1	<i>LGR4</i>	leucine rich repeat containing G protein-coupled receptor 4

---

---

P49257	<i>LMAN1</i>	lectin, mannose binding 1
Q07954	<i>LRP1</i>	LDL receptor related protein 1
O95372	<i>LYPLA2</i>	lysophospholipase 2
P46821	<i>MAP1B</i>	microtubule associated protein 1B
Q96JE9	<i>MAP6</i>	microtubule associated protein 6
C9JLW8	<i>MCRIP1</i>	MAPK regulated corepressor interacting protein 1
Q15773	<i>MLF2</i>	myeloid leukemia factor 2
Q13015	<i>MLLT11</i>	MLLT11 transcription factor 7 cofactor
Q14168	<i>MPP2</i>	membrane palmitoylated protein 2
P11586	<i>MTHFD1</i>	methylenetetrahydrofolate dehydrogenase, cyclohydrolase and formyltetrahydrofolate synthetase 1
P35580	<i>MYH10</i>	myosin heavy chain 10
O14950	<i>MYL12A</i>	myosin light chain 12A
P12829	<i>MYL4</i>	myosin light chain 4
P60660	<i>MYL6</i>	myosin light chain 6
Q9Y4I1	<i>MYO5A</i>	myosin VA
Q9ULV0	<i>MYO5B</i>	myosin VB
Q16718	<i>NDUFA5</i>	NADH:ubiquinone oxidoreductase subunit A5
O95168	<i>NDUFB4</i>	NADH:ubiquinone oxidoreductase subunit B4
O75306	<i>NDUFS2</i>	NADH:ubiquinone oxidoreductase core subunit S2
P49821	<i>NDUFV1</i>	NADH:ubiquinone oxidoreductase core subunit V1
P12036	<i>NEFH</i>	neurofilament heavy
P46459	<i>NSF</i>	N-ethylmaleimide sensitive factor, vesicle fusing ATPase
Q9BRJ7	<i>NUDT16L1</i>	nudix hydrolase 16 like 1
Q9BZF1	<i>OSBPL8</i>	oxysterol binding protein like 8
P11940	<i>PABPC1</i>	poly(A) binding protein cytoplasmic 1
Q13310	<i>PABPC4</i>	poly(A) binding protein cytoplasmic 4
Q6VY07	<i>PACS1</i>	phosphofurin acidic cluster sorting protein 1
Q96AQ6	<i>PBXIP1</i>	PBX homeobox interacting protein 1
O95206	<i>PCDH8</i>	protocadherin 8
P17858	<i>PFKL</i>	phosphofructokinase, liver type
Q01813	<i>PFKP</i>	phosphofructokinase, platelet
Q15149	<i>PLEC</i>	plectin
P62191	<i>PSMC1</i>	proteasome 26S subunit, ATPase 1

---

---

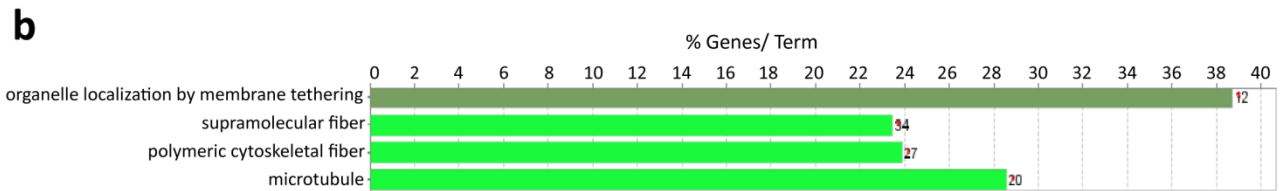
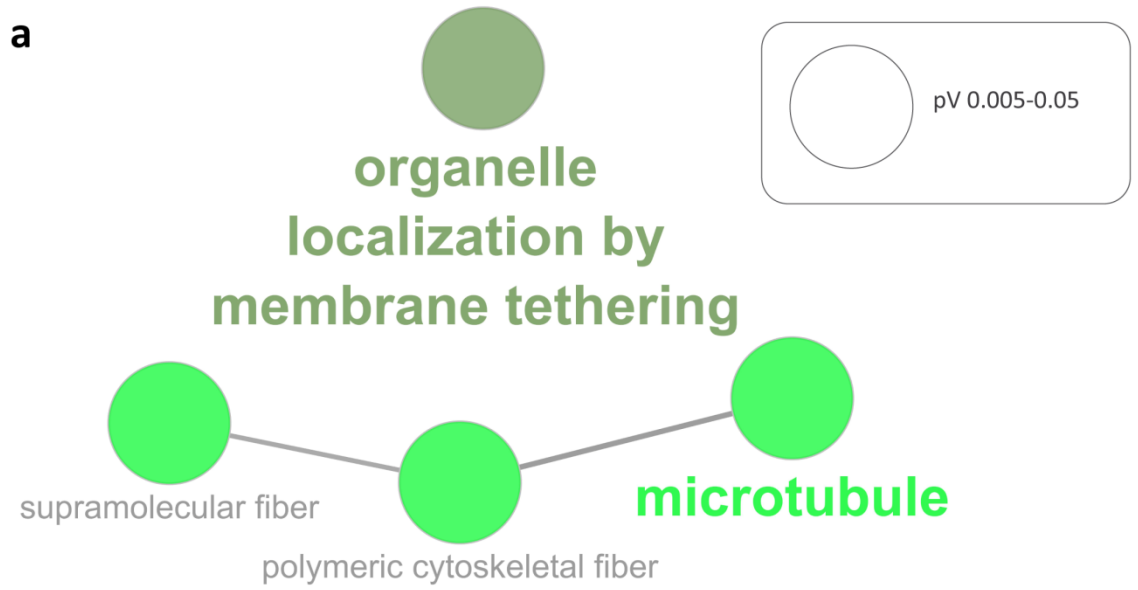
P62333	<i>PSMC6</i>	proteasome 26S subunit, ATPase 6
P10586	<i>PTPRF</i>	protein tyrosine phosphatase receptor type F
P47897	<i>QARS1</i>	glutaminyl-tRNA synthetase 1
Q15293	<i>RCN1</i>	reticulocalbin 1
Q14257	<i>RCN2</i>	reticulocalbin 2
Q96NR8	<i>RDH12</i>	retinol dehydrogenase 12
P62906	<i>RPL10A</i>	ribosomal protein L10a
P30050	<i>RPL12</i>	ribosomal protein L12
P40429	<i>RPL13A</i>	ribosomal protein L13a
P84098	<i>RPL19</i>	ribosomal protein L19
P46776	<i>RPL27A</i>	ribosomal protein L27a
P62888	<i>RPL30</i>	ribosomal protein L30
P36578	<i>RPL4</i>	ribosomal protein L4
P62424	<i>RPL7A</i>	ribosomal protein L7a
P62277	<i>RPS13</i>	ribosomal protein S13
P39019	<i>RPS19</i>	ribosomal protein S19
P15880	<i>RPS2</i>	ribosomal protein S2
Q8TD47	<i>RPS4Y2</i>	ribosomal protein S4 Y-linked 2
P62241	<i>RPS8</i>	ribosomal protein S8
O00442	<i>RTCA</i>	RNA 3'-terminal phosphate cyclase
Q9Y310	<i>RTCB</i>	RNA 2',3'-cyclic phosphate and 5'-OH ligase
P55735	<i>SEC13</i>	SEC13 homolog, nuclear pore and COPII coat complex component
O15027	<i>SEC16A</i>	SEC16 homolog A, endoplasmic reticulum export factor
Q15393	<i>SF3B3</i>	splicing factor 3b subunit 3
Q9NR46	<i>SH3GLB2</i>	SH3 domain containing GRB2 like, endophilin B2
Q02978	<i>SLC25A11</i>	solute carrier family 25 member 11
Q00325	<i>SLC25A3</i>	solute carrier family 25 member 3
P12236	<i>SLC25A6</i>	solute carrier family 25 member 6
Q9Y2P4	<i>SLC27A6</i>	solute carrier family 27 member 6
P17987	<i>TCP1</i>	t-complex 1
Q9NZ01	<i>TECR</i>	trans-2,3-enoyl-CoA reductase
Q9UL33	<i>TRAPPC2L</i>	trafficking protein particle complex 2 like
Q71U36	<i>TUBA1A</i>	tubulin alpha 1a
P68366	<i>TUBA4A</i>	tubulin alpha 4a

---

---

A6NHL2	<i>TUBAL3</i>	tubulin alpha like 3
P07437	<i>TUBB</i>	tubulin beta class I
Q13509	<i>TUBB3</i>	tubulin beta 3 class III
P04350	<i>TUBB4A</i>	tubulin beta 4A class IVa
P68371	<i>TUBB4B</i>	tubulin beta 4B class IVb
P23258	<i>TUBG1</i>	tubulin gamma 1
P49411	<i>TUFM</i>	Tu translation elongation factor, mitochondrial
O95292	<i>VAPB</i>	VAMP associated protein B and C
O94967	<i>WDR47</i>	WD repeat domain 47
P27348	<i>YWHAQ</i>	14-3-3 protein theta

---



**Supplementary Figure S2.** ITM2B interactome in the retina with the 140 common proteins purified with the mouse and the rabbit antibody. (A) Go-term network analysis (B) Functional clusters and pathways enriched by upregulated proteins. %Genes/Term corresponds to the proportion of genes enriched in the functional clusters. Bars with the same color belong to the same functional cluster.

**Supplementary Table S6.** GO-Terms enrichment analysis of the ITM2B retinal interactome of the 140 common proteins purified with both mouse and rabbit anti-ITM2B antibodies.

<b>GO-Term</b>	<b>% Associated Genes</b>	<b>Nr Genes</b>	<b>Associated Proteins</b>
organelle localization by membrane tethering	38,71	12,00	ALB, ESYT1, KCNB1, NSF, TUBA1A, TUBA4A, TUBB, TUBB3, TUBB4A, TUBB4B, TUBG1, VAPB
supramolecular fiber	23,45	34,00	ACTB, ACTC1, ALB, ATP2B2, CAD, CDK5, CLASP2, DCLK2, DYNLRB1, EMD, FXR1, ITIH3, KIF21A, LMAN1, MAP1B, MAP6, MYH10, MYL12B, MYL4, MYO5A, NEFH, PBXIP1, PLEC, TCP1, TUBA1A, TUBA4A, TUBAL3, TUBB, TUBB3, TUBB4A, TUBB4B, TUBG1, WDR47, YWHAQ
polymeric cytoskeletal fiber	23,89	27,00	ACTB, ACTC1, ALB, CDK5, CLASP2, DCLK2, DYNLRB1, EMD, ITIH3, KIF21A, MAP1B, MAP6, MYO5A, NEFH, PBXIP1, PLEC, TCP1, TUBA1A, TUBA4A, TUBAL3, TUBB, TUBB3, TUBB4A, TUBB4B, TUBG1, WDR47, YWHAQ
Microtubule	28,57	20,00	CDK5, CLASP2, DCLK2, DYNLRB1, EMD, KIF21A, MAP1B, MAP6, MYO5A, PBXIP1, TCP1, TUBA1A, TUBA4A, TUBAL3, TUBB, TUBB3, TUBB4A, TUBB4B, TUBG1, WDR47

**Supplementary Table S7.** GO-Terms enrichment analysis of the ITM2B retinal interactome purified with the mouse anti-ITM2B antibody only.

GO-Term	% Associated Genes	Nr Genes	Associated Proteins
Microtubule	42,86	30,00	C11orf58, CCT3, CCT5, CCT8, CDK5, CKAP5, CLASP2, DCLK2, DYNC1H1, DYNLRB1, EMD, KIF21A, MAP1B, MAP6, MAPRE2, MYO5A, PBXIP1, RCC2, SRPRB, TCP1, TUBA1A, TUBA4A, TUBAL3, TUBB, TUBB2A, TUBB3, TUBB4A, TUBB4B, TUBG1, WDR47
organonitrogen compound biosynthetic process	33,33	70,00	ABCE1, ACSL3, AIMP2, ATG16L1, ATP5PO, B4GAT1, CAD, DARS1, DCAKD, EARS2, EEF1A1, EEF1D, EEF1E1, EEF1G, EEF2, EIF3L, EIF4A1, GARS1, GLS, HSD17B12, HSPD1, IMPDH1, KARS1, L1CAM, LARS1, LMAN1, MARS1, MOGS, MTHFD1, MYO5A, NAMPT, PABPC1, PABPC4, PNPLA6, PRELP, PRPS1, QARS1, RACK1, RARS1, RPL10A, RPL12, RPL13A, RPL19, RPL23, RPL26, RPL27, RPL27A, RPL30, RPL4, RPL7A, RPS13, RPS16, RPS18, RPS19, RPS2, RPS20, RPS27A, RPS3, RPS4X, RPS4Y2, RPS8, RPSA, SLC25A12, SRM, TARS1, TARS3, TECR, TUFM, VAPB, VARS1
peptide metabolic process	37,40	49,00	ABCE1, AIMP2, DARS1, EARS2, EEF1A1, EEF1D, EEF1E1, EEF1G, EEF2, EIF3L, EIF4A1, GARS1, HSPD1, KARS1, LARS1, MARS1, PABPC1, PABPC4, PCSK2, QARS1, RACK1, RARS1, RPL10A, RPL12, RPL13A, RPL19, RPL23, RPL26, RPL27, RPL27A, RPL30, RPL4, RPL7A, RPS13, RPS16, RPS18, RPS19, RPS2, RPS20, RPS27A, RPS3, RPS4X, RPS4Y2, RPS8, RPSA, TARS1, TARS3, TUFM, VARS1
Translation	41,03	48,00	ABCE1, AIMP2, DARS1, EARS2, EEF1A1, EEF1D, EEF1E1, EEF1G, EEF2, EIF3L, EIF4A1, GARS1, HSPD1, KARS1, LARS1, MARS1, PABPC1, PABPC4, QARS1, RACK1, RARS1, RPL10A, RPL12, RPL13A, RPL19, RPL23, RPL26, RPL27, RPL27A, RPL30, RPL4, RPL7A, RPS13, RPS16, RPS18, RPS19, RPS2, RPS20, RPS27A, RPS3, RPS4X, RPS4Y2, RPS8, RPSA, TARS1, TARS3, TUFM, VARS1

**Supplementary Table S8.** List representing 124 proteins which are in common between the 440 proteins identified by LC-MS/MS and purified with the mouse anti-ITM2B antibody (FC>2 and p-value<0.05) and the 511 rat cerebral proteins identified in a previous study<sup>1</sup>.

Uniprot accession	Gene name	Protein name
P06238	<i>A2m</i>	Alpha-2-macroglobulin
P60711	<i>Actb</i>	Actin, cytoplasmic 1
P68035	<i>Actc1</i>	Actin, alpha cardiac muscle 1
O70511	<i>Ank3</i>	Ankyrin-3
P84092	<i>Ap2m1</i>	AP-2 complex subunit mu
P06687	<i>Atp1a3</i>	Sodium/potassium-transporting ATPase subunit alpha-3
P11507	<i>Atp2a2</i>	Sarcoplasmic/endoplasmic reticulum calcium ATPase 2
P11506	<i>Atp2b2</i>	Calcium-transporting ATPase Plasma membrane calcium-transporting ATPase 2
Q64542	<i>Atp2b4</i>	Calcium-transporting ATPase Plasma membrane calcium-transporting ATPase 4
P35435	<i>Atp5f1c</i>	ATP synthase subunit gamma, mitochondrial
P35434	<i>Atp5f1d</i>	ATP synthase subunit delta, mitochondrial
Q9JJW3	<i>Atp5md</i>	ATP synthase membrane subunit DAPIT, mitochondrial
P31399	<i>Atp5pd</i>	ATP synthase subunit d, mitochondrial
Q06647	<i>Atp5po</i>	ATP synthase subunit O, mitochondrial
P01026	<i>C3</i>	Complement C3
Q66HR5	<i>Calcoco1</i>	Calcium-binding and coiled-coil domain-containing protein 1
P11275	<i>Camk2a</i>	Calcium/calmodulin-dependent protein kinase type II subunit alpha
P15791	<i>Camk2d</i>	Calcium/calmodulin-dependent protein kinase type II
Q3T1K5	<i>Capza2</i>	F-actin-capping protein subunit alpha-2
Q5XI32	<i>Capzb</i>	F-actin-capping protein subunit beta
Q6P502	<i>Cct3</i>	T-complex protein 1 subunit gamma
Q7TPB1	<i>Cct4</i>	T-complex protein 1 subunit delta
Q68FQ0	<i>Cct5</i>	T-complex protein 1 subunit epsilon
Q03114	<i>Cdk5</i>	Cyclin-dependent-like kinase 5
Q99JD4	<i>Clasp2</i>	CLIP-associating protein 2
P08081	<i>CltA</i>	Clathrin light chain A
P13233	<i>Cnp</i>	2',3'-cyclic-nucleotide 3'-phosphodiesterase
P12075	<i>Cox5b</i>	Cytochrome c oxidase subunit 5B, mitochondrial
P35171	<i>Cox7a2</i>	Cytochrome c oxidase subunit 7A2, mitochondrial
O08875	<i>Dclk1</i>	Serine/threonine-protein kinase DCLK1
P38650	<i>Dync1h1</i>	Cytoplasmic dynein 1 heavy chain 1 Dynein
P62630	<i>Eef1a1</i>	Elongation factor 1-alpha 1
Q68FR6	<i>Eef1g</i>	Elongation factor 1-gamma
P05197	<i>Eef2</i>	Elongation factor 2
B5DEH2	<i>Erlin2</i>	Erlin-2
Q5XI81	<i>Fxr1</i>	Fragile X mental retardation syndrome-related protein 1
P97874	<i>Gak</i>	Cyclin-G-associated kinase
P04897	<i>Gnai2</i>	Guanine nucleotide-binding protein G(i) subunit alpha-2

P63095	<i>Gnas</i>	Guanine nucleotide-binding protein G(s) subunit alpha isoforms short
P19627	<i>Gnaz</i>	Guanine nucleotide-binding protein G(z) subunit alpha
Q64428	<i>Hadha</i>	Trifunctional enzyme subunit alpha, mitochondrial
Q8VHV7	<i>Hnrnp1</i>	Heterogeneous nuclear ribonucleoprotein H RRM domain-containing protein
P82995	<i>Hsp90aa1</i>	Heat shock protein HSP 90-alpha
P34058	<i>Hsp90ab1</i>	Heat shock protein HSP 90-beta
Q66HD0	<i>Hsp90b1</i>	Endoplasmic reticulum chaperone BiP
O88600	<i>Hspa4</i>	Heat shock 70 kDa protein 4L
P06761	<i>Hspa5</i>	Endoplasmic reticulum chaperone BiP
P63039	<i>Hspa8</i>	Heat shock cognate 71 kDa protein
P63039	<i>Hspd1</i>	60 kDa heat shock protein, mitochondrial
Q63617	<i>Hyou1</i>	Hypoxia up-regulated protein 1
Q3KR86	<i>Immt</i>	MICOS complex subunit Mic60
P23565	<i>Ina</i>	Alpha-internexin
Q63416	<i>Itih3</i>	Inter-alpha-trypsin inhibitor heavy chain H3
Q2PQA9	<i>Kif5b</i>	Kinesin-1 heavy chain
O08873	<i>Madd</i>	MAP kinase-activating death domain protein
P15205	<i>Map1b</i>	Microtubule-associated protein 1B
Q63560	<i>Map6</i>	Microtubule-associated protein 6
Q9JLT0	<i>Myh10</i>	Myosin-10
Q64119	<i>Myl6</i>	Myosin light polypeptide 6
Q9QYF3	<i>Myo5a</i>	Unconventional myosin-Va
P85969	<i>Napb</i>	Beta-soluble NSF attachment protein
P13596	<i>Ncam1</i>	Neural cell adhesion molecule 1
Q561S0	<i>Ndufa10</i>	NADH dehydrogenase [ubiquinone] 1 alpha subcomplex subunit 10, mitochondrial
Q641Y2	<i>Ndufs2</i>	NADH dehydrogenase [ubiquinone] iron-sulfur protein 2, mitochondrial
P19234	<i>Ndufv2</i>	NADH dehydrogenase [ubiquinone] flavoprotein 2, mitochondrial
P16884	<i>Nefh</i>	Neurofilament heavy polypeptide
P19527	<i>Nefl</i>	Neurofilament light polypeptide
P12839	<i>Nefm</i>	Neurofilament medium polypeptide
Q9QUL6	<i>Nsf</i>	Vesicle-fusing ATPase
P04785	<i>P4hb</i>	Protein disulfide-isomerase
Q6AYD3	<i>Pa2g4</i>	Proliferation-associated protein 2G4
Q9EPH8	<i>Pabpc1</i>	Polyadenylate-binding protein 1
P47858	<i>Pfkm</i>	ATP-dependent 6-phosphofructokinase, muscle type
P47860	<i>Pfkp</i>	ATP-dependent 6-phosphofructokinase, platelet type
P62963	<i>Pfn1</i>	Profilin-1 Profilin
O08662	<i>Pi4ka</i>	Phosphatidylinositol 4-kinase alpha
P30427	<i>Plec</i>	Plectin
P10111	<i>Ppia</i>	Peptidyl-prolyl cis-trans isomerase A
Q4FZT9	<i>Psmd2</i>	26S proteasome non-ATPase regulatory subunit 2
P53534	<i>Pygb</i>	Alpha-1,4 glucan phosphorylase Glycogen phosphorylase, brain form
P61107	<i>Rab14</i>	Ras-related protein Rab-14

---

P63245	<i>Rack1</i>	Receptor of activated protein C kinase 1
Q62703	<i>Rcn2</i>	Reticulocalbin-2
P62914	<i>Rpl11</i>	60S ribosomal protein L11
P23358	<i>Rpl12</i>	60S ribosomal protein L12
P47198	<i>Rpl22</i>	60S ribosomal protein L22
P61354	<i>Rpl27</i>	60S ribosomal protein L27
P50878	<i>Rpl4</i>	60S ribosomal protein L4
P21533	<i>Rpl6</i>	60S ribosomal protein L6
P19945	<i>Rplp0</i>	60S acidic ribosomal protein P0
P62250	<i>Rps16</i>	40S ribosomal protein S16
P60868	<i>Rps20</i>	40S ribosomal protein S20
P62909	<i>Rps3</i>	40S ribosomal protein S3
P49242	<i>Rps3a</i>	40S ribosomal protein S3a
P62703	<i>Rps4x</i>	40S ribosomal protein S4, X isoform
Q6AYT3	<i>Rtcb</i>	RNA-splicing ligase RtcB homolog
Q6P799	<i>Sars1</i>	Serine--tRNA ligase, cytoplasmic
Q5PPJ9	<i>Sh3glb2</i>	Endophilin-B2
Q63633	<i>Slc12a5</i>	Solute carrier family 12 member 5
P97700	<i>Slc25a11</i>	Mitochondrial 2-oxoglutarate/malate carrier protein
P16036	<i>Slc25a3</i>	Phosphate carrier protein, mitochondrial
Q05962	<i>Slc25a4</i>	ADP/ATP translocase 1
Q09073	<i>Slc25a5</i>	ADP/ATP translocase 2
P11167	<i>Slc2a1</i>	Solute carrier family 2, facilitated glucose transporter member 1
Q9QXY2	<i>Srcin1</i>	SRC kinase signaling inhibitor 1
P61765	<i>Stxbp1</i>	Syntaxin-binding protein 1
Q7TP47	<i>Syncrip</i>	Heterogeneous nuclear ribonucleoprotein Q
P12346	<i>Tf</i>	Serotransferrin
P70566	<i>Tmod2</i>	Tropomodulin-2
P68370	<i>Tuba1a</i>	Tubulin alpha-1A chain
Q5XIF6	<i>Tuba4a</i>	Tubulin alpha-4A chain
Q6AY56	<i>Tuba8</i>	Tubulin alpha-8 chain
P85108	<i>Tubb2a</i>	Tubulin beta-2A chain
Q3KRE8	<i>Tubb2b</i>	Tubulin beta-2B chain
Q4QRB4	<i>Tubb3</i>	Tubulin beta-3 chain
Q6P9T8	<i>Tubb4b</i>	Tubulin beta-4B chain Tubulin beta chain
P69897	<i>Tubb5</i>	Tubulin beta chain Tubulin beta-5 chain
P85834	<i>Tufm</i>	Elongation factor Tu Elongation factor Tu, mitochondrial
Q7TQ16	<i>Uqcrcq</i>	Cytochrome b-c1 complex subunit 8
Q04462	<i>Vars1</i>	Valine--tRNA ligase
Q793F9	<i>Vps4a</i>	Vacuolar protein sorting-associated protein 4A
Q9ERH3	<i>Wdr7</i>	WD repeat-containing protein 7
P68255	<i>Ywhaq</i>	14-3-3 protein theta
P63102	<i>Ywhaz</i>	14-3-3 protein zeta/delta

---

**Supplementary Table S9.** GO-Terms enrichment analysis of the ITM2B retinal interactome purified with the rabbit anti-ITM2B only.

GO-Term	% Associated Genes	Nr Genes	Associated Proteins
Mitochondrion	43,08	109,00	AARS2, ABCE1, ABHD11, ACAD9, ACADM, ACADSB, ACSF3, AK4, ALDH18A1, ANK2, ARL2, ATAD3A, ATP5F1A, ATP5F1C, ATP5MD, ATP5PF, BAG5, BSG, CAMK2A, CNP, COQ8B, COX2, COX4I1, COX5A, COX5B, COX6C, COX7A2, COX7A2L, CRYAB, CYC1, CYP27A1, DDX6, DGKE, DNAJA3, DNMT1L, EARS2, EEF1A2, FKBP8, FOXRED1, GFM2, GIT1, GLS, GNAS, GUF1, HADHA, HADHB, HIGD1A, HK2, HKDC1, IARS2, IDH2, IDH3A, IMMT, KMT2D, LDHD, LIG3, MCCC1, MCCC2, MFF, MTCH2, MTHFD1, MTHFD1L, NDUFA10, NDUFA13, NDUFA2, NDUFA3, NDUFA5, NDUFA6, NDUFA7, NDUFA9, NDUFB10, NDUFB4, NDUFB5, NDUFB6, NDUFB7, NDUFB8, NDUFB9, NDUFS1, NDUFS2, NDUFS3, NDUFS4, NDUFS5, NDUFS6, NDUFS7, NDUFS8, NDUFV1, NDUFV2, NDUFV3, NUBPL, OAT, PC, PPOX, PYCR2, QARS1, SDHA, SLC25A11, SLC25A3, SLC25A6, STOML2, STXBP1, SUCLA2, SUCLG1, TUFM, UQCRC1, UQCRC2, UQCRCQ, VDAC2, YARS2, YWHAQ
myosin complex	80,00	12,00	[MYH10, MYH14, MYH9, MYL12B, MYL4, MYL6, MYL9, MYO18A, MYO1C, MYO5A, MYO5B, MYO7A
mitochondrial matrix	50,54	47,00	[ABCE1, ACADM, ACADSB, ACSF3, AK4, ARL2, ATAD3A, ATP5F1A, ATP5F1C, ATP5PF, CYP27A1, DGKE, DNAJA3, DNMT1L, EARS2, GFM2, GLS, GUF1, HADHA, HADHB, IARS2, IDH2, IDH3A, LDHD, MCCC1, MCCC2, MTHFD1L, NDUFA10, NDUFA7, NDUFA9, NDUFB8, NDUFS1, NDUFS2, NDUFS3, NDUFS7, NDUFS8, NUBPL, OAT, PC, PYCR2, QARS1, SUCLA2, SUCLG1, TUFM, UQCRC2, VDAC2, YARS2
mitochondrial protein complex	63,24	43,00	ATP5F1A, ATP5F1C, ATP5MD, ATP5PF, COX4I1, COX5A, CYC1, FOXRED1, HADHA, IMMT, MCCC1, MCCC2, NDUFA10, NDUFA13, NDUFA2, NDUFA3, NDUFA5, NDUFA6, NDUFA7, NDUFA9, NDUFB10, NDUFB4, NDUFB5, NDUFB6, NDUFB7, NDUFB8, NDUFB9, NDUFS1, NDUFS2, NDUFS3, NDUFS4,

			NDUFS5, NDUFS6, NDUFS7, NDUFS8, NDUFV1, NDUFV2, NDUFV3, SDHA, SLC25A6, UQCRC1, UQCRC2, UQCRQ
oxidative phosphorylation	72,41	42,00	ATP5F1A, ATP5F1C, ATP5PF, COX2, COX4I1, COX5A, COX5B, COX6C, COX7A2L, CYC1, LDHD, NDUFA10, NDUFA13, NDUFA2, NDUFA3, NDUFA5, NDUFA6, NDUFA7, NDUFA9, NDUFB10, NDUFB4, NDUFB5, NDUFB6, NDUFB7, NDUFB8, NDUFB9, NDUFS1, NDUFS2, NDUFS3, NDUFS4, NDUFS5, NDUFS6, NDUFS7, NDUFS8, NDUFV1, NDUFV2, NDUFV3, SDHA, STOML2, UQCRC1, UQCRC2, UQCRQ
electron transfer activity	73,08	19,00	COX2, COX4I1, COX5A, COX5B, COX6C, COX7A2, COX7A2L, CYC1, KMT2D, LDHD, NDUFS1, NDUFS2, NDUFS3, NDUFS6, NDUFV2, SDHA, UQCRC1, UQCRQ, VDAC2
organelle inner membrane	56,25	63,00	ACAD9, ALDH18A1, ATAD3A, ATP5F1A, ATP5F1C, ATP5MD, ATP5PF, CNP, COQ8B, COX2, COX4I1, COX5A, COX5B, COX6C, COX7A2, COX7A2L, CYC1, CYP27A1, EMD, FOXRED1, GUF1, HADHA, HADHB, HIGD1A, IMMT, LDHD, MTCH2, NDUFA10, NDUFA13, NDUFA2, NDUFA3, NDUFA5, NDUFA6, NDUFA7, NDUFA9, NDUFB10, NDUFB4, NDUFB5, NDUFB6, NDUFB7, NDUFB8, NDUFB9, NDUFS1, NDUFS2, NDUFS3, NDUFS4, NDUFS5, NDUFS6, NDUFS7, NDUFS8, NDUFV1, NDUFV2, NDUFV3, PPOX, SDHA, SLC25A11, SLC25A3, SLC25A6, STOML2, TMPO, UQCRC1, UQCRC2, UQCRQ
cellular respiration	67,74	42,00	COX2, COX4I1, COX5A, COX5B, COX6C, COX7A2L, CYC1, IDH2, IDH3A, LDHD, NDUFA10, NDUFA13, NDUFA2, NDUFA3, NDUFA5, NDUFA6, NDUFA7, NDUFA9, NDUFB10, NDUFB4, NDUFB5, NDUFB6, NDUFB7, NDUFB8, NDUFB9, NDUFS1, NDUFS2, NDUFS3, NDUFS4, NDUFS5, NDUFS6, NDUFS7, NDUFS8, NDUFV1, NDUFV2, NDUFV3, SDHA, SUCLA2, SUCLG1, UQCRC1, UQCRC2, UQCRQ
mitochondrial envelope	51,45	71,00	ACAD9, ACADM, ALDH18A1, ARL2, ATAD3A, ATP5F1A, ATP5F1C, ATP5MD, ATP5PF, CNP, COQ8B, COX2, COX4I1, COX5A, COX5B, COX6C, COX7A2, COX7A2L, CYC1, CYP27A1, DNM1L, FKBP8, FOXRED1, GNAS, GUF1, HADHA, HADHB, HIGD1A, HK2, HKDC1, IMMT, KMT2D, LDHD, MFF, MTCH2,

			NDUFA10, NDUFA13, NDUFA2, NDUFA3, NDUFA5, NDUFA6, NDUFA7, NDUFA9, NDUFB10, NDUFB4, NDUFB5, NDUFB6, NDUFB7, NDUFB8, NDUFB9, NDUFS1, NDUFS2, NDUFS3, NDUFS4, NDUFS5, NDUFS6, NDUFS7, NDUFS8, NDUFV1, NDUFV2, NDUFV3, PPOX, SDHA, SLC25A11, SLC25A3, SLC25A6, STOML2, UQCRC1, UQCRC2, UQCRQ, VDAC2
mitochondrial membrane	50,37	68,00	ACAD9, ACADM, ALDH18A1, ATAD3A, ATP5F1A, ATP5F1C, ATP5MD, ATP5PF, CNP, COQ8B, COX2, COX4I1, COX5A, COX5B, COX6C, COX7A2, COX7A2L, CYC1, CYP27A1, DNMT1, FKBP8, FOXRED1, GUF1, HADHA, HADHB, HIGD1A, HK2, HKDC1, IMMT, LDHD, MFF, MTCH2, NDUFA10, NDUFA13, NDUFA2, NDUFA3, NDUFA5, NDUFA6, NDUFA7, NDUFA9, NDUFB10, NDUFB4, NDUFB5, NDUFB6, NDUFB7, NDUFB8, NDUFB9, NDUFS1, NDUFS2, NDUFS3, NDUFS4, NDUFS5, NDUFS6, NDUFS7, NDUFS8, NDUFV1, NDUFV2, NDUFV3, PPOX, SDHA, SLC25A11, SLC25A3, SLC25A6, STOML2, UQCRC1, UQCRC2, UQCRQ, VDAC2
inner mitochondrial membrane protein complex	70,18	40,00	ATP5F1A, ATP5F1C, ATP5MD, ATP5PF, COX4I1, COX5A, CYC1, FOXRED1, IMMT, NDUFA10, NDUFA13, NDUFA2, NDUFA3, NDUFA5, NDUFA6, NDUFA7, NDUFA9, NDUFB10, NDUFB4, NDUFB5, NDUFB6, NDUFB7, NDUFB8, NDUFB9, NDUFS1, NDUFS2, NDUFS3, NDUFS4, NDUFS5, NDUFS6, NDUFS7, NDUFS8, NDUFV1, NDUFV2, NDUFV3, SDHA, SLC25A6, UQCRC1, UQCRC2, UQCRQ
mitochondrial respirasome	81,82	36,00	COX4I1, COX5A, COX7A2, COX7A2L, CYC1, FOXRED1, NDUFA10, NDUFA13, NDUFA2, NDUFA3, NDUFA5, NDUFA6, NDUFA7, NDUFA9, NDUFB10, NDUFB4, NDUFB5, NDUFB6, NDUFB7, NDUFB8, NDUFB9, NDUFS1, NDUFS2, NDUFS3, NDUFS4, NDUFS5, NDUFS6, NDUFS7, NDUFS8, NDUFV1, NDUFV2, NDUFV3, SDHA, UQCRC1, UQCRC2, UQCRQ
mitochondrial inner membrane	59,80	61,00	ACAD9, ALDH18A1, ATAD3A, ATP5F1A, ATP5F1C, ATP5MD, ATP5PF, CNP, COQ8B, COX2, COX4I1, COX5A, COX5B, COX6C, COX7A2, COX7A2L, CYC1, CYP27A1, FOXRED1, GUF1, HADHA, HADHB, HIGD1A, IMMT, LDHD, MTCH2, NDUFA10,

			NDUFA13, NDUFA2, NDUFA3, NDUFA5, NDUFA6, NDUFA7, NDUFA9, NDUFB10, NDUFB4, NDUFB5, NDUFB6, NDUFB7, NDUFB8, NDUFB9, NDUFS1, NDUFS2, NDUFS3, NDUFS4, NDUFS5, NDUFS6, NDUFS7, NDUFS8, NDUFV1, NDUFV2, NDUFV3, PPOX, SDHA, SLC25A11, SLC25A3, SLC25A6, STOML2, UQCRC1, UQCRC2, UQCRQ
mitochondrial respiratory chain complex I assembly	82,86	29,00	ACAD9, FOXRED1, NDUFA10, NDUFA13, NDUFA2, NDUFA3, NDUFA5, NDUFA6, NDUFA7, NDUFA9, NDUFB10, NDUFB4, NDUFB5, NDUFB6, NDUFB7, NDUFB8, NDUFB9, NDUFS1, NDUFS2, NDUFS3, NDUFS4, NDUFS5, NDUFS6, NDUFS7, NDUFS8, NDUFV1, NDUFV2, NDUFV3, NUBPL
mitochondrial ATP synthesis coupled electron transport	80,85	38,00	COX2, COX4I1, COX5A, COX5B, COX6C, COX7A2L, CYC1, LDHD, NDUFA10, NDUFA13, NDUFA2, NDUFA3, NDUFA5, NDUFA6, NDUFA7, NDUFA9, NDUFB10, NDUFB4, NDUFB5, NDUFB6, NDUFB7, NDUFB8, NDUFB9, NDUFS1, NDUFS2, NDUFS3, NDUFS4, NDUFS5, NDUFS6, NDUFS7, NDUFS8, NDUFV1, NDUFV2, NDUFV3, SDHA, UQCRC1, UQCRC2, UQCRQ
mitochondrial respiratory chain complex I	81,82	27,00	FOXRED1, NDUFA10, NDUFA13, NDUFA2, NDUFA3, NDUFA5, NDUFA6, NDUFA7, NDUFA9, NDUFB10, NDUFB4, NDUFB5, NDUFB6, NDUFB7, NDUFB8, NDUFB9, NDUFS1, NDUFS2, NDUFS3, NDUFS4, NDUFS5, NDUFS6, NDUFS7, NDUFS8, NDUFV1, NDUFV2, NDUFV3
mitochondrial electron transport, NADH to ubiquinone	81,82	27,00	LDHD, NDUFA10, NDUFA13, NDUFA2, NDUFA3, NDUFA5, NDUFA6, NDUFA7, NDUFA9, NDUFB10, NDUFB4, NDUFB5, NDUFB6, NDUFB7, NDUFB8, NDUFB9, NDUFS1, NDUFS2, NDUFS3, NDUFS4, NDUFS5, NDUFS6, NDUFS7, NDUFS8, NDUFV1, NDUFV2, NDUFV3
NADH dehydrogenase (ubiquinone) activity	81,25	26,00	NDUFA10, NDUFA13, NDUFA2, NDUFA3, NDUFA5, NDUFA6, NDUFA7, NDUFA9, NDUFB10, NDUFB4, NDUFB5, NDUFB6, NDUFB7, NDUFB8, NDUFB9, NDUFS1, NDUFS2, NDUFS3, NDUFS4, NDUFS5, NDUFS6, NDUFS7, NDUFS8, NDUFV1, NDUFV2, NDUFV3

**Supplementary Table S10.** List representing 150 proteins which are in common between the 615 proteins identified by LC-MS/MS and purified with the rabbit anti-ITM2B antibody (FC>2 and p-value<0.05) and the 511 rat cerebral proteins identified in a previous study<sup>1</sup>.

Uniprot accession	Gene name	Protein name
P06238	<i>A2m</i>	Alpha-2-macroglobulin-P Alpha-2-macroglobulin
Q6KC51	<i>Ablim2</i>	Actin-binding LIM protein 2
P60711	<i>Actb</i>	Actin, cytoplasmic 1
P68035	<i>Actc1</i>	Actin, alpha cardiac muscle 1
Q63028	<i>Add1</i>	Alpha-adducin
O08838	<i>Amph</i>	Amphiphysin BAR domain-containing protein
O70511	<i>Ank3</i>	Ankyrin-3
P06685	<i>Atp1a1</i>	Sodium/potassium-transporting ATPase subunit alpha-1
P06687	<i>Atp1a3</i>	Sodium/potassium-transporting ATPase subunit alpha-3
P07340	<i>Atp1b1</i>	Sodium/potassium-transporting ATPase subunit beta-1
P13638	<i>Atp1b2</i>	Sodium/potassium-transporting ATPase subunit beta-2
P11505	<i>Atp2b1</i>	Plasma membrane calcium-transporting ATPase 1
P11506	<i>Atp2b2</i>	Plasma membrane calcium-transporting ATPase 2
Q64542	<i>Atp2b4</i>	Plasma membrane calcium-transporting ATPase 4
P15999	<i>Atp5f1a</i>	ATP synthase subunit alpha, mitochondrial ATP synthase subunit alpha
P10719	<i>Atp5f1b</i>	ATP synthase subunit beta, mitochondrial ATP synthase subunit beta
P35435	<i>Atp5f1c</i>	ATP synthase subunit gamma, mitochondrial ATP synthase subunit gamma, mitochondrial
Q9JJW3	<i>Atp5md</i>	ATP synthase membrane subunit DAPIT, mitochondrial
P31399	<i>Atp5pd</i>	ATP synthase subunit d, mitochondrial
P21571	<i>Atp5pf</i>	ATP synthase-coupling factor 6, mitochondrial
Q06647	<i>Atp5po</i>	ATP synthase subunit O, mitochondrial
P25286	<i>Atp6v0a1</i>	V-type proton ATPase 116 kDa subunit a isoform 1
P62815	<i>Atp6v1b2</i>	V-type proton ATPase subunit B, brain isoform
O08839	<i>Bin1</i>	Myc box-dependent-interacting protein 1
P01026	<i>C3</i>	Complement C3
P54290	<i>Cacna2d1</i>	Voltage-dependent calcium channel subunit alpha-2/delta-1
P62161	<i>Calm1</i>	Calmodulin-1
P11275	<i>Camk2a</i>	Calcium/calmodulin-dependent protein kinase type II subunit alpha
P08413	<i>Camk2b</i>	Calcium/calmodulin-dependent protein kinase type II subunit beta
P15791	<i>Camk2d</i>	Calcium/calmodulin-dependent protein kinase type II subunit delta
P11730	<i>Camk2g</i>	Calcium/calmodulin-dependent protein kinase type II subunit gamma
Q63092	<i>Camkv</i>	CaM kinase-like vesicle-associated protein
P97536	<i>Cand1</i>	Cullin-associated NEDD8-dissociated protein 1
Q3T1K5	<i>Capza2</i>	F-actin-capping protein subunit alpha-2 F-actin-capping protein subunit alpha

---

Q5XI32	<i>Capzb</i>	F-actin-capping protein subunit beta
Q7TPB1	<i>Cct4</i>	T-complex protein 1 subunit delta
Q68FQ0	<i>Cct5</i>	T-complex protein 1 subunit epsilon
Q03114	<i>Cdk5</i>	Cyclin-dependent-like kinase 5
Q99JD4	<i>Clasp2</i>	CLIP-associating protein 2 TOG domain-containing protein
P13233	<i>Cnp</i>	2',3'-cyclic-nucleotide 3'-phosphodiesterase
Q63198	<i>Cntn1</i>	Contactin-1
P97536	<i>Cntnap1</i>	Contactin-associated protein 1
P10888	<i>Cox4i1</i>	Cytochrome c oxidase subunit 4 isoform 1, mitochondrial
P11240	<i>Cox5a</i>	Cytochrome c oxidase subunit 5A, mitochondrial
P12075	<i>Cox5b</i>	Cytochrome c oxidase subunit 5B, mitochondrial
P35171	<i>Cox7a2</i>	Cytochrome c oxidase subunit 7A2, mitochondrial
P19139	<i>Csnk2a1</i>	Casein kinase II subunit alpha
Q9WU82	<i>Cttnb1</i>	Catenin beta-1
O08875	<i>Dclk1</i>	Serine/threonine-protein kinase DCLK1
		Dihydrolipoyllysine-residue succinyltransferase component of 2-
Q01205	<i>Dlst</i>	oxoglutarate dehydrogenase complex, mitochondrial
P21575	<i>Dnm1</i>	Dynamin-1
O35303	<i>Dnm1l</i>	Dynamin-1-like protein
P38650	<i>Dync1h1</i>	Cytoplasmic dynein 1 heavy chain 1
P62630	<i>Eef1a1</i>	Elongation factor 1-alpha 1
P05197	<i>Eef2</i>	Elongation factor 2
B5DEH2	<i>Erlin2</i>	Erlin-2
Q5XI81	<i>Fxr1</i>	Fragile X mental retardation syndrome-related protein 1
P97874	<i>Gak</i>	Cyclin-G-associated kinase
P04897	<i>Gnai2</i>	Guanine nucleotide-binding protein G(i) subunit alpha-2
P59215	<i>Gnao1</i>	Guanine nucleotide-binding protein G(o) subunit alpha
		Guanine nucleotide-binding protein G(s) subunit alpha isoforms
P63095	<i>Gnas</i>	short
P19627	<i>Gnaz</i>	Guanine nucleotide-binding protein G(z) subunit alpha
Q68FP1	<i>Gsn</i>	Gelsolin
Q64428	<i>Hadha</i>	Trifunctional enzyme subunit alpha, mitochondrial
Q60587	<i>Hadhb</i>	Trifunctional enzyme subunit beta, mitochondrial
Q794E4	<i>Hnrnpf</i>	Heterogeneous nuclear ribonucleoprotein F
		Heterogeneous nuclear ribonucleoprotein H RRM domain-
Q8VHV7	<i>Hnrnph1</i>	containing protein
Q6AY09	<i>Hnrnph2</i>	Heterogeneous nuclear ribonucleoprotein H2
P63039	<i>Hspd1</i>	60 kDa heat shock protein, mitochondrial
Q63617	<i>Hyou1</i>	Hypoxia up-regulated protein 1
P56574	<i>Idh2</i>	Isocitrate dehydrogenase [NADP], mitochondrial
Q99NA5	<i>Idh3a</i>	Isocitrate dehydrogenase [NAD] subunit alpha, mitochondrial
P41565	<i>Idh3g</i>	Isocitrate dehydrogenase [NAD] subunit gamma 1, mitochondrial
Q3KR86	<i>Immt</i>	MICOS complex subunit Mic60
P23565	<i>Ina</i>	Alpha-internexin IF rod domain-containing protein
Q63416	<i>Itih3</i>	Inter-alpha-trypsin inhibitor heavy chain H3
Q62813	<i>Lsamp</i>	Limbic system-associated membrane protein

---

---

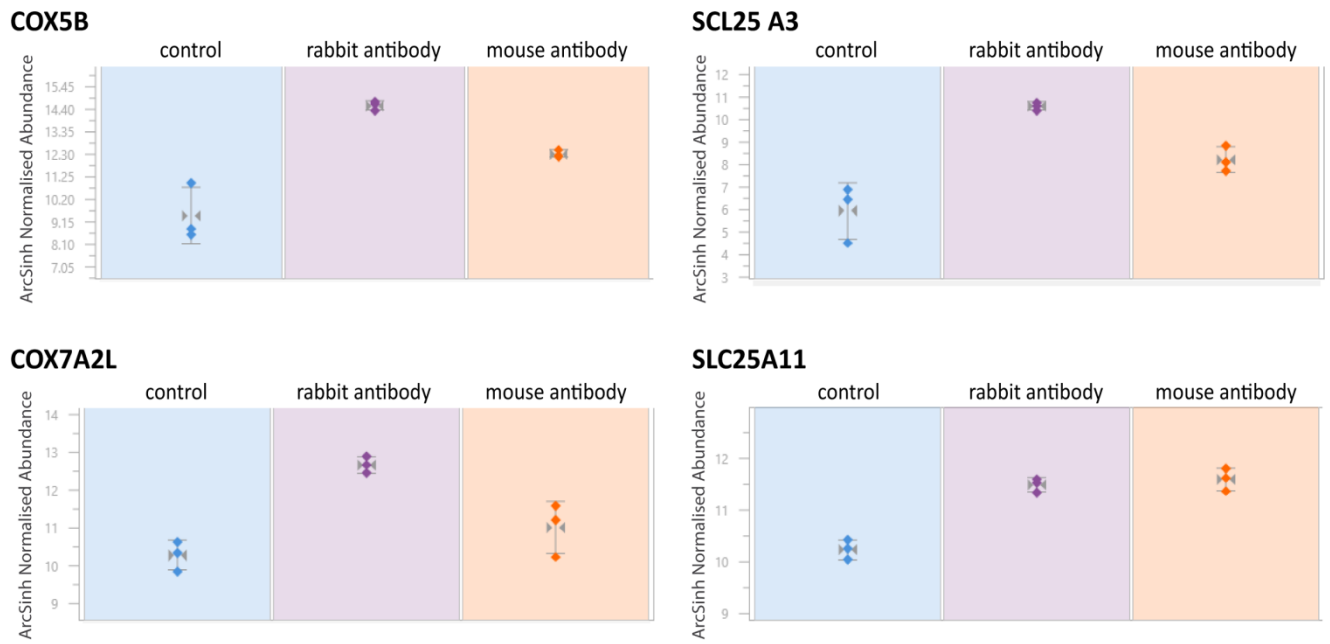
D3ZHV2	<i>Macf1</i>	Microtubule-actin cross-linking factor 1
O08873	<i>Madd</i>	MAP kinase-activating death domain protein
P15205	<i>Map1b</i>	Microtubule-associated protein 1B
Q63560	<i>Map6</i>	Microtubule-associated protein 6
Q00566	<i>Mecp2</i>	Methyl-CpG-binding protein 2
Q9JLT0	<i>Myh10</i>	Myosin-10
Q62812	<i>Myh9</i>	Myosin-9 Myosin_tail_1 domain-containing protein
Q64122	<i>MyI9</i>	Myosin regulatory light polypeptide 9
Q9QYF3	<i>Myo5a</i>	Unconventional myosin-Va
P13596	<i>Ncam1</i>	Neural cell adhesion molecule 1
Q561S0	<i>Ndufa10</i>	NADH dehydrogenase [ubiquinone] 1 alpha subcomplex subunit 10, mitochondrial
Q5BK63	<i>Ndufa9</i>	NADH dehydrogenase [ubiquinone] 1 alpha subcomplex subunit 9, mitochondrial
Q66HF1	<i>Ndufs1</i>	NADH-ubiquinone oxidoreductase 75 kDa subunit, mitochondrial NADH dehydrogenase [ubiquinone] iron-sulfur protein 2, mitochondrial
Q641Y2	<i>Ndufs2</i>	mitochondrial
P19234	<i>Ndufv2</i>	NADH dehydrogenase [ubiquinone] flavoprotein 2, mitochondrial
P16884	<i>Nefh</i>	Neurofilament heavy polypeptide
P19527	<i>Nefl</i>	Neurofilament light polypeptide
P12839	<i>Nefm</i>	Neurofilament medium polypeptide
Q9QUL6	<i>Nsf</i>	Vesicle-fusing ATPase
Q62718	<i>Ntm</i>	Neurotrimin
Q2TA68	<i>Opa1</i>	Dynamin-like 120 kDa protein, mitochondrial
Q9EPH8	<i>Pabpc1</i>	Polyadenylate-binding protein 1
P52873	<i>Pc</i>	Pyruvate carboxylase, mitochondrial Pyruvate dehydrogenase E1 component subunit beta, mitochondrial
P49432	<i>Pdhb</i>	mitochondrial
P47858	<i>Pfkm</i>	ATP-dependent 6-phosphofructokinase, muscle type
P47860	<i>Pfkp</i>	ATP-dependent 6-phosphofructokinase, platelet type
O08662	<i>Pi4ka</i>	Phosphatidylinositol 4-kinase alpha
P30427	<i>Plec</i>	Plectin
P86252	<i>Pura</i>	Transcriptional activator protein Pur-alpha
Q6RUV5	<i>Rac1</i>	Ras-related C3 botulinum toxin substrate 1
Q62703	<i>Rcn2</i>	Reticulocalbin-2
P23358	<i>Rpl12</i>	60S ribosomal protein L12
P47198	<i>Rpl22</i>	60S ribosomal protein L22
P61354	<i>Rpl27</i>	60S ribosomal protein L27
P50878	<i>Rpl4</i>	60S ribosomal protein L4
P19945	<i>Rplp0</i>	60S acidic ribosomal protein P0
P62282	<i>Rps11</i>	40S ribosomal protein S11
P62250	<i>Rps16</i>	40S ribosomal protein S16
P62703	<i>Rps4x</i>	40S ribosomal protein S4 40S ribosomal protein S4, X isoform
Q6AYT3	<i>Rtcb</i>	RNA-splicing ligase RtcB homolog
Q5PPJ9	<i>Sh3glb2</i>	Endophilin-B2
Q63633	<i>Slc12a5</i>	Solute carrier family 12 member 5

---

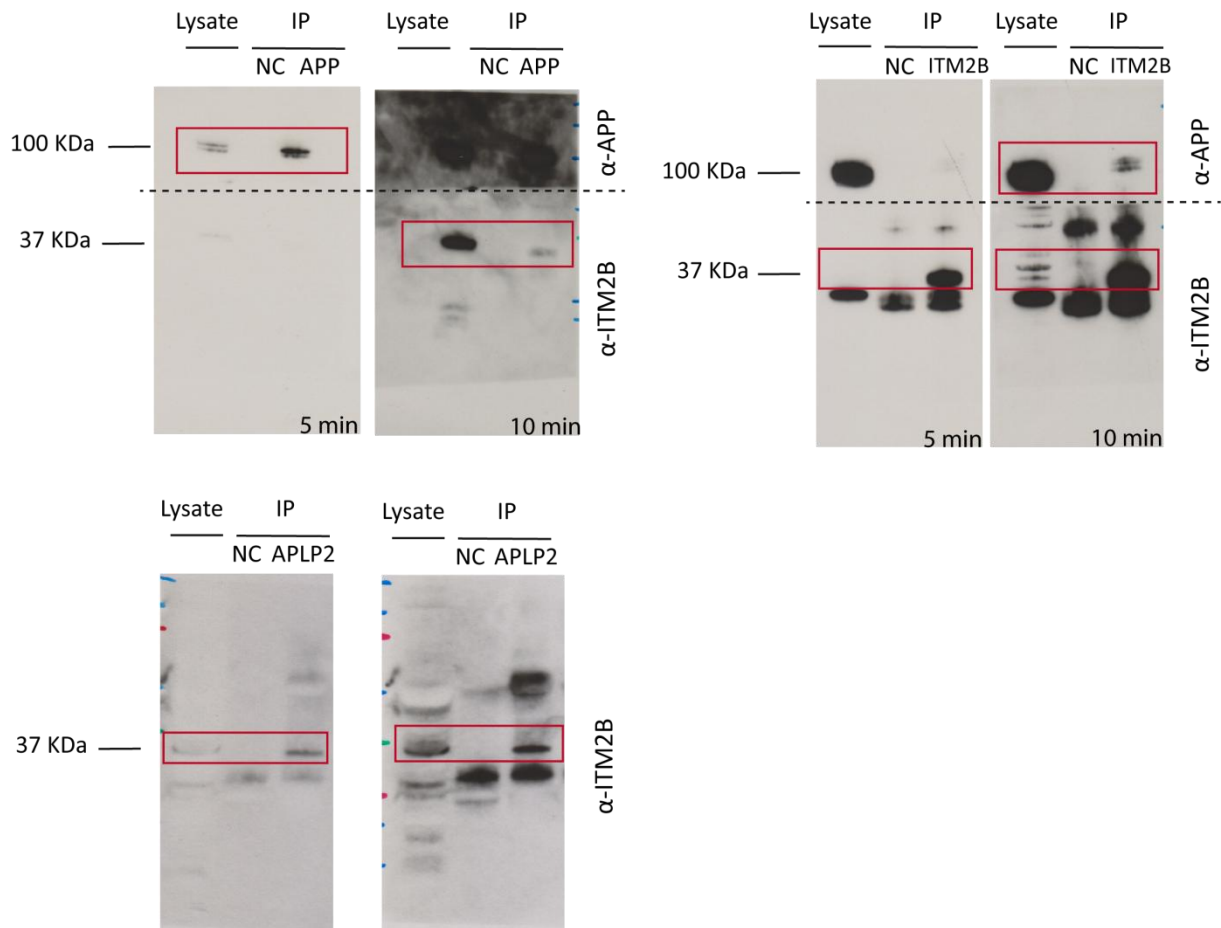
---

P97700	<i>Slc25a11</i>	Mitochondrial 2-oxoglutarate/malate carrier protein
P16036	<i>Slc25a3</i>	Phosphate carrier protein, mitochondrial
P11167	<i>Slc2a1</i>	Solute carrier family 2, facilitated glucose transporter member 1
P16086	<i>Sptan1</i>	Spectrin alpha chain, non-erythrocytic 1
Q9QWN8	<i>Sptbn2</i>	Spectrin beta chain, non-erythrocytic 2
Q9QXY2	<i>Srcin1</i>	SRC kinase signaling inhibitor 1
Q4FZT0	<i>Stoml2</i>	Stomatin-like protein 2, mitochondrial
P61265	<i>Stx1b</i>	Syntaxin-1B
P61765	<i>Stxbp1</i>	Syntaxin-binding protein 1
P13086	<i>Suclg1</i>	Succinate--CoA ligase [ADP/GDP-forming] subunit alpha, mitochondrial Heterogeneous nuclear ribonucleoprotein Q RRM domain-containing protein
Q7TP47	<i>Syncrip</i>	
P70566	<i>Tmod2</i>	Tropomodulin-2
P09495	<i>Tpm4</i>	Tropomyosin alpha-4 chain
P68370	<i>Tuba1a</i>	Tubulin alpha-1A chain
Q5XIF6	<i>Tuba4a</i>	Tubulin alpha-4A chain
Q6AY56	<i>Tuba8</i>	Tubulin alpha-8 chain
P85108	<i>Tubb2a</i>	Tubulin beta-2A chain
Q3KRE8	<i>Tubb2b</i>	Tubulin beta-2B chain
Q4QRB4	<i>Tubb3</i>	Tubulin beta-3 chain
Q6P9T8	<i>Tubb4b</i>	Tubulin beta-4B chain
P69897	<i>Tubb5</i>	Tubulin beta-5 chain
P85834	<i>Tufm</i>	Elongation factor Tu Elongation factor Tu, mitochondrial
P32551	<i>Uqcrc2</i>	Cytochrome b-c1 complex subunit 2, mitochondrial
Q7TQ16	<i>Uqcrcq</i>	Cytochrome b-c1 complex subunit 8
Q9Z2L0	<i>Vdac1</i>	Voltage-dependent anion-selective channel protein 1
P81155	<i>Vdac2</i>	Voltage-dependent anion-selective channel protein 2
Q9R1Z0	<i>Vdac3</i>	Voltage-dependent anion-selective channel protein 3
P31000	<i>Vim</i>	Vimentin
Q793F9	<i>Vps4a</i>	Vacuolar protein sorting-associated protein 4A
Q9ERH3	<i>Wdr7</i>	WD repeat-containing protein 7
P68255	<i>Ywhaq</i>	14-3-3 protein theta

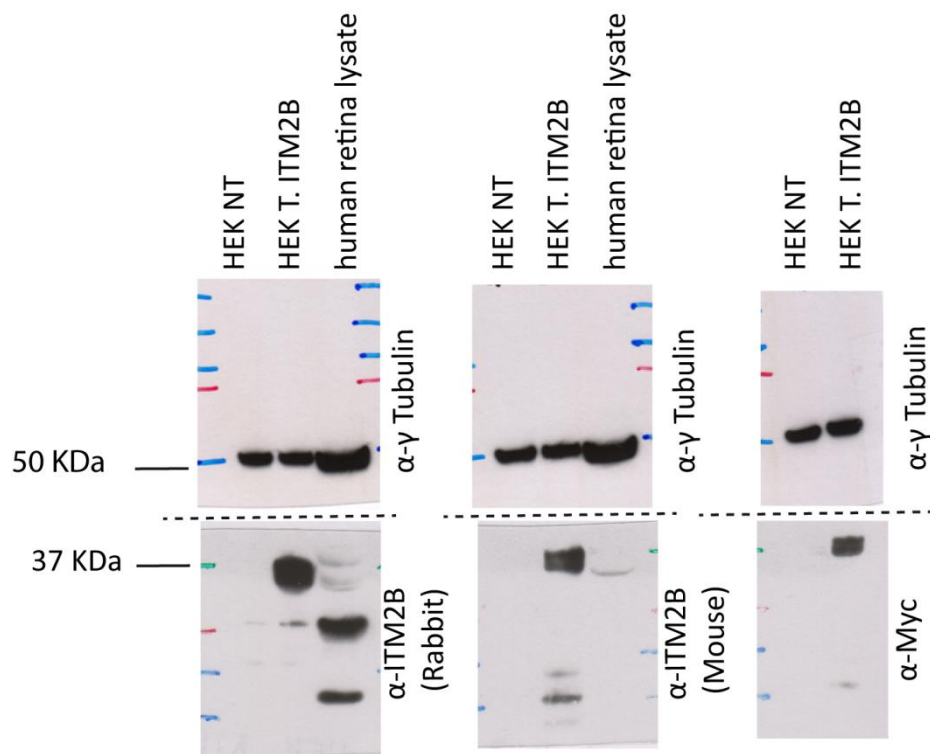
---



**Supplementary Figure S3.** Mitochondrial proteins identified with both antibodies in the ITM2B interactome and also present in the ITM2B rat brain interactome. Graphical representation of protein abundance purified with the control unspecific antibody, the rabbit antibody and the mouse antibody using Progenesis Q1 software.



**Supplementary Figure S4.** Original blots referring to Figure 3B. Red boxes highlight the regions of the immunoblots selected for presentation in the Figure 3B. Lysate: retinal protein extract; IP: immunoprecipitation; NC: negative control; α-: indicates the antibody used for the staining. Black dotted lines indicate where membranes were cut.



**Supplementary Figure S5.** Original blots referring to Figure 7d. α-: indicates the antibody used for the staining. Black dotted lines indicate where membranes were cut.

**Supplementary Table S11:** PCR protocol and reaction for *ITM2B* short form

PCR Mix		Cycle conditions
Q5 <sup>®</sup> High-Fidelity 2X Master Mix	12.5 $\mu$ l	98 °C 1 min
1shortF	1.25 $\mu$ l	98 °C 10s
1shortR	1.25 $\mu$ l	63 °C 30s
H <sub>2</sub> O	8 $\mu$ l	72 °C 20s
Human Retina QUICK-Clone cDNA	1 $\mu$ l (2 ng)	72 °C 2 min
		10 °C $\infty$
Total	24 $\mu$ l	

X40

**Supplementary Table S12:** PCR protocol and reaction for *ITM2B* long form

PCR Mix		Cycle conditions
Mix 2 mM	6.5 $\mu$ l	95 °C 15 min
1longF	0.5 $\mu$ l	95 °C 45s
1longR	0.5 $\mu$ l	60 °C 1 min
H <sub>2</sub> O	3 $\mu$ l	72 °C 1 min
Human Retina QUICK-Clone cDNA	2 $\mu$ l (4 ng)	72 °C 10 min
		10 °C $\infty$
Total	12.5 $\mu$ l	

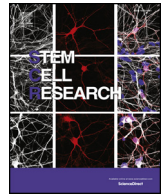
X30

## Supplementary Reference

- 1 Martins, F. *et al.* Identification and characterization of the BRI2 interactome in the brain. *Scientific reports* **8**, 3548, doi:10.1038/s41598-018-21453-3 (2018).

### **3. Generation of human induced pluripotent stem cell lines from a patient with ITM2B-related retinal dystrophy and a non mutated brother**

In order to develop our disease modeling strategy, we first generated iPSC lines from fibroblasts of an affected RD subject and from one unaffected sibling. Subsequently, iPSC lines were characterized for the absence of chromosomal aberration, their pluripotency and for ITM2B genotype.



Lab Resource: Multiple Cell Lines

## Generation of human induced pluripotent stem cell lines from a patient with ITM2B-related retinal dystrophy and a non mutated brother

Juliette Wohlschlegel<sup>a,\*</sup>, Camille Letellier<sup>a</sup>, Bingqian Liu<sup>a</sup>, Cécile Méjécase<sup>a</sup>,  
Amélie Slembrouck-Brec<sup>a</sup>, Christel Condroyer<sup>a</sup>, Christelle Michiels<sup>a</sup>, José-Alain Sahel<sup>a,b,c,d,e</sup>,  
Sacha Reichman<sup>a</sup>, Christina Zeitz<sup>a</sup>, Olivier Goureau<sup>a</sup>, Isabelle Audo<sup>a,b,\*</sup>

<sup>a</sup> INSERM, CNRS, Institut de la Vision, Sorbonne Université, 17 rue Moreau, Paris, F-75012, France

<sup>b</sup> CHNO des Quinze-Vingts, INSERM-DGOS CIC 1423, 28 rue de Charenton, Paris, F-75012, France

<sup>c</sup> Fondation Ophtalmologique Adolphe de Rothschild, Paris, F-75019, France

<sup>d</sup> Académie des Sciences-Institut de France, Paris, F-75006, France

<sup>e</sup> Department of Ophthalmology, The University of Pittsburgh School of Medicine, Pittsburg, PA, 15213, United States

### ABSTRACT

Human induced pluripotent stem cell (iPSC) lines were generated from fibroblasts of a patient affected with an autosomal dominant retinal dystrophy carrying the mutation c.782A>C, p.Glu261Ala in *ITM2B* and from an unaffected brother. Three different iPSC lines were generated and characterized from primary dermal fibroblasts of the affected subject and two from the unaffected brother. All iPSC lines expressed the pluripotency markers, were able to differentiate into the three germ layers and presented normal karyotypes. This cellular model will provide a powerful tool to study this retinal dystrophy and better understand the role of *ITM2B*.

Resource table		Method of modification	N/A
Unique stem cell lines identifier	IDVi003-A IDVi003-B IDVi003-C IDVi004-A IDVi004-B	Name of transgene or resistance	N/A
Alternative names of stem cell lines	ITM2B-5286-3 (IDVi003-A) ITM2B-5286-12 (IDVi003-B) ITM2B-5286-19 (IDVi003-C) ITM2B-5269-1 (IDVi004-A) ITM2B-5269-2 (IDVi004-B)	Inducible/constitutive system	N/A
Institution	Institut de la Vision, Paris, France	Date archived/stock date	Date cell line archived or deposited in repository
Contact information of distributor	Isabelle Audo isabelle.audo@inserm.fr Juliette.wohlschlegel@inserm.fr	Cell line repository/bank	N/A
Type of cell lines	Human induced pluripotent stem cells (hiPSC)	Ethical approval	Approval by French regulatory agencies: CPP Ile de France V (2012-A01333-40; P12-02) and the ANSM (B121362-32)
Origin	Human		
Cell Source	Dermal fibroblasts		
Clonality	Clonal		
Method of reprogramming	Transgene free (Sendai virus)		
Multiline rationale	Control and disease pair with three different clones		
Gene modification	Yes		
Type of modification	Hereditary		
Associated disease	ITM2B-related retinal dystrophy		
Gene/locus	<i>ITM2B</i> (MIM *603904), c.782A>C; p.Glu261Ala		

### 1. Resource utility

All the cell lines presented herein constitute a unique tool for disease modeling and for studying ITM2B-related retinal dystrophy. By generating retinal organoids, these cell lines will help to better understand the role of ITM2B in the retina and its associated pathogenic mechanisms.

### 2. Resource details

ITM2B (also named BRI or BRI2 encoding the Integral Membrane Protein 2B) is a ubiquitous protein of 266 amino acids. The function of ITM2B remains unknown and has never been studied in the retina. In 2014, our group identified through whole exome sequencing a missense

\* Corresponding authors at: Institut de la Vision, 17 rue Moreau, Paris, F-75012, France.

E-mail addresses: [Juliette.wohlschlegel@inserm.fr](mailto:Juliette.wohlschlegel@inserm.fr) (J. Wohlschlegel), [Isabelle.audo@inserm.fr](mailto:Isabelle.audo@inserm.fr) (I. Audo).

<https://doi.org/10.1016/j.scr.2019.101625>

Received 19 September 2019; Received in revised form 2 October 2019; Accepted 14 October 2019

Available online 05 November 2019

1873-5061/ © 2019 Published by Elsevier B.V. This is an open access article under the CC BY-NC-ND license (<http://creativecommons.org/licenses/by-nc-nd/4.0/>).

change [c.782A>C; p.Glu261Ala] in *ITM2B*, co-segregating in a large pedigree with an unusual autosomal dominant retinal-restricted disease (RD) (Audo et al., 2014). Affected subjects have a very peculiar retinal degeneration combining retinal ganglion cell (RGC) abnormalities, inner retinal dysfunction, progressive cone degeneration and hyperreflective material within the retina (Audo et al., 2014).

Interestingly, there were two previous reports of *ITM2B* mutations in two large pedigrees with autosomal dominant Alzheimer-like dementia and cerebral amyloid deposits namely, the familial British dementia (Vidal et al., 1999) and the familial Danish dementia (Vidal et al., 2000). In these cases, the respective mutations lead to a longer protein at the C-terminus. Of note, none of the patients with *ITM2B*-associated RD have dementia and there was no report of retinal degeneration in the dementia families apart from a distinct vascular angiopathy.

In this study, skin fibroblasts from an affected 53-year-old man and his unaffected 49-year-old brother were reprogrammed into iPSCs using a non-integrative Sendai virus approach containing the following reprogramming factors OCT3/4, SOX2, CMYC, and KLF4. From several emerging iPSC clones, three different cell lines for the affected and two different cell lines for the unaffected subject were chosen and characterized. All the iPSC lines expressed the pluripotency markers as the transcription factors OCT4 and NANOG, as well as the cell surface markers SSEA4 and TRA1-81 (Fig. 1A; scale bar: 100 µm) and displayed specific ES-like morphology (Fig. 1B; scale bar: 100 µm). The presence of the c.782A>C substitution in exon 6 of *ITM2B* was also confirmed in iPSC lines derived from the affected subject and its absence in all the lines derived from the unaffected brother (Fig. 1C). Single nucleotide polymorphism (SNP) genotyping confirmed the genomic integrity of all the cell lines (Supplementary data) and >99% identity between cell lines and their associated fibroblasts (Fig. 1D). Cell culture was tested negative for *Mycoplasma* contamination (Fig. 1E). The capacity of differentiation in the 3-germ layers was demonstrated by RT-qPCR using Scorecard analysis showing the expression of specific markers after spontaneous embryoid body differentiation (Fig. 1F). Finally, the absence of genomic integration of Sendai virus and exogenous reprogramming factors was controlled for all iPSC lines by qPCR after 10 passages (Fig. 1G). The characterization of iPSCs is summarized in Tables 1 and 2.

We have successfully generated and characterized iPSC lines derived from an individual affected with an unusual retinal dystrophy carrying a mutation in *ITM2B* and from his unaffected brother.

These new human iPSC lines will provide a powerful tool for disease modeling to better understand the role of *ITM2B* in the retina as well in as other tissues.

### 3. Materials and methods

#### 3.1. Human fibroblast culture and reprogramming

Human dermal fibroblasts from the affected and unaffected subject (control) were obtained at the Quinze-Vingts hospital after skin biopsy and expanded as described before (Terray et al., 2017). They were subsequently reprogrammed into iPSCs using the CytoTune® Sendai reprogramming vectors OCT3/4, SOX2, CMYC, and KLF4 (Thermo Fisher Scientific) (Terray et al., 2017). The iPSC colonies obtained were first expanded under feeder conditions and then adapted under feeder free conditions following (Reichman et al., 2017) protocol. From patient and control fibroblasts, respectively three and two iPSC lines were generated and characterized (mutated cell lines: ITM2B-5286-3 (IDVi003-A); ITM2B-5286-12 (IDVi003-B); ITM2B-5286-19 (IDVi003-C); control cell lines: ITM2B-5269-1 (IDVi004-A); ITM2B-5269-2 (IDVi004-B) (Table 1).

#### 3.2. Cell culture

iPSCs were grown on vitronectin coating with Essential 8™ (Thermo Fisher Scientific) medium changed every day and passaged once a week using the Gentle Dissociation Reagent Buffer (Stem Cell Technologies). Cells were routinely maintained at 37 °C in a standard (5% CO<sub>2</sub>) air incubator.

#### 3.3. Sequencing and mutation analysis

Genomic DNA extraction was performed for each cell line using the DNeasy Blood & Tissue Kit following the manufacturer's guidelines (Qiagen). PCR amplification and sequencing of exon 6 and flanking regions were performed (Audo et al., 2014).

#### 3.4. Immunofluorescence

Cells were fixed in paraformaldehyde 4% for 15 min. Lamellae were incubated 1h at room temperature (RT) with a blocking buffer (Phosphate Buffer Saline (PBS), 0.2% gelatin, and 0.25% Triton X-100) and overnight at 4 °C with the primary antibody (Table 3). Slides were incubated for 1h at RT with the secondary antibody in blocking buffer with DAPI (Life Technologies). Coverslips were mounted using fluoromount (Sigma-Aldrich) and imaged with an upright confocal microscope (Olympus).

#### 3.5. Real-Time PCR analysis

Total RNAs were extracted using NucleoSpin RNA XS kit (Macherey-Nagel) and cDNA synthesized using the QuantiTect reverse transcription kit (Qiagen) following the manufacturer's recommendations. RT-qPCR analysis was performed on 7500 Fast System real-time PCR machine (Applied Biosystems) with TaqMan Gene expression Master Mix (Life Technologies) following the manufacturer's instructions (Table 3). All primers and MGB (Minor Groove Binder) probes labeled with FAM (fluorescein) for amplification were purchased from Life Technologies. Ct analysis results were normalized against the expression of the 18S. Positive control corresponds to infected fibroblasts and negative controls correspond to the original fibroblasts from the unaffected and affected subjects.

#### 3.6. Scorecard assay

*In vitro* differentiation capacity was tested by spontaneous differentiation of embryoid bodies (EBs). Cells were cultured in suspension in ultra-low adherence plate. EBs were fed with Essential 6® medium (Thermo Fisher Scientific) every 2–3 days during 20 days and were maintained in the incubator (37 °C, 5% CO<sub>2</sub>). On day 0 and day 20 RNA from EBs and corresponding iPSCs were extracted using NucleoSpin RNA XS kit (Macherey-Nagel) and analyzed using the Scorecard technique (Thermo Fisher Scientific).

#### 3.7. SNP analysis

Genomic DNA (100 ng/µl) was extracted from the five iPSC lines and the corresponding fibroblasts (Qiagen). The samples were analyzed by Single Nucleotide Polymorphism arrays (SNP) using Illumina InfiniumCore-24 technique (Illumina) at IntegraGen (Evry, France). LogR ratio plots were generated in GenomeStudio software (Illumina, Inc.) to compare each iPSC lines to parental fibroblasts. The percentage of SNP concordance between fibroblasts and corresponding cell lines was assessed for each line.

#### 3.8. Mycoplasma

The absence of *Mycoplasma* in human iPSC culture was tested using

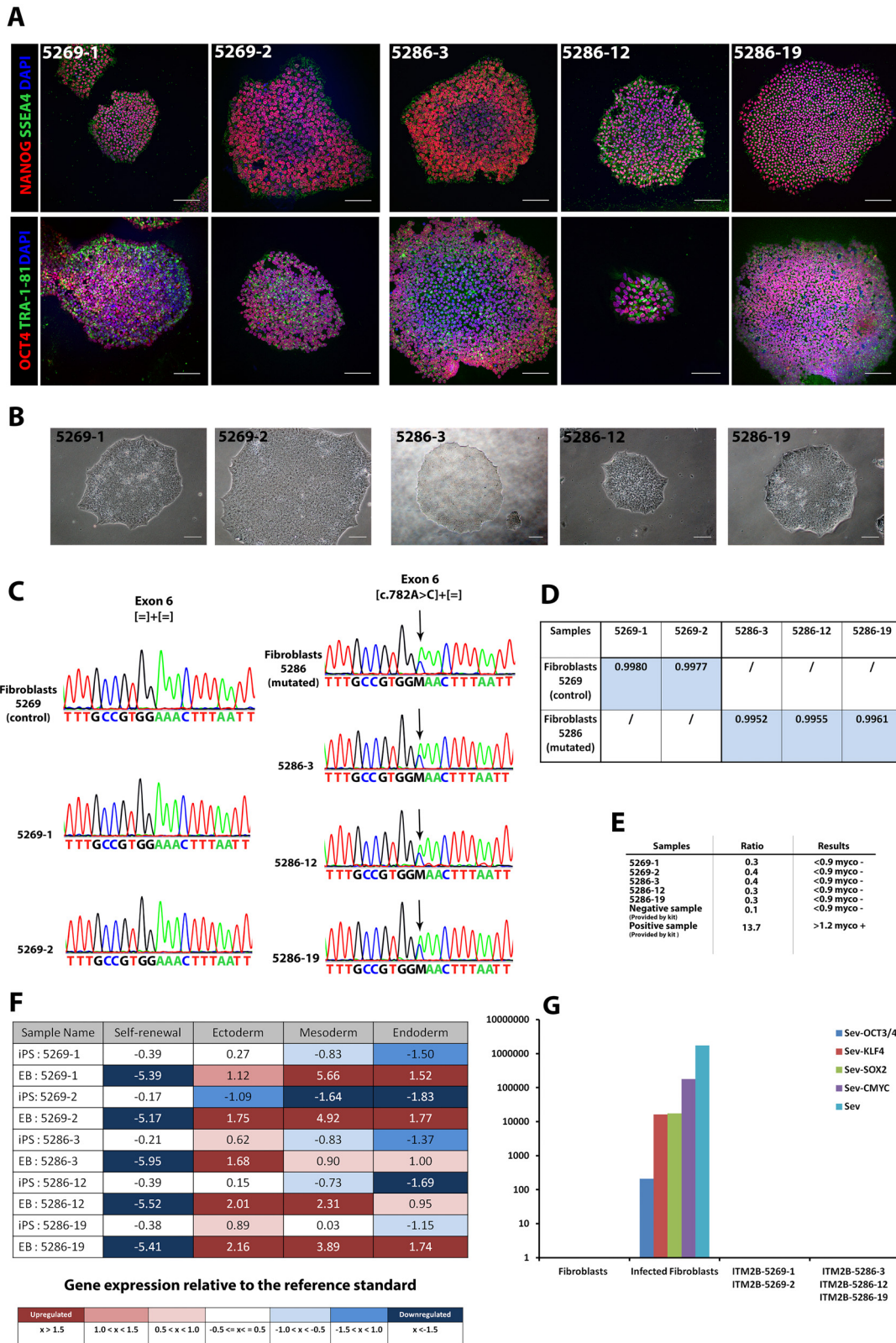


**Fig. 1.** Characterization of all the ITM2B-derived iPSC lines. A) Immunofluorescence against pluripotent specific proteins OCT4, NANOG, and surface markers SSEA-4, and TRA-1-81. DAPI stained the nucleus (blue). Scale bar: 100  $\mu$ m. B) Phase contrast imaging of cells showing typical round shape colonies under feeder-free condition. C) Electropherograms showing the heterozygous mutation, c.782A > C, of *ITM2B* present in the 5286-3, 5286-12, 5286-19 iPSC lines and absent in the 5269-1 and 5269-2 iPSC lines. D) Percentage of SNP concordance between fibroblasts and corresponding cell lines assessed for each line. E) Negative Mycoplasma test for all the iPSC lines. F) Embryoid bodies formation *in vitro* expressing the three germ layers' markers for endoderm, mesoderm and ectoderm. G) Quantitative PCR verification of Sendai virus and exogenous reprogramming factors clearance in all iPSC lines after 10 passages. SeV transduced fibroblasts were used as positive control.

**Table 1**  
Summary of lines.

iPSC line names	Abbreviation in figures	Gender	Age	Ethnicity	Genotype of locus	Disease
ITM2B-5286-3 (IDVi003-A)	5286-3	Male	53	Caucasian	<i>ITM2B</i> Exon 6 (c.782A>C, p.Glu261Ala)	Retinal Dystrophy
ITM2B-5286-12 (IDVi003-B)	5286-12	Male	53	Caucasian	<i>ITM2B</i> Exon 6 (c.782A>C, p.Glu261Ala)	Retinal Dystrophy
ITM2B-5286-19 (IDVi003-C)	5286-19	Male	53	Caucasian	<i>ITM2B</i> Exon 6 (c.782A>C, p.Glu261Ala)	Retinal Dystrophy
ITM2B-5269-1 (IDVi004-A)	5269-1	Male	49	Caucasian	<i>ITM2B</i> No mutation	Unaffected
ITM2B-5269-2 (IDVi004-B)	5269-2	Male	49	Caucasian	<i>ITM2B</i> No Mutation	Unaffected

**Table 2**  
Characterization and validation.

Classification	Test	Result	Data
Morphology	Photography	Human ESC-like normal appearance	Fig. 1 panel B
Phenotype	Qualitative analysis	Expression of pluripotency markers: OCT4, NANOG, SSEA4 and TRA1-81	Fig. 1 panel A
	Immunocytochemistry		
	Qualitative analysis Scorcard	Expression of self-renewal markers and are undifferentiated	Fig. 1 panel F
	Quantitative analysis	Expression of NANOG (ITM2B-5286-3 = 96%, ITM2B-5286-12 = 96%, ITM2B-5286-19 = 98%; ITM2B-5269-1 = 91%, ITM2B-5269-2 = 90%).	Fig. 1 panel A
Immunocytochemistry counting		Expression of OCT4 (ITM2B-5286-3 = 95%, ITM2B-5286-12 = 97%, ITM2B-5286-19 = 94 %; ITM2B-5269-1 = 95%, ITM2B-5269-2 = 98%,)	
Genotype	SNP analysis InfiniumCore-24	Normal Karyotype 46 XX Resolution: 0.5 Mb	Supplementary File 1
Identity	SNP analysis InfiniumCore-24	Identical genotypes for iPSC lines and parental fibroblasts.	Fig. 1 panel D
	Genetic analysis		
Mutation analysis (IF APPLICABLE)	Sanger Sequencing	c.782A>C, p.Glu261Ala in <i>ITM2B</i> present in all iPSC lines derived from fibroblast of the affected patient and absent in all iPSC lines derived from fibroblasts of the unaffected patient.	Fig. 1 panel C
Microbiology and virology	Southern Blot OR WGS	N/A	
	Mycoplasma testing by luminescence.	All iPSC lines are negative.	Fig. 1 panel E
Differentiation potential	Embryoid body formation and Scorecard analysis.	Expression of markers of the three germs layers after 20 days of differentiation.	Fig. 1 panel F
Donor screening (OPTIONAL)	HIV 1 + 2 Hepatitis B, Hepatitis C	N/A	
Genotype additional info (OPTIONAL)	Blood group genotyping	N/A	
	HLA tissue typing	N/A	

**Table 3**  
Reagents details.

Antibodies used for immunocytochemistry/flow-citometry	Antibody	Dilution	Company Cat # and RRID
Pluripotency Markers	Rabbit anti NANOG	1:200	Cell Signaling Technology Cat# 4903, <b>RRID:AB_10559205</b>
Pluripotency Markers	Rabbit anti OCTO4	1:200	Cell Signaling Technology Cat# 2840, <b>RRID:AB_2167691</b>
Pluripotency Markers	Mouse anti SSEA4	1:200	Cell Signaling Technology Cat# 4755, <b>RRID:AB_1264259</b>
Pluripotency Markers	Mouse anti TRA-1-81	1:200	Cell Signaling Technology Cat# 4745, <b>RRID:AB_2119060</b>
Secondary antibodies	Donkey Anti-Rabbit IgG	1:1000	Jackson ImmunoResearch Cat# 711-165-152, <b>RRID:AB_2616595</b>
Secondary antibodies	Donkey Anti-Mouse IgG	1:1000	Jackson ImmunoResearch Cat# 711-545-150, <b>RRID:AB_2340846</b>
Secondary antibodies	Goat Anti-Mouse IgM	1:1000	ThermoFisher Scientific Cat# A-21042, <b>RRID:AB_2535711</b>

Primers	Target	Forward/Reverse primer (5' – 3')
Elimination of Sendai virus transgenes (qPCR - TaqMan)	SEV-CMYC	Assay ID: Mr04269876_mr
Elimination of Sendai virus transgenes (qPCR – TaqMan)	SEV-OCT3/4	Assay ID: Mr04269878_mr
Elimination of Sendai virus transgenes (qPCR – TaqMan)	SEV-KLF4	Assay ID: Mr04421256_mr
Elimination of Sendai virus transgenes (qPCR – TaqMan)	SEV	Assay ID: Mr04269880_mr
Elimination of Sendai virus transgenes (qPCR – TaqMan)	SEV-SOX2	Assay ID: Mr04269881_mr
House-Keeping Gene (qPCR-TaqMan)	18S	Assay ID: Hs99999901_s1
PCR primers targeted <i>ITM2B</i> mutation	<i>ITM2B</i> exon 6	F1: 5'AGTCAGCCTT ACACGTGCC 3' R1: 5'CTGTTTGCTACTTACATGAAAG 3'

MycoAlert™ MycoPlasma Detection kit (Lonza).

**Supplementary materials**

Supplementary material associated with this article can be found, in the online version, at [doi:10.1016/j.scr.2019.101625](https://doi.org/10.1016/j.scr.2019.101625).

**Declaration of Competing Interest**

The authors declare that they have no known competing financial interests or personal relationships that could have appeared to influence the work reported in this paper.

**References**

Audo, I., Bujakowska, K., Orhan, E., El Shami, S., Sennlaub, F., Guillonnet, X., Zeitz, C., 2014. The familial dementia gene revisited: a missense mutation revealed by whole-

- exome sequencing identifies ITM2B as a candidate gene underlying a novel autosomal dominant retinal dystrophy in a large family. *Hum. Mol. Genet.* 23 (2), 491–501. <https://doi.org/10.1093/hmg/ddt439>.
- Reichman, S., Slembrouck, A., Gagliardi, G., Chaffiol, A., Terray, A., Nanteau, C., Goureau, O., 2017. Generation of storable retinal organoids and retinal pigmented epithelium from adherent human iPS cells in Xeno-Free and feeder-free conditions. *Stem Cells* 35 (5), 1176–1188. <https://doi.org/10.1002/stem.2586>.
- Terray, A., Fort, V., Slembrouck, A., Nanteau, C., Sahel, J.A., Reichman, S., Goureau, O., 2017. Establishment of an induced pluripotent stem (iPS) cell line from dermal fibroblasts of an asymptomatic patient with dominant PRPF31 mutation. *Stem Cell Res.* 25, 26–29. <https://doi.org/10.1016/j.scr.2017.10.007>.
- Vidal, R., Frangione, B., Rostagno, A., Mead, S., Revesz, T., Plant, G., Ghiso, J., 1999. A stop-codon mutation in the BRI gene associated with familial British dementia. *Nature* 399 (6738), 776–781. <https://doi.org/10.1038/21637>.
- Vidal, R., Revesz, T., Rostagno, A., Kim, E., Holton, J.L., Bek, T., Frangione, B., 2000. A decamer duplication in the 3' region of the BRI gene originates an amyloid peptide that is associated with dementia in a Danish kindred. *Proc. Natl. Acad. Sci. U. S. A* 97 (9), 4920–4925. <https://doi.org/10.1073/pnas.080076097>.

## 4. Disease modeling of ITM2B related retinal dystrophy

This part presents the generation of retinal organoids from previously characterized iPSCs. We aimed at performing disease modeling to better characterize the disease development and thus at approaching pathological mechanisms underlying ITM2B-related RD. Although, this work represents the main part of my PhD project and personal dedication, it has also been challenged by several hurdles (constraints inherent to cell culture, covid 19 outbreaks). Nevertheless, we obtained encouraging preliminary data which shed light on other aspects of this complex disorder and will need to be further investigated.

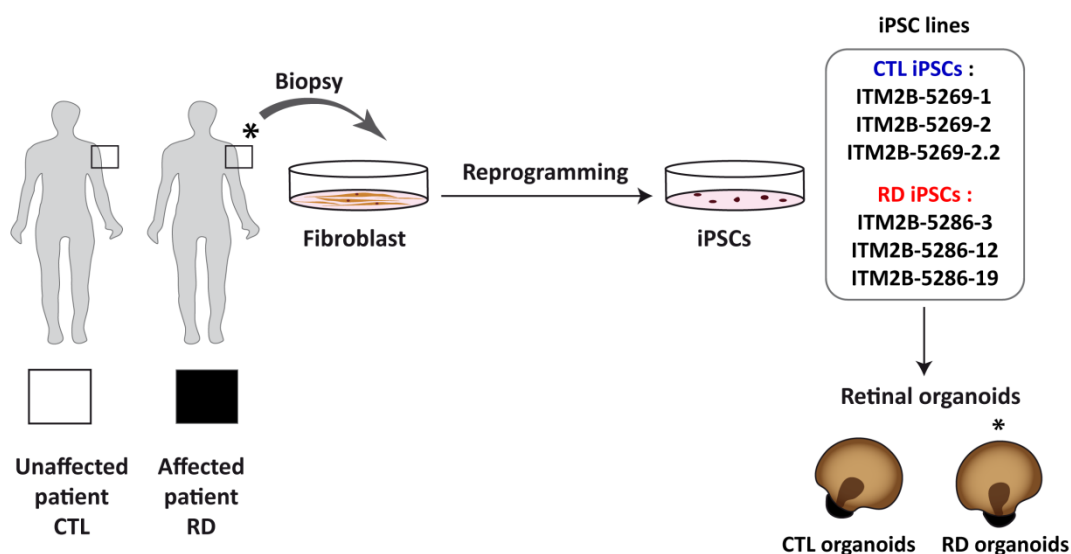


**Figure 18 Generation of iPSC lines from skin fibroblasts of one affected subject and one unaffected sibling.**

Reprogramming was performed with Sendai virus. Respectively, three and two independent clonal lines were generated and isolated for from iPSC derived RD patient and from iPSC derived CTL patient. One sub-clone was also generated from the ITM2B-5269-2 and properly characterized. All cell lines were subsequently differentiated into retinal organoids.

## **Further insights into the Integral membrane protein 2B and its implication in retinal disease**

J. Wohlschlegel<sup>1</sup>, C. Letellier<sup>1</sup>, B. Liu<sup>1</sup>, C. Zeitz<sup>1</sup>, O. Goureau<sup>1</sup>, I. Audo<sup>1,3\*</sup>

1. Sorbonne Université, INSERM, CNRS, Institut de la Vision, 17 rue Moreau, F-75012 Paris, France

2. CHNO des Quinze-Vingts, INSERM-DGOS CIC 1423, 28 rue de Charenton, F-75012 Paris, France

3. Department of Genetics, UCL-Institute of Ophthalmology, 11–43 Bath Street, London EC1V 9EL, UK

## Introduction

Inherited retinal dystrophies (IRDs) are a heterogeneous group of disorders caused by one or more gene defects. So far, mutations in over 200 genes have been implicated in IRDs<sup>1</sup>. However, limited therapeutic options are available for these disorders which lead to progressive visual dysfunction or blindness and are often associated with severe handicap. Deciphering the pathological mechanisms involved in IRDs is an essential key to establish and develop new therapies for these yet incurable conditions.

Through next generation sequencing, our team identified a missense mutation (c.782A>C, p.Glu261Ala) in *ITM2B* (also named *BRI* or *BRI2* encoding the Integral Membrane Protein 2B) in one family affected with an unusual autosomal dominant retinal dystrophy (RD)<sup>2</sup>. Affected subjects present a very unique phenotype which does not resemble any of the previously described IRDs, including retinal ganglion cell (RGC) death, inner retinal dysfunction, and progressive cone degeneration<sup>2</sup>. This was the first time that *ITM2B* was associated with a retina-restricted disease.

However, two other autosomal dominant mutations in *ITM2B* have previously been associated with Alzheimer-like dementia namely Familial British Dementia (MIM# 176500, FBD mutant: c.799T>A; p.Stop267Argext\*11)<sup>3</sup> and FBD and Familial Danish Dementia (MIM# 117300, FDD mutant: c.795-796insTTTAATTTGT; p.Ser266Pheext\*11)<sup>4</sup>. Interestingly, all the identified mutations (i.e. RD, FBD and FDD) are present in the last exon of *ITM2B* encoding for the C-terminal part of the protein. In normal conditions, *ITM2B* is cleaved at the C-terminal part by a furin-like protease, releasing a 23-amino acid secreted peptide called Bri23<sup>5</sup>. In case of FBD and FDD, mutations lead to a longer protein product and subsequently longer secreted peptides respectively termed ABri and ADan. The RD mutation does not affect the length of the protein but is predicted to modify the 3D structure of the secreted peptide<sup>6</sup>. In case of *ITM2B*-related dementia, misfolded peptides form insoluble aggregates and lead to the formation of amyloid plaques in brains of affected subjects<sup>7,8</sup>. *ITM2B* interacts with APP (Amyloid  $\beta$  Precursor Protein)<sup>9,10</sup> in the brain where it may act as a modulator of its processing particularly by acting as an inhibitor of Amyloid  $\beta$  (A $\beta$ ) oligomerization<sup>11</sup>, a major component of amyloid plaques in Alzheimer disease. *ITM2B* also co-localize with APP in the retina<sup>2</sup> and we recently demonstrated their direct interactions through proteomic experiments on postmortem human retina samples<sup>12</sup>.

However, the current knowledge on ITM2B remains limited, particularly in the retina where very few investigations have been conducted. In a recent paper, we reported additional details on the clinical characteristics of the ITM2B-related RD<sup>6</sup> such as possibly progressive cone photoreceptor degeneration and a peculiar hyperreflectivity of the inner retina on spectral domain optical coherence tomography<sup>6</sup>. Of notes, this retinopathy does not seem to be associated with a microangiopathy unlike ocular vascular alterations reported in FDD affected subjects<sup>6,13</sup>. Altogether, these findings outline the unique phenotype associated with the (c.782A>C, p.Glu261Ala) ITM2B mutation which pathogenic mechanisms remains unclear requiring further investigations. Preliminary data on ITM2B as well as the deep phenotyping performed in the ITM2B-related RD raise several questions: does the RD-mutation lead to a decrease in *ITM2B* expression, to a loss of function or to a dominant negative effect? Does it modify the interaction between ITM2B and APP, its major partner and with other putative partners? What is the primary cell type involved with the disease? What represent the hyperreflective material seen on patients' optical coherence tomography?

This past decade induced pluripotent stem cells (iPSCs) have emerged as an interesting tool for disease modeling and represent an alternative to animal model<sup>14,15</sup>. This is particularly interesting for IRDs, since access to retinal tissue is limited and animal models often fail to recapitulate the hallmarks of the disease. iPSCs can be generated from patients, carry the same genetic background and therefore provide an *in vitro* personalized cellular model for human disorders. Recently, several studies used iPSC-derived retinal organoids to perform disease modeling and investigate pathologic mechanisms involved in IRDs<sup>16-18</sup>. However, to our knowledge, no study has been conducted on ITM2B-related RD. In this present study, we used retinal organoids derived from different iPSC lines generated from an affected subject carrying the ITM2B-RD mutation and from an unaffected sibling in order to gain further insights into ITM2B-related retinopathy.

## Results

### ***The RD mutation does not modify ITM2B interaction with APP in a HEK 293 over-expressing system.***

Protein extracts from HEK 293 co-transfected cells over expressing either the wild type or the RD-mutant ITM2B, and APP were submitted to co-immunoprecipitation to document their putative interaction. We demonstrated that wild type (WT) ITM2B and APP interact in this over expressing system (Figure 1A) as suggested in the literature. Moreover, this interaction is not modified in the construct expressing the mutant ITM2B-RD in the same system (Figure 1B).

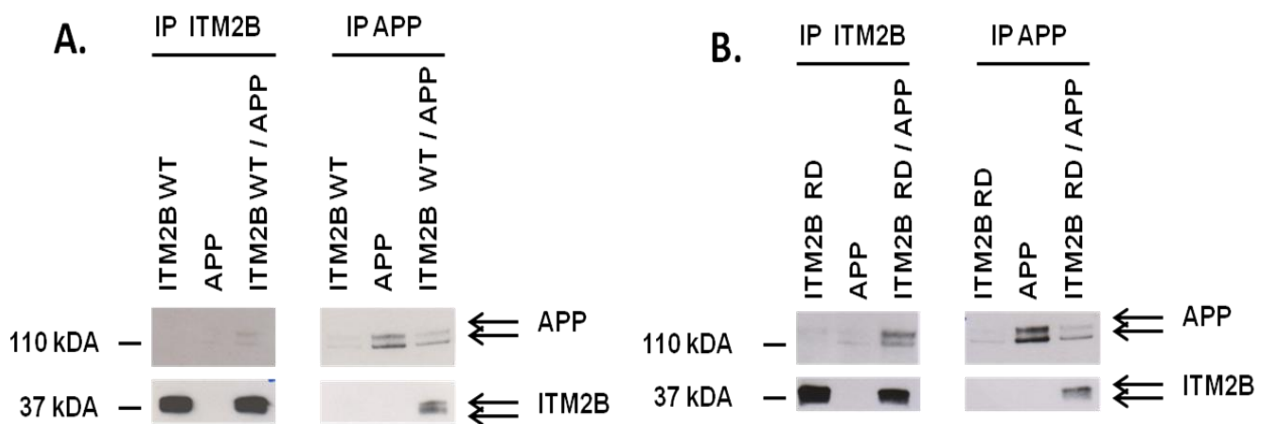


**Figure 1.** ITM2B WT and RD interact with APP in an over expressing system: HEK 293 cells were transfected with the Myc-tagged ITM2B WT vector, APP vector or co-transfected with Myc-tagged ITM2B WT – APP vectors (even if HEK 293 cells stably expressing APP). (A) Co-immunoprecipitation of ITM2B WT and APP from HEK 293 transfected cells. (B) Co-immunoprecipitation of ITM2B RD and APP from HEK 293 transfected cells.

### ***Generation and characterization of RD and Control patient iPSCs derived retinal organoids.***

One patient carrying the heterozygous ITM2B RD mutation (c.782A>C, p.Glu261Ala) and his unaffected brother were unrolled in this study. Subsequently fibroblasts from each subject were isolated after skin biopsy and were reprogrammed into iPSCs using a non-integrative Sendai virus approach as previously demonstrated<sup>19</sup>. For each condition, independent clonal lines were generated. Three iPSC lines for the affected subject (ITM2B-5286-3, ITM2B-5286-12, ITM2B-5286-19) and two cell lines for the unaffected control (ITM2B-5269-1 and ITM2B-

5286-2) were selected, isolated, and properly characterized. Thereafter, one sub-clone of the 5269-2 line was generated (i.e. ITM2B-5269-2.2) and characterized following the same methods we performed for the other cell lines (Figure S1). Briefly, the genomic integrity of 5286-2.2 cell line was confirmed by single nucleotide polymorphism (SNP) genotyping. iPSCs round shape colonies were positive for pluripotency markers (PAX6, OCTO4, SSEA4 and TRA-1-81). We also controlled the absence of the RD mutation in the exon 6 of *ITM2B*. Pluripotency status was also validated by the spontaneous formation of embryoid bodies which express genes from the three embryonic germ layers compared to iPSCs, as documented by scorecard analysis. Finally, we confirmed the absence of exogenous reprogramming factors and genomic Sendai integration in the iPSC line after 10 passages. Each cell lines were then expanded to generate retinal organoids following a stepwise 2D/3D protocol as previously described<sup>20,21</sup>. Briefly, on day 28 of differentiation, 2D self-forming neuroepithelial-like structures were manually collected and put into a floating medium where they form 3D retinal organoids<sup>20,21</sup>(Figure 2A). At this time, similar round shaped organoids were obtained. After one week in the floating medium, organoids thick bright spheres become darker and increase in size over time. All along the development of the retinal organoids, we did not detect any noticeable morphological differences between retinal dystrophy iPSC-derived retinal organoids (RD organoids) and control iPSC-derived retinal organoids (CTL organoids) (Figure 2B). After 60 days of differentiation, organoids are composed of internal rosette and immunostaining showed the presence of PAX6/ChX10 positive cells confirming their retinal cell fate specification (Figure 2C).

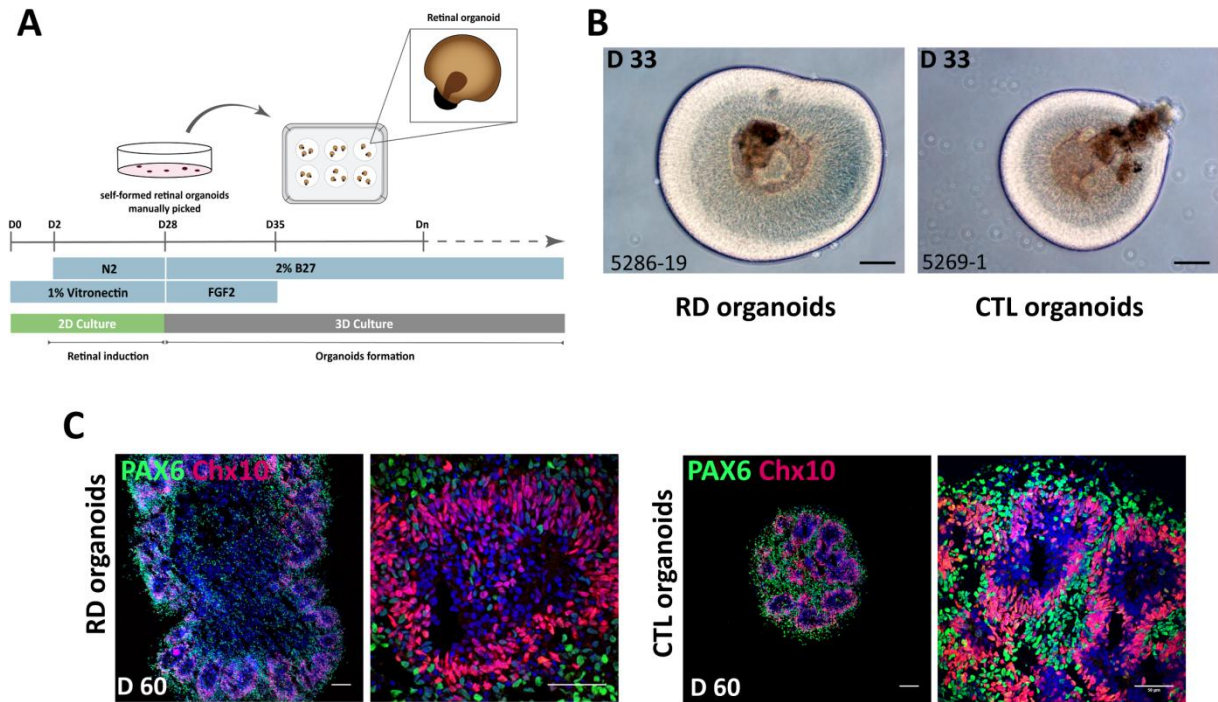


**Figure 2.** Generation and characterization of the retinal dystrophy and control iPSC derived retinal organoids (CTL organoids and RD organoids). (A) Schematic of retinal organoids' timeline differentiation protocol. (B) Bright field images of RD and CTL retinal organoid structures after 33 days of differentiation. Scale bar, 100 $\mu$ m. (C) anti-ChX10 and anti-PAX6 immunostaining in retinal organoids after 60 days of differentiation. Scale bar, 100 $\mu$ m (left) and scale bar, 50  $\mu$ m (right) for each condition.

### ***Retinal organoids from mutant and control cell lines express sequential retinal cellular markers during differentiation***

Retinal organoids were left in differentiation from each cell line and collected at six different time points, from 40 up to 200 days of differentiation. When sufficient organoids had been harvested for RNA extraction for each condition and for each time point, expression of specific retinal markers was tested by RT-qPCR. Based on clinical data we particularly focused on markers specific of five retinal cell types; RGCs, photoreceptors (rods and cones), bipolar and Müller glial cells. *POU4F1*, marker of the early differentiated RGCs is transient, with a peak of expression around 60 days of differentiation (Figure 3). Thereafter, its expression drastically decreased correlating with the absence of RGCs in retinal organoids up to 100 days of differentiation. Expression of *PKCA* and *SLC1A3* respectively bipolar cell and Müller glial cell markers constantly increases over time from 40 to 200 days of differentiation (Figure 3). The expression of *CRX*, early marker involved in the photoreceptor lineage, increases until 100 days of differentiation before reaching a plateau thus correlating with the emergence of late retinal cell types: rods and cones. Indeed, the expression of Rhodopsin (*RHO*) and Long wave and medium length-sensitive Opsin (*OPN1LW/MW*) markers is undetectable before 100 days of differentiation, and then rises until 200 days of differentiation (Figure 3).

The expression time course of these retinal markers is in accordance with previous studies using the same differentiation protocol<sup>21</sup>. This first result confirms the generation of RD and CTL iPSC-derived retinal organoids. Furthermore, in the RD organoids, all tested markers follow normal time course as CTL retinal organoids, with cell types appearing in a sequential manner in accordance with human retinogenesis. Of note, we observed some expected inter-cellular line variability.

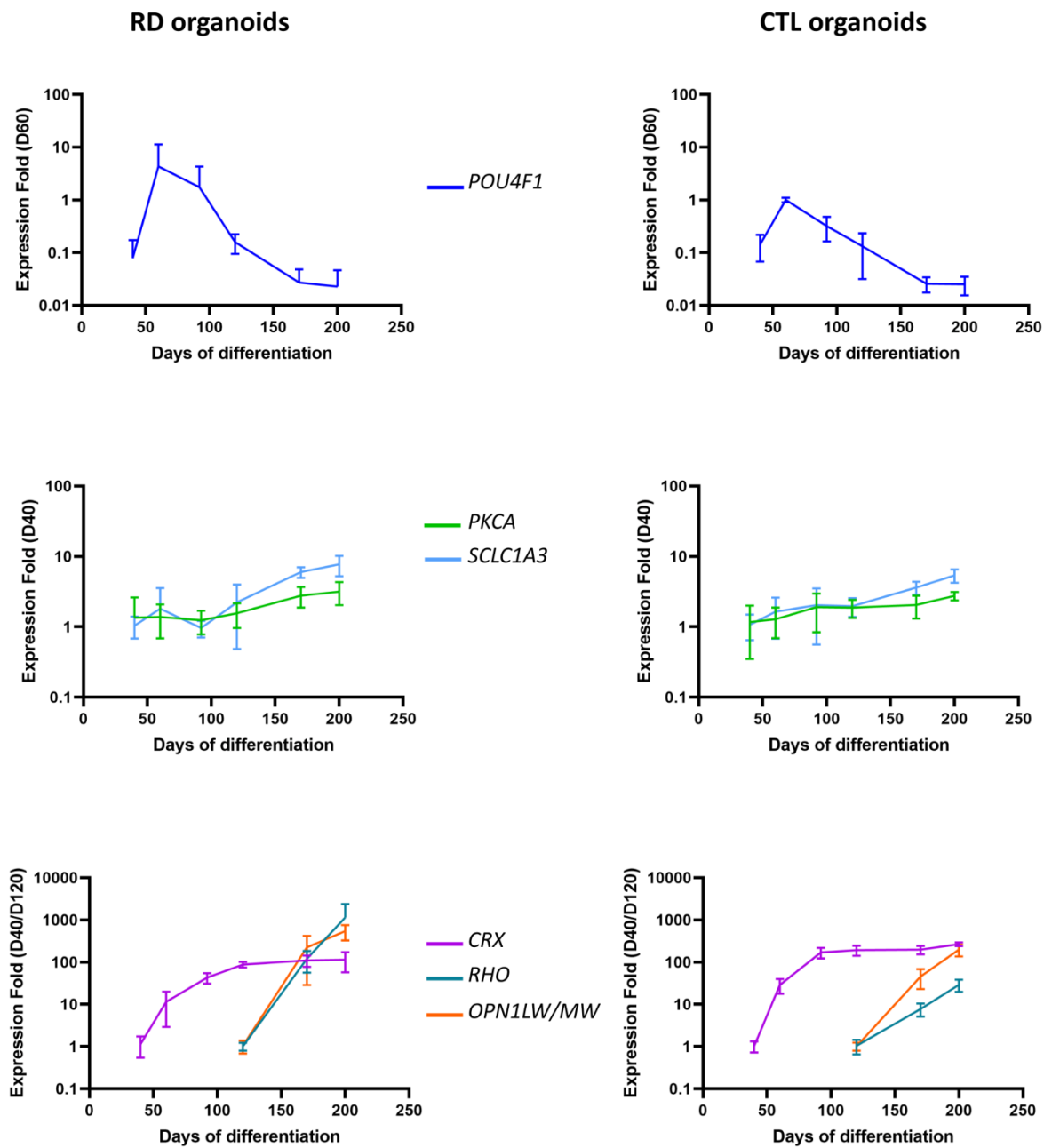


**Figure 3.** Time course of several retinal markers expression in RD and CTL organoids at different time points (40, 60, 92, 120, 170 and 200 days of differentiation). In each condition, data were normalized to organoids at D40 for *POU4F1*, *PKCA*, *SLC1A3*, *CRX* and normalized to organoids at D120 for *RHO* and *OPN1LW/MV*.

***ITM2B is stably expressed in retinal organoids over time, equally in mutant and control organoids***

We then investigated the expression of *ITM2B* by RT-qPCR in iPSC lines and retinal organoids during developmental stages. Our results showed that *ITM2B* is expressed in iPSC lines (before differentiation), however we did not report a significant difference between mutated and control iPSC lines (Figure S2). We next examined the kinetic of *ITM2B* expression in RD versus CTL retinal organoids. In both conditions, *ITM2B* is expressed at all development stages and this expression seems to be constant. As the expression of retinal cell markers follow a specific curve (Figure 3), this result suggests that *ITM2B* is not specific of one particular cell type. The expression of *ITM2B* was then compared between RD and CTL organoids for each time point previously described (40, 60, 92, and 120, 170 and 200 days of differentiation) and showed no significant difference (Figure 4B). Furthermore, immunostaining against *ITM2B* showed that the protein is ubiquitously localized in the organoids at 40 days (Figure 4C) and at 200 days of differentiation (Figure 4D). However, we noticed a strong *ITM2B* staining after 200 days of differentiation, at the border of the rosette, where the photoreceptors mature (Figure 4D).

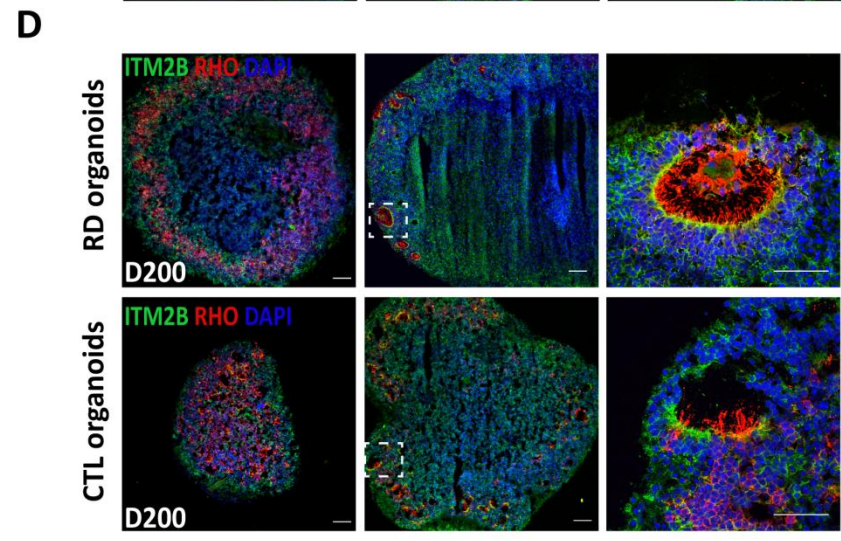
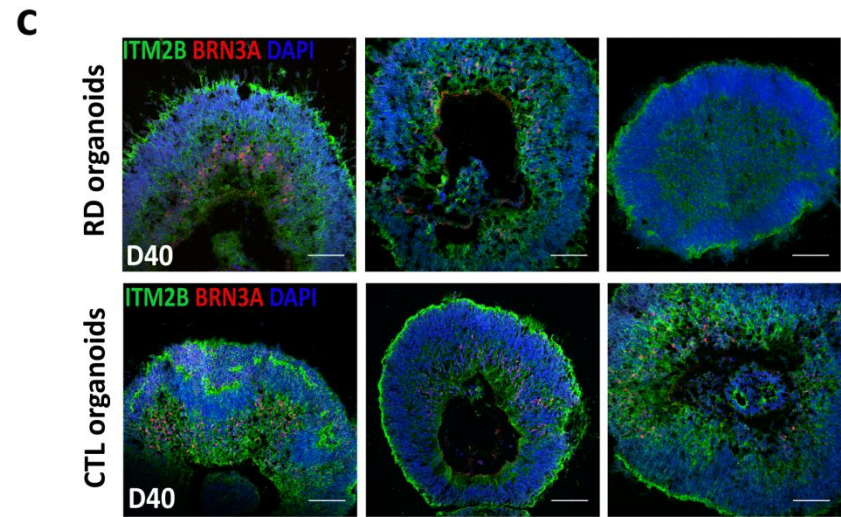
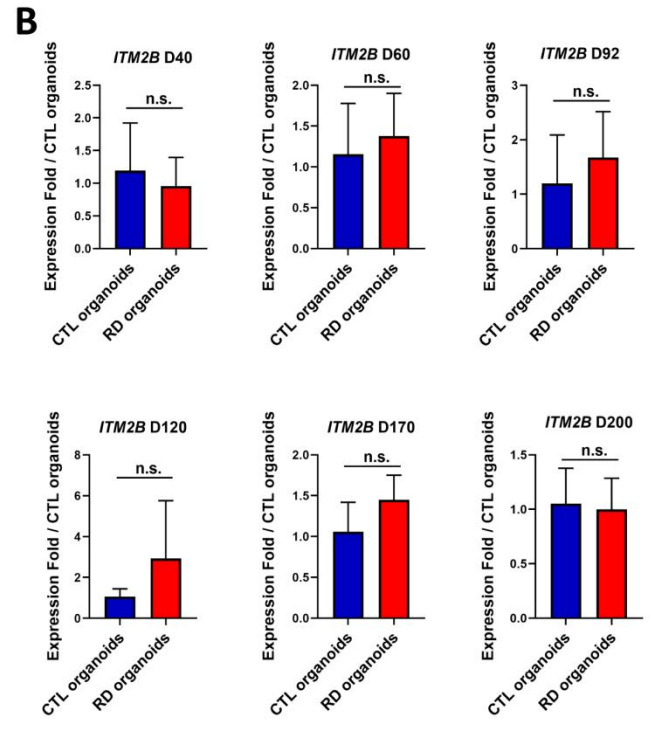
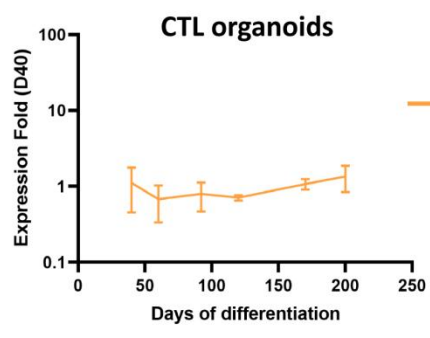
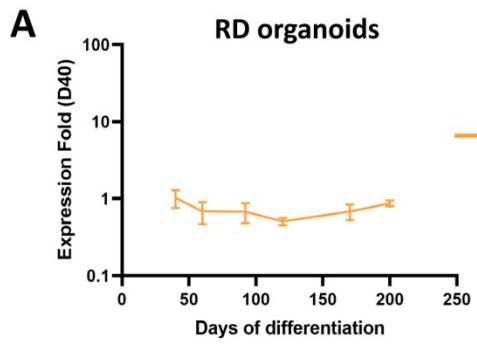
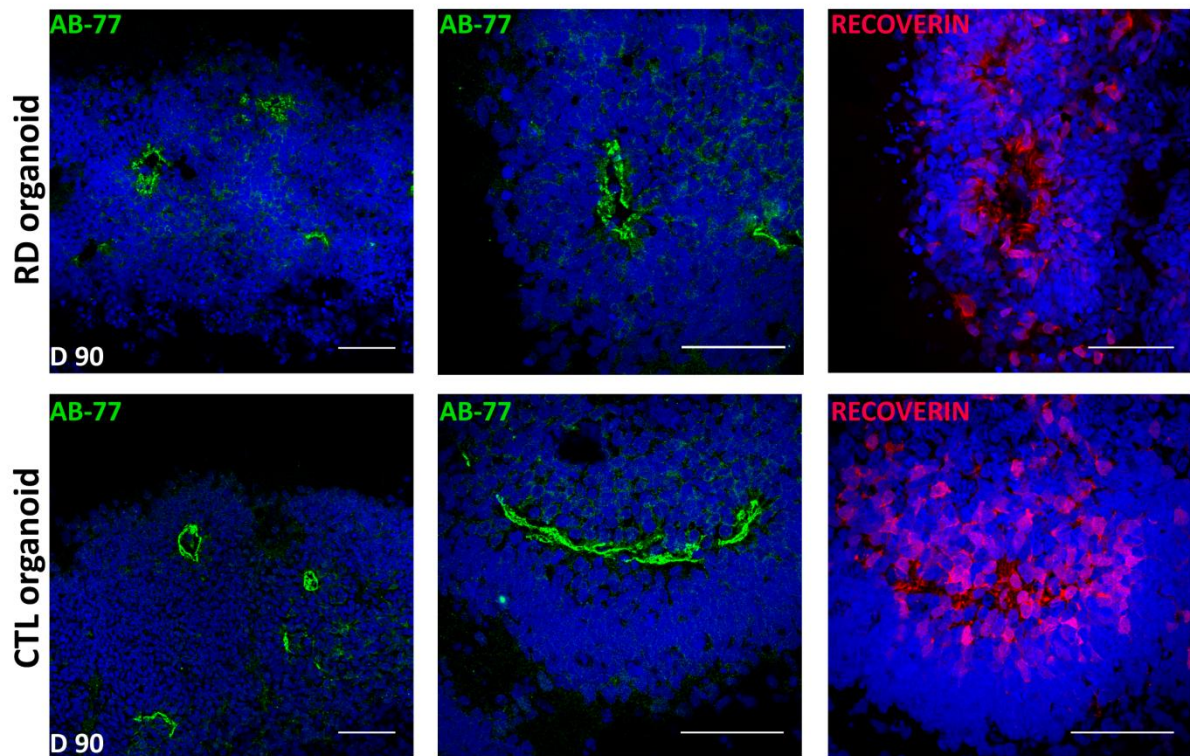


**Figure 4.** *ITM2B* is ubiquitously expressed in retinal organoids. (A) Time course of *ITM2B* expression in RD and CTL organoids at different time points (40, 60, 92, 120, 170 and 200 days of differentiation). Data were normalized to organoids at D40. (B) RT-qPCR analysis of *ITM2B* in RD and CTL organoids at different time points. For each time points, *ITM2B* expression was compared between RD and CTL organoids. Gene expression is indicated relative to CTL organoids at the indicated time points. Statistical significance was determined using Mann-Whitney test, n.s. =not significant. (C) Immunostaining against ITM2B and BRN3A in retinal RD and CTL organoids at 40 days of differentiation. Scale bar, 100  $\mu\text{m}$ . (D) Immunostaining of against RHO and ITM2B in retinal CTL and RD organoids at 200 days of differentiation. Scale, 100  $\mu\text{m}$ . Zoomed pictures scale bar, 50  $\mu\text{m}$ .

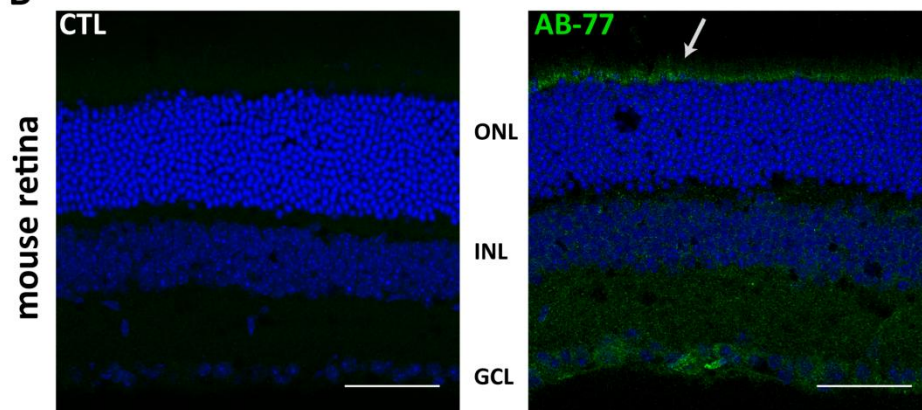
### ***BRI23 seems to accumulate in the rosette of retinal organoids***

We then tested a new antibody (AB-77, a gift from Pr. Oliver Wirth (Universitäts medizin Göttingen Georg August universität) raised against BRI23, ITM2B C-terminal secreted part, site of all ITM2B mutations were reported so far<sup>22</sup>). Interestingly, our data showed a stronger staining of AB-77 inside the rosettes of the organoids at 90 days of differentiation in both RD and CTL conditions. At this development stage, precursors of the photoreceptor are present all around the rosette structures as shown by anti-recoverin staining (Figure 5A). Furthermore, AB-77 staining on adult mouse retina demonstrated a localization of this secreted peptide in photoreceptor cells probably in their inner segments, at the outer limiting membrane (Figure 5B). Both these results strongly support an association between photoreceptors and the ITM2B C-terminal secreted peptide.

**A**



**B**

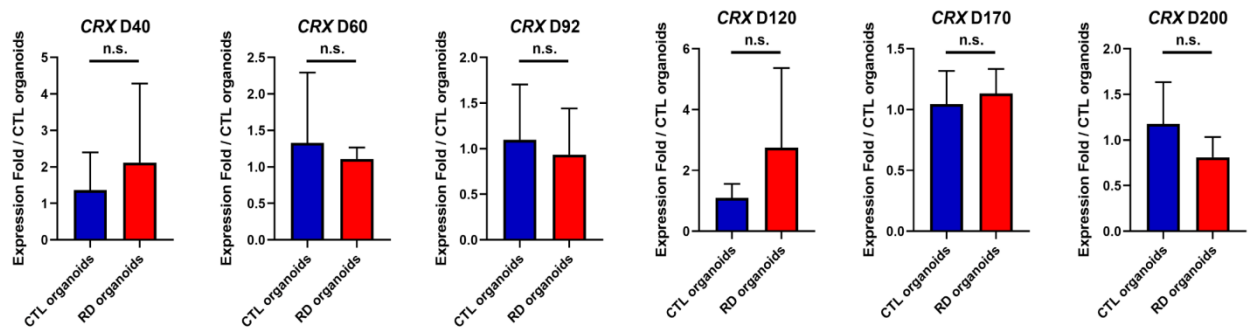
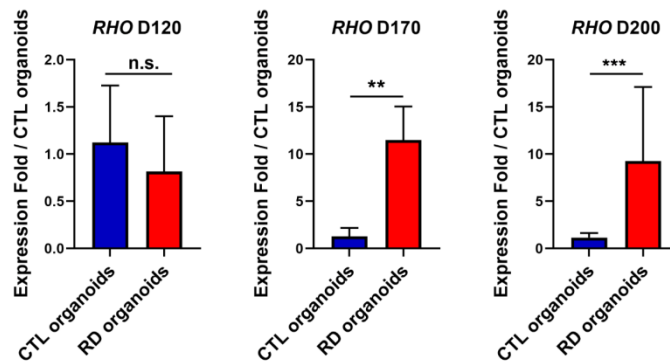
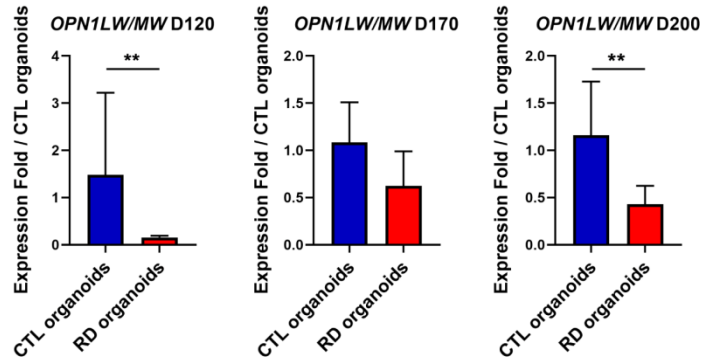


**Figure 5.** BRI23 specific immunolocalization in the rosettes of retinal organoids. (A) Immunostaining anti-BRI23 and anti-recoverin in RD and CTL retinal organoids at 90 days of differentiation. Scale bar, 50  $\mu\text{m}$ . (B) Immunostaining of AB-77 on mouse retina ONL: Outer Nuclear Layer, INL: Inner Nuclear Layer, GCL: Ganglion Cell layer. Arrow indicates AB-77 staining in the inner segment of the photoreceptors. Scale bar, 30  $\mu\text{m}$ .

***RD organoids reveal an up regulation of rhodopsin (RHO) and a down regulation of cone opsin (OPN1LW/MW) compared to CTL organoids***

To investigate the role of the RD mutation on photoreceptors, we first compared the expression of *CRX*, between RD and CTL organoids at six developmental points (40, 60, 92, 120, 170 and 200 days of differentiation). Our results did not show significant difference in *CRX* expression between RD and CTL organoids. We next compared the expression *RHO* and *OPN1L/MW*. Of note, the expression of these two markers is low before 120 days of differentiation and therefore we focused on three time points (120, 170 and 200 days of differentiation). Expression of *RHO* was significantly higher in RD organoids compared to CTL organoids at 170 and 200 days of differentiation but not at 120 days. At 170 and 200, *RHO* significantly increased 10-fold in the RD condition compared to the CTL. *OPN1L/MW* expression on the contrary significantly decreased at 120 and 200 days of differentiation in RD organoids (Figure 6).

There was however no differences between CTL and RD organoids with other cell markers including RGC markers such as *POUAF1*, *RBPM5* and *POU4F2* (Figure S3), bipolar cell marker (*PKCA*) (Figure S4A), and the Müller cell marker (*SLC1A3*) (Figure S4B) suggesting an impact of the RD mutation in photoreceptor cells on RD organoids.

**A****B****C**

**Figure 6.** RT-qPCR analysis of photoreceptor makers in RD and CTL organoids at different time points. (A) *CRX* expression in RD and CTL organoids at different time points (40, 60, 92, and 120, 170 and 200 days of differentiation). (B) *RHO* expression in RD and CTL organoids at different time points (120, 170 and 200 days of differentiation). (C) *RHO* expression in RD and CTL organoids at different time points (120, 170 and 200 days of differentiation). For each time points, *ITM2B* expression was compared between RD and CTL organoids. Gene expression is indicated relative to CTL organoids at the indicated time points. Statistical significance was determined using Mann-Whitney test, \* $p < 0.05$ , \*\* $p < 0.01$ , \*\*\* $p < 0.001$ , n.s. = not significant.

## Discussion

ITM2B-related retinal dystrophy (RD) is a rare disorder, combining retinal ganglion cell abnormalities, inner retinal and cone dysfunctions. ITM2B function is still unclear and little information is available except for its interaction with APP in the brain. Our recent work has shown that ITM2B also interacts with APP in the human retina. Subsequently, using an overexpressing system in HEK 293 transfected cells, our results confirmed that the RD mutation does not impact the interaction between ITM2B and APP. Then, to gain insights into ITM2B-related RD we generated and characterized patient-specific iPSCs from one affected subject and one unaffected sibling. Due to the fact that only one family is affected by this rare disorder, only two subjects were enrolled in this study. However, at least two independent clonal cell lines were generated. Each cell line was then expanded to obtain 3D retinal organoids and to further investigate RD cellular phenotype. The global morphology of the retinal organoids was similar between the RD and CTL organoids. Moreover, retinal organoids follow a normal development as shown by the emergence of the different retinal cell type in both conditions. These results suggest that the RD mutation does not have an impact on retinal organoids development.

Expression of ITM2B is stable during organoid development indicating that ITM2B is not specific to one of the 6 retinal cell types. Our result is consistent with previous work demonstrating ITM2B ubiquitous localization in the retina<sup>6</sup>. Furthermore, the RD mutation does not modify *ITM2B* expression in retinal organoids. This, together with previous work documenting the absence of RD-ITM2B missplicing, suggest that the pathogenic mechanism is not associated with a decreased expression of the gene but may rather impact the structure of the protein. All ITM2B mutations are present in the C-terminal part of the protein which is cleaved generating a 23-amino acid secreted peptide, called BRI23 in normal conditions. Applying a new ITM2B antibody (AB-77) recognizing BRI23, we showed a specific staining inside the rosettes of the retinal organoids after 90 days of differentiation. At this stage, photoreceptor markers start to appear inside the rosette where they will mature over time. Interestingly, AB-77 staining on mouse retina showed a sub cellular localization in the inner segment of the photoreceptors. For the first time we obtained a restricted localization of ITM2B where the photoreceptors are undergoing their maturation. BRI23 staining within the rosettes may represent an accumulation of this secreted peptide and therefore indicates that ITM2B may be differently processed in photoreceptor cells compared to other cell

types. Interestingly, in previous work, we reported that the RD mutation may change the 3D structure of BRI23 to a more opened conformation<sup>6</sup>. Therefore, misfolded BRI23 may accumulate specifically RD conditions over time. This would be an explanation for the hyper reflective material seen on spectral domain optical coherence tomography of patients with ITM2B-related retinopathy<sup>2</sup>. The accumulation of mutant BRI23 may induce a direct cellular toxicity as it was demonstrated with in FDD and FBD.

Interestingly, although *CRX* expression, a marker of the photoreceptor lineage, is unchanged in RD organoids, the presence of the RD mutation induced an increase in *RHO* and a decrease in *OPN1L/MW* expression in this model. The exact explanation for these findings would require further investigations. However, these preliminary results along with the staining against mutant BRI23 may suggest that the accumulation of the mutant peptide may have a toxic effect on cone photoreceptors hence the decreased expression in *OPN1L/W*). In line with this hypothesis, subjects affected with the ITM2B-related RD show a progressive cone system dysfunction and most likely degeneration in the course of their disease<sup>6</sup>. The increased expression of *RHO* is an intriguing finding which does not correlate with any known clinical sign of the ITM2B-related RD. This increased expression may be a feedback mechanism linked to the decreased in *OPN1L/WN*. However, we cannot exclude that the RD mutant has an impact in photoreceptor maturation in retinal organoids. A broader transcriptomic analysis of RD versus CTL expressed genes may shed further light in these alterations.

Due to the fact that we used a xeno-free differentiation protocol, retinal organoids that we obtained are composed of rosette structures. Recently, we started to generate retinal organoids following the same 2D/3D step-wise protocol but enabling the generation of laminated organoids. We hope that laminated organoids which represent a more suitable model for disease modeling will help to better characterize ITM2B-related RD.

Our previous work reveals evidence for an early RGC degeneration over the course of the ITM2B-related RD. However, our study did not show any changes in expression of RGC cell markers between RD and CTL organoids. In retinal organoids RGC degenerate after 90 days of differentiation and therefore are not the best model to study RGC alterations.

## **Material and Methods**

### ***Cell Lines and Transfection***

GripTite 293 MSR (macrophage scavenger receptor) (Thermo Fisher Scientific, Waltham, USA) cells were used for transfection and co-transfection experiments using Lipofectamine 2000 as transfection reagent (Invitrogen) and the standard manufacturer's protocol. Cells were transfected with pBudCE4\_1 APP / pBudCE4\_1ITM2B expression vectors. Of note this expression vector generates a fusion protein with a Myc-tag sequence which is placed after the ATG of the cDNA (N-terminal). For both genes the sequence integrated in the plasmid corresponds to the human wild-type (WT) cDNA sequence of *APP* (Refseq NM\_000484.3) and *ITM2B* (Refseq NM\_021999.4).

### ***Co-Immunoprecipitation***

HEK 293 MSR cells were harvested and suspended in a lysis buffer (10mM Hepes, NaOH pH7.4, 100mM NaCl, 0.5% NP40, 2mM Ethlenediaminetetraacetic acid (EDTA), cocktail inhibitor antiphosphatases 2, 3 and antiproteases (1/100) (Merck, Darmstadt, Germany)). The mix was placed on ice during 30 min and vortexed every 10 min. Homogenates were centrifuged (4°C, 5 min, 13 000 RPM). Then supernatants containing protein extracts were collected. Immunoprecipitation was performed using 50 µl of Dynabeads Protein G (Thermo Fisher Scientific, Waltham, USA), then the addition of 5 µg of antibody diluted in PBS 0.02% Tween 20 (anti-ITM2B PA5 31441 Thermo Fisher Scientific and anti-APP HPA001462 (MERCK)), the system was rotated 90 min at 4 °C. Beads were washed once with PBS 0.02% Tween 20 before adding cell extracts and rotation at 4 °C for an additional 90 min. Beads were washed again twice with PBS 0.02% Tween 20 and the last wash with PBS. The captured proteins released by the addition of 9.5 µl of lysis buffer, 8 µl Laemmli solubilization buffer (0.4 M SDS, 0.4 M Tris, 40 mM EDTA, 50% glycerol, bromphenol blue) and 2.5 µl of DTT separated in SDS-PAGE. After transfer, membranes were incubated with blocking buffer (1h, RT). After blocking, the membranes were incubated with the primary antibodies: anti-Myc tag 11667149001 (Roche) 1 /500 in order to detect ITM2B proteins and APP MAB 348 (MERCK) 1/500 in order to detect APP proteins, overnight at 4°C. The following morning the membranes were washed (PBST, 4 x 5min) and incubated with the respective secondary antibodies anti-HRP mouse (Jackson, 1/10000, 1h, RT), washed again

(PBST, 4 x 5min) and revealed using Pierce™ ECL western blotting Substrate 5 minutes (Thermo Fisher Scientific).

### ***Human iPSC cultures and differentiation***

Established human iPSC lines were derived from dermal fibroblasts as described before<sup>19</sup>. Briefly cells were routinely cultured at 37°C in a standard 5%CO<sub>2</sub>/95% air incubator. Cells were maintained on feeder-free conditions, coated with recombinant human vitronectin (rhVTN-N; 1/100) (Thermo Fisher Scientific) and cultivated with Essential 8™ (Thermo Fisher Scientific).

For non laminated protocol, retinal differentiation was based on previous established protocols<sup>21</sup>. Briefly, iPSCs were cultured in Essential 6 medium for two days and then switched to E6N2 medium with 1% N2 supplement (Thermo Fisher Scientific). The medium was changed every 2-3 days. At D28, identified self-formed retinal organoids were mechanically isolated and transferred to floating cultures into a ProB27 medium with: DMEM:F12 (1:1), 2% B27 supplement (Thermo Fisher Scientific), 1% non-essential amino acid, 0.1% Penicillin-Streptomycin and completed with 10ng/ml of FGF2 the first week. Half of the medium was then changed every 2-3 days. At D35, FGF2 was removed and half of the medium was changed every 2-3 days during necessary time to see appear desired retinal cell types.

### ***Cryosection and Immunostaining***

Retinal organoids were fixed in 4% paraformaldehyde at 4 °C during 15 min then washed in PBS1X. Structures were incubated at 4 °C in PBS1X/30% Sucrose (Merck, Darmstadt, Germany) solution overnight. The next day, retinal organoids were embedded in a solution of PBS, 7.5% gelatin (from porcine skin type A (Merck)), 10% Sucrose and frozen in isopentane at -50 °C, and 10-µm-thick cryosections were collected and conserved at -80 °C. For immunostaining, slides were incubated for 1 h at room temperature with a blocking solution (PBS, 0.2% gelatin, and 0.25% Triton X- 100) and then overnight at 4 °C with the primary antibody. Slides were washed three times in PBS with Tween 0.1% and then incubated for 1 h at room temperature with the appropriate secondary antibody diluted at 1/600 in blocking buffer with 1/1000 DAPI.

**Table 1. List of primary and secondary antibodies.**

Antigens	Species	Dilution	Source
PAX6	Rabbit	1/1000	Merck (AB2237)
ChX10	Mouse	1/500	Santa Cruz (sc-365519)
ITM2B	Rabbit	1/1000	Thermo Fisher (PA531441)
Rhodopsin	mouse	1/500	Abcam (ab98887)
BRN3A	mouse	1/125	Milipore (MAB1585)

***RNA extraction and RT-qPCR (TaqMan assay)***

RNAs from organoids were extracted using NReasy Micro kit (Qiagen, Hilden, Germany) according to the manufacturer's recommendations. Quality of extracted RNAs was then validated on Nanodrop spectrophotometer (Thermo Fisher Scientific). cDNA was synthesized from 100 ng of total RNAs with QuantiTect reverse transcription kit (Qiagen) and were then diluted at 1/20 in DNase-free water. Quantitative PCR (qPCR) analysis was performed on an Applied Biosystems real-time PCR machine (7500 Fast System) with custom TaqMan Array (Table 2) 96-Well Fast plates and TaqMan Gene expression Master Mix following the manufacturer's instructions. All primers and MGB probes labeled with FAM for amplification were purchased from Life Technologies. Results were normalized against 18S housekeeping gene. All experiments were performed in minimum independent biological triplicates and DeltaCt method was used to quantify gene expression (Table 3 and Table 4).

Results of qPCR analysis are expressed as the mean  $\pm$  S.E.M. and statistical significance was determined using an unpaired Mann-Whitney test. Statistical analysis was performed using Prism 7 (GraphPad software).

**Table 2. TaqMan Gene Expression ID Assays used for qPCR.**

Gene symbols	Assay IDs (Thermo Fisher Scientific)
POU4F1	Hs00366711_m1
ITM2B	Hs00222753_m1
PKC alpha	Hs00925195_m1
CRX	Hs00230899_m1
RHO	Hs00892431_m1
OPN1LW/MW	Hs00241039_m1
SLC1A3	Hs00188193_m1
18 S	Hs99999901_s1

**Table 3.** Samples used for the time course of several retinal markers expression in RD and CTL organoids at different time points (Figure 3), performed in three independent technical experiments. P = passage.

D40	D60	D92	D120	D170	D200
5269-1 p17	5269-1 p17	5269-1 p17	5269-1 p18	5269-1 p27	5269-1 p19
5269-2 p34	5269-2 p39	5269-2 p36	5269-2 p34	5269-2 p34	5269-2 p31
5269-2.2 p19	5269-2.2 p26	5269-2.2 p26	5269-2.2 p26	5269-2.2 p19	5269-2.2 p28
5286-3 p17	5286-3 p17	5286-3 p21	5286-3 p21	5286-3 p20	5286-3 p21
5286-12 p20	5286-12 p32	5286-12 p22	5286-12 p32	5286-12 p20	5286-12 p20
5286-19 p20	5286-19 p14	5286-19 p11	5286-19 p13	5286-19 p12	5286-19 p12

**Table 4.** Quantification of relative gene expression was based on the DeltaCt Method (18S housekeeping gene). Experiments were performed separately for each time point on the samples listed below. P = passage.

<b>D40</b>	<b>D60</b>	<b>D92</b>	<b>D120</b>	<b>D170</b>	<b>D200</b>
5269-2.2 p19	5269-2.2 p26	5269-2.2 p26	5269-2.2 p26	5269-2.2 p19	5269-2.2 p28
5269-2.2 p39	5269-2.2 p20	5269-2.2 p17	5269-2.2 p17	5269-2.2 p29	5269 -2.2 p26
5269-1 p17	5269-2.2 p18	5269-2.2 p29	5269-2.2 p29	5269-2.2 p30	5269-2.2 p30
5269-2 p34	5269 -1 p17	5269-1 p17	5269-2.2 p30	5269-2.2 p26	5269-2.2 p29
5269-2 p38	5269-1 p20	5269-2 p36	5269-1 p18	5269-1 p27	5269-1 p19
5269 -2 p37	5269-2 p39	5269-2 p34	5269-1 p28	5269-1 p26	5269-1 p27
5269-2 p36	5269-2 p37	5269-2 p37	5269-2 p34	5269-2 p34	5269-1 p34
5286-12 p20	5269-2 p36	5286-12 p22	5269 -2 p36	5269-2 p36	5269-2 p31
5286-3 p17	5286-12 p32	5286-12 p32	5269 -2 p39	5269-2 p39	5269-2 p36
5286-19 p20	5286-12 p24	5286-3 p21	5286-12 p32	5286-12 p20	5269 -2 p60
	5286- 3 p17	586-19 p11	5286-12 p20	5286 -12 p32	5269-2 p39
	5286-19 p14	5286-19 p16	5286-3 p21	5286 -3 p20	5286-12 p20
			5286-19 p13	5286 -19 p12	5286-12 p32
					5286 -3 p21
					5286 -3 p19
					5286 -19 p12

## Acknowledgements

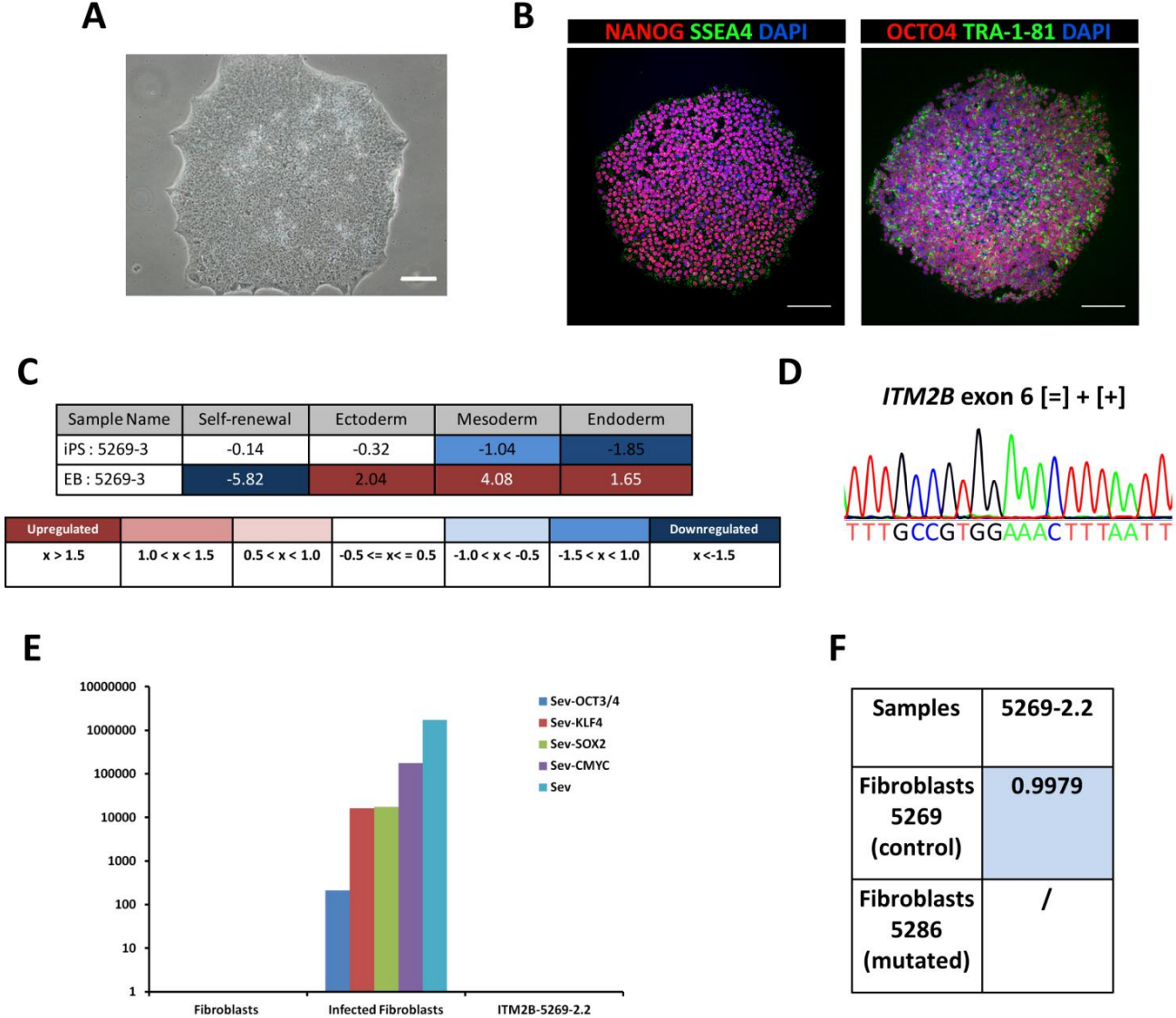
We gratefully thank Pr Oliver Wirth (Universitäts medizin Göttingen Georg Augut universität) for AB-77 antibody.

## References

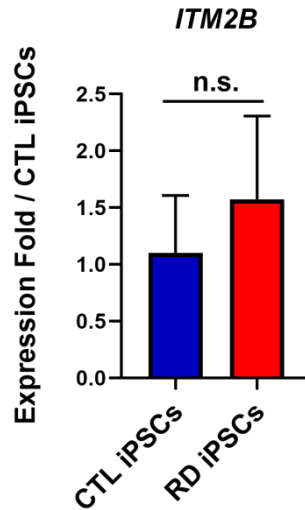
- 1 Khan, M., Fadaie, Z., Cornelis, S. S., Cremers, F. P. M. & Roosing, S. Identification and Analysis of Genes Associated with Inherited Retinal Diseases. *Methods in molecular biology* **1834**, 3-27, doi:10.1007/978-1-4939-8669-9\_1 (2019).
- 2 Audo, I. *et al.* The familial dementia gene revisited: a missense mutation revealed by whole-exome sequencing identifies ITM2B as a candidate gene underlying a novel autosomal dominant retinal dystrophy in a large family. *Human molecular genetics* **23**, 491-501, doi:10.1093/hmg/ddt439 (2014).
- 3 Vidal, R. *et al.* A stop-codon mutation in the BRI gene associated with familial British dementia. *Nature* **399**, 776-781, doi:10.1038/21637 (1999).
- 4 Vidal, R. *et al.* A decamer duplication in the 3' region of the BRI gene originates an amyloid peptide that is associated with dementia in a Danish kindred. *Proceedings of the National Academy of Sciences of the United States of America* **97**, 4920-4925, doi:10.1073/pnas.080076097 (2000).
- 5 Choi, S. I., Vidal, R., Frangione, B. & Levy, E. Axonal transport of British and Danish amyloid peptides via secretory vesicles. *FASEB journal : official publication of the Federation of American Societies for Experimental Biology* **18**, 373-375, doi:10.1096/fj.03-0730fje (2004).
- 6 Nassisi\*, M. *et al.* Deep-phenotyping and further insights in itm2b-related retinal dystrophy. *Retina in press* (2020).
- 7 Plant, G. T., Revesz, T., Barnard, R. O., Harding, A. E. & Gautier-Smith, P. C. Familial cerebral amyloid angiopathy with nonneuritic amyloid plaque formation. *Brain : a journal of neurology* **113 ( Pt 3)**, 721-747, doi:10.1093/brain/113.3.721 (1990).
- 8 Tomidokoro, Y. *et al.* Familial Danish dementia: co-existence of Danish and Alzheimer amyloid subunits (ADan AND Abeta) in the absence of compact plaques. *The Journal of biological chemistry* **280**, 36883-36894, doi:10.1074/jbc.M504038200 (2005).
- 9 Fotinopoulou, A. *et al.* BRI2 interacts with amyloid precursor protein (APP) and regulates amyloid beta (Abeta) production. *The Journal of biological chemistry* **280**, 30768-30772, doi:10.1074/jbc.C500231200 (2005).
- 10 Matsuda, S. *et al.* The familial dementia BRI2 gene binds the Alzheimer gene amyloid-beta precursor protein and inhibits amyloid-beta production. *The Journal of biological chemistry* **280**, 28912-28916, doi:10.1074/jbc.C500217200 (2005).
- 11 Kim, J. *et al.* BRI2 (ITM2b) inhibits Abeta deposition in vivo. *The Journal of neuroscience : the official journal of the Society for Neuroscience* **28**, 6030-6036, doi:10.1523/JNEUROSCI.0891-08.2008 (2008).
- 12 Wohlschlegel, J. *et al.* First identification of ITM2B interactome in the human retina. *Submitted* (2020).
- 13 Bek, T. Ocular changes in heredo-oto-ophthalmo-encephalopathy. *The British journal of ophthalmology* **84**, 1298-1302, doi:10.1136/bjo.84.11.1298 (2000).

- 14 Lancaster, M. A. & Knoblich, J. A. Organogenesis in a dish: modeling development and disease using organoid technologies. *Science* **345**, 1247125, doi:10.1126/science.1247125 (2014).
- 15 Kruczek, K. & Swaroop, A. Pluripotent stem cell-derived retinal organoids for disease modeling and development of therapies. *Stem cells*, doi:10.1002/stem.3239 (2020).
- 16 Huang, K. C. *et al.* Morphological and Molecular Defects in Human Three-Dimensional Retinal Organoid Model of X-Linked Juvenile Retinoschisis. *Stem cell reports* **13**, 906-923, doi:10.1016/j.stemcr.2019.09.010 (2019).
- 17 Buskin, A. *et al.* Disrupted alternative splicing for genes implicated in splicing and ciliogenesis causes PRPF31 retinitis pigmentosa. *Nature communications* **9**, 4234, doi:10.1038/s41467-018-06448-y (2018).
- 18 Shimada, H. *et al.* In Vitro Modeling Using Ciliopathy-Patient-Derived Cells Reveals Distinct Cilia Dysfunctions Caused by CEP290 Mutations. *Cell reports* **20**, 384-396, doi:10.1016/j.celrep.2017.06.045 (2017).
- 19 Wohlschlegel, J. *et al.* Generation of human induced pluripotent stem cell lines from a patient with ITM2B-related retinal dystrophy and a non mutated brother. *Stem cell research* **41**, 101625, doi:10.1016/j.scr.2019.101625 (2019).
- 20 Reichman, S. *et al.* From confluent human iPS cells to self-forming neural retina and retinal pigmented epithelium. *Proceedings of the National Academy of Sciences of the United States of America* **111**, 8518-8523, doi:10.1073/pnas.1324212111 (2014).
- 21 Reichman, S. *et al.* Generation of Storable Retinal Organoids and Retinal Pigmented Epithelium from Adherent Human iPS Cells in Xeno-Free and Feeder-Free Conditions. *Stem cells* **35**, 1176-1188, doi:10.1002/stem.2586 (2017).
- 22 Saul, A. *et al.* Abundant pyroglutamate-modified ABri and ADan peptides in extracellular and vascular amyloid deposits in familial British and Danish dementias. *Neurobiology of aging* **34**, 1416-1425, doi:10.1016/j.neurobiolaging.2012.11.014 (2013).

Supplementary Data



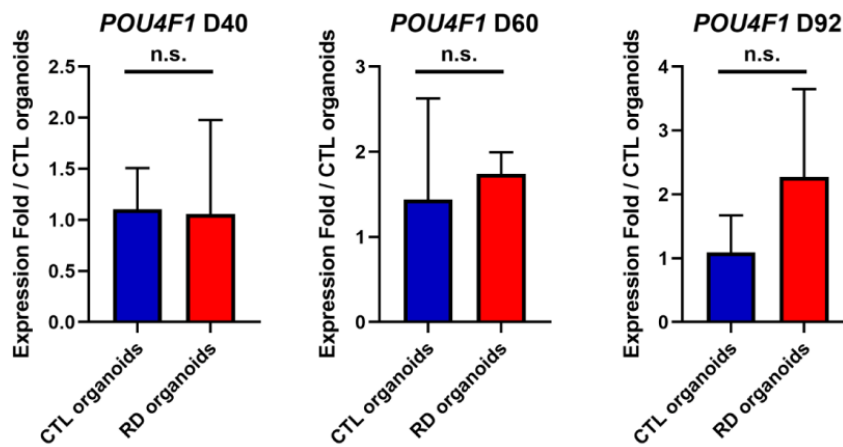
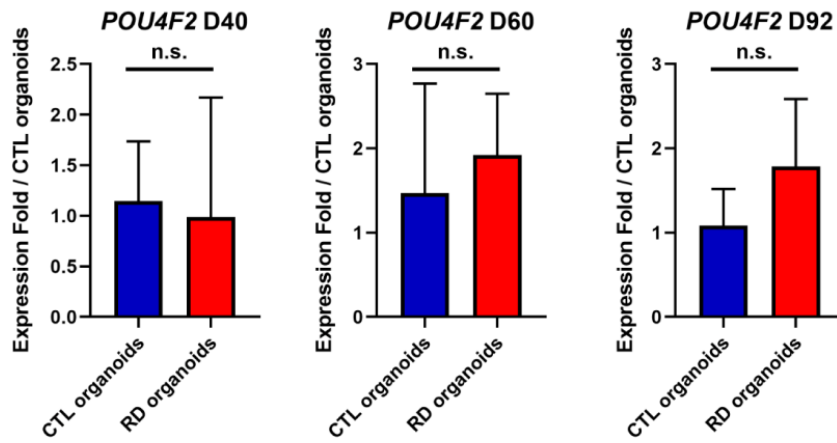
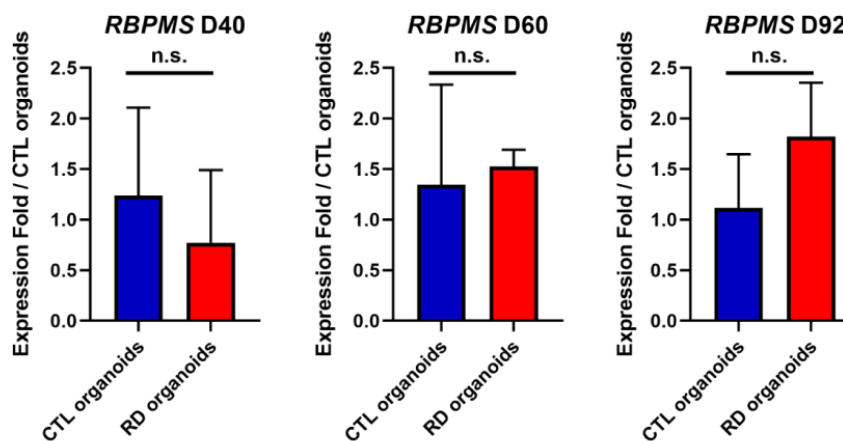
**Figure S1.** Characterization of ITM2B 5269-2.2 iPSC line (CTL iPSC line). (A) Phase contrast imaging of one iPSC colony under feeder free condition. (B) Immunostaining of pluripotency markers: NANOG, SSEA4 and TRA-1-81, OCT4, scale bar: 100  $\mu$ m. (C) Embryoid bodies formation *in vitro* expressing the three germ layers' markers for endoderm, mesoderm and ectoderm. (D) Electropherogram showing the absence of ITM2B-RD mutation in the control iPSC line (E) Expression of Sendai virus and exogenous reprogramming factors in the infected fibroblasts and their clearance after 10 passages in ITM2B-5269-2.2.(F) Percentage of SNP concordance between fibroblasts and the corresponding cell line.



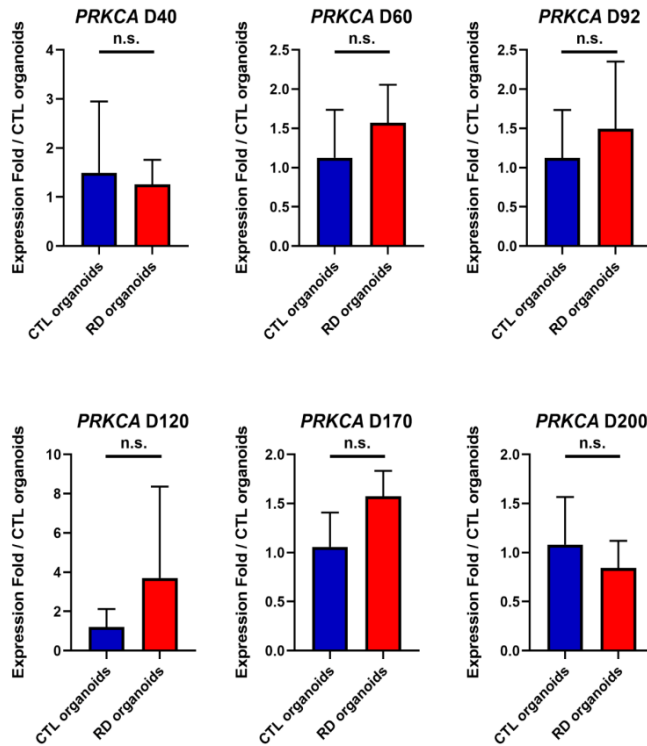
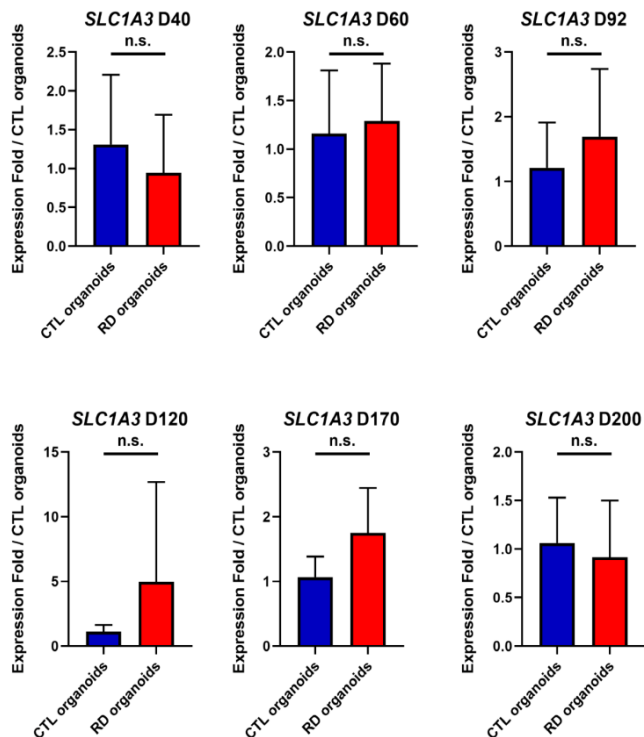
**Figure S2.** RT-qPCR analysis of ITM2B in RD and CTL iPSCs. Gene expression is indicated relative to CTL iPSCs. Statistical significance was determined using Mann-Whitney test, n.s. =not significant.

**Table S1.** List of the samples used for the quantification of ITM2B expression in RD and CTL iPSCs. P = passage.

Samples CTL	Samples RD
iPSCs 5269-2.2 p20	iPSCs 5286-3 p23
iPSCs 5269-2.2 p23	iPSCs 5286-3 p25
iPSCs 5269-2.2 p24	iPSCs 5286-3 p26
iPSCs 5269-2.2 p26	iPSCs 5286-3 p27
iPSCs 5269-2 p36	iPSCs 5286-12 p29
iPSCs 5269-2 p37	iPSCs 5286-12 p30
iPSCs 5269-2 p38	iPSCs 5286-12 p31
iPSCs 5269-2 p39	iPSCs 5286-12 p32
iPSCs 5269-1 p28	iPSCs 5286-19 p26
iPSCs 5269-1 p29	iPSCs 5286-19 p27
iPSCs 5269-1 p31	iPSCs 5286-19 p28
iPSCs 5269-1 p32	iPSCs 5286-19 p29

**A****B****C**

**Figure S3.** RT-qPCR analysis of different RGCs markers does not show a difference between RD and CTL organoids at different time points (40, 60 and 92 days of differentiation). Data are normalized to organoids at D40. For each time point, (A) *POU4F1*, (B) *POU4F2* (C) *RBPMS* expression was compared between RD and CTL organoids. Gene expression is indicated relative to CTL organoids at the indicated time points. Statistical significance was determined using Mann-Whitney test, n.s. = not significant.

**A****B**

**Figure S4.** RT-qPCR analysis of bipolar cell (*PKCA*) and Müller cell *SLC1A3* markers does not show a difference between RD and CTL organoids at different time points (40, 60, 92, 120, 170 and 200 days of differentiation). Data are normalized to organoids at D40. For each time point, (A) *PKCA*, (B) *SLC1A3* expression was compared between RD and CTL organoids. Gene expression is indicated relative to CTL organoids at the indicated time points. Statistical significance was determined using Mann-Whitney test, n.s. = not significant.

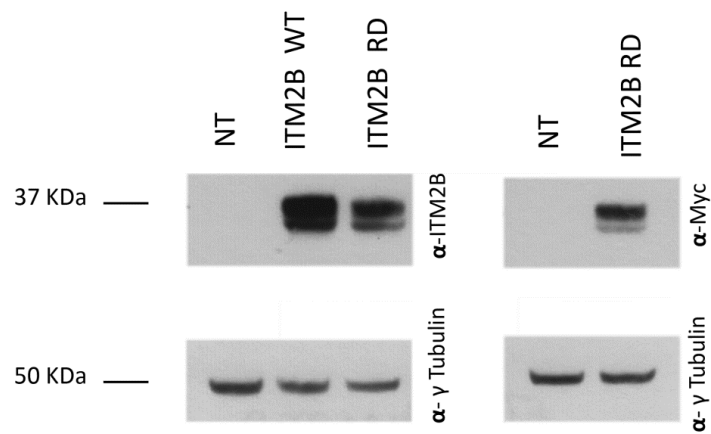


**Figure S5.** Validation of the ITM2B-Myc construction. Western Blotting on HEK 293 cells transfected or not with Myc-tagged ITM2B vector; NT = Non Transfected, WT = HEK 293 transfected with Myc-tagged ITM2B WT vector, RD =HEK 293 transfected with Myc-tagged ITM2B RD vector;  $\gamma$  Tubulin is used as a loading control and  $\alpha$ -: indicates the antibody used for the revelation.

## **5. Complementary results**

***Personalized interactome profiles of retinal organoids carrying the ITM2B-related retinal dystrophy mutation compared to controls after 90 days of differentiation***

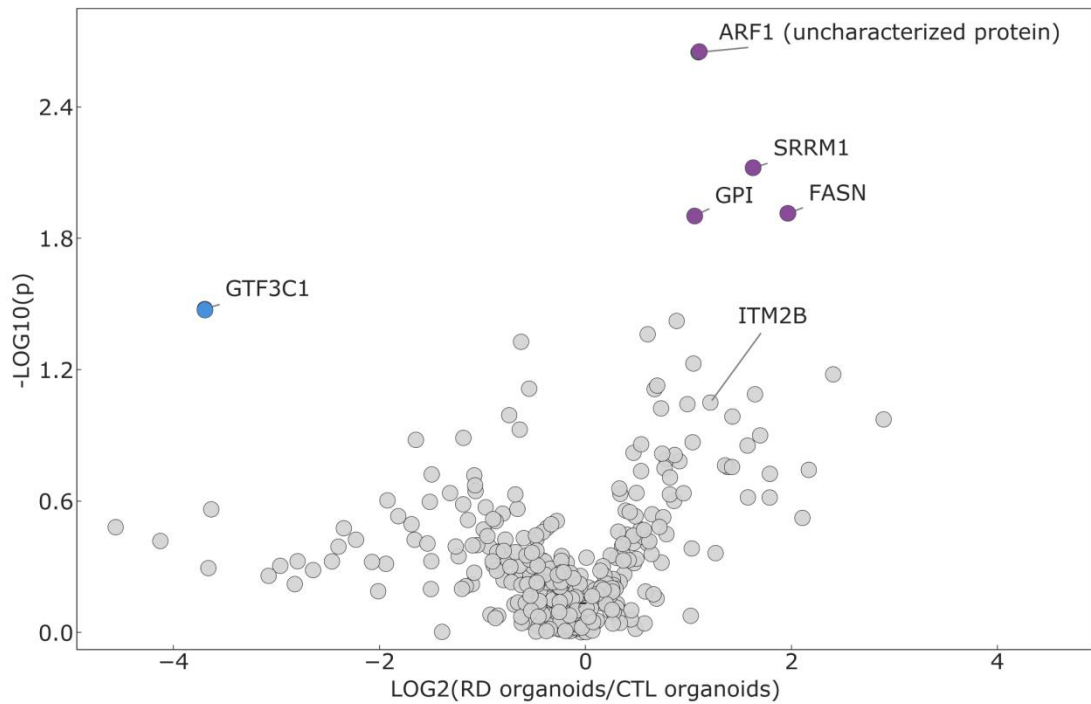
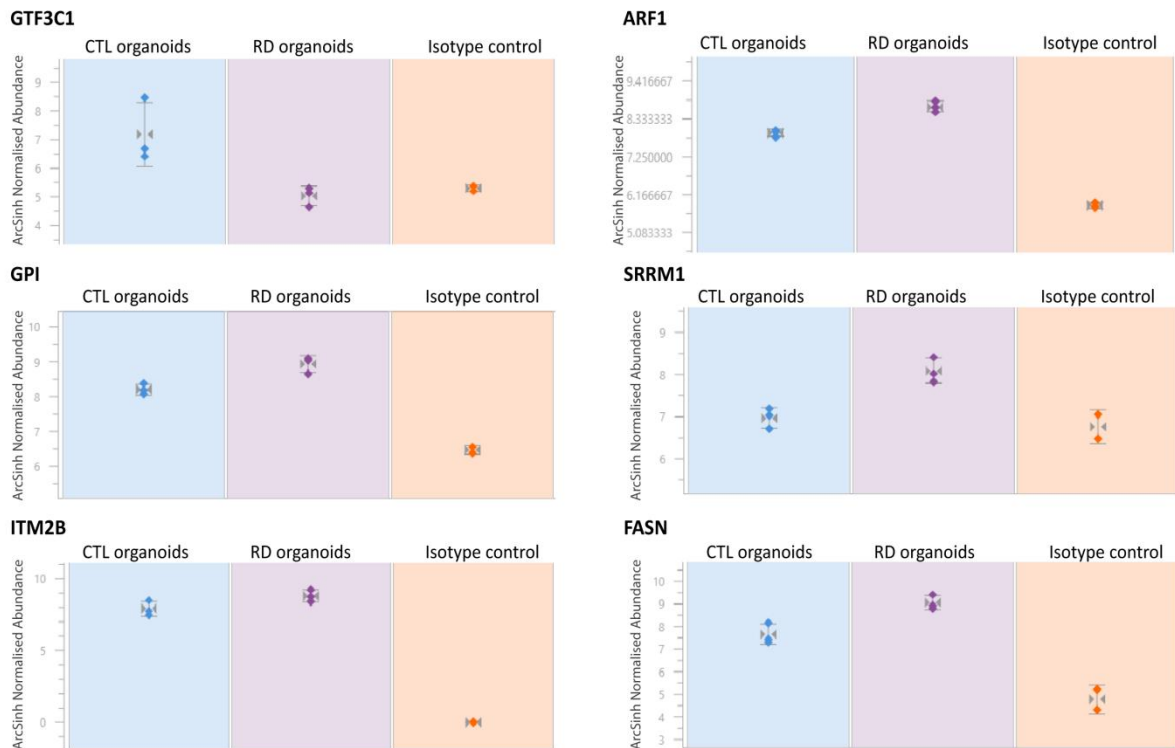
In order to approach pathological mechanisms involved in the ITM2B-related retinal dystrophy (RD), we applied quantitative mass spectrometry-based proteomics to iPSCs-derived retinal organoids originating from an affected subject and from an unaffected sibling, as a control (CTL). For this purpose, we generated retinal organoids from 3 RD and 3 CTL iPSC lines and extracted proteins after 90 days of differentiation. Six independent immunoprecipitations (IP) were performed using one anti-ITM2B antibody. Additionally, a mix of proteins extracted from the 3 RD conditions and a mix of proteins extracted from the 3 CTL conditions were submitted to IP using an IgG isotypic control in order to reduce the identification of unspecific ITM2B interactors. Immunopurified proteins were digested by trypsin and subsequent generated peptides were analyzed using LC-MS/MS.

Data were processed and 227 proteins were identified after standard filtering. In order to eliminate unspecific ITM2B interactors, we then focused on protein with a fold change  $>2$  (FC  $>2$ ) and  $p\text{-value} < 0.05$  compared to the isotypic control. Overall, 154 proteins were identified as specific ITM2B interactors in RD and CTL retinal organoids as shown in the volcano plot (Figure 1A). Among this total of 154 proteins, 5 proteins present a significantly different abundance profile between RD and CTL organoids: Uncharacterized protein (probable ARF1, F5H423), Glucose-6-phosphate isomerase (GPI, P06744), Fatty acid synthase (FASN, P49327), Serine/arginine repetitive matrix protein 1 (SRRM1, Q8IYB3), and General transcription factor 3C polypeptide 1 (GTF3C1, Q12789) (Figure 1B). Interestingly, we did not report a difference in ITM2B detection between RD and CTL organoids demonstrating that the protein was equally present and therefore immunoprecipitated in each condition. Moreover, ITM2B was not detected with the isotypic control antibody thus showing the specificity of the anti-ITM2B antibody (Figure 1B).

Three proteins were more present in RD-mutant protein extracts than in the non mutant control samples: ARF1, GPI, and FASN. Little information is available on ARF1 except that this protein might belong to the small GTPase superfamily. However, both GPI and FASN are proteins involved in different aspects of the metabolism. Indeed, FASN is an enzyme that catalyzes de novo lipid and a knock-out mouse model for the protein showed a rapid neurodegeneration of the retina<sup>1</sup>.

Interestingly, SRRM1 was not detected in the CTL organoids thus demonstrating a new potential interaction between ITM2B-RD mutant and this protein. On the contrary, GTF3C1 is absent in RD-mutant protein samples but significantly present in CTL samples. This would suggest that the interaction between ITM2B and GTF3C1 is lost in case of the RD mutation. Both SRRM1 and GTF3C1 are involved in translation processes.

This work represents preliminary data on differential ITM2B interactomes associated with the RD mutant and CTL protein using retinal organoids in development.

**A****B**

**Figure 1.** Volcano plots with  $-\log_{10}$  p-value vs.  $\log_2$ FC (FC: RD organoids/ CTL organoids). Each point represents an identified protein. Proteins with significantly different abundances (in purple and blue  $p$ -value $<0.05$ ). On the right side are the proteins enriched in the CTL condition with  $FC>2$  while on the left side are the proteins enriched in RD condition with  $FC>2$ . (B) Graphical representation of protein abundance between CTL organoids, RD organoids and Isotype control using Progenesis software.

## **Material and Method**

### **Proteomic**

#### ***Proteins extraction and Immunoprecipitation***

Retinal organoids from six different iPSC lines (3 from an ITM2B-RD mutant carrier and 3 from a non mutant sibling as a control) were collected after 90 days of differentiation. At this stage, batch of retinal organoids were frozen in 650  $\mu$ l of lysis buffer (50 mM Tris pH 7.5, 150 mM NaCl, 1% Triton 100 X) and conserved at -80 °C. Total proteins were extracted from retinal organoids in the lysis buffer with the addition of protease and phosphatase inhibitors (1 % Phosphatase inhibitor cocktail 2 and 3 Sigma, 1% Protease inhibitor cocktail , Merck, Darmstadt, Germany). The mix of lysis buffer and organoids was kept on ice during 30 min with vortexing every 10 min. After centrifugation at 13 000 rpm for 10 min, the supernatant was collected for immunoprecipitation. For each sample, 50  $\mu$ l mix of beads (Dynabeads protein G, Thermo Fisher Scientific, Waltham, USA) were used. After removing the solution, the remaining beads were incubated with rotation for 1 hour and 30 min at 4°C with 6  $\mu$ g of anti-ITM2B antibody (sc-374362, Santa Cruz Biotechnology, Dallas, USA) and a total of 500  $\mu$ l PBS 1X 0.02 % Tween 20. After one wash with 500  $\mu$ l PBS 0.02 % Tween 20, 200  $\mu$ l of proteins extracted from the retinal organoids were applied to the mix antibody-Dynabeads and incubated overnight at 4°C with rotation. Immunoprecipitates were then washed each twice with 500  $\mu$ l of PBS 0.02 % Tween 20 and one last time with 500  $\mu$ l of PBS 1X.

#### ***LC-MS/MS acquisition***

Samples with beads were digested with trypsin (0.2  $\mu$ g/ $\mu$ l) in  $\text{NH}_4\text{HCO}_3$  25mM buffer overnight at 37°C. Samples were then desalted using ZipTip C18 Pipette Tips (Thermo Fisher Scientific) and analyzed by an Orbitrap Tribrid Fusion mass spectrometer in positive mode coupled to a Nano-LC Proxeon 1200 equipped with a NSI EASY-spray ion source (all from Thermo Fisher Scientific). Peptides were separated by liquid chromatography with the following parameters: Acclaim PepMap100 C18 pre-column reversed phase (2 cm, 3  $\mu$ m, 100 Å), EASY-spray C18 column reversed phase (P/N ES805A, 75 cm, 75  $\mu$ m i.d., 2  $\mu$ m, 100 Å), 300 nl/min flow rate, gradient from 95 % solvent A (water, 0.1 % formic acid) to 40 % solvent B (80 % acetonitrile, 0.1% formic acid) over a period of 120 minutes, followed by a column regeneration of 20 min, giving a total run time of 140 minutes. Peptides were analyzed in the Orbitrap cell, in full ion scan mode, at a resolution of 120,000 with a mass range of  $m/z$  350-

1550 and an AGC target of  $4 \times 10^5$ . Fragments were obtained by Higher-energy C-trap Dissociation (HCD) activation with a collisional energy of 27%, and a quadrupole isolation window of 1.6 Da. MS/MS data were acquired in the Ion trap in a Top-Speed mode with 3 seconds cycles, with an AGC target of  $1 \times 10^4$  and with a dynamic exclusion of 60 seconds. MS/MS of most intense precursor were firstly acquired. Peptides with charge states = 2 to 8 were included for the acquisition. The maximum ion accumulation times were set to 100 ms for MS acquisition and 35 ms for MS/MS acquisition.

### ***LC-MS/MS data processing***

Label Free quantification was performed using Progenesis Q1 for proteomics software (Waters) using HI-3 method for quantification of proteins. Data were processed with Proteome Discoverer 2.4 software (Thermo Fisher Scientific). Identification of proteins was performed with the Mascot search server on Proteome Discoverer. The mass tolerance of fragment ions was set to 7 ppm for precursor mass tolerance and 0.5 Da for fragment mass tolerance. The identification of tryptic peptides related to proteins was performed on the following database Uniprot Refseq from *Homo sapiens* taxonomy (2019 update). Post-translational modifications were searched in dynamics parameters: oxidation (M) phosphorylation (S/T/Y), acetylation (Protein N-terminal). The maximum number of missed cleavages was limited to 2 for trypsin digestion. P-values of peptides were calculated using the percolator algorithm, and a 1% filter was applied as a false-discovery rate threshold.

### ***Statistical analysis***

Volcano plot representing protein abundance variations between RD organoids and CTL organoids according to p-values was generated with Instant Clue (version 0.5.3)<sup>2</sup>.

### **Acknowledgments**

We thank the proteomics core facility at the Institut Jacques Monod for the LC-MS/MS and experiments, the region Ile-de-France (SESAME), the Paris University, and CNRS for funding parts of the LC-MS/MS equipments.

## References

- 1 Rajagopal, R. *et al.* Retinal de novo lipogenesis coordinates neurotrophic signaling to maintain vision. *JCI insight* **3**, doi:10.1172/jci.insight.97076 (2018).
- 2 Bindea, G. *et al.* ClueGO: a Cytoscape plug-in to decipher functionally grouped gene ontology and pathway annotation networks. *Bioinformatics* **25**, 1091-1093, doi:10.1093/bioinformatics/btp101 (2009).

# Discussion and Perspectives

In 2013, our team identified a heterozygous missense mutation in the *ITM2B* gene in a large family affected by an unusual retinal disorder (40). As the mutation is heterozygous, ITM2B RD mutation may lead either to a loss of function and/or a dominant negative effect. To this date, the function of ITM2B was unclear and had never been investigated in the retina. In addition, this peculiar disorder mostly characterized by retinal ganglion cell abnormalities, inner retinal and cone dysfunctions does not correspond to any clinical presentation previously reported in the literature. From this starting point, the objectives of my thesis project were to better understand the role of ITM2B in the retina, both in physiological and pathological conditions.

## Clinical aspects of the disorder

The disease is characterized by an early onset RGC loss as showed by the pale optic nerve, thinning of the nerve fiber layers and ganglion cell layers on the OCT visible at disease presentation.

In addition, one crucial functional aspect of the disorder is the electronegative waveform observed on the ERG under scotopic conditions in the affected subjects. This feature is commonly shared by several retinal ischemic and synaptic disorders, such as complete and incomplete congenital stationary night blindness. A severe decrease of the b-wave is a key feature of post photoreceptor dysfunctions (i.e. inner retinal dysfunctions). Therefore, it may reflect either a dysfunction in photoreceptor-to-bipolar cell synaptic transmission or a primary alteration of bipolar cells. Furthermore, an unusual and persistent hyperreflectivity of the inner retinal layers is observed in RD patients. As OCT imaging is based on light reflected back after it goes through different tissues, we presumed that this hyperreflectivity could be due to the accumulation of abnormal material. Considering that we ruled out missplicing associated with RD mutation, the mutant product conserved the full length of the normal protein. Based on our knowledge on the physiopathology of ITM2B in other disorders (e.g. FBD and FDD), the hyperreflective material might consist of an accumulation of the ITM2B secreted peptide (called BRI23 in normal conditions). In fact, in FBD and FDD, ITM2B mutated secreted fragments (ABri and ADan respectively) generate extracellular non-

neuritic plaques in the brain of affected subjects (42, 43). As the RD mutation affects the same part of the protein than the mutations underlying FBD and FDD, it may also lead to the misfolding of this peptide and subsequently generate the formation of aggregates after the normal cleavage of the 23-amino acid peptide. However, unlike FBD and FDD, the RD mutation does not affect the length of the protein product but may rather disturb the structure of the secreted fragment. We used *in silico* tools to predict the structure of BRI23 in normal and in mutated conditions (196). Of note, we also attempted to predict the structure of ADan and ABri peptides, but, contrary to the RD peptide, the software used (Quark, <https://zhanglab.ccmb.med.umich.edu/QUARK/>) did not allow a reliable prediction for these peptides. *In silico* structural predictions suggested that, in normal conditions, BRI23 is composed of two antiparallel  $\beta$ -strands. The overall structure of BRI23 seems to be conserved with the RD mutation. Nevertheless, the two  $\beta$ -stands look more parallel and distant from each other (Figure S3 p83). This is probably due to the change of a negatively charged glutamic acid for a neutrally charged amino acid at codon number 261 which does not interact the same way with the positively charged arginine at codon 252. This more opened conformation might lead to the misfolding of the peptide and thus generate aggregates and/or modify its clearance.

If present, these aggregates would therefore support the hypothesis that the RD-ITM2B mutant exerts a dominant negative effect. In addition, these aggregates may have a role in the inner retinal dysfunction feature. For ethical reason, we did not examine mutant subjects at a pre-symptomatic stage. Therefore, we still do not know if the electronegative ERG is a congenital characteristic linked to a synaptic defect or if it is an acquire feature which could be a secondary consequence of the hyperreflective material accumulation. Both hypothesis may also co-exist and may only be resolved by ERG recordings early in the life of mutant subjects.

Through several years of clinical follow up, we demonstrated that functional exams better documented the slow progression of the disease, notably with decreased amplitudes in photopic responses on the ERG (196). At disease onset, all affected subjects presented very mild alterations of the photopic ERG. However, we observed a distinct decrease in photopic responses on the ERG over time. In photopic conditions, ERG components driven by cones are generated at the inner retinal level with the contribution of both ON- and OFF-bipolar

cells. The progressive decrease in the ERG photopic amplitudes may therefore be due either to progressive primary cone and/or inner retinal dysfunction. Multimodal retinal imaging with loss of autofluorescence combined with the presence of hyperreflective material in the foveal ONL observed in some patients would also suggest a possible secondary photoreceptor degeneration (196).

Brain magnetic resonance imaging (MRI) performed on RD subjects confirmed the absence of major cerebral alterations in areas primarily affected in FBD and FDD subjects (i.e. cerebral cortex, cerebellar cortex and hippocampus). However, this test is based on structural alterations and does not exclude minor cerebral alterations or amyloid plaque deposition. Other techniques such as positron emission tomography (PET) imaging, based on the absorption of radiopharmaceuticals or specific biomarkers could provide a more accurate diagnosis as it is already the case for AD (197, 198). Of note, PET imaging has been performed on one FBD affected subject using Pittsburgh compound B (11C-PiB) biomarker which selectively binds to A $\beta$  amyloid plaques (197, 199). Interestingly, this study demonstrated significant retention of (11C-PiB) in the cerebellar area which is consistent with previous FBD neuropathological reports (199). To date, no specific biomarker for ITM2B accumulation exists. Therefore, PET imaging on ITM2B mutated subjects would rely on the hypothesis that current biomarkers binds to A $\beta$  and ITM2B deposits (i.e. ABri, ADan and potential BRI23-RD) the same way.

Interestingly, we also reported common clinical features within ITM2B-related disorders. For instance, as in FDD patients, hearing loss in high frequencies was reported in three affected RD subjects without history of auditory trauma. Nevertheless, an audiogram should be performed on other members of the family, whether affected or unaffected, in order to better correlate this new clinical feature with the ocular disorder and the RD mutation.

Hearing loss and ocular alterations, such as cataract and microangiopathy, were also reported in FDD affected subjects. In addition, the only study published on postmortem retinal sections of FDD patient mostly demonstrated photoreceptor degeneration combined with retinal microangiopathy and neovascular complications (71). Our clinical study revealed that RD patients present vascular abnormalities that are secondary to retinal changes with no evidence of microangiopathy.

Intriguingly, no apparent ocular alterations are present in FBD patients. Nevertheless, to our knowledge, no thorough clinical ophthalmologic investigations were conducted in these subjects. It would also be interesting to better characterize the retinal phenotype of subjects affected by FBD and FDD in order to investigate specifically whether they also display early onset ganglion cell abnormalities, inner retinal dysfunction and hyperreflective material, or whether these features are unique to RD. However, the neurological phenotype of FBD and FDD is severe and lead to an early death hampering a detailed study such as the one we conducted on the RD patients. Moreover, to our knowledge, patients from the FBD family are no longer followed-clinically.

### **Investigate the function of ITM2B in normal conditions**

At the beginning of my work, I faced the lack of information about ITM2B function in the retina. However, before studying pathological mechanisms involved in RD, it was necessary to first approach the functions of this protein in normal conditions. All previous published works about ITM2B referred to its putative role in the human and rodent brain (95, 200). However, even if the retina is a window to the brain, both organs have different functions, organization, and physiology. Moreover, although, FDB, FDD and RD share common symptoms, RD subjects do not present cerebral alterations, thus leading to the hypothesis that ITM2B may have specific functions in the retina (196). Gaining insight into ITM2B retinal partners may be a valuable source of information to access functions of this enigmatic protein, notably if its localization in the cell and the function of its partners are well documented in the literature. In this respect, we performed quantitative proteomics on human retinal protein extracts, with two different anti-ITM2B antibodies (one mouse and one rabbit antibody) in order to establish and characterize the ITM2B interactome in this tissue.

Due to the considerable amount of data obtained from quantitative proteomics after standard filtering, more stringent filtering processes were applied in order to restrain our analysis to the most relevant proteins. Specific markers of retinal cell types were found in our data, including specific proteins of photoreceptors, RGCs, Muller glia, amacrine and horizontal cells, thus consolidating our previous data suggesting the ubiquitous localization of ITM2B in the retina. Among cellular protein markers, a significant proportion is specific to

photoreceptor cells. Since photoreceptor cells are the most abundant cells in the retina that may, at least partially, explain the abundance of specific photoreceptor proteins. Therefore, the identification of a high number of proteins associated with photoreceptor cells does not necessarily reflect a stronger involvement of ITM2B in these cells.

Gene Ontology analyses of the whole retinal interactome revealed several terms associated to cytoskeleton, translation and more surprisingly mitochondria. The association between ITM2B and mitochondrial processes was intriguing and engaging, as it could be related with different aspects of the RD disorder. Indeed, RGC and optic nerve loss observed on the OCT of RD affected subjects resemble to characteristic features of hereditary optic neuropathies such as Leber hereditary optic neuropathy and dominant optic atrophy. Interestingly, both diseases are neurodegenerative disorders with primary mitochondrial alterations (201, 202). In the retina, mitochondria play a crucial role in neuronal survival. Retinal cells, notably RGCs, have a high energy requirement and are particularly exposed to mitochondrial dysfunctions. RGC axons forming the optic nerve contain abundant mitochondria in their unmyelinated segment prior to the lamina cribrosa.

Although mitochondrial proteins were purified with both antibodies, gene ontology revealed mitochondrial annotation terms only for ITM2B interactome specifically purified with the rabbit anti-ITM2B antibody. Therefore, this result suggests that the rabbit antibody is more prone to purify ITM2B mitochondrial partners. This difference may be explained by several hypotheses which are not mutually exclusive. ITM2B is cleaved by different enzymes at different localization in the cell generating fragments with distinct functions. Therefore, it is likely that each fragment interacts with specific partners during the protein processing thus generating distinct interactomes underlying their respective functions. In addition, the mouse anti-ITM2B antibody is monoclonal and binds a single specific site which mostly encompasses ITM2B intracellular domain, whereas the rabbit antibody is polyclonal and so, is composed of a mix population of antibodies which binds different sites spanning almost the entire protein (Figure 1 p93).

Additionally, we also demonstrated the presence of a new *ITM2B* transcript in the retina. The resultant predicted protein product, only recognized by the rabbit antibody, may also participate to the different ITM2B interactome profiles we obtained. Interestingly, this

shorter form has already been reported in the murine T cells and may have a pro-apoptotic effect (203). As there is no specific antibody against this isoform, the ITM2B canonical form and the new isoform were differentiated by their molecular weight after migration and revelation on a western blot (203). Interestingly, we performed a western blot on retinal protein extracts and did find a band corresponding to the predicted molecular weight for the shorter isoform (Figure 7 p104). Moreover, this band was absent when the membrane was revealed with the mouse antibody. The next step would be to characterize this band with proteomics to confirm or invalidate the ITM2B short form hypothesis.

Overall, our findings support the hypothesis that ITM2B, either in its canonical and/or short form, may have a role in the mitochondrial homeostasis. Further investigations will be needed to better characterize ITM2B function in the mitochondrial signaling and document its putative dysfunction in RD-derived cells.

We also compared our results with the ITM2B interactome previously characterized in rodent brains and other studies. This comparison allowed us to highlight differences and similarities between both interactomes. In each pool of proteins identified by both antibodies, about 40% of the ITM2B interactors were also present in the rodent brain interactome. This proportion not only supports the robustness of our study but also strongly consolidates the hypothesis that ITM2B may act differently in the brain and in the retina. Common proteins associated with the cytoskeleton and vesicular trafficking are present in both brain and retinal interactomes, showing that ITM2B is probably brought to the membrane through similar mechanisms but interacts with different partners in both organs.

Human retinal tissue is a rare and precious material. One of the major constraints we faced was scarcity of the material, notably to establish our protocols with the different antibodies. In that respect, retinal organoids represent a great tool to substitute human tissue. In our case, a perfect model of RD pathology would be of great help to compare data from our present study and could contribute to unravel some pathological mechanisms. As it appears from our data that ITM2B is likely to have distinct role in different cell types, it would be interesting to perform quantitative proteomics on a targeted area or cell type (e.g. RGCs, photoreceptors). In their study, Kwok *et al.*, isolated the outer segment of the photoreceptors from other cell types with a sucrose gradient before applying the mass

spectrometry-based proteomics approach (204). Using iPSCs, other techniques enable to isolate specific retinal cell types more accurately. Indeed, different iPSC lines with reporters corresponding to specific cell types have been generated. For instance, the Brn3-tdTomato iPSC line confers the advantage to easily detect RGCs (205). Then, using Fluorescence-activated cell sorting (FACS), the mCherry expressing cells could be isolated thus allowing to perform proteomics only on RGCs. As our iPSC lines do not contain specific cell reporters, we could also use magnetic-activated cell sorting (MACS) to isolate specific cell types as it has been demonstrated for photoreceptor cells (206). However, unlike RNA sequencing which includes a PCR step, mass spectrometry does not contain an amplification step and therefore would require the collection of enough material necessary to perform proteomic analysis.

However, it is necessary to keep in mind that our proteomic analyses have some limitations. One limitation is inherent to our specimens which are postmortem tissues that may induce bias depending of the time laps between death and tissue processing. In addition, due to the difficulties in accessing human retinal tissue, we used only one control antibody (anti-mouse IgG) for the study. In this context, few unspecific ITM2B partners could have been included when we analyzed proteins identified using the rabbit antibody. However, in order to limit all these factors, our experiment was performed in triplicate and stringent filtering method was applied to identify proteins. For instance, only peptides identified with  $p\text{-value} < 0.01$  were retained for our GO analyses. Moreover, several interactions with already described partners were identified in our study and confirmed by Co-IP and immunoblotting.

Also, LC-MS/MS like every biochemical techniques have some limitations which may lead to artefacts. LC-MS/MS enables detection of partners which interact directly or indirectly with the targeted protein. Actually, potential pitfalls would not directly result from protein identification by LC-MS/MS but rather from previous experimental steps. For instance, immunoprecipitation may lead to purification of protein complex resulting in the identification of protein that may not directly interact with the protein of interest. In addition, protein extraction produces “unphysiological conditions” where proteins are all mixed together in a tube. Interactions that have been identified by LC-MS/MS may occur *ex vivo* but not *in vivo* for the reason that these proteins may act in different cell types or cell compartments and so may never interact *in vivo*. Moreover, plasma membrane proteins have poor solubility which complicate their purification and so their detection. Protein

solubility may be influenced by the tissue, the lysate buffer used and/or the experimentator. In that context, false positive interactors, co-complex proteins purified with the different antibodies could have been identified and may have impacted and influenced our gene ontology analysis. On the contrary, relevant interactors could have been missed. Altogether, these variables should be taken into account for proteomics data interpretations.

### **Physiopathological mechanisms underlying the RD**

We investigated the physiopathological mechanisms involved in RD by performing disease modeling with induced pluripotent stem cells (iPSCs). We generated several iPSCs lines derived from skin biopsies of an RD patient and of an unaffected sibling (CTL). Then, a complete characterization of all cell lines was reported (207). A feeder-free and xeno-free differentiation protocol established by Goureau's team was used to generate 3D retinal organoids (176, 177). Subsequently, retinal organoids were developed from the different cell lines (RD and CTL organoids) and harvested at different time points of differentiation (from 40 to 200 Days of differentiation).

ITM2B is constantly expressed and we did not report a drastic modification of its expression during the development and maturation of RD and CTL organoids. This result confirms that ITM2B is not specific to one retinal cell type as its expression does not correlate with the emergence of one particular cell type. Our findings did not reveal any difference in the level of ITM2B expression in retinal organoids generated from RD and control cell lines thus demonstrating that ITM2BmRNA expression is not modified by the RD mutation. Moreover, RD retinal organoids display a normal morphology and follow a regular development as shown by the expected kinetic expression of retinal cell markers over time. Interestingly, when we compared the expression of different retinal cell markers between RD and CTL organoids, a significantly increased expression of Rhodopin (*RHO*) was found in RD derived organoids at 170 and 200 days of differentiation. On the contrary, *OPN1MW/LW* expression was significantly decreased in RD organoids. However, the expression of *CRX*, involved in photoreceptor lineage was not different between RD and CTL organoids, thus suggesting that the differentiation of photoreceptor cells is not altered. This finding was unexpected and at least two hypotheses may explain *RHO* over expression in RD organoids; whether RD organoids contain more rod cells compared to CTL organoids and/or rod cell number is

equivalent in both conditions but RHOmRNA is over expressed in RD organoids. These preliminary results will need further investigations.

One of the major issues that we faced all along this work was the variability among iPSC lines and subsequently among retinal organoids. Each cell line even derived from the same subject presents differences after reprogramming. In addition, we noticed heterogeneity during retinal organoids development, independently of RD or CTL conditions. Indeed, organoids do not develop exactly the same in a dish. In this respect, it was difficult to isolate and characterize the RD phenotype from the heterogenic back ground noise. In order to limit this factor, and improve reproducibility, a staging method would be a better interest, as the organoids are stopped according to morphological criteria more than precise differentiation date (180). We first generated non-laminated organoids and we recently changed for a laminated protocol which enables generating a more accurate organ-like model, more suitable for a disease modeling purpose (179). We hope that our new generated organoids will contribute to characterize RD phenotype, notably because this protocol has been optimized for cone differentiation (179).

However, laminated organoids are also facing some of the challenges of non-laminated organoids. Indeed, RGCs still degenerate over time and the inner retinal layer is also disorganized. Combining all the last advances in the stem cell field, retinal organoids still not display the same complex cellular architecture and connectivity as the mature human retina. Lack of vascularization, microglial cells and inconsistent lamination contribute to limit the full success of using organoids to recapitulate a retinal disease.

As our clinical data seem to point out to inner retinal layer involvement in the RD, including bipolar cells, caution should be given to the stage of retinal organoid differentiation and the paucity of the respective inner retinal cells in these organoids. In addition, in RD, as in other IRDs, symptoms appear in adulthood, which is rather late when considering that retinal organoids are modeling retinal cell development. Indeed, organoids after 200 days of differentiation are similar to fetal retina at 125 days of development (33). Nevertheless, pathogenic mechanisms underlying later retinal degeneration usually occur years prior to disease symptoms and may be present even during early development, and thus the mechanism of disease can still be studied in organoids. In this context, using iPSCs and retinal organoids would not be fruitless.

Moreover, our main hypothesis for the RD pathogenesis is a dominant negative effect of the mutated copy. Interestingly, we observed a more specific localization of BRI23 in the rosette of retinal organoids. Protein modeling suggests that the RD mutation may lead to BRI23 misfolding. This may lead to the accumulation of the abnormal peptide and subsequent cell death. This mechanism may take time to develop and this feature could not be observed in retina organoids. These last points raise the challenge of reproducing age-related defects in organoids. Nowadays, different techniques enable to induce an aging effect in organoids by adding chemical component usually a stressor in the culture medium (208). This method has been used to promote aging on iPSCs modeling late onset neurodegenerative disease including Parkinson's disease, but not yet on retinal organoids (208). However, organoids are a relatively young field and we have to keep in mind that we do not control every aspect of their development such as epigenetic. Also, what is "aging" compare to "maturation" should be clearly addressed, and how to quantify or at least observe the aging effect. Recent study starts to demonstrate that organoids are a good model for aging because they conserve an epigenetic clock based on aging DNA methylation profile (209, 210).

RD is an adult-onset degenerative disease and thanks to clinical data obtained over the years, we do now have a better idea of the progression of the disease at later stage. However, we still do not know what happen at an early stage as we never investigated young asymptomatic mutant subjects. More specifically, we do not know whether the inner retinal dysfunction seen in symptomatic adult patients is a congenital defect such as seen in congenital stationary night blindness (211).

RD is a complex and rare disorder and ITM2B is a ubiquitous protein which probably acts through different mechanisms in different cell types. Altogether, these factors contribute to challenge RD disease modeling. Only one family is affected by this unusual retinal dystrophy and there is no available animal model for this pathology. Furthermore, animal models often failed to encompass all the hallmarks of a disease, as it is the case for FBD and FDD rodent models. Although retinal organoids model have some limitations, iPSC derived directly from patients and provide an *in vitro* personalized model for human disorders.

CRISPR-Cas9 gene editing will allow correcting the RD mutation in the mutated organoids and thus would be the most suitable control for disease modeling experiment as it contains

the same genetic background. Isogenic controls have become essential while performing disease modeling as it represents the proper control limiting the influence of confounders. For instance, the absence of a phenotype in a CRISPR-Cas9 edited cell line while present in the non-edited cells provides a proof of causality for a specific gene defect and a basis for subsequent pathophysiological studies. This part of my work is currently on going, and will also help to fully characterize the RD phenotype in the organoids. For instance, it would give more information about the increased expression of *RHO* in RD derived organoids.

As ITM2B is not a well-studied protein, the generation of a complete knockout model for the protein would permit to validate the different anti-ITM2B antibodies. Furthermore, knockout organoids may also be a valuable tool to understand the role of ITM2B in retinal development. More specifically, it will determine if ITM2B is essential for retinogenesis and if not, what would be the impact of the absence of ITM2B in the retinal development. Secondly, for proteomics experiments as it would allow the elimination of unspecific partners (proteins immunopurified with the anti-ITM2B antibodies).

Additionally, gene editing would allow to generate FBD or FDD mutations in iPSCs, and to then differentiate them into retinal organoids. The constructions for the specific gRNA have already been designed for both disorders and this would bring new insights on the role of ITM2B in the retina studying different mutations.

Combining advanced techniques such as proteomics and retinal organoids may provide insights on the pathological mechanisms involved in RD. Our findings showed different interactome profiles between RD and CTL control organoids. Interestingly, 5 proteins present a significantly different abundance profile in both conditions. Among these proteins, two are of particular interest since their interaction with ITM2B is either present or absent specifically in the RD condition, respectively GTF3C1 and SRRM1. Interestingly, these two proteins are involved in translational processes. This result obtained with retinal organoids at a developmental stage are consistent with our previous results obtained in the adult human retina.

## Compare and contrast

All along this work we used different approaches to better understand the role of ITM2B in the retina. Although these approaches are complementary, they also brought apparent contradicting results. One of the main hypotheses for the RD disease is a dominant negative effect of the mutated copy. This hypothesis is supported by the accumulation of ABri and ADan mutated peptides in FBD and FDD. Furthermore, the modelisation of the RD peptide shows a structural difference compared to BRI23 (ITM2B normal secreted peptide). Also, if this accumulation exists, it might explain the hyperreflectivity observed on the OCT. We also found an accumulation of the BRI23 peptide in the rosettes of the CTL and RD organoids. Although no difference was observed between the two types of organoids, this selective staining of BRI23 might suggest a specific cleavage or clearance of BRI23 in the photoreceptors.

Interestingly, clinical data suggest direct involvement of the inner retina and the RGCs but a later and minor impact on photoreceptor cells in the disease. With proteomic data, we found ITM2B partners present in all the different retinal cell types. This result is consistent with the ubiquitous localization of ITM2B in the retina. In this pool of interactors, several of them were specific to the photoreceptor cells. These results may be not significant and may be only related to the fact that photoreceptors are highly present in the retina compared to other cell type. Furthermore, ITM2B expression during retinal organoid development shows a continuous and regular ITM2B expression which suggests that ITM2B is not specific of one retinal cell types but is ubiquitously expressed in the retinal tissue.

Gene ontology analyses highlighted potential ITM2B retinal pathways in the normal retina. Consistent with previous published studies, we found partners associated with synaptic vesicles and cytoskeleton (105, 200, 212). This result has to be confronted with the absence of the b-wave in scotopic conditions which is characteristic of a synaptic defect between photoreceptors and the inner retinal layer. Gene ontology also suggests a potential role of ITM2B in metabolic process and mitochondrial homeostasis. Mitochondrial homeostasis is of particular interest since RGCs are sensitive to mitochondrial dysfunctions and other retinal disorders with primary mitochondrial alterations resemble to some aspects of the RD.

Finally, developing organoids shows a significantly increased expression of Rhodopin (*RHO*) and decreased expression of *OPN1MW/LW* in RD organoids. Although this result needs to be

confirmed (with a proper isogenic control) it may also reveal another role of ITM2B during the photoreceptor development.

Although these results may seem inconsistent, they may not be exclusive. Further key experiments will help to validate or invalidate hypothesis. For instance, clinical investigations on a young asymptomatic mutated subject will bring new insights on the RD disease.

## Conclusions

The work presented here aim to better understand the function of ITM2B in the retina, in normal and mutated conditions. Through clinical follow up, we were able to better characterize the phenotype of the subjects affected by the mutation. Our work demonstrated the slow progression of the disease which is better characterized with functional test. Our work showed that this disorder is complex and not only restricted to the retina but also affects hearing loss. Proteomic experiments performed on human retinal protein extracts showed a unique ITM2B retinal interactome suggesting that ITM2B may have a specific role in this tissue. In addition, our data suggested a potential role of ITM2B in the mitochondria. Interestingly, this finding correlates with some clinical aspects of the disease, notably the RGC loss. Finally, we used iPSC derived retinal organoids to perform disease modeling and approach the potential pathological mechanisms involved in RD. Our results showed a specific localization of BRI23, inside the rosettes of the organoids where the photoreceptor mature. Furthermore, we demonstrated a significantly increased expression of rhodopin and a decreased expression of opsin in RD organoids. In conclusion, this complex disorder may be the combination of different factors. Indeed, two different hypotheses co exists: mitochondrial dysfunction which primary affects RGC, and the toxic accumulation of BRI23 mutant in the OPL which generates an electronegative waveform on the ERG. However, both hypotheses are not exclusive and further investigations will be needed to better understand this peculiar retinal dystrophy.

# Bibliography

1. Euler T, Haverkamp S, Schubert T, Baden T. Retinal bipolar cells: elementary building blocks of vision. *Nature reviews Neuroscience*. 2014;15(8):507-19.
2. Masland RH. The neuronal organization of the retina. *Neuron*. 2012;76(2):266-80.
3. Bachleda AR, Pevny LH, Weiss ER. Sox2-Deficient Muller Glia Disrupt the Structural and Functional Maturation of the Mammalian Retina. *Investigative ophthalmology & visual science*. 2016;57(3):1488-99.
4. Byrne LC, Khalid F, Lee T, Zin EA, Greenberg KP, Visel M, et al. AAV-mediated, optogenetic ablation of Muller Glia leads to structural and functional changes in the mouse retina. *PloS one*. 2013;8(9):e76075.
5. Wohl SG, Jorstad NL, Levine EM, Reh TA. Muller glial microRNAs are required for the maintenance of glial homeostasis and retinal architecture. *Nature communications*. 2017;8(1):1603.
6. Bringmann A, Grosche A, Pannicke T, Reichenbach A. GABA and Glutamate Uptake and Metabolism in Retinal Glial (Muller) Cells. *Frontiers in endocrinology*. 2013;4:48.
7. Baker SA, Kerov V. Photoreceptor inner and outer segments. *Current topics in membranes*. 2013;72:231-65.
8. Mustafi D, Engel AH, Palczewski K. Structure of cone photoreceptors. *Progress in retinal and eye research*. 2009;28(4):289-302.
9. Bowmaker JK, Hunt DM. Evolution of vertebrate visual pigments. *Current biology : CB*. 2006;16(13):R484-9.
10. Provis JM, Hendrickson AE. The foveal avascular region of developing human retina. *Archives of ophthalmology*. 2008;126(4):507-11.
11. Koike C, Numata T, Ueda H, Mori Y, Furukawa T. TRPM1: a vertebrate TRP channel responsible for retinal ON bipolar function. *Cell calcium*. 2010;48(2-3):95-101.
12. Koike C, Obara T, Uriu Y, Numata T, Sanuki R, Miyata K, et al. TRPM1 is a component of the retinal ON bipolar cell transduction channel in the mGluR6 cascade. *Proceedings of the National Academy of Sciences of the United States of America*. 2010;107(1):332-7.
13. Panda S, Provencio I, Tu DC, Pires SS, Rollag MD, Castrucci AM, et al. Melanopsin is required for non-image-forming photic responses in blind mice. *Science*. 2003;301(5632):525-7.
14. Gagliardi G, Ben M'Barek K, Goureau O. Photoreceptor cell replacement in macular degeneration and retinitis pigmentosa: A pluripotent stem cell-based approach. *Progress in retinal and eye research*. 2019;71:1-25.
15. Ahmad I, Teotia P, Erickson H, Xia X. Recapitulating developmental mechanisms for retinal regeneration. *Progress in retinal and eye research*. 2019:100824.

- 16.** Zuber ME. Eye field specification in *Xenopus laevis*. *Current topics in developmental biology*. 2010;93:29-60.
- 17.** Heavner W, Pevny L. Eye development and retinogenesis. *Cold Spring Harbor perspectives in biology*. 2012;4(12).
- 18.** Geng X, Speirs C, Lagutin O, Inbal A, Liu W, Solnica-Krezel L, et al. Haploinsufficiency of Six3 fails to activate Sonic hedgehog expression in the ventral forebrain and causes holoprosencephaly. *Developmental cell*. 2008;15(2):236-47.
- 19.** Graw J. Eye development. *Current topics in developmental biology*. 2010;90:343-86.
- 20.** Yun S, Saijoh Y, Hirokawa KE, Kopinke D, Murtaugh LC, Monuki ES, et al. Lhx2 links the intrinsic and extrinsic factors that control optic cup formation. *Development*. 2009;136(23):3895-906.
- 21.** Hendrickson A. Development of Retinal Layers in Prenatal Human Retina. *American journal of ophthalmology*. 2016;161:29-35 e1.
- 22.** Young RW. Cell differentiation in the retina of the mouse. *The Anatomical record*. 1985;212(2):199-205.
- 23.** Livesey FJ, Cepko CL. Vertebrate neural cell-fate determination: lessons from the retina. *Nature reviews Neuroscience*. 2001;2(2):109-18.
- 24.** Lu Y, Shiao F, Yi W, Lu S, Wu Q, Pearson JD, et al. Single-Cell Analysis of Human Retina Identifies Evolutionarily Conserved and Species-Specific Mechanisms Controlling Development. *Developmental cell*. 2020;53(4):473-91 e9.
- 25.** Boije H, MacDonald RB, Harris WA. Reconciling competence and transcriptional hierarchies with stochasticity in retinal lineages. *Current opinion in neurobiology*. 2014;27:68-74.
- 26.** Gomes FL, Zhang G, Carbonell F, Correa JA, Harris WA, Simons BD, et al. Reconstruction of rat retinal progenitor cell lineages in vitro reveals a surprising degree of stochasticity in cell fate decisions. *Development*. 2011;138(2):227-35.
- 27.** He J, Zhang G, Almeida AD, Cayouette M, Simons BD, Harris WA. How variable clones build an invariant retina. *Neuron*. 2012;75(5):786-98.
- 28.** Hoshino A, Ratnapriya R, Brooks MJ, Chaitankar V, Wilken MS, Zhang C, et al. Molecular Anatomy of the Developing Human Retina. *Developmental cell*. 2017;43(6):763-79 e4.
- 29.** Mellough CB, Bauer R, Collin J, Dorgau B, Zerti D, Dolan DWP, et al. An integrated transcriptional analysis of the developing human retina. *Development*. 2019;146(2).
- 30.** Liang Q, Dharmat R, Owen L, Shakoob A, Li Y, Kim S, et al. Single-nuclei RNA-seq on human retinal tissue provides improved transcriptome profiling. *Nature communications*. 2019;10(1):5743.
- 31.** Voigt AP, Whitmore SS, Flamme-Wiese MJ, Riker MJ, Wiley LA, Tucker BA, et al. Molecular characterization of foveal versus peripheral human retina by single-cell RNA sequencing. *Experimental eye research*. 2019;184:234-42.
- 32.** Lukowski SW, Lo CY, Sharov AA, Nguyen Q, Fang L, Hung SS, et al. A single-cell transcriptome atlas of the adult

human retina. *The EMBO journal*. 2019;38(18):e100811.

**33.** Sridhar A, Hoshino A, Finkbeiner CR, Chitsazan A, Dai L, Haugan AK, et al. Single-Cell Transcriptomic Comparison of Human Fetal Retina, hPSC-Derived Retinal Organoids, and Long-Term Retinal Cultures. *Cell reports*. 2020;30(5):1644-59 e4.

**34.** Yang Z, Ding K, Pan L, Deng M, Gan L. Math5 determines the competence state of retinal ganglion cell progenitors. *Developmental biology*. 2003;264(1):240-54.

**35.** Brzezinski JA, Prasov L, Glaser T. Math5 defines the ganglion cell competence state in a subpopulation of retinal progenitor cells exiting the cell cycle. *Developmental biology*. 2012;365(2):395-413.

**36.** Hoon M, Okawa H, Della Santina L, Wong RO. Functional architecture of the retina: development and disease. *Progress in retinal and eye research*. 2014;42:44-84.

**37.** Schmitz-Valckenberg S, Holz FG, Bird AC, Spaide RF. Fundus autofluorescence imaging: review and perspectives. *Retina*. 2008;28(3):385-409.

**38.** Dryja TP. Human genetics. Deficiencies in sight with the candidate gene approach. *Nature*. 1990;347(6294):614.

**39.** Chaitankar V, Karakulah G, Ratnapriya R, Giuste FO, Brooks MJ, Swaroop A. Next generation sequencing technology and genomewide data analysis: Perspectives for retinal research. *Progress in retinal and eye research*. 2016;55:1-31.

**40.** Audo I, Bujakowska K, Orhan E, El Shamieh S, Sennlaub F, Guillonneau X, et al. The familial dementia gene revisited: a missense mutation revealed by whole-exome sequencing identifies ITM2B as a candidate gene underlying a novel autosomal dominant retinal dystrophy in a large family. *Human molecular genetics*. 2014;23(2):491-501.

**41.** Audo I, Robson AG, Holder GE, Moore AT. The negative ERG: clinical phenotypes and disease mechanisms of inner retinal dysfunction. *Survey of ophthalmology*. 2008;53(1):16-40.

**42.** Vidal R, Frangione B, Rostagno A, Mead S, Revesz T, Plant G, et al. A stop-codon mutation in the BRI gene associated with familial British dementia. *Nature*. 1999;399(6738):776-81.

**43.** Vidal R, Revesz T, Rostagno A, Kim E, Holton JL, Bek T, et al. A decamer duplication in the 3' region of the BRI gene originates an amyloid peptide that is associated with dementia in a Danish kindred. *Proc Natl Acad Sci U S A*. 2000;97(9):4920-5.

**44.** Rambaran RN, Serpell LC. Amyloid fibrils: abnormal protein assembly. *Prion*. 2008;2(3):112-7.

**45.** Grundke-Iqbal I, Iqbal K, Quinlan M, Tung YC, Zaidi MS, Wisniewski HM. Microtubule-associated protein tau. A component of Alzheimer paired helical filaments. *The Journal of biological chemistry*. 1986;261(13):6084-9.

**46.** Grundke-Iqbal I, Iqbal K, Tung YC, Quinlan M, Wisniewski HM, Binder LI. Abnormal phosphorylation of the microtubule-associated protein tau (tau) in Alzheimer cytoskeletal pathology.

Proceedings of the National Academy of Sciences of the United States of America. 1986;83(13):4913-7.

**47.** Wang Y, Mandelkow E. Tau in physiology and pathology. *Nature reviews Neuroscience*. 2016;17(1):5-21.

**48.** Alonso AC, Zaidi T, Grundke-Iqbal I, Iqbal K. Role of abnormally phosphorylated tau in the breakdown of microtubules in Alzheimer disease. *Proceedings of the National Academy of Sciences of the United States of America*. 1994;91(12):5562-6.

**49.** Kang J, Lemaire HG, Unterbeck A, Salbaum JM, Masters CL, Grzeschik KH, et al. The precursor of Alzheimer's disease amyloid A4 protein resembles a cell-surface receptor. *Nature*. 1987;325(6106):733-6.

**50.** Spires-Jones TL, Hyman BT. The intersection of amyloid beta and tau at synapses in Alzheimer's disease. *Neuron*. 2014;82(4):756-71.

**51.** Coulson EJ, Paliga K, Beyreuther K, Masters CL. What the evolution of the amyloid protein precursor supergene family tells us about its function. *Neurochemistry international*. 2000;36(3):175-84.

**52.** O'Brien RJ, Wong PC. Amyloid precursor protein processing and Alzheimer's disease. *Annual review of neuroscience*. 2011;34:185-204.

**53.** Chen GF, Xu TH, Yan Y, Zhou YR, Jiang Y, Melcher K, et al. Amyloid beta: structure, biology and structure-based therapeutic development. *Acta pharmacologica Sinica*. 2017;38(9):1205-35.

**54.** Haass C, Selkoe DJ. Soluble protein oligomers in neurodegeneration: lessons from the Alzheimer's amyloid beta-peptide. *Nature reviews Molecular cell biology*. 2007;8(2):101-12.

**55.** Selkoe DJ. Alzheimer's disease: genes, proteins, and therapy. *Physiological reviews*. 2001;81(2):741-66.

**56.** Lacor PN, Buniel MC, Furlow PW, Clemente AS, Velasco PT, Wood M, et al. Abeta oligomer-induced aberrations in synapse composition, shape, and density provide a molecular basis for loss of connectivity in Alzheimer's disease. *The Journal of neuroscience : the official journal of the Society for Neuroscience*. 2007;27(4):796-807.

**57.** Chesarone MA, Goode BL. Actin nucleation and elongation factors: mechanisms and interplay. *Current opinion in cell biology*. 2009;21(1):28-37.

**58.** Cohen SI, Linse S, Luheshi LM, Hellstrand E, White DA, Rajah L, et al. Proliferation of amyloid-beta42 aggregates occurs through a secondary nucleation mechanism. *Proceedings of the National Academy of Sciences of the United States of America*. 2013;110(24):9758-63.

**59.** Tornquist M, Michaels TCT, Sanagavarapu K, Yang X, Meisl G, Cohen SIA, et al. Secondary nucleation in amyloid formation. *Chemical communications*. 2018;54(63):8667-84.

**60.** Worster-Drought C, Hill TR, McMenemey WH. Familial Presenile Dementia with Spastic Paralysis. *The Journal of neurology and psychopathology*. 1933;14(53):27-34.

- 61.** McMenemey WH, Worster-Drought C, Flind J, Williams HG. Familial Presenile Dementia: Report of Case with Clinical and Pathological Features of Alzheimer's Disease. *Journal of neurology and psychiatry*. 1939;2(4):293-302.
- 62.** Griffiths RA, Mortimer TF, Oppenheimer DR, Spalding JM. Congophilic angiopathy of the brain: a clinical and pathological report on two siblings. *Journal of neurology, neurosurgery, and psychiatry*. 1982;45(5):396-408.
- 63.** Plant GT, Revesz T, Barnard RO, Harding AE, Gautier-Smith PC. Familial cerebral amyloid angiopathy with nonneuritic amyloid plaque formation. *Brain : a journal of neurology*. 1990;113 ( Pt 3):721-47.
- 64.** Revesz T, Holton JL, Doshi B, Anderton BH, Scaravilli F, Plant GT. Cytoskeletal pathology in familial cerebral amyloid angiopathy (British type) with non-neuritic amyloid plaque formation. *Acta neuropathologica*. 1999;97(2):170-6.
- 65.** Holton JL, Ghiso J, Lashley T, Rostagno A, Guerin CJ, Gibb G, et al. Regional distribution of amyloid-Bri deposition and its association with neurofibrillary degeneration in familial British dementia. *The American journal of pathology*. 2001;158(2):515-26.
- 66.** Mead S, James-Galton M, Revesz T, Doshi RB, Harwood G, Pan EL, et al. Familial British dementia with amyloid angiopathy: early clinical, neuropsychological and imaging findings. *Brain : a journal of neurology*. 2000;123 ( Pt 5):975-91.
- 67.** Kim SH, Wang R, Gordon DJ, Bass J, Steiner DF, Lynn DG, et al. Furin mediates enhanced production of fibrillogenic ABri peptides in familial British dementia. *Nature neuroscience*. 1999;2(11):984-8.
- 68.** Ghiso JA, Holton J, Miravalle L, Calero M, Lashley T, Vidal R, et al. Systemic amyloid deposits in familial British dementia. *The Journal of biological chemistry*. 2001;276(47):43909-14.
- 69.** Stromgren E, Dalby A, Dalby MA, Ranheim B. Cataract, deafness, cerebellar ataxia, psychosis and dementia--a new syndrome. *Acta neurologica Scandinavica*. 1970;46(S43):261-2.
- 70.** Holton JL, Lashley T, Ghiso J, Braendgaard H, Vidal R, Guerin CJ, et al. Familial Danish dementia: a novel form of cerebral amyloidosis associated with deposition of both amyloid-Dan and amyloid-beta. *Journal of neuropathology and experimental neurology*. 2002;61(3):254-67.
- 71.** Bek T. Ocular changes in heredo-oto-ophthalmo-encephalopathy. *The British journal of ophthalmology*. 2000;84(11):1298-302.
- 72.** Tomidokoro Y, Lashley T, Rostagno A, Neubert TA, Bojsen-Moller M, Braendgaard H, et al. Familial Danish dementia: co-existence of Danish and Alzheimer amyloid subunits (ADan AND A{beta}) in the absence of compact plaques. *The Journal of biological chemistry*. 2005;280(44):36883-94.
- 73.** Schilling S, Wasternack C, Demuth HU. Glutaminyl cyclases from animals and plants: a case of functionally convergent protein evolution. *Biological chemistry*. 2008;389(8):983-91.
- 74.** Saido TC, Yamao-Harigaya W, Iwatsubo T, Kawashima S. Amino- and carboxyl-terminal heterogeneity of beta-

amyloid peptides deposited in human brain. *Neuroscience letters*. 1996;215(3):173-6.

**75.** Harigaya Y, Saido TC, Eckman CB, Prada CM, Shoji M, Younkin SG. Amyloid beta protein starting pyroglutamate at position 3 is a major component of the amyloid deposits in the Alzheimer's disease brain. *Biochemical and biophysical research communications*. 2000;276(2):422-7.

**76.** Schilling S, Zeitschel U, Hoffmann T, Heiser U, Francke M, Kehlen A, et al. Glutamyl cyclase inhibition attenuates pyroglutamate Abeta and Alzheimer's disease-like pathology. *Nature medicine*. 2008;14(10):1106-11.

**77.** Schlenzig D, Manhart S, Cinar Y, Kleinschmidt M, Hause G, Willbold D, et al. Pyroglutamate formation influences solubility and amyloidogenicity of amyloid peptides. *Biochemistry*. 2009;48(29):7072-8.

**78.** Saul A, Lashley T, Revesz T, Holton J, Ghiso JA, Coomaraswamy J, et al. Abundant pyroglutamate-modified ABri and ADan peptides in extracellular and vascular amyloid deposits in familial British and Danish dementias. *Neurobiology of aging*. 2013;34(5):1416-25.

**79.** Kim SH, Creemers JW, Chu S, Thinakaran G, Sisodia SS. Proteolytic processing of familial British dementia-associated BRI variants: evidence for enhanced intracellular accumulation of amyloidogenic peptides. *The Journal of biological chemistry*. 2002;277(3):1872-7.

**80.** Giannoccaro MP, Bartoletti-Stella A, Piras S, Casalena A, Oppi F, Ambrosetto G, et al. The First Historically Reported

Italian Family with FTD/ALS Teaches a Lesson on C9orf72 RE: Clinical Heterogeneity and Oligogenic Inheritance. *Journal of Alzheimer's disease : JAD*. 2018;62(2):687-97.

**81.** Bartoletti-Stella A, Baiardi S, Stanzani-Maserati M, Piras S, Caffarra P, Raggi A, et al. Identification of rare genetic variants in Italian patients with dementia by targeted gene sequencing. *Neurobiology of aging*. 2018;66:180 e23-e31.

**82.** Pittois K, Deleersnijder W, Merregaert J. cDNA sequence analysis, chromosomal assignment and expression pattern of the gene coding for integral membrane protein 2B. *Gene*. 1998;217(1-2):141-9.

**83.** Vidal R, Calero M, Revesz T, Plant G, Ghiso J, Frangione B. Sequence, genomic structure and tissue expression of Human BRI3, a member of the BRI gene family. *Gene*. 2001;266(1-2):95-102.

**84.** Deleersnijder W, Hong G, Cortvrindt R, Poirier C, Tylzanowski P, Pittois K, et al. Isolation of markers for chondro-osteogenic differentiation using cDNA library subtraction. Molecular cloning and characterization of a gene belonging to a novel multigene family of integral membrane proteins. *The Journal of biological chemistry*. 1996;271(32):19475-82.

**85.** Akiyama H, Kondo H, Arai T, Ikeda K, Kato M, Iseki E, et al. Expression of BRI, the normal precursor of the amyloid protein of familial British dementia, in human brain. *Acta neuropathologica*. 2004;107(1):53-8.

**86.** Choi SI, Vidal R, Frangione B, Levy E. Axonal transport of British and Danish

amyloid peptides via secretory vesicles. *FASEB journal : official publication of the Federation of American Societies for Experimental Biology*. 2004;18(2):373-5.

**87.** Martin L, Fluhrer R, Reiss K, Kremmer E, Saftig P, Haass C. Regulated intramembrane proteolysis of Bri2 (Itm2b) by ADAM10 and SPPL2a/SPPL2b. *The Journal of biological chemistry*. 2008;283(3):1644-52.

**88.** Sanchez-Pulido L, Devos D, Valencia A. BRICHOS: a conserved domain in proteins associated with dementia, respiratory distress and cancer. *Trends in biochemical sciences*. 2002;27(7):329-32.

**89.** Martin L, Fluhrer R, Haass C. Substrate requirements for SPPL2b-dependent regulated intramembrane proteolysis. *The Journal of biological chemistry*. 2009;284(9):5662-70.

**90.** Fluhrer R, Martin L, Klier B, Haug-Kroper M, Grammer G, Nuscher B, et al. The alpha-helical content of the transmembrane domain of the British dementia protein-2 (Bri2) determines its processing by signal peptide peptidase-like 2b (SPPL2b). *The Journal of biological chemistry*. 2012;287(7):5156-63.

**91.** Fotinopoulou A, Tsachaki M, Vlavaki M, Pouloupoulos A, Rostagno A, Frangione B, et al. BRI2 interacts with amyloid precursor protein (APP) and regulates amyloid beta (A $\beta$ ) production. *The Journal of biological chemistry*. 2005;280(35):30768-72.

**92.** Matsuda S, Matsuda Y, Snapp EL, D'Adamio L. Maturation of BRI2 generates a specific inhibitor that reduces APP processing at the plasma membrane and in endocytic vesicles. *Neurobiology of aging*. 2011;32(8):1400-8.

**93.** Matsuda S, Giliberto L, Matsuda Y, Davies P, McGowan E, Pickford F, et al. The familial dementia BRI2 gene binds the Alzheimer gene amyloid-beta precursor protein and inhibits amyloid-beta production. *The Journal of biological chemistry*. 2005;280(32):28912-6.

**94.** Matsuda S, Senda T. BRI2 as an anti-Alzheimer gene. *Medical molecular morphology*. 2019;52(1):1-7.

**95.** Kim J, Miller VM, Levites Y, West KJ, Zwizinski CW, Moore BD, et al. BRI2 (ITM2b) inhibits A $\beta$  deposition in vivo. *The Journal of neuroscience : the official journal of the Society for Neuroscience*. 2008;28(23):6030-6.

**96.** Hedlund J, Johansson J, Persson B. BRICHOS - a superfamily of multidomain proteins with diverse functions. *BMC research notes*. 2009;2:180.

**97.** Willander H, Hermansson E, Johansson J, Presto J. BRICHOS domain associated with lung fibrosis, dementia and cancer--a chaperone that prevents amyloid fibril formation? *The FEBS journal*. 2011;278(20):3893-904.

**98.** Peng S, Fitzen M, Jornvall H, Johansson J. The extracellular domain of Bri2 (ITM2B) binds the ABri peptide (1-23) and amyloid beta-peptide (A $\beta$ 1-40): Implications for Bri2 effects on processing of amyloid precursor protein and A $\beta$  aggregation. *Biochemical and biophysical research communications*. 2010;393(3):356-61.

**99.** Willander H, Presto J, Askarieh G, Biverstal H, Frohm B, Knight SD, et al. BRICHOS domains efficiently delay fibrillation of amyloid beta-peptide. *The*

Journal of biological chemistry. 2012;287(37):31608-17.

**100.** Cohen SIA, Arosio P, Presto J, Kurudenkandy FR, Biverstal H, Dolfe L, et al. A molecular chaperone breaks the catalytic cycle that generates toxic Abeta oligomers. *Nature structural & molecular biology*. 2015;22(3):207-13.

**101.** Poska H, Haslbeck M, Kurudenkandy FR, Hermansson E, Chen G, Kostallas G, et al. Dementia-related Bri2 BRICHOS is a versatile molecular chaperone that efficiently inhibits Abeta42 toxicity in Drosophila. *The Biochemical journal*. 2016;473(20):3683-704.

**102.** Arosio P, Michaels TC, Linse S, Mansson C, Emanuelsson C, Presto J, et al. Kinetic analysis reveals the diversity of microscopic mechanisms through which molecular chaperones suppress amyloid formation. *Nature communications*. 2016;7:10948.

**103.** Chen G, Abelein A, Nilsson HE, Leppert A, Andrade-Talavera Y, Tambaro S, et al. Bri2 BRICHOS client specificity and chaperone activity are governed by assembly state. *Nature communications*. 2017;8(1):2081.

**104.** Yao W, Yin T, Tambini MD, D'Adamio L. The Familial dementia gene ITM2b/BRI2 facilitates glutamate transmission via both presynaptic and postsynaptic mechanisms. *Scientific reports*. 2019;9(1):4862.

**105.** Schwenk J, Perez-Garci E, Schneider A, Kollewe A, Gauthier-Kemper A, Fritzius T, et al. Modular composition and dynamics of native GABAB receptors identified by high-resolution proteomics. *Nature neuroscience*. 2016;19(2):233-42.

**106.** Pickford F, Coomaraswamy J, Jucker M, McGowan E. Modeling familial British dementia in transgenic mice. *Brain pathology*. 2006;16(1):80-5.

**107.** Vidal R, Barbeito AG, Miravalle L, Ghetti B. Cerebral amyloid angiopathy and parenchymal amyloid deposition in transgenic mice expressing the Danish mutant form of human BRI2. *Brain pathology*. 2009;19(1):58-68.

**108.** Coomaraswamy J, Kilger E, Wolfing H, Schafer C, Kaeser SA, Wegenast-Braun BM, et al. Modeling familial Danish dementia in mice supports the concept of the amyloid hypothesis of Alzheimer's disease. *Proceedings of the National Academy of Sciences of the United States of America*. 2010;107(17):7969-74.

**109.** Giliberto L, Matsuda S, Vidal R, D'Adamio L. Generation and initial characterization of FDD knock in mice. *PLoS One*. 2009;4(11):e7900.

**110.** Tamayev R, Giliberto L, Li W, d'Abramo C, Arancio O, Vidal R, et al. Memory deficits due to familial British dementia BRI2 mutation are caused by loss of BRI2 function rather than amyloidosis. *The Journal of neuroscience : the official journal of the Society for Neuroscience*. 2010;30(44):14915-24.

**111.** Tamayev R, Matsuda S, Fa M, Arancio O, D'Adamio L. Danish dementia mice suggest that loss of function and not the amyloid cascade causes synaptic plasticity and memory deficits. *Proceedings of the National Academy of Sciences of the United States of America*. 2010;107(48):20822-7.

**112.** Lansbury PT, Lashuel HA. A century-old debate on protein aggregation

and neurodegeneration enters the clinic. *Nature*. 2006;443(7113):774-9.

**113.** Onos KD, Sukoff Rizzo SJ, Howell GR, Sasner M. Toward more predictive genetic mouse models of Alzheimer's disease. *Brain research bulletin*. 2016;122:1-11.

**114.** Baker CL, Pera MF. Capturing Totipotent Stem Cells. *Cell stem cell*. 2018;22(1):25-34.

**115.** Brack AS, Rando TA. Tissue-specific stem cells: lessons from the skeletal muscle satellite cell. *Cell stem cell*. 2012;10(5):504-14.

**116.** Schofield R. The relationship between the spleen colony-forming cell and the haemopoietic stem cell. *Blood cells*. 1978;4(1-2):7-25.

**117.** Evans MJ, Kaufman MH. Establishment in culture of pluripotential cells from mouse embryos. *Nature*. 1981;292(5819):154-6.

**118.** Thomson JA, Itskovitz-Eldor J, Shapiro SS, Waknitz MA, Swiergiel JJ, Marshall VS, et al. Embryonic stem cell lines derived from human blastocysts. *Science*. 1998;282(5391):1145-7.

**119.** Zarbin M, Sugino I, Townes-Anderson E. Concise Review: Update on Retinal Pigment Epithelium Transplantation for Age-Related Macular Degeneration. *Stem cells translational medicine*. 2019;8(5):466-77.

**120.** Gurdon JB. The developmental capacity of nuclei taken from intestinal epithelium cells of feeding tadpoles. *Journal of embryology and experimental morphology*. 1962;10:622-40.

**121.** Wilmut I, Schnieke AE, McWhir J, Kind AJ, Campbell KH. Viable offspring derived from fetal and adult mammalian cells. *Nature*. 1997;385(6619):810-3.

**122.** Noggle S, Fung HL, Gore A, Martinez H, Satriani KC, Prosser R, et al. Human oocytes reprogram somatic cells to a pluripotent state. *Nature*. 2011;478(7367):70-5.

**123.** Takahashi K, Yamanaka S. Induction of pluripotent stem cells from mouse embryonic and adult fibroblast cultures by defined factors. *Cell*. 2006;126(4):663-76.

**124.** Boland MJ, Hazen JL, Nazor KL, Rodriguez AR, Gifford W, Martin G, et al. Adult mice generated from induced pluripotent stem cells. *Nature*. 2009;461(7260):91-4.

**125.** Daley GQ, Lensch MW, Jaenisch R, Meissner A, Plath K, Yamanaka S. Broader implications of defining standards for the pluripotency of iPSCs. *Cell stem cell*. 2009;4(3):200-1; author reply 2.

**126.** Takahashi K, Tanabe K, Ohnuki M, Narita M, Ichisaka T, Tomoda K, et al. Induction of pluripotent stem cells from adult human fibroblasts by defined factors. *Cell*. 2007;131(5):861-72.

**127.** Yu J, Vodyanik MA, Smuga-Otto K, Antosiewicz-Bourget J, Frane JL, Tian S, et al. Induced pluripotent stem cell lines derived from human somatic cells. *Science*. 2007;318(5858):1917-20.

**128.** Stadtfeld M, Nagaya M, Utikal J, Weir G, Hochedlinger K. Induced pluripotent stem cells generated without viral integration. *Science*. 2008;322(5903):945-9.

- 129.** Fusaki N, Ban H, Nishiyama A, Saeki K, Hasegawa M. Efficient induction of transgene-free human pluripotent stem cells using a vector based on Sendai virus, an RNA virus that does not integrate into the host genome. *Proceedings of the Japan Academy Series B, Physical and biological sciences.* 2009;85(8):348-62.
- 130.** Warren L, Manos PD, Ahfeldt T, Loh YH, Li H, Lau F, et al. Highly efficient reprogramming to pluripotency and directed differentiation of human cells with synthetic modified mRNA. *Cell stem cell.* 2010;7(5):618-30.
- 131.** Yu J, Hu K, Smuga-Otto K, Tian S, Stewart R, Slukvin, II, et al. Human induced pluripotent stem cells free of vector and transgene sequences. *Science.* 2009;324(5928):797-801.
- 132.** Kim D, Kim CH, Moon JI, Chung YG, Chang MY, Han BS, et al. Generation of human induced pluripotent stem cells by direct delivery of reprogramming proteins. *Cell stem cell.* 2009;4(6):472-6.
- 133.** Huangfu D, Maehr R, Guo W, Eijkelenboom A, Snitow M, Chen AE, et al. Induction of pluripotent stem cells by defined factors is greatly improved by small-molecule compounds. *Nature biotechnology.* 2008;26(7):795-7.
- 134.** Aasen T, Izpisua Belmonte JC. Isolation and cultivation of human keratinocytes from skin or plucked hair for the generation of induced pluripotent stem cells. *Nature protocols.* 2010;5(2):371-82.
- 135.** Haase A, Olmer R, Schwanke K, Wunderlich S, Merkert S, Hess C, et al. Generation of induced pluripotent stem cells from human cord blood. *Cell stem cell.* 2009;5(4):434-41.
- 136.** Zhou T, Benda C, Duzinger S, Huang Y, Li X, Li Y, et al. Generation of induced pluripotent stem cells from urine. *Journal of the American Society of Nephrology : JASN.* 2011;22(7):1221-8.
- 137.** Marti M, Mulero L, Pardo C, Morera C, Carrio M, Laricchia-Robbio L, et al. Characterization of pluripotent stem cells. *Nature protocols.* 2013;8(2):223-53.
- 138.** Itskovitz-Eldor J, Schuldiner M, Karsenti D, Eden A, Yanuka O, Amit M, et al. Differentiation of human embryonic stem cells into embryoid bodies compromising the three embryonic germ layers. *Molecular medicine.* 2000;6(2):88-95.
- 139.** Lund RJ, Narva E, Lahesmaa R. Genetic and epigenetic stability of human pluripotent stem cells. *Nature reviews Genetics.* 2012;13(10):732-44.
- 140.** International Stem Cell I, Amps K, Andrews PW, Anyfantis G, Armstrong L, Avery S, et al. Screening ethnically diverse human embryonic stem cells identifies a chromosome 20 minimal amplicon conferring growth advantage. *Nature biotechnology.* 2011;29(12):1132-44.
- 141.** Lefort N, Feyeux M, Bas C, Feraud O, Bennaceur-Griscelli A, Tachdjian G, et al. Human embryonic stem cells reveal recurrent genomic instability at 20q11.21. *Nature biotechnology.* 2008;26(12):1364-6.
- 142.** Markouli C, Couvreur De Deckersberg E, Regin M, Nguyen HT, Zambelli F, Keller A, et al. Gain of 20q11.21 in Human Pluripotent Stem Cells Impairs TGF-beta-Dependent

Neuroectodermal Commitment. Stem cell reports. 2019;13(1):163-76.

**143.** Assou S, Bouckenheimer J, De Vos J. Concise Review: Assessing the Genome Integrity of Human Induced Pluripotent Stem Cells: What Quality Control Metrics? Stem cells. 2018;36(6):814-21.

**144.** Assou S, Girault N, Plinet M, Bouckenheimer J, Sansac C, Combe M, et al. Recurrent Genetic Abnormalities in Human Pluripotent Stem Cells: Definition and Routine Detection in Culture Supernatant by Targeted Droplet Digital PCR. Stem cell reports. 2020;14(1):1-8.

**145.** Bar-Nur O, Russ HA, Efrat S, Benvenisty N. Epigenetic memory and preferential lineage-specific differentiation in induced pluripotent stem cells derived from human pancreatic islet beta cells. Cell stem cell. 2011;9(1):17-23.

**146.** Polo JM, Liu S, Figueroa ME, Kulal W, Eminli S, Tan KY, et al. Cell type of origin influences the molecular and functional properties of mouse induced pluripotent stem cells. Nature biotechnology. 2010;28(8):848-55.

**147.** Ohi Y, Qin H, Hong C, Blouin L, Polo JM, Guo T, et al. Incomplete DNA methylation underlies a transcriptional memory of somatic cells in human iPS cells. Nature cell biology. 2011;13(5):541-9.

**148.** Kim K, Doi A, Wen B, Ng K, Zhao R, Cahan P, et al. Epigenetic memory in induced pluripotent stem cells. Nature. 2010;467(7313):285-90.

**149.** Lo Sardo V, Ferguson W, Erikson GA, Topol EJ, Baldwin KK, Torkamani A. Influence of donor age on induced

pluripotent stem cells. Nature biotechnology. 2017;35(1):69-74.

**150.** Andrews PW, Ben-David U, Benvenisty N, Coffey P, Eggan K, Knowles BB, et al. Assessing the Safety of Human Pluripotent Stem Cells and Their Derivatives for Clinical Applications. Stem cell reports. 2017;9(1):1-4.

**151.** Araki H, Miura F, Watanabe A, Morinaga C, Kitaoka F, Kitano Y, et al. Base-Resolution Methylome of Retinal Pigment Epithelial Cells Used in the First Trial of Human Induced Pluripotent Stem Cell-Based Autologous Transplantation. Stem cell reports. 2019;13(4):761-74.

**152.** Mandai M, Kurimoto Y, Takahashi M. Autologous Induced Stem-Cell-Derived Retinal Cells for Macular Degeneration. The New England journal of medicine. 2017;377(8):792-3.

**153.** Takagi S, Mandai M, Gocho K, Hirami Y, Yamamoto M, Fujihara M, et al. Evaluation of Transplanted Autologous Induced Pluripotent Stem Cell-Derived Retinal Pigment Epithelium in Exudative Age-Related Macular Degeneration. Ophthalmology Retina. 2019;3(10):850-9.

**154.** Takahashi J. Preparing for first human trial of induced pluripotent stem cell-derived cells for Parkinson's disease: an interview with Jun Takahashi. Regenerative medicine. 2019;14(2):93-5.

**155.** Shi Y, Inoue H, Wu JC, Yamanaka S. Induced pluripotent stem cell technology: a decade of progress. Nature reviews Drug discovery. 2017;16(2):115-30.

**156.** Zhao X, Liu J, Ahmad I. Differentiation of embryonic stem cells into retinal neurons. Biochemical and

biophysical research communications. 2002;297(2):177-84.

**157.** Okabe S, Forsberg-Nilsson K, Spiro AC, Segal M, McKay RD. Development of neuronal precursor cells and functional postmitotic neurons from embryonic stem cells in vitro. *Mechanisms of development*. 1996;59(1):89-102.

**158.** Watanabe K, Kamiya D, Nishiyama A, Katayama T, Nozaki S, Kawasaki H, et al. Directed differentiation of telencephalic precursors from embryonic stem cells. *Nature neuroscience*. 2005;8(3):288-96.

**159.** Ikeda H, Osakada F, Watanabe K, Mizuseki K, Haraguchi T, Miyoshi H, et al. Generation of Rx+/Pax6+ neural retinal precursors from embryonic stem cells. *Proceedings of the National Academy of Sciences of the United States of America*. 2005;102(32):11331-6.

**160.** Lamba DA, Karl MO, Ware CB, Reh TA. Efficient generation of retinal progenitor cells from human embryonic stem cells. *Proceedings of the National Academy of Sciences of the United States of America*. 2006;103(34):12769-74.

**161.** Meyer JS, Shearer RL, Capowski EE, Wright LS, Wallace KA, McMillan EL, et al. Modeling early retinal development with human embryonic and induced pluripotent stem cells. *Proceedings of the National Academy of Sciences of the United States of America*. 2009;106(39):16698-703.

**162.** Munoz-Sanjuan I, Brivanlou AH. Neural induction, the default model and embryonic stem cells. *Nature reviews Neuroscience*. 2002;3(4):271-80.

**163.** Wilson HV. A New Method by Which Sponges May Be Artificially Reared. *Science*. 1907;25(649):912-5.

**164.** Dutta D, Heo I, Clevers H. Disease Modeling in Stem Cell-Derived 3D Organoid Systems. *Trends in molecular medicine*. 2017;23(5):393-410.

**165.** Lancaster MA, Knoblich JA. Organogenesis in a dish: modeling development and disease using organoid technologies. *Science*. 2014;345(6194):1247125.

**166.** Takasato M, Er PX, Chiu HS, Maier B, Baillie GJ, Ferguson C, et al. Kidney organoids from human iPS cells contain multiple lineages and model human nephrogenesis. *Nature*. 2015;526(7574):564-8.

**167.** Schwank G, Koo BK, Sasselli V, Dekkers JF, Heo I, Demircan T, et al. Functional repair of CFTR by CRISPR/Cas9 in intestinal stem cell organoids of cystic fibrosis patients. *Cell stem cell*. 2013;13(6):653-8.

**168.** Lancaster MA, Knoblich JA. Generation of cerebral organoids from human pluripotent stem cells. *Nature protocols*. 2014;9(10):2329-40.

**169.** Dye BR, Hill DR, Ferguson MA, Tsai YH, Nagy MS, Dyal R, et al. In vitro generation of human pluripotent stem cell derived lung organoids. *eLife*. 2015;4.

**170.** Nakano T, Ando S, Takata N, Kawada M, Muguruma K, Sekiguchi K, et al. Self-formation of optic cups and storable stratified neural retina from human ESCs. *Cell stem cell*. 2012;10(6):771-85.

- 171.** Eiraku M, Watanabe K, Matsuo-Takasaki M, Kawada M, Yonemura S, Matsumura M, et al. Self-organized formation of polarized cortical tissues from ESCs and its active manipulation by extrinsic signals. *Cell stem cell*. 2008;3(5):519-32.
- 172.** Eiraku M, Takata N, Ishibashi H, Kawada M, Sakakura E, Okuda S, et al. Self-organizing optic-cup morphogenesis in three-dimensional culture. *Nature*. 2011;472(7341):51-6.
- 173.** Kuwahara A, Ozone C, Nakano T, Saito K, Eiraku M, Sasai Y. Generation of a ciliary margin-like stem cell niche from self-organizing human retinal tissue. *Nature communications*. 2015;6:6286.
- 174.** Meyer JS, Howden SE, Wallace KA, Verhoeven AD, Wright LS, Capowski EE, et al. Optic vesicle-like structures derived from human pluripotent stem cells facilitate a customized approach to retinal disease treatment. *Stem cells*. 2011;29(8):1206-18.
- 175.** Zhong X, Gutierrez C, Xue T, Hampton C, Vergara MN, Cao LH, et al. Generation of three-dimensional retinal tissue with functional photoreceptors from human iPSCs. *Nature communications*. 2014;5:4047.
- 176.** Reichman S, Terray A, Slembrouck A, Nanteau C, Orioux G, Habeler W, et al. From confluent human iPS cells to self-forming neural retina and retinal pigmented epithelium. *Proceedings of the National Academy of Sciences of the United States of America*. 2014;111(23):8518-23.
- 177.** Reichman S, Slembrouck A, Gagliardi G, Chaffiol A, Terray A, Nanteau C, et al. Generation of Storable Retinal Organoids and Retinal Pigmented Epithelium from Adherent Human iPS Cells in Xeno-Free and Feeder-Free Conditions. *Stem cells*. 2017;35(5):1176-88.
- 178.** Gonzalez-Cordero A, Kruczek K, Naeem A, Fernando M, Kloc M, Ribeiro J, et al. Recapitulation of Human Retinal Development from Human Pluripotent Stem Cells Generates Transplantable Populations of Cone Photoreceptors. *Stem cell reports*. 2017;9(3):820-37.
- 179.** Slembrouck-Brec A, Rodrigues A, Rabesandratana O, Gagliardi G, Nanteau C, Fouquet S, et al. Reprogramming of Adult Retinal Muller Glial Cells into Human-Induced Pluripotent Stem Cells as an Efficient Source of Retinal Cells. *Stem cells international*. 2019;2019:7858796.
- 180.** Capowski EE, Samimi K, Mayerl SJ, Phillips MJ, Pinilla I, Howden SE, et al. Reproducibility and staging of 3D human retinal organoids across multiple pluripotent stem cell lines. *Development*. 2019;146(1).
- 181.** DiStefano T, Chen HY, Panebianco C, Kaya KD, Brooks MJ, Gieser L, et al. Accelerated and Improved Differentiation of Retinal Organoids from Pluripotent Stem Cells in Rotating-Wall Vessel Bioreactors. *Stem cell reports*. 2018;10(1):300-13.
- 182.** Ovando-Roche P, West EL, Branch MJ, Sampson RD, Fernando M, Munro P, et al. Use of bioreactors for culturing human retinal organoids improves photoreceptor yields. *Stem cell research & therapy*. 2018;9(1):156.
- 183.** Achberger K, Probst C, Haderspeck J, Bolz S, Rogal J, Chuchuy J, et al. Merging organoid and organ-on-a-chip technology to generate complex multi-layer tissue

models in a human retina-on-a-chip platform. *eLife*. 2019;8.

**184.** Wimmer RA, Leopoldi A, Aichinger M, Kerjaschki D, Penninger JM. Generation of blood vessel organoids from human pluripotent stem cells. *Nature protocols*. 2019;14(11):3082-100.

**185.** Wimmer RA, Leopoldi A, Aichinger M, Wick N, Hantusch B, Novatchkova M, et al. Human blood vessel organoids as a model of diabetic vasculopathy. *Nature*. 2019;565(7740):505-10.

**186.** Kruczek K, Swaroop A. Pluripotent stem cell-derived retinal organoids for disease modeling and development of therapies. *Stem cells*. 2020.

**187.** Buskin A, Zhu L, Chichagova V, Basu B, Mozaffari-Jovin S, Dolan D, et al. Disrupted alternative splicing for genes implicated in splicing and ciliogenesis causes PRPF31 retinitis pigmentosa. *Nature communications*. 2018;9(1):4234.

**188.** den Hollander AI, Roepman R, Koenekoop RK, Cremers FP. Leber congenital amaurosis: genes, proteins and disease mechanisms. *Progress in retinal and eye research*. 2008;27(4):391-419.

**189.** den Hollander AI, Koenekoop RK, Yzer S, Lopez I, Arends ML, Voesenek KE, et al. Mutations in the CEP290 (NPHP6) gene are a frequent cause of Leber congenital amaurosis. *American journal of human genetics*. 2006;79(3):556-61.

**190.** Drivas TG, Wojno AP, Tucker BA, Stone EM, Bennett J. Basal exon skipping and genetic pleiotropy: A predictive model of disease pathogenesis. *Science translational medicine*. 2015;7(291):291ra97.

**191.** Parfitt DA, Lane A, Ramsden CM, Carr AJ, Munro PM, Jovanovic K, et al. Identification and Correction of Mechanisms Underlying Inherited Blindness in Human iPSC-Derived Optic Cups. *Cell stem cell*. 2016;18(6):769-81.

**192.** Shimada H, Lu Q, Insinna-Kettenhofen C, Nagashima K, English MA, Semler EM, et al. In Vitro Modeling Using Ciliopathy-Patient-Derived Cells Reveals Distinct Cilia Dysfunctions Caused by CEP290 Mutations. *Cell reports*. 2017;20(2):384-96.

**193.** Molday RS, Kellner U, Weber BH. X-linked juvenile retinoschisis: clinical diagnosis, genetic analysis, and molecular mechanisms. *Progress in retinal and eye research*. 2012;31(3):195-212.

**194.** Huang KC, Wang ML, Chen SJ, Kuo JC, Wang WJ, Nhi Nguyen PN, et al. Morphological and Molecular Defects in Human Three-Dimensional Retinal Organoid Model of X-Linked Juvenile Retinoschisis. *Stem cell reports*. 2019;13(5):906-23.

**195.** Saini JS, Corneo B, Miller JD, Kiehl TR, Wang Q, Boles NC, et al. Nicotinamide Ameliorates Disease Phenotypes in a Human iPSC Model of Age-Related Macular Degeneration. *Cell stem cell*. 2017;20(5):635-47 e7.

**196.** Nassisi\* M, Wohlschlegel\* J, Liu B, Letellier C, Michiels C, Aubois A, et al. Deep-phenotyping and further insights in itm2b-related retinal dystrophy. *Retina*. 2020;in press.

**197.** Suppiah S, Didier MA, Vinjamuri S. The Who, When, Why, and How of PET Amyloid Imaging in Management of Alzheimer's Disease-Review of Literature

and Interesting Images. *Diagnostics*. 2019;9(2).

**198.** Clark CM, Pontecorvo MJ, Beach TG, Bedell BJ, Coleman RE, Doraiswamy PM, et al. Cerebral PET with florbetapir compared with neuropathology at autopsy for detection of neuritic amyloid-beta plaques: a prospective cohort study. *The Lancet Neurology*. 2012;11(8):669-78.

**199.** Villemagne VL, Pike K, Pejoska S, Boyd A, Power M, Jones G, et al. 11C-PiB PET ABri imaging in Worster-Drought syndrome (familial British dementia): a case report. *Journal of Alzheimer's disease : JAD*. 2010;19(2):423-8.

**200.** Martins F, Marafona AM, Pereira CD, Muller T, Loosse C, Kolbe K, et al. Identification and characterization of the BRI2 interactome in the brain. *Scientific reports*. 2018;8(1):3548.

**201.** Yu-Wai-Man P, Turnbull DM, Chinnery PF. Leber hereditary optic neuropathy. *Journal of medical genetics*. 2002;39(3):162-9.

**202.** Lenaers G, Hamel C, Delettre C, Amati-Bonneau P, Procaccio V, Bonneau D, et al. Dominant optic atrophy. *Orphanet journal of rare diseases*. 2012;7:46.

**203.** Fleischer A, Ayllon V, Dumoutier L, Renauld JC, Rebollo A. Proapoptotic activity of ITM2B(s), a BH3-only protein induced upon IL-2-deprivation which interacts with Bcl-2. *Oncogene*. 2002;21(20):3181-9.

**204.** Kwok MC, Holopainen JM, Molday LL, Foster LJ, Molday RS. Proteomics of photoreceptor outer segments identifies a subset of SNARE and Rab proteins implicated in membrane vesicle trafficking

and fusion. *Molecular & cellular proteomics : MCP*. 2008;7(6):1053-66.

**205.** Lam PT GC, Del Rio-Tsonis K, Robinson ML. Generation of a Retina Reporter hiPSC Line to Label Progenitor, Ganglion, and Photoreceptor Cell Types. *BioRxiv*. 2019;658963.

**206.** Gagliardi G, Ben M'Barek K, Chaffiol A, Slembrouck-Brec A, Conart JB, Nanteau C, et al. Characterization and Transplantation of CD73-Positive Photoreceptors Isolated from Human iPSC-Derived Retinal Organoids. *Stem cell reports*. 2018;11(3):665-80.

**207.** Wohlschlegel J, Argentini M, Foster V, Condroyer C, He Z, Thuret G, et al. First identification of ITM2B interactome in the human retina. Submitted 2020.

**208.** Nguyen HN, Byers B, Cord B, Shcheglovitov A, Byrne J, Gujar P, et al. LRRK2 mutant iPSC-derived DA neurons demonstrate increased susceptibility to oxidative stress. *Cell stem cell*. 2011;8(3):267-80.

**209.** Lewis SK, Nachun D, Martin MG, Horvath S, Coppola G, Jones DL. DNA Methylation Analysis Validates Organoids as a Viable Model for Studying Human Intestinal Aging. *Cellular and molecular gastroenterology and hepatology*. 2020;9(3):527-41.

**210.** Hoshino A, Horvath S, Sridhar A, Chitsazan A, Reh TA. Synchrony and asynchrony between an epigenetic clock and developmental timing. *Scientific reports*. 2019;9(1):3770.

**211.** Zeitz C, Robson AG, Audo I. Congenital stationary night blindness: an analysis and update of genotype-phenotype correlations and pathogenic

mechanisms. *Progress in retinal and eye research*. 2015;45:58-110.

**212.** Dinamarca MC, Raveh A, Schneider A, Fritzius T, Fruh S, Rem PD, et al. Complex formation of APP with GABAB receptors links axonal trafficking to amyloidogenic processing. *Nature communications*. 2019;10(1):1331.